Design, modelling, synthesis, and evaluation of inhibitors of human MPP1 and KifC1, two potential targets to drug development in cancer chemotherapy

Helal Abdulghani Helal

June 2023

Thesis submitted in accordance with the requirements of UCL School of Pharmacy for the degree of Doctor of Philosophy

UCL School of Pharmacy University College London

Supervised by:

Dr Geoff Wells

Plagiarism statement

This thesis describes research conducted in the UCL School of Pharmacy, between the 15th of December 2017 and the 14th of June 2023 under the supervision of Dr Geoff Wells. I certify that the research described is original and that any parts of the work that have been written aid the text herein and have clearly indicated by suitable citation any part of this dissertation that has already appeared in the publication.

Signed.................................   Date.....................................

Abstract

Kinesins are a family of molecular motor proteins that travel unidirectionally along microtubule tracks (MT) to perform a diverse range of functions from intracellular transport to cell division. Several compounds that inhibit either of two mitotic kinesins M phase phosphoprotein 1 (MPP1) and kinesin family member C1 (KifC1) are potential candidates for drug development in cancer chemotherapy. Human MPP1 is an N-terminal motor that travel towards the MT (+) end of microtubules and is necessary for the completion of cytokinesis. Previous studies have shown that MPP1 is upregulated in various types of bladder cancer. Recently natural products originally from lichens known as depsidones, and ascochitine from *Ascochyta pisi* Lib and *Ascochyta fabae* Speg were found to inhibit MPP1. Based on these observations a series of related compounds were designed, synthesised, tested and modelled as inhibitors of MPP1. Although the chromenone and quinolone derivative compounds as ascochitine-based inhibitors are less active compared to the depsidones and ascochitine in MPP1 ATPase inhibition assays, they are synthetically accessible analogues that could be further derivatised and optimised in order to improve their biological activity.

On the other hand, KifC1, is a C-terminal motor that cross-links with MTs during spindle assembly and move towards the MT (-) end. A set of small molecule fragments were identified using NMR-based screening, that formed the basis for a further structure-activity relationship study of the initial hits. A series of KifC1 inhibitor analogues were synthesized successfully based on the structures of the fragment hits. Molecular docking studies were also used to predict the binding affinity of the fragment analogues, suggesting fragment analogues may not compete with ATP and may interact with a potential allosteric binding site adjacent to the Mg-ADP binding pocket, which is located on the L5/α2/α3 regions of the protein. Most of the new fragment analogues that were tested showed weak binding to KifC1 in basal ATPase measurements, although partial inhibition was identified in some cases, suggesting that testing the remaining compounds is justified and that the compounds could be further improved in future studies.

The work presented improves our understanding of the SAR requirements for inhibition of MPP1 and KifC1 and provides a series of potential routes to the development of more potent analogues.

Impact statement

This PhD project has made contributions to the field of anticancer drug development by investigating two promising cancer drug targets, human mitotic kinesins MPP1 and KifC1. Both proteins play roles in cell division and blocking their activity in cancer cells has the potential to arrest cell growth and have a cytotoxic effect. The project focused on identifying potential new small molecule inhibitors of these targets and understanding their inhibitory effects on each kinesin.

For MPP1, the original hit compound R-ascochitine, was used as a starting point. Ascochitine is a natural product that is difficult to synthesise and is both chemically and metabolically unstable. Using pharmacophore-based searches, novel small molecule compounds with chromenone-3-carboxylic acid and quinolone-3-carboxylic acid core structures were identified. These compounds were successfully synthesized, modelled, and tested for their ability to inhibit MPP1 ATPase activity. Some of the new compounds have inhibitory activity comparable to that of ascochitine and have the potential to be easier to derivatise and more stable in biological environments. They provide new insights into the medicinal chemistry of the MPP1 target and have the potential to be developed into treatments for bladder cancer, a tumour type in which MPP1 is frequently overexpressed.

Additionally, the project investigated inhibitors targeting KifC1. A series of small molecule inhibitors were synthesized, modelled, and evaluated. These inhibitors were derived from fragment hits identified through complementary NMR fragment screening techniques, enabling the development of more potent fragment analogues. Once the testing of the compounds is complete, the structure-activity relationships of the fragments and their analogues can be fully evaluated. This will provide insights into how these compounds can be further modified and optimised into lead inhibitors of KifC1. Thus, this part of the project has contributed to the early-stage characterisation of KifC1 inhibitors as potential anticancer therapeutic agents of the future.

The project has made use of a number of computational methods during its course, reflecting current trends in structure-based drug design. The molecular models used in the project were generated with the assistance of artificial intelligence using Alphafold and insights into the binding modes of the compounds were obtained using open-source molecular docking software. Pharmacophore searches of compound databases have also been used to plan the synthetic chemistry parts of the project. In combination with future structural studies using x-ray crystallography we will be able to evaluate the contribution of these computational methods to the drug discovery pipeline for these targets. Taken together, the work presented in this thesis should be of interest to researchers working in the fields of medicinal chemistry, anticancer drug development, and specifically researchers working on inhibitors of mitotic kinesins in academia and the pharmaceutical industry. The successful development and refinement of the compounds described in the thesis has the potential to improve the treatment of cancer patients over the longer term.

Acknowledgements

Table of contents

Abbreviations

Å	Ångström
AA	Amino Acid
ADP	Adenosine diphosphate
ATP	Adenosine triphosphate
Aal	Alanine
Arg	Arginine
Asn	Asparagine
Asp	Aspartic acid
ACN	Acetonitrile
AcOH	Acetic acid
Aq.	Aqueous
BA	Binding affinity
BE	Binding energy
°C	Degrees Celsius
Cdk	Cyclin-dependent kinases
CENPE	Centromere-associated protein E
CPMG	Carr-Purcell-Meiboom-Gill
^{13}C-NMR	Carbon Nuclear Magnetic Resonance
d	Doublet
dd	Doublet-doublet
Da	Dalton
DMSO	Dimethylsulfoxide
DMSO-d6	Deuterated dimethyl sulfoxide
DCM	Dichloromethane
DMF	*N,N*-Dimethylformamide
DCC	*N,N*-Dicyclohexylcarbodiimide
DIPEA	*N,N*-Diisopropylethylamine
DMAP	4-Dimethylaminopyridine
DNA	Deoxyribonucleic acid
EtOH	Ethanol
EtOAc	Ethyl acetate

EDCI	*N*-Ethyl-*N'*-(3-dimethylaminopropyl) carbodiimide
Et$_3$N	Triethylamine
EtOAc	Ethyl acetate
Equiv.	Equivalent
FBDD	Fragment-based drug development
Fe	Iron powder
G$_1$	Gap phase 1
G$_2$	Gap phase 2
Glu	Glutamic acid
Gln	Glutamine
Gly	Glycine
g	gram(s)
h	Hours
H$^+$	Proton
H-B	Hydrogen bond
HRMS	High resolution mass spectrometry
HCl	Hydrochloric acid
^{1}H-NMR	Proton Nuclear Magnetic Resonance
HPLC	High Pressure Liquid Chromatography
HRMS	High Resolution Mass Spectroscopy
IC$_{50}$	Half maximal inhibitory concentration
IR	Infrared spectroscopy
ILE	Isoleucine
J	Coupling constant
kDa	Kilo Daltons
KOH	Potassium hydroxide
KIFs	Kinesin superfamily proteins
K$_2$CO$_3$	Potassium carbonate
L	Litre
LC-MS	Liquid chromatography–mass spectrometry
Leu	Leucine
Lys	Lysine
m	multiplet

M	Mitosis
M	Moles
mg	Milligrams
$MgSO_4$	Magnesium sulphate
MeCN	Acetonitrile
Me	Methyl
MeOH	Methanol
MTs	Microtubules
MTOC	Microtubule organizing centre
MAPs	Microtubule-associated proteins
MPP1	M-phase phosphoprotein 1
mg	Milligrams
mRNA	Messenger RNA
MHz	Megahertz
Min	Minutes
mmol	Millimoles
m/z	Mass-to-charge ratio
mM	Millimolar
µM	Micromolar
mL	Millilitre
µmol	Micromoles
µL	Microlitre
m.p	Melting point
MD	Motor domain
MKLP2	Mitotic Kinesin-Like Protein 2
MW	Molecular weight
NaOH	Sodium hydroxide
$NaHCO_3$	Sodium bicarbonate
NCD	Non-Claret disjunctional
NH_4Cl	Ammonium chloride
NMR	Nuclear mangentic resonance
NIS	Neck-linker initial sequences
nm	Nanometer
PDB	Protein data bank

Pd/C	Palladium on carbon
PPh$_3$	Triphenylphosphine
ppm	Parts per million
pH	Potential of hydrogen to specify acidity or basicity of aqueous solution
Pro	Proline
S	Synthesis
s	Singlet
SER	Serine
SMIs	Small molecule inhibitors
STD	Saturation-transfer difference
sat	saturated
SAR	Structure-activity relationship
siRNA	Small interfering RNA
q	Quartet
RT	Room temperature
rt	Room temperature
t$_R$	Retention time
t	Triplet
TBAHS	Tetrabutylammonium hydrogen sulphate
TSA	Thermal Shift Assay
TFA	Trifluoroacetic acid
THIQ	Tetrahydroisoquinoline
TLC	Thin layer chromatography
TMS	Tetramethylsilane
Thr	Threonine
Tyr	Tyrosine
Val	Valine
VEGF	Vascular endothelial growth factor
δ	Chemical shift

1 Introduction

This thesis describes the development of molecules to target mitotic kinesins, motor proteins that are essential to the process of cell division in mammalian cells. In this chapter the process of cell division will be discussed briefly, followed by a discussion of its relevance to cancer. The following sections will focus on kinesins as potential therapeutic targets in cancer.

1.1 Cell Cycle

Cellular reproduction is an essential process in the development of multicellular organisms and the replacement of cells that die. It involves a sequence of growth and division stages called the cell cycle [3]. The process can be divided into four stages. There are two gap phases (G1 and G2) and a synthesis phase (S phase) (Figure **1-1** A), in which the genetic material is duplicated, together these three stages G1, S and G2 are known as the interphase. The remaining stage, called the mitotic (M) phase, is made up of nuclear division (karyokinesis) and cell division (cytokinesis) which leads to the formation of two daughter cells. When the cell has left the cell cycle and has stopped dividing the cell becomes quiescent. Thus, the cell cycle is the period from the beginning of one division to the beginning of the next [4, 5].
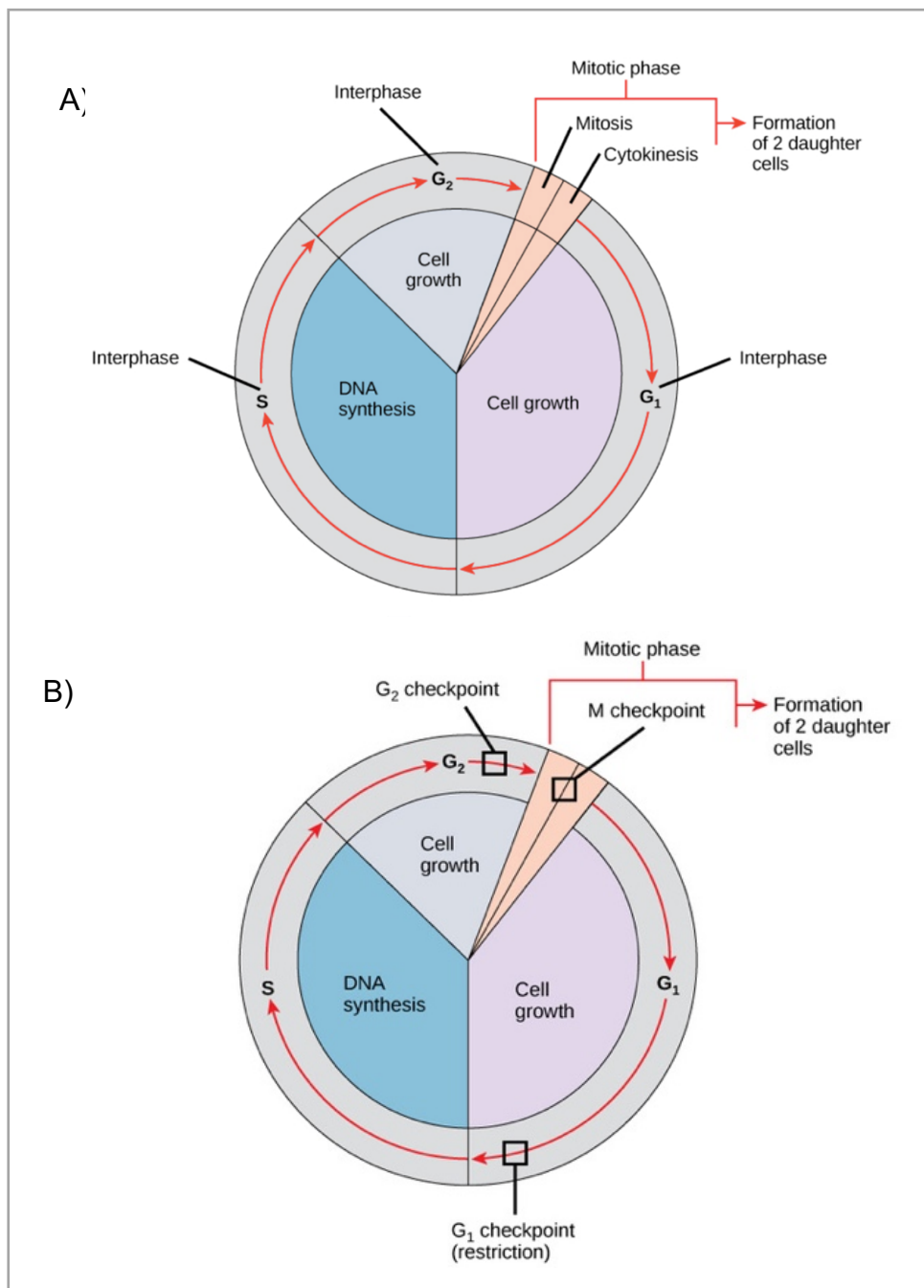
Figure 1-1 A) The Cell Cycle and B) Internal checkpoints during the cell cycle [5].

1.1.1 Interphase

The interphase period between mitotic divisions (G1, S and G2) is a period of growth and DNA replication. The G1 phase is the first growth stage after cell division. The cell matures by expanding the cytoplasm, making organelles, and adapting metabolism to prepare for division. This is followed by the synthesis

phase (S), in which DNA is replicated. After this point each chromosome consists of two sister chromatids. Subsequently, the cell enlarges during the second gap phase (G2) during which the centrioles and cell structures required for division are synthesised and assembled for mitosis and cytokinesis in (Figure **1-2**) [4, 6,7].
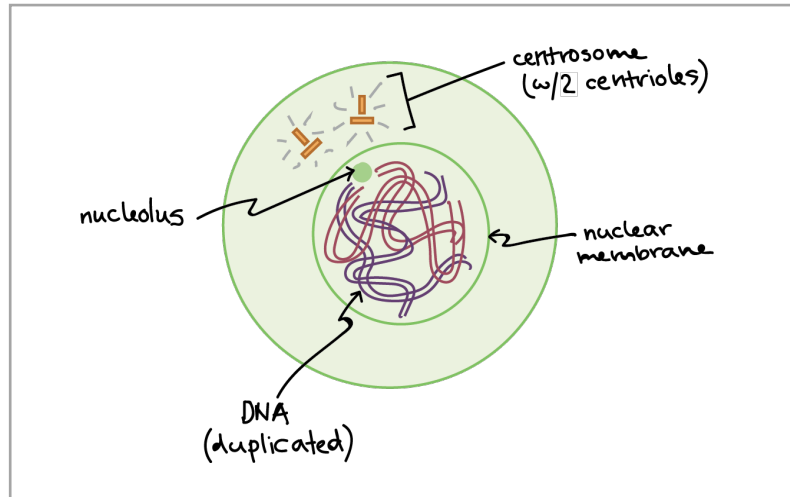
Figure 1-2 Cell in Interphase or Late G2. Figure adapted from [7].

1.1.2 Mitotic Phase

1.1.2.1 The Mitotic Spindle and Microtubules (MTs)

MTs are major components of the cytoskeleton. They are composed of polymers of hetero dimers of α-tubulin and β-tubulin, which bind together to form protofilaments. Thirteen protofilaments arrange into a cylindrical pattern (a 25 nm wide hollow cylinder) to form a microtubule [8, 9]. MTs are polar molecules, with a positively charged end that grows relatively fast and a negatively charged end that grows relatively slowly. The protofilaments are arranged in a parallel fashion in the microtubule, so that the (+) end of the MT always has (β) subunits exposed, and the (-) end has (α) subunits exposed (Figure **1-3**). Tubulin is an important and essential protein in many cellular processes, including cell division, intracellular transport, and the maintenance of cell shape [8, 10].
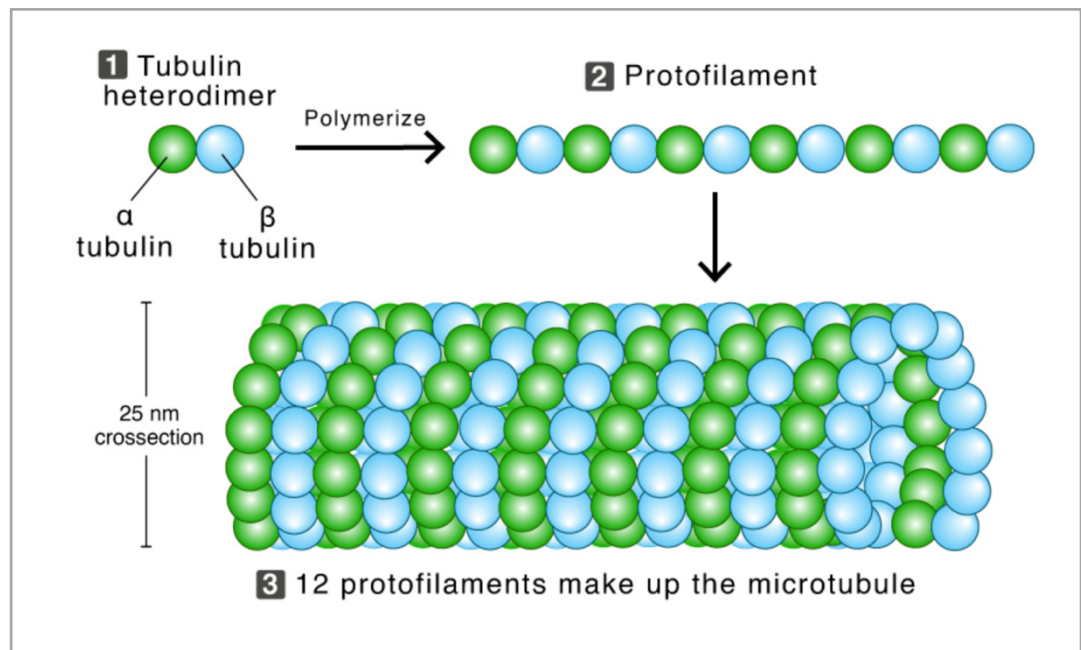
Figure 1-3 Microtubule Structure [9].

The primary structure of the spindle is an antiparallel array of MTs with their negative (-) end concentrated and anchored at the spindle poles and their positive (+) end projecting towards the chromosomes [10]. The centrosome is the main microtubule organizing centre (MTOC) of animal cells, which is composed of two centrioles. MTs play a key role in forming the mitotic spindle during cell division. The mitotic spindle plays a role in organizing and separating the chromosomes into the two separate daughter cells. Its components include microtubules, the MTOC and microtubule-associated proteins (MAPs). Three subgroups of MTs aid in the process of mitosis: astral, polar, and kinetochore microtubules. Astral microtubules radiate from the MTOCs of a cell to the cell membrane, keeping the mitotic spindle in place [11]. Polar microtubules intertwine between two MTOCs and help separate chromosomes. Kinetochore microtubules attach to assist their separation. They are tethered to the chromosomes via a complex of proteins (the kinetochore) (Figure **1-4**) [12].
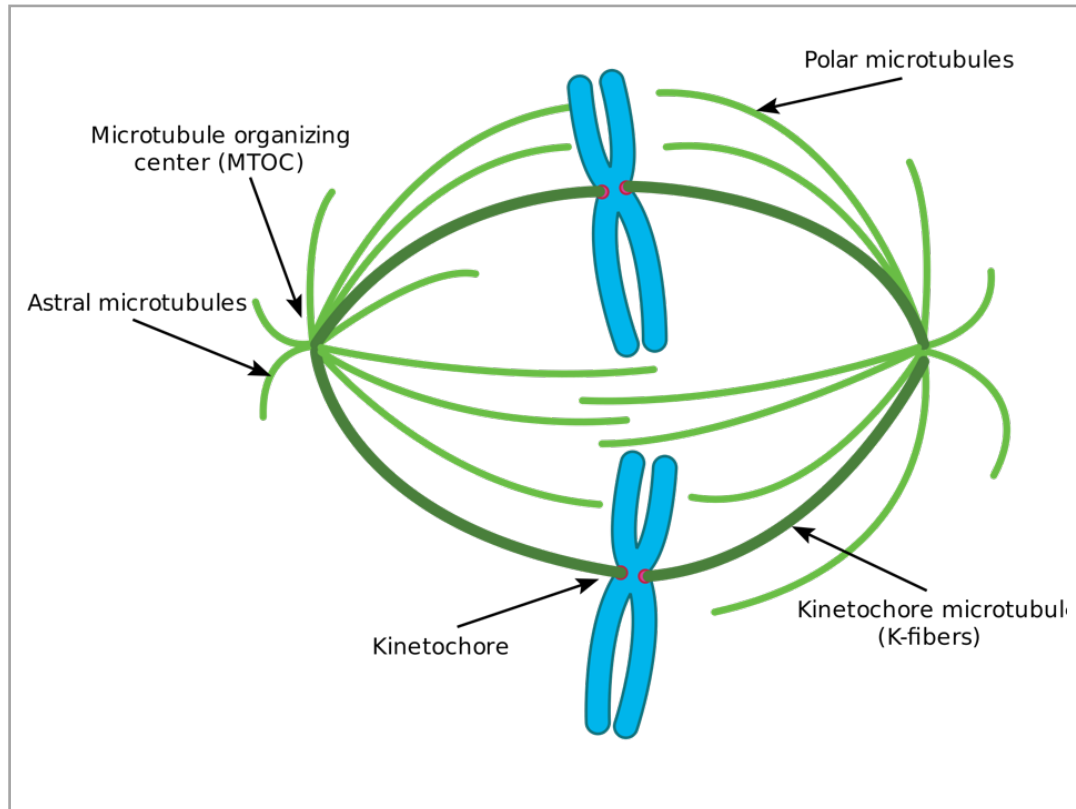
Figure 1-4 Mitotic Spindle in Cell Division [12].

1.1.2.2 Mitosis (Cell Division)

Mitosis plays a role in cell replacement, wound healing and tumour formation, although a continuous process, it is usually considered in five stages: prophase, prometaphase, metaphase, anaphase and telophase [7].

1.1.2.2.1 Prophase

In early prophase the cell starts to break down some structures such as nucleus and nuclear envelope and build others up such as mitotic spindle, setting the stage for division of the chromosomes. Chromatin in the nucleus starts to condense to form visible chromosomes after that the nucleus breaks down. The centrosome is duplicated during interphase to form two daughter centrosomes that migrate to opposite ends of the cell in early prophase. The centrosomes organise the production of MTs that form the spindle fibres that constitute the

mitotic spindle in (Figure **1-5** A). Each replicated chromosome can be seen to consist of two identical or sister chromatids which are held together by a structure known as the centromere. In late prophase, also called prometaphase the spindle fibres bind to the kinetochore. Individual fibres bind to a kinetochore structure on each side of the centromere and the chromosomes finish condensing, so they are very compact, and the nuclear envelope breaks down, releasing the chromosomes as the mitotic spindle continues to grow (Figure **1-5** B) [7].
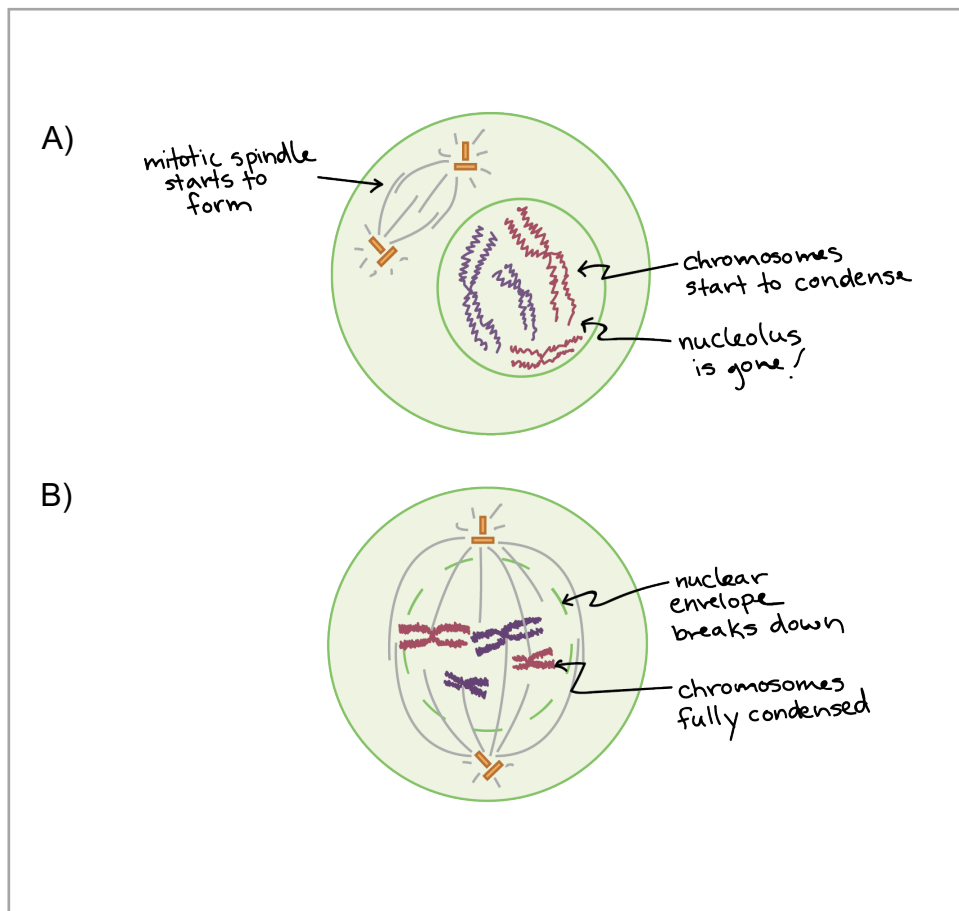
Figure 1-5 A) Cell in Early Prophase B) Cell in Late prophase and Prometaphase. Figure adapted from [7].

1.1.2.2.2 Metaphase

The kinetochores attach the chromosomes to the mitotic spindle and are arranged at the equator of the cell (the metaphase plate) (Figure **1-6**).
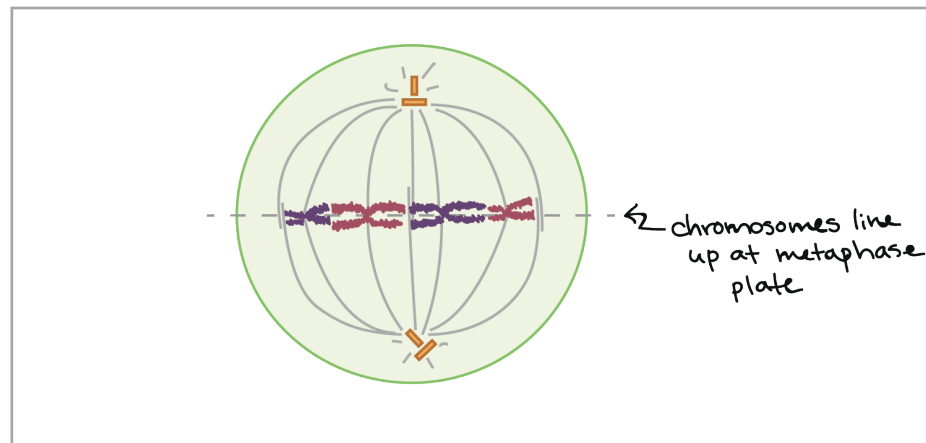
Figure 1-6 Cell in Metaphase. Figure adapted from [7].

1.1.2.2.3 Anaphase

The centrosomes divide, and each chromosome splits making the two sister chromatids free to move to opposite ends of the cell. The separated sister chromatids are referred to as daughter chromosomes (Figure **1-7**).
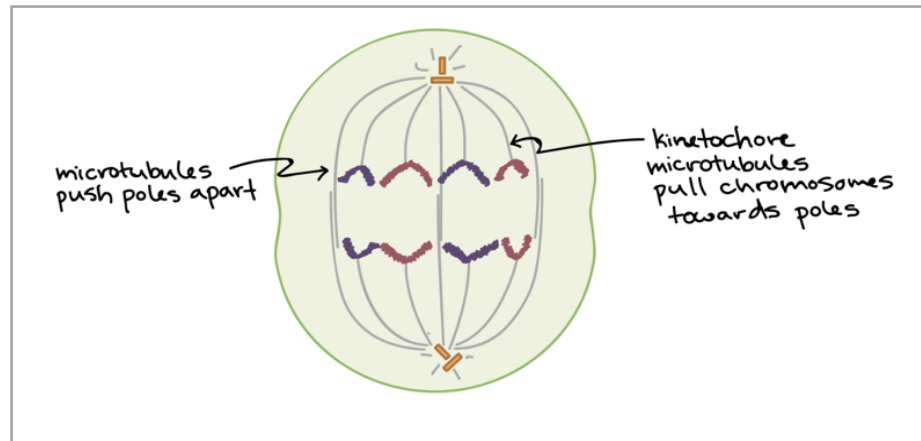
Figure 1-7 Cell in Anaphase. Figure adapted from [7].

1.1.2.2.4 Telophase

In the final stage of mitosis, the nuclear membrane and nucleus reform around the chromosomes collected at either pole of the cell, the chromosomes decondense, and the spindle fibers disperse (Figure **1-8**).
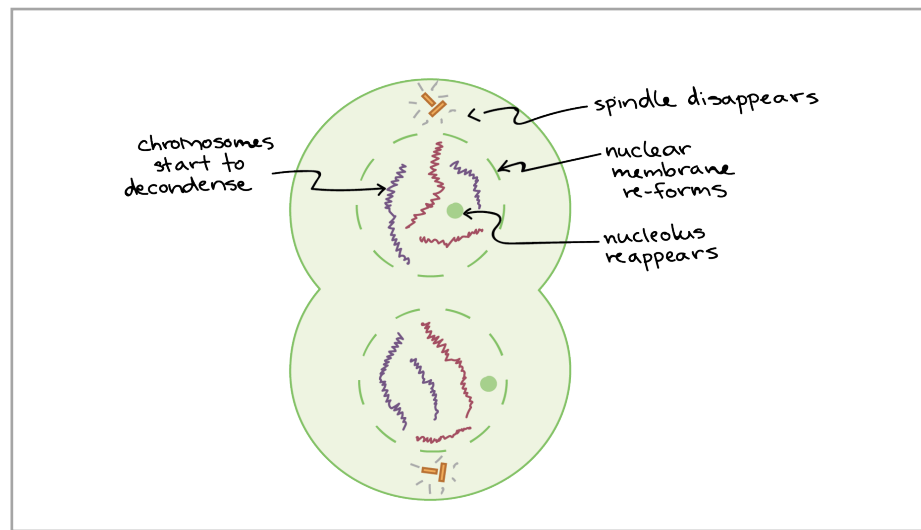
Figure 1-8 Cell in Telophase. Figure adapted from [7].

1.1.2.3 Cytokinesis

The division of the cell cytoplasm produces two daughter cells via formation of a cleavage furrow, which results in separation of the two daughter cells (Figure **1-9**).
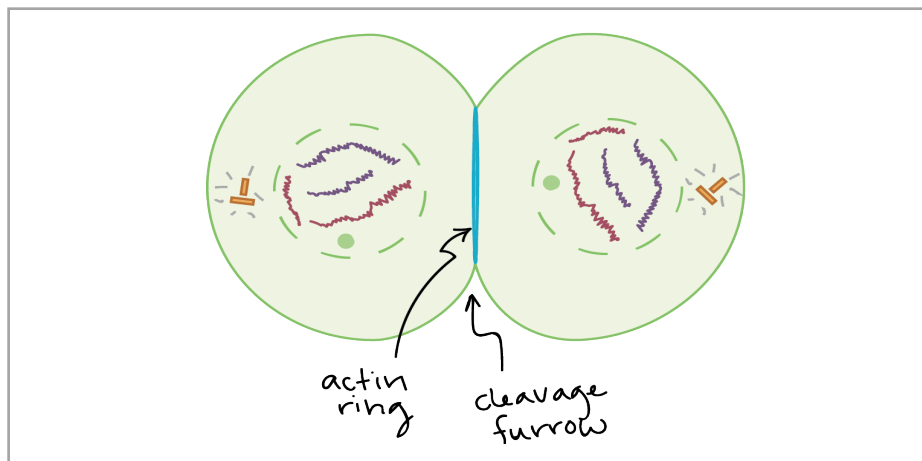
Figure 1-9 Cytokinesis and Daughter Cells after Cytokinesis. Figure adapted from [7].

The cell cycle is dependent on the organised movement of genetic material to the poles of the mitotic spindle and into the daughter cells. Spindle formation, chromosome separation and motility of the chromosomes all

require a series of dedicated mechanisms which function in a robust and organised manner. The various elements of the cell cycle are controlled by a series of cell-cycle control systems. These are based on the activities of cyclin-dependent kinases (Cdk), the master regulators of the cell cycle [4]. The activity of these regulators influence define the cell cycle state and are coupled to a system of three independent checkpoints, which integrate signals concerning the current state of the cell and block transition into to the next cell cycle state until error free progression can be ensured for example, the spindle assembly checkpoint (SAC) also called M checkpoint monitors the correct attachment of chromosomes to the mitotic spindle (Figure **1-1** B). Because the separation of the sister chromatids during anaphase is an irreversible step, the cycle will not proceed until the chromosomes are firmly attached to at least two spindle fibres from opposite poles of the cell [13].

1.2 Cancer

Cancer is characterized by the uncontrolled growth and division of cells. This often results from mutations in genes that regulate the cell cycle, leading to a loss of normal cell cycle control. As a result, cells can divide and multiply without normal regulation, leading to the formation of a mass of abnormal cells (a tumour) that can invade and spread to other parts of the body through the blood and lymphatic systems, a process called metastasis [14]. There are several main types of cancer. Carcinomas are cancers that originate in the skin or in tissues that line or cover internal organs. Sarcomas are cancers that begins in bone, cartilage, fat, muscle, blood vessels, or other connective or supportive tissues. Leukaemias are cancers that starts in blood-forming tissue, such as the bone marrow, cause large numbers of abnormal blood cells to be produced and enter the blood. Lymphomas and multiple myeloma are cancers that originate from the cells of the immune system. Central nervous system cancers are cancers that begin in the tissues of the brain and spinal cord [15]. Cancer results from the clonal expansion of progenitor cells that have incurred genetic damage and consequently acquired mutations. Mutations in one or more normal regulatory genes (proto-oncogenes, tumor suppresser genes, genes that regulate apoptosis

and/or cell death via apoptosis, DNA repair genes) leads to non-lethal genetic damage that may result in cancer [16]. Abnormalities in the cell cycle and the genetic mutations that drive them are an important hallmark of cancer. Understanding these cellular and genetic changes is crucial for the development of new and effective treatments for cancer.

1.2.1 Hallmarks of Cancer

The " Hallmarks of Cancer " is a concept in cancer biology that was introduced in original paper that published in 2000 by Robert Weinberg and Douglas Hanahan, It describes six essential characteristics that are common to most types of cancer and are crucial for the development and progression of the disease [15]. These hallmarks include self-sufficiency in growth signals, insensitivity to growth inhibitory signals, resistance of apoptosis, limitless replicative potential, sustained angiogenesis, and invasion of and metastasis (Figure **1-10** A) [17]. In 2011, Robert Weinberg and Douglas Hanahan published an updated paper titled "The Hallmarks of Cancer: The Next Generation," which expanded on the original six hallmarks and identified two emerging hallmarks: deregulating cellular energetics and evasion of immune destruction. They also added two enabling characteristics: genome instability and tumour-promoting inflammation (Figure **1-10** B) [16].
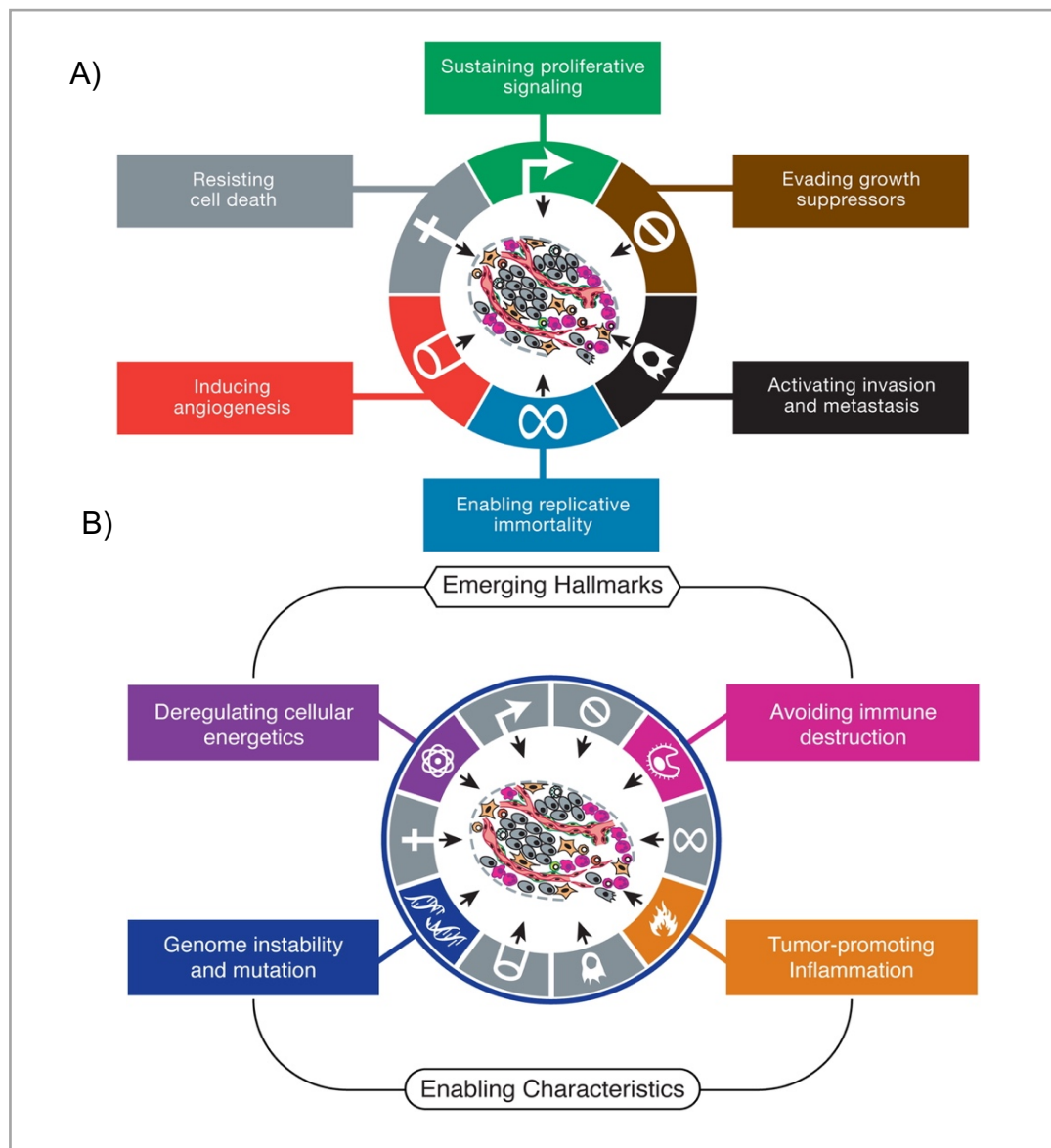
Figure 1-10 A)The original hallmarks of cancer presented by Hanahan and Weinberg in 2000 [17] B) The emerging hallmarks of cancer and enabling characteristics by Hanahan and Weinberg in 2011[16].

1.2.1.1 Self-sufficiency in growth signals

Cancer cells can grow and divide in the absence of normal signals that regulate cell growth and division. Normally, cells receive signals from other cells and their environment that stimulate or inhibit cell growth and division. In cancer, these signals become deregulated, allowing cells to grow and divide even without normal stimulation. A demonstration of this difference is that unlike normal cells

that require the addition of growth factors to be cultured outside the body (Figure **1-11**), cancer cells can proliferate *ex vivo* without the addition of growth factors or growth-stimulating protein signals [16].
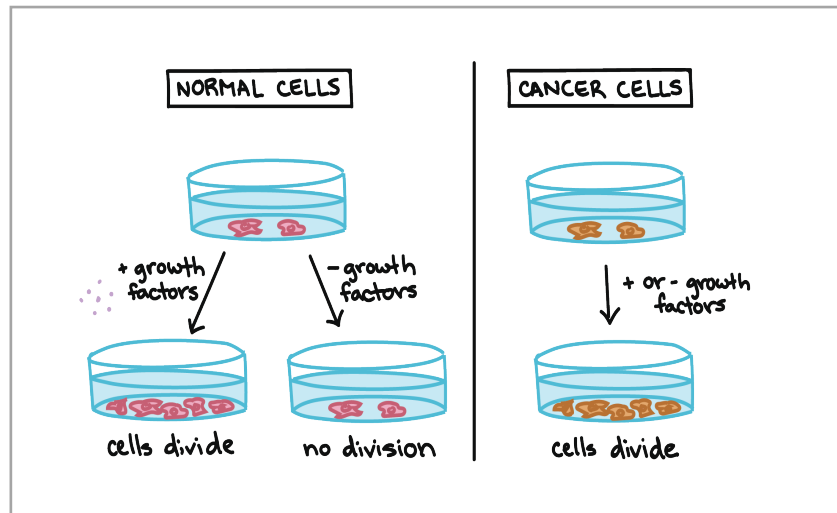
Figure 1-11 Differences in growth between normal cell and cancer cell. Figure adapted from [16].

The growth factor pathways in these cells are frequently in a state of permanent activation. Cancer cells may acquire growth self-sufficiency, by acquiring the ability to synthesize the growth factors to which they are responsive.

Cancer cells may also have mutations in growth signalling pathways which can result in activity in the absences of growth signals. These oncoproteins do not depend on growth factors or other external signals [16].

1.2.1.2 Insensitivity to growth inhibitory signals

Normally the cell cycle is regulated and balanced by antigrowth signals as well as growth signals. Tumour suppressor genes inhibit cell cycle progression that leads to cell proliferation. When these genes operate normally, they prevent tumours from forming. In cancer, these inhibitory regulators may be inactive or non-functional or have a low level of activity [18].

1.2.1.3 Resistance of apoptosis

Cancer cells can evade programmed cell death (apoptosis), allowing them to survive and multiply even in the face of DNA damage or other stress [15, 19].

1.2.1.4 Limitless replicative potential

Most human cells have the ability to undergo 60-70 doubling cycles, after this point cell will enter non-replicative senescence, resulting from shortening of the telomeres at the ends of chromosomes. Loss of telomeres beyond a certain point lead to chrosomal abnormalities and death. In cancer, cells have unlimited replicative potential, meaning they can divide and multiply indefinitely [20].

1.2.1.5 Development of sustained angiogenesis

Tumour angiogenesis is a process in which tumours develop and grow new blood vessels to maintain a supply of oxygen and nutrients to sustain growth and survival [21, 22].

1.2.1.6 Ability to invade and metastasize

Cancer cells can break away from their site or organ of origin to invade surrounding tissues and spread to distant parts of the body, a process called metastasis, allowing to establish secondary tumours and increase the risk of disease progression [21, 22].

1.2.1.7 Reprogramming of cellular metabolism

The highly emerging hallmarks of cancer is reprogramming of cellular metabolism which refers to the changes in metabolic pathways and processes that occur in cells under different conditions or in response to specific stimuli [23]. These changes are often necessary for cells to adapt to new environments, respond to stress or damage, or support growth and proliferation [24, 25].

1.2.1.8 Evading immune destruction

Another highly emerging hallmarks of cancer is evading immune destruction which refers to the ability of certain cells or organisms to evade the immune system's detection and attack. This can occur in a variety of contexts, such as in the case of cancer cells or pathogenic viruses that have developed mechanisms to avoid recognition by the immune system [26].

1.2.1.9 Genome instability

The tendency of a genome to acquire mutations or changes in its DNA sequence, which can lead to genetic disorders and diseases, including cancer. It can occur due to a variety of factors, such as errors during DNA replication, exposure to environmental mutagens, or defects in DNA repair mechanisms [27, 28].

1.2.1.10 Tumor-promoting inflammation

Tumour-promoting inflammation is a type of chronic inflammation that occurs in the microenvironment of tumours and promotes their growth and spread. This type of inflammation involves the infiltration of immune cells, such as macrophages, into the tumour site, where they release cytokines, chemokines, growth factors, and other signalling molecules that stimulate tumour cell proliferation, angiogenesis, and metastasis [29].

Targeting tumour-promoting inflammation is a promising approach for cancer prevention and treatment. Several anti-inflammatory drugs, such as nonsteroidal anti-inflammatory drugs (NSAIDs), have been shown to reduce the risk of certain cancers, including colorectal cancer. Immunotherapy, which harnesses the power of the immune system to attack cancer cells, also holds promise for targeting tumour-promoting inflammation and improving cancer outcomes [30].

These hallmarks provide a framework for understanding the complex biology of cancer and for developing new strategies for its prevention, diagnosis, and treatment [31].

1.2.2 Anticancer therapy

Anticancer therapy refers to the use of treatments to target and kill cancer cells in the body. The goal of anticancer therapy is to prevent the growth and spread of cancer cells, while minimizing damage to healthy cells and tissues. There are several types of anticancer therapy, including surgery, radiation therapy, chemotherapy, immunotherapy, and targeted therapy. Surgery involves the physical removal of cancerous tissue from the body. It is often used to remove solid tumours and is usually combined with other treatments, such as radiation therapy or chemotherapy. Radiation therapy uses high-energy radiation to kill cancer cells. It can be delivered externally (external beam radiation) or internally (brachytherapy). Chemotherapy usually refers to use of cytotoxic (cell-killing) chemical agents in an attempt to cure the cancer or reduce its size and slow its growth. Anticancer agents are divided into several classes based on their mechanism and site of action; commonly used drug classes include alkylating agents, antimetabolites, and topoisomerase inhibitors. In most cases, combination therapy with different classes of chemotherapy drugs is used to increase efficacy and reduce toxicity and resistance. This is because different classes of drugs target cancer cells in different ways and using a combination of drugs can increase the chances of killing cancer cells while minimizing damage to healthy cells [32].

The choice of therapy depends on the type and stage of cancer, as well as the patient's overall health and other factors. Often, a combination of therapies is used to treat cancer, in order to maximize the chances of success [33].

1.3 Kinesins

The kinesin superfamily of proteins (KIFs) are microtubule-based molecular motors that are involved in the transport of cargo within cells. They are part of a larger family of motor proteins that includes dyneins, which move in the opposite direction using the microtubule (MT) system transporting a variety of cargos including cellular proteins, macromolecules, and organelles. Kinesins convert the

chemical energy of adenosine triphosphate (ATP) into motility by driving internal conformational changes [34]. They travel unidirectionally along (MT) tracks in both minus-end and plus-end directions (Figure **1-12**) [34]. KIFs play critical roles in various cellular processes, including cell division, intracellular transport, and cilia and flagella motility. They are also involved in the maintenance of cellular architecture and the regulation of signal transduction pathways.
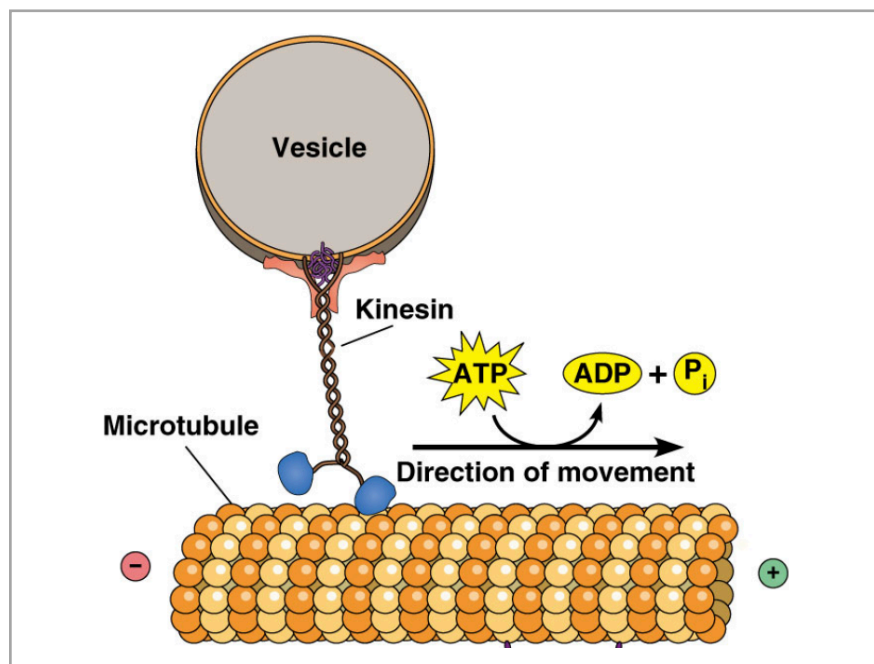
Figure 1-12 Kinesin 'walks' along the microtubule [24.]

The first kinesin was purified and identified in 1985 when a unique motile protein was separated from the cytoplasm of the giant axons in squid [35, 36]. This protein was named kinesin-1 (also known as conventional kinesin, Kif5B). In the following decades an increasing number of kinesins with a highly conserved motor domain were identified [37]. Up to now, more than 650 KIFs have been identified in eukaryotes. However, kinesins seem to be absent in bacteria and archaea [1]. Currently, mammalian kinesins can be classified into 16 subfamilies, which are termed kinesin-1 to kinesin-14B, based on phylogenetic analysis of the motor domain (Figure **1-13**) [38]. The human genome harbours 44 different kinesins and several have been reported to play crucial roles in the development of various diseases [39].
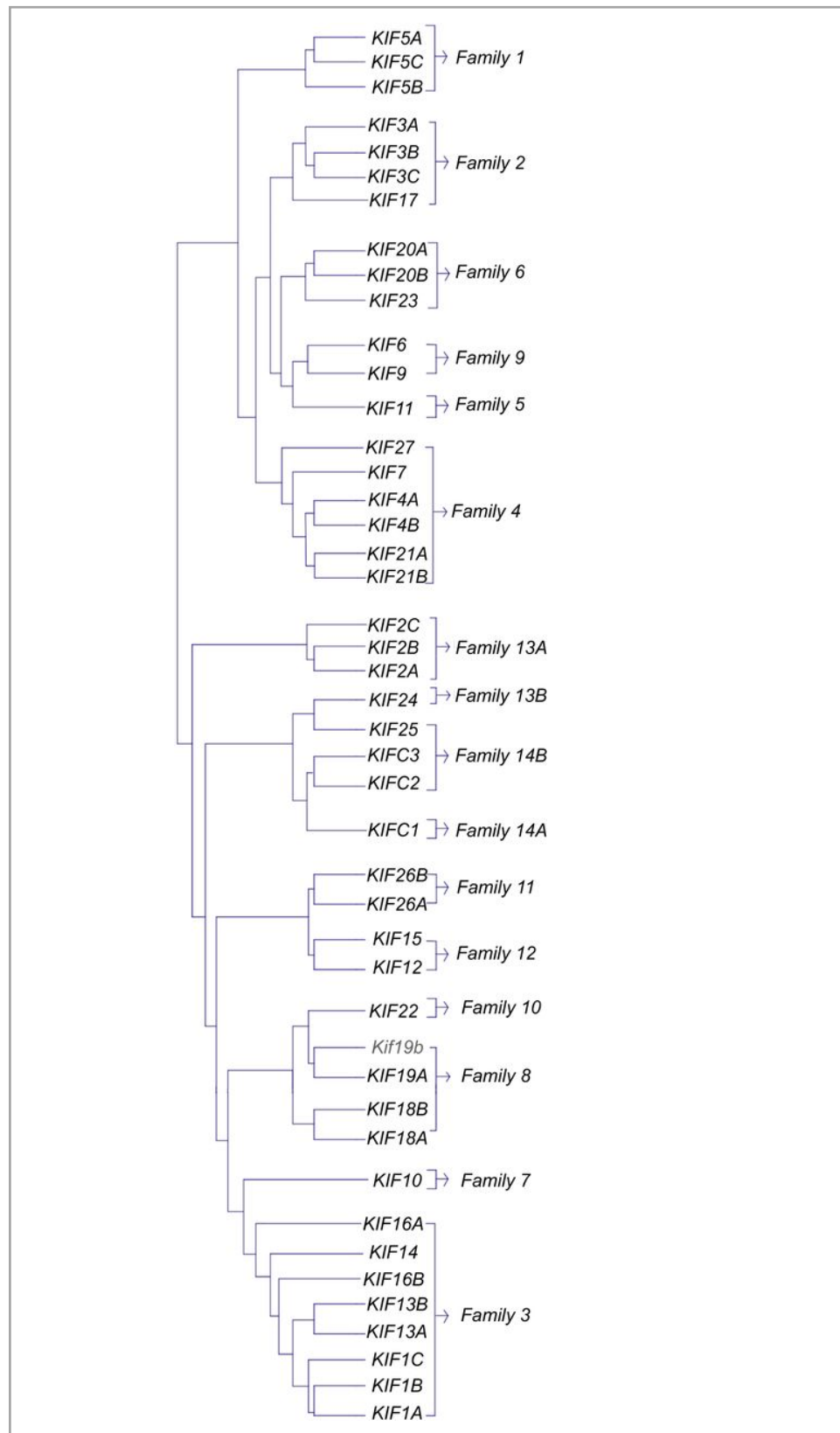
Figure 1-13 KIFs can be classified into 16 families by phylogenetic analysis of their motor domains [38].

1.3.1 Structure of Kinesins

A typical kinesin is composed of three main domains: the head domain, also referred to as the motor domain (MD), connected to a tail via a stalk, and typically form dimers. The motor domain contains a catalytically active ATPase site as well as an MT binding site [35]. It also supports force generation with the aid of the small neck linker region that follows the motor domain, the tail domain which binds diverse cargos or vesicles directly or in assistance with adaptor or scaffold proteins, and a coiled coil domain or the stalk which is connected to the motor and tail domains (Figure **1-14**) [39].
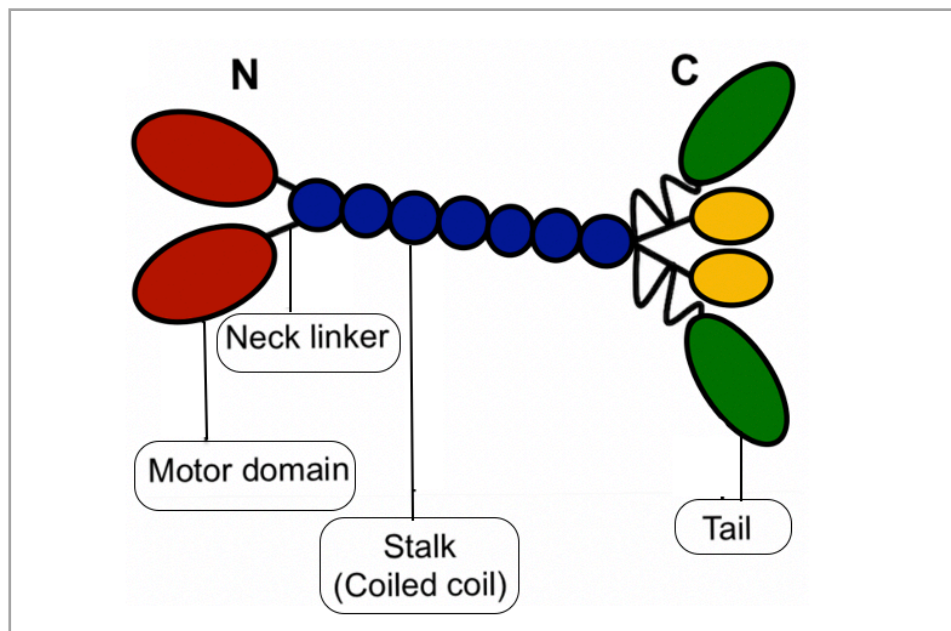
Figure 1-14 Schematic figure of a typical N-terminal motor kinesins dimer. Some kinesins bind directly to cargos through their globular tails (yellow) as homodimers while others, for example, Kif5B, bind to their cargos as heterodimers in assistance with kinesin light chains (green).

In addition to the motor domains and coiled-coil stalk, some kinesins contain additional structural elements, such as light chains, which can regulate the activity of the motor. The number, size, and sequence of these elements vary among different kinesins and are used to classify them into different subfamilies.

1.3.1.1 Kinesin motor domain

Generally, KIFs can be grouped into three types based on the location of their motor domain, namely N-terminal kinesins, which have their motor domain in the N-terminal region, M-kinesins which have a motor domain in the middle of the polypeptide chain and the C-terminal kinesins, which have their motor domain in the carboxyl-terminal region. N-terminal and C-terminal kinesins drive MT plus and minus end motilities, respectively, while M-kinesins depolymerize MTs (Figure **1-15**) [40].
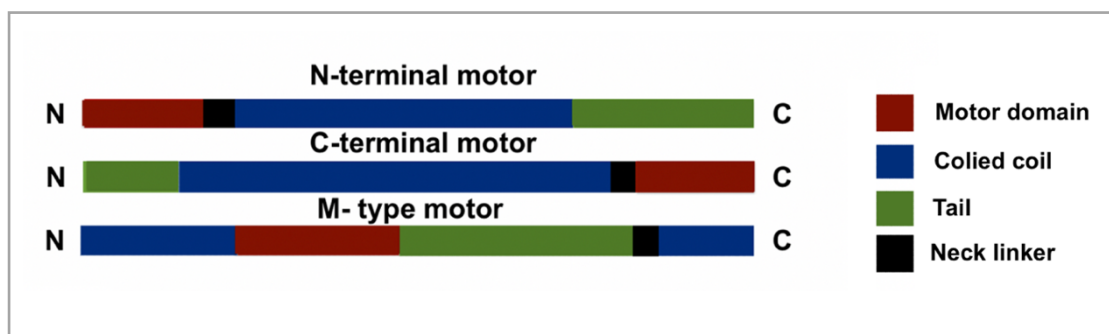

Figure 1-15 Three domain structure of KIFs. Motor domains (red), coiled-coil (blue), neck linker (black), and tail domains (green) are marked. N-terminal kinesins have their motor domain in the N-terminal region, M-type kinesins have a motor domain in the middle of the polypeptide chain and C-terminal kinesins have their motor domain in the C-terminal region.

The overall structure of the kinesin motor domain consists of an eight-stranded mixed β-sheet surrounded by three α-helices on each side (Figure **2-16** A). To hydrolyse ATP and convert the chemical energy into motility, the motor domain harbours a highly conserved motif (Walker motif), namely the P-loop, which interacts with the α and β-phosphates of bound ADP [41, 42]. Other highly conserved motifs in the motor domain include the switch I and switch II regions, which experience continuous conformational changes during the ATP hydrolysis cycle [43]. These switch regions translate local changes from the motor into larger conformational changes that are responsible for motility (Figure **2-16** B) [44]. The MT binding site lies on the opposite side of the P-loop helix α4 and helix α5 primarily form the MT binding site that communicates with MTs via electrostatic interactions [45].

1.3.1.2 Structure of conventional kinesin (Kinesin-1)

More than 100 crystal structures of kinesins have been deposited in the Protein Data Bank (PDB). They show the conserved nature of the motor domain irrespective of the position of the motor domain in the protein. The general layout of the crucial features in kinesin motor domains is discussed below.

In conventional kinesins, such as Kinesin-1, the neck linker that links the motor domain and the stalk is a short polypeptide that is reported to play a crucial role in the movement of the motor along MTs. The neck linker is in an "undocked" condition when kinesin binds to MTs. While ATP binds to the motor, ADP is released. The neck linker is subsequently put into a "docked" form to help with switches I and II when ATP is hydrolysed (Figure **2-16** A B) [46]. Even while some kinesins, such kinesin-14 motors and NCD (Non-Claret Disjunctional) do not have the neck linker structure, they possess similar structures with the same function [47]. The stalk following the neck linker region is responsible for the oligomerisation of kinesins [48]. Homodimerization is necessary for the function of certain kinesins. Also, the stalk domain is reported to regulate the activity of the motor domain by helping in facilitating interactions between the motor domain and the tail domain [49]. The typical structure of the stalk domain is a coiled-coil where the presence of heptad repeats facilitates the formation of this structure [50]. The tail domain links to the stalk domain, which is responsible for the binding of cargos directly or indirectly with the help of adapter/scaffold proteins [51]. In some kinesins, for example kinesin-1 and MCAK, the tail domain is also reported to interact with the motor domain and form a closed conformation to restrict unwanted use of ATP when not activated [52, 53]. The tail domains share low similarities among different kinesins, which explains the specificity for diverse cargos including vesicles, proteins, and organelles. Also, some tail domains are capable of binding to MTs in a nucleotide-independent manner, which induces the formation of large protofilament sheets, suggesting potential roles in MT bundling [54].
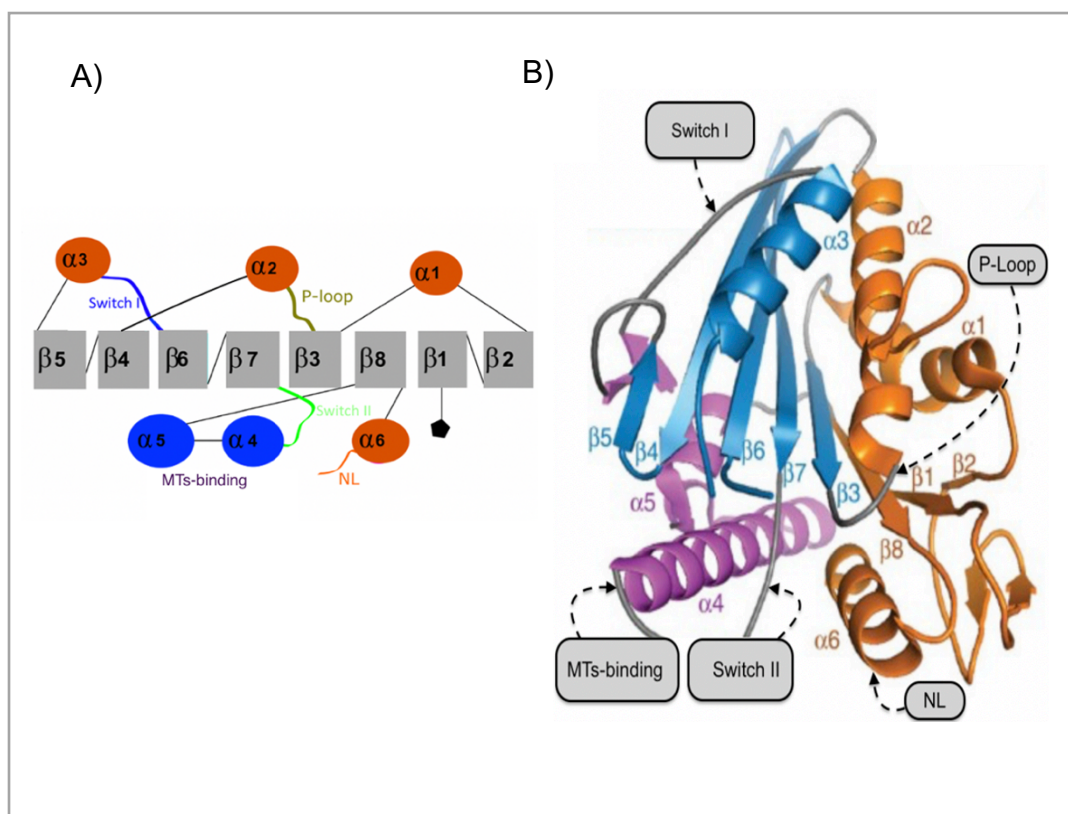
Figure 1-16 (A) Schematic figure showing major secondary structural elements of the kinesin motor domain showing the P-loop, switch I, switch II, P-Loop, MT-binding regions and neck linker regions (NL). The α-helixes are illustrated as circles while the β-strands are illustrated as squares.(B) nucleotide-free kinesin-1 motor domain (PDB entry: 5LT0) marked with major secondary structural elements including the P-loop, switch I, switch II, MT-binding interface, N-terminus, C-terminus, and neck linker region (NL). Figure adapted from [2].

There are two primary inhibitor binding sites in kinesins: L5/α2/α3 (the region between loop 5, and α-helices 2 and 3) and α4/α6 (the region between α-helices 4 and 6). L5/α2/α3 was the first binding pocket identified in kinesins and is known to bind a wide range of structurally different inhibitors. Inhibitors binding to this pocket can cause allosteric, ATP-noncompetitive effects by affecting the release of ADP from the motor without directly competing with ATP for binding. The L5/α2/α3 inhibitor binding pocket has been identified in Eg5 (kinesin-5) and CENP-E (kinesin-7) and it is frequently utilized by Eg5 and CENP-E inhibitors, for example, ispinesib **1** and GSK923295 **5**, respectively [55, 56]. Recently, a new kinesin inhibitor-binding site was identified in Eg5, which is composed of helices

α4 and α6. An Eg5 inhibitor, BI8 has been reported to bind to this pocket (Figure **1-17**) [57].
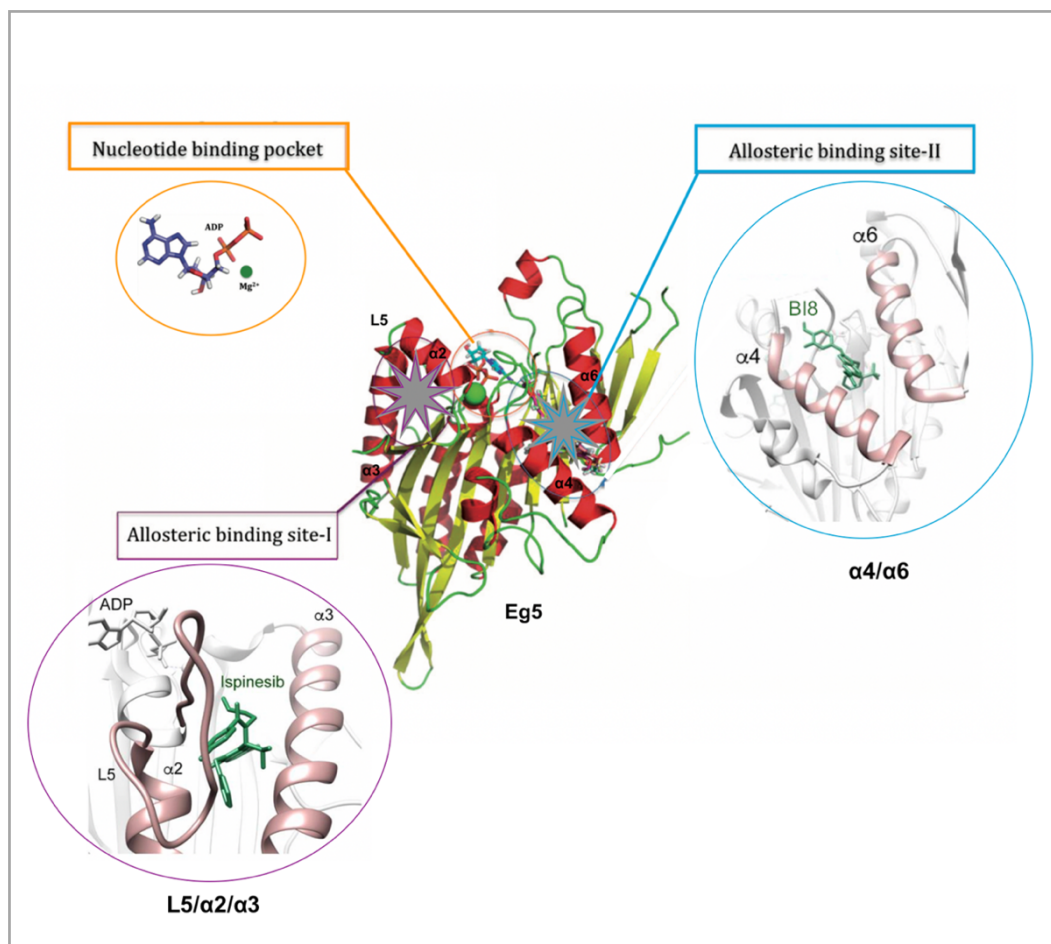
**Figure 1-17** Kinesin L5/α2/α3 and α4/α6 inhibitor binding sites. Top left ADP binding pocket. Bottom Left, kinesin-5-ADP-ispinesib (PDB 4AP0; L5/α2/α3, pink; ispinesib, green). Right, kinesin-5-ADP-BI8 (PDB 3ZCW; α4/α6, pink; BI8, green). Figure adapted from [58].

1.3.2 Function of Kinesins

Kinesins can be classified as mitotic kinesins (which are the focus of this research project) based on their functions during cell division in mitosis and cytokinesis, or non-mitotic kinesins (which are involved in intracellular transport). Mitotic kinesins are involved in various stages of mitosis by facilitating spindle assembly, chromosome alignment, mitotic checkpoint control and cytokinesis [59, 60].

Mitotic kinesins can either have a single function, such as centromere-associated protein E (CENPE) and Eg5 or be functionally involved at different stages of the mitotic phase, such as the KIF4 family, which have been shown to have multiple roles during chromosome alignment, anaphase and cytokinesis (Table **1-1** and Figure **1-18**) [59, 61].
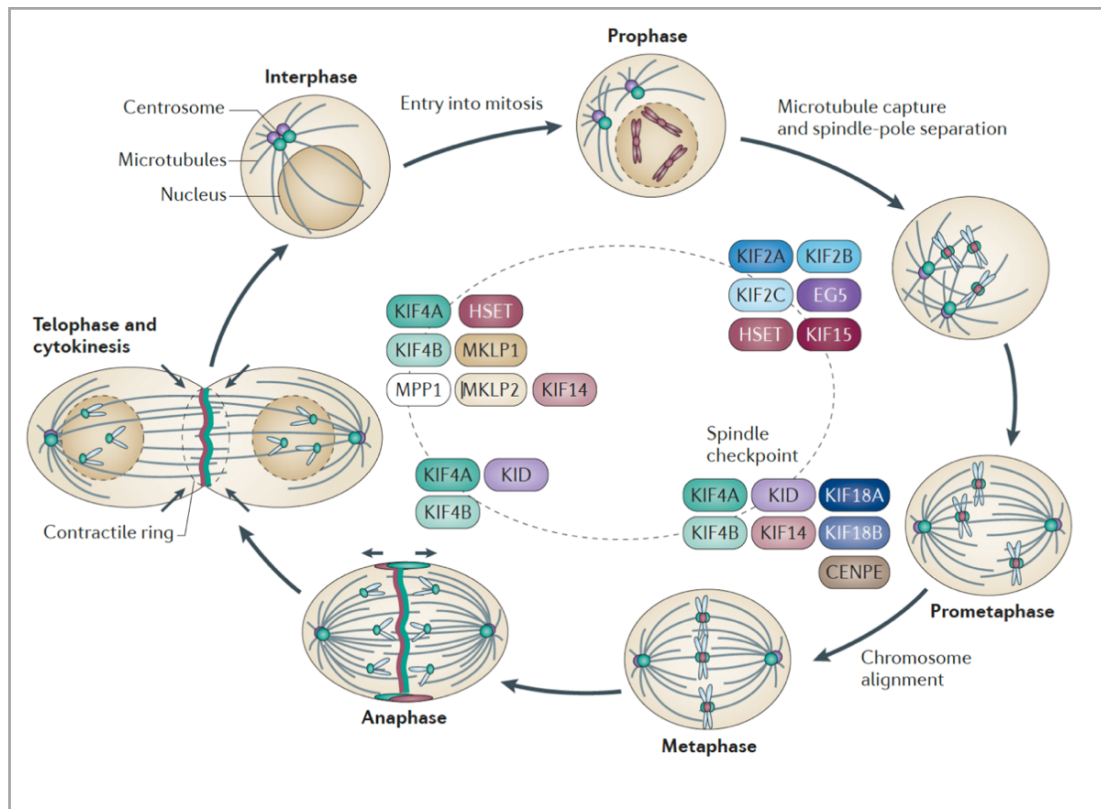
Figure 1-18 Human mitotic kinesins at different stages of mitosis and cytokinesis [1]

Several kinesins have redundant functions. For example, in clinical trials of chemotherapeutic molecules targeting Eg5, tumour cells acquired drug resistance [62]. Subsequent investigations indicated that tumour cells used a different endogenous kinesin, Kif15, in bipolar spindle formation to compensate for the activity loss of Eg5 and rescue mitosis [63]. To make the system even more complex, several kinesins play crucial roles in both mitosis and neuronal development [1].

Table 1-1 Representation functions of human mitotic kinesins at different stages of mitosis and cytokinesis.

Family	Kinesin	Phase of mitosis	Functions
Family 3	KIF14	Metaphase Telophase/ Cytokinesis	Regulation of kinetochore-microtubule attachment and regulation of cytokinesis
Family 4	KIF4A KIF4B	Anaphase Telophase/ Cytokinesis	Regulation of chromosome structure and dynamics
Family 5	EG5 (KIFC11)	Prophase/ Prometaphase	Regulation of bipolar spindle formation
Family 6	MKLP1 (KIF23) MKLP2 (KIF20A) MPP1 (KIF20B)	Telophase/ Cytokinesis	Regulation of cytokinesis
Family 7	CENPE (KIF10)	Metaphase	Kinetochore-associated protein Regulation of progression from metaphase to anaphase
Family 8	KIF18A KIF18B	Metaphase	Regulation of chromosome condensation
Family 10	KID (KIF22)	Metaphase/ Anaphase	Regulation of chromosome condensation
Family 12	KIF15	Prophase/ Prometaphase	Regulation of bipolar spindle formation
Family 13	KIF2A KIF2B	Prophase /Prometaphase	Regulation of bipolar spindle formation
Family 13	MCAK (KIF2C) (KIF24)	Metaphase	Regulation of bipolar spindle formation and regulation of kinetochore-microtubule attachment
Family 14	HSET (KIFC1)	Prophase/ Prometaphase	Regulation of bipolar spindle formation

Kinesins play a crucial role in the generation and normal functioning of neurons and are also involved in maintaining the proper functioning of synapses [39]. In addition to their role in intracellular transport, kinesin-1 has been implicated in the pathology of a number of neurodegenerative diseases, such as Alzheimer's, Huntington's, and Parkinson's disease [64]. This highlights the importance of kinesins in the proper functioning of the nervous system. Furthermore, kinesins are also involved in the transport of organelles in somatic cells, such as the endoplasmic reticulum and Golgi apparatus, to their respective destinations within cells. This helps to maintain the proper functioning and organization of cellular processes [65]. Moreover, kinesins have been reported to regulate transport inside cilia and flagella [66, 67]. Overall, kinesins play a vital role in the proper functioning of cells, and their malfunction can have serious consequences for the health and survival of cells and organisms.

1.3.3 Kinesins as an anti-cancer drug target.

In recent years, several kinesins have been implicated in various diseases, including cancer [39]. Targeting kinesins with small molecule inhibitors has been proposed as a therapeutic strategy for cancer, as well as for other diseases. These inhibitors have been shown to be effective in animal models and are currently being tested in clinical trials [68]. For example, several inhibitors for two human mitotic kinesins CENP-E [69] and Eg5 [70] (also known as KIF11), have entered phase I and II clinical trials such as GSK923295 **5** [56] and ispinesib **1** [71, 72]. Recently, the most promising compound, filanesib (ARRY-520) **2** entered phase III trials [73]. Some examples of human mitotic kinesins and their inhibitors are shown in Figure **1-19** and Table **1-2**.
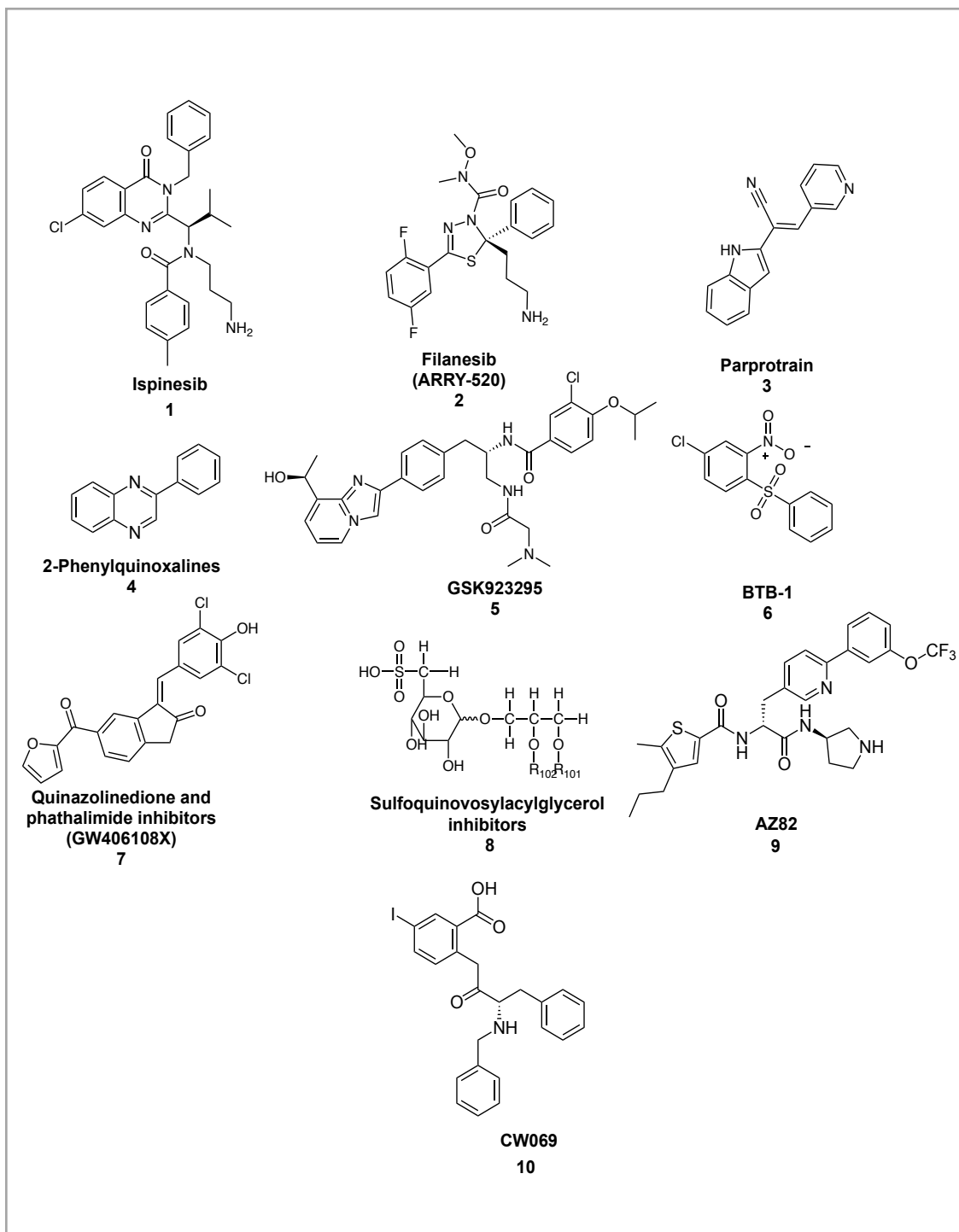
Figure 1-19 Structures of published human mitotic kinesins inhibitors.

Table 1-2 Published human mitotic kinesins inhibitors from clinical development.

Family	Human mitotic kinesin	Inhibitors
Family 5	EG5	Ispinesib **1** [71, 72], Filanesib (ARRY-520) **2** [73]
Family6	MKLP2	Parprotrain **3** [74]
Family 6	MPP1	2-Phenylquinoxaline **4** [75]
Family 7	CENP-E	GSK923295 **5** [56]
Family 8	KIF18A	BTB-1 **6** [76]
Family 12	KIF15	Quinazolinedione and phathalimide inhibitors (GW406108X) **7** [1]
Family 13	MCAK	Sulfoquinovosylacylglycerol inhibitors **8** [77]
Family 14	KIFC1	Az82 **9** [78], CW069 **10** [78]

1.4 MPP1: A member of the kinesin-6-family

Human M-phase phosphoprotein 1 (MPP1), also known as KIF20B, KRMP1 (Kinesin-related M-phase phosphoprotein 1) and MPHOSPH1 is an N-terminal motor protein made up of 1853 amino acid residues, which belongs to the kinesin-6 family, which has two other members: MKLP1 mitotic kinesin like protein 1 (known as KIF23), MKLP2 mitotic kinesin like protein 2 (also known as KIF20A) [79]. They are all N-terminal motors with plus-end motility. Kinesin-6 members are involved in the metaphase-to-anaphase transition leading to the physical division of the cell into two daughter cells via cytokinesis [80, 81].

1.4.1 Structure of MPP1

Members of the kinesin-6 family are unique amongst the kinesin superfamily, because they contain an exceptionally long insertion (8 - 10 kDa) of unknown function in the loop L6 region of the motor domain and contain an extension of around 100 amino acid residues at the N-terminus preceding the motor domain (Figure **1-20** A-B).
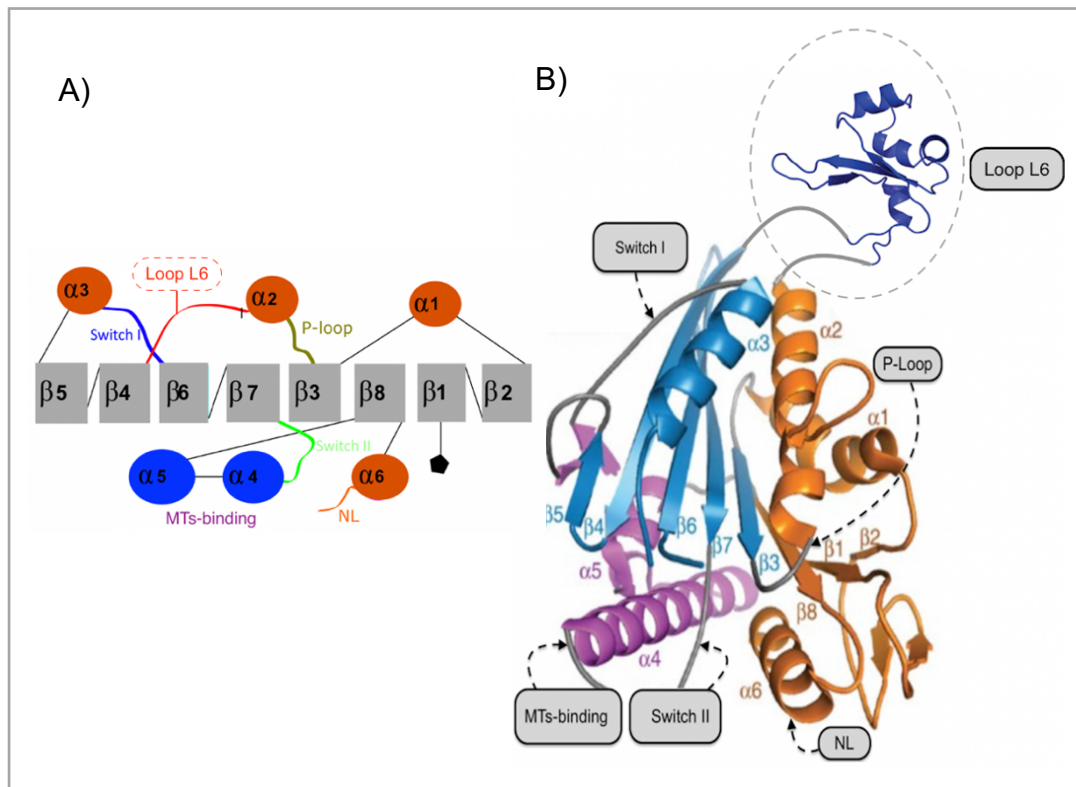
Figure 1-20 (A) Schematic figure showing major secondary structural elements of the kinesin-6 motor domain showing the P-loop, switch I, switch II, P-Loop, MT-binding regions and neck linker regions (NL). The α-helixes are illustrated as circles while the β-strands are illustrated as squares. (B) nucleotide-free kinesin-1 motor domain (PDB entry: 5LT0)) marked with major secondary structural elements including the P-loop, switch I, switch II, MT-binding interface, N-terminus, C-terminus, neck linker region (NL) and predicts structural of MPP1 motor domain with long Loop L6 (in pale blue) Figure adapted from [2]

Following the motor domain is the α-helical coiled-coil stalk, which is connected to the motor domain via the neck linker region. Compared with other kinesins, the stalk of MPP1 is significantly longer, spanning amino acid residues 500-1520 [80]. It is also substantially longer than the stalk region of other kinesin-6 members including MKLP-1 and MKLP-2. The stalk region mediates the dimerization of MPP1, which is pivotal for the physiological function of MPP1 (Figure **1-21** A) [82]. The tail region of MPP1 is composed of approximately 200 amino acid residues. One significant difference between the tail region of MPP1 and other kinesin-6 proteins is the lack of a leucine zipper, a motif composed of lecuine-rich α-helices (Figure**1-21** B) [83].
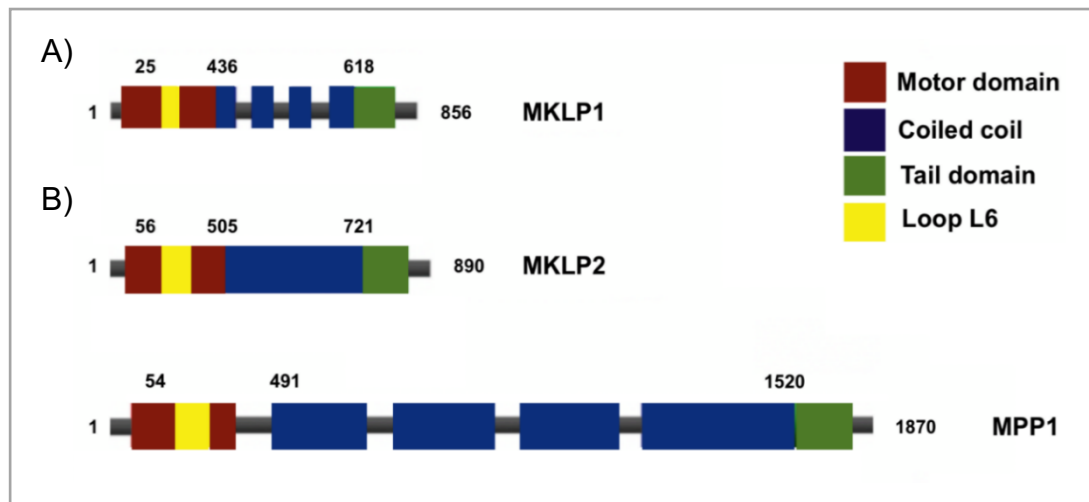
Figure 1-21 Bar diagram of three *H. sapiens* kinesin-6 members, MKLP1, MKLP2 and MPP1.

Much of the motor domain of human MPP1 can be modelled using homology modelling methods using other kinesins as reference structures. One such reference structures is Zen4 (PDBID: 5X3E) a kinesin from *Caenorhabditis elegans* [84]. It is the only X-ray structure of a kinesin-6 motor domain that is available to predict the structure of human MPP1 motor domain. To date, crystallisation trials of the human MPP1 motor domain have been unsuccessful. The difficulties in acquiring kinesin-6 protein crystals have been attributed to the high flexibility of the L6 insertion. Based on secondary structure predictions, loop L6 is likely to be unstructured. [85]. Also, little is known about the 10-15 residue neck linker of MPP1 following the motor domain which is thought to be involved in controlling the MT-binding site. Another structural feature of the kinesin-6 superfamily is an extension of 54 amino acids preceding the conserved motor domain [82]. The extension is also predicated as structurally disordered and the function of it is still unknown (Figure **1-22**) [86, 87].
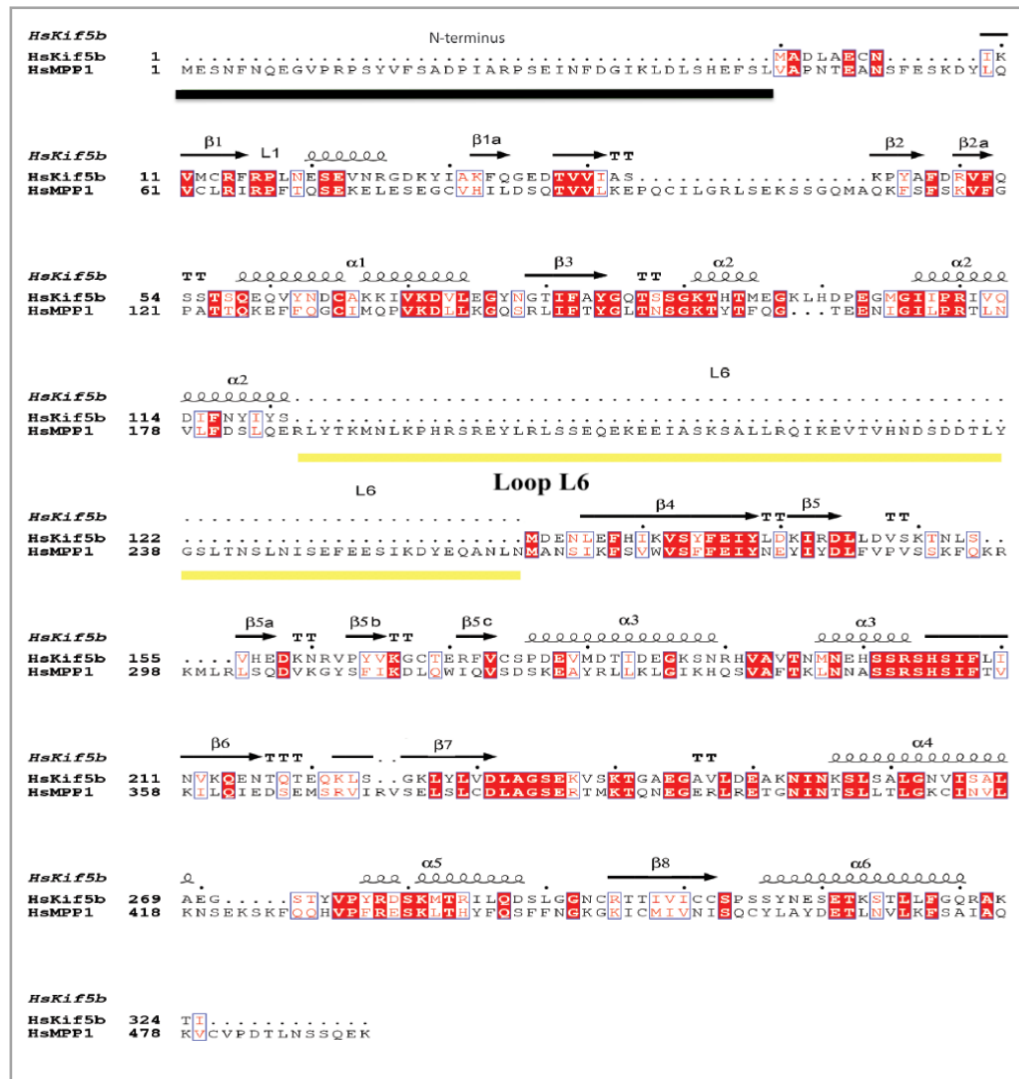
Figure 1-22 Sequence alignment of the motor domain of Eg5 (HsKif5b), for which the crystal structure is available, with Kinesin-6 family members. The alignment shows the characteristic long inserting in the motor domain of MPP1 inserted in the loop L6 region (aa186-262) (marked with a yellow) of the motor domain with unknown function following the helix α2. The sequence alignment was performed using ClustalW at EMBLEBI. Secondary structure elements of the Eg5 motor domain were extracted from the coordinates of its crystal structure (PDB ID: 1ll6) using ESPript 3.0. Figure adapted from [86].

MPP1 was reported to be regulated *in vivo* by posttranslational modification through phosphorylation in the C-terminal tail domain at Thr1604 by cdc2 kinase. Phosphorylation activates MPP1 and induces the mitotic peptidyl-prolyl isomerase (Pin1) to bind to MPP1 via the Pin1 WW domain [82]. On the other hand, casein kinase II is thought to phosphorylate the motor domain of MPP1. However, the importance of these interactions has not been fully investigated.

1.4.2 MPP1 as an anti-cancer drug target

As discussed previously, MPP1 belongs to the kinesin-6 family that plays crucial roles in cytokinesis. MPP1 disperses throughout the cytoplasm in metaphase and subsequently concentrates in the midbody during mitosis. Experiments carried out in HCT116 colon carcinoma cells, have shown that RNAi-induced depletion of MPP1 leads to defects during cytokinesis, which can result in apoptotic cell death [88]. Cell death or apoptosis occurring through two different mechanisms were proposed: firstly, the midbody of RNAi treated cells survive without abscission and the two physically connected daughter cells undergo apoptosis. Secondly, the midbody regresses causing the emergence of binucleated cells that undergo apoptosis. Subsequent studies showed that only specific cancer cell lines including 26 from bladder cancers (e.g. J82, HT-1376, HT-1179,SW780, RT4 and UM-UC-3) and large B cell lymphomas are highly reliant on MPP1 for cytokinesis. In contrast, no significant defects in cytokinesis were observed during MPP1 depletion in HeLa cervical carcinoma cells [85]. Thus, MPP1 is viewed as a potential target for bladder cancer drug development [88].

1.5 KifC1: A Member of the kinesin-14-family

Human KifC1, also known as Human Spleen, Embryo and Testes Protein (HSET) or kinesin-like protein KifC1 belongs to the kinesin-14 family, which has two other members: KIFC2 and KIFC3. They are all C-terminal motors with minus-end motility. Kinesin-14 members are that cross-link with MTs during spindle assembly [89].

1.5.1 Structure of KifC1

Human KifC1 consists of 673 amino acid residues with three major domains, namely an N-terminal tail domain, a continuous coiled-coil stalk domain and a C-terminal globular motor domain, which contains the nucleotide-binding pocket

and the MT-interacting region (Figure **1-23**). As a C-terminal kinesin, KifC1 moves towards the minus-end of MTs with a slow gliding rate of ~5 μm/min in fluorescent microtubule gliding assays, which is much slower than the motility rate of conventional kinesins, which is between 30-48 μm/min [90].
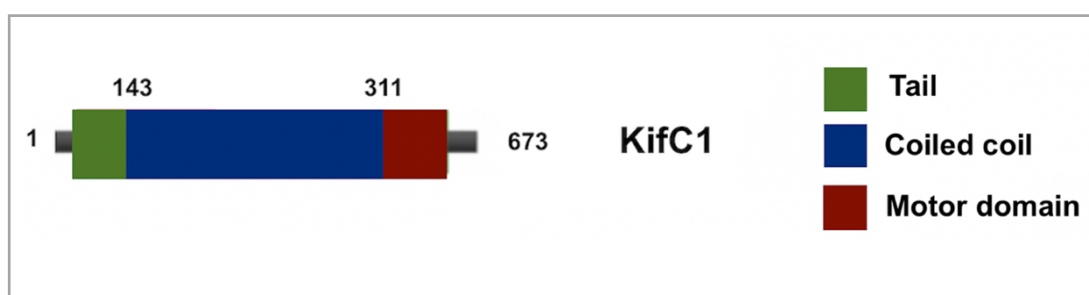
Figure 1-23 Bar diagram of H. sapiens KifC1 showing its three-domain structure.

In a structural study of the KifC1 motor domain (PDBID: 5WDH), the His-tagged protein was crystallised with Mg-ADP bound (Figure **1-24** A). The analysis indicated that the allosteric L5/α2/α3 inhibitor binding pocket has a reduced volume and is less accessible for some current KifC1 inhibitors including AZ82 **9**. However, the α4/α6 binding pocket that also exists in KifC1 is large enough to harbour potential KifC1 inhibitors (Figure **1-24** B). Recently, the mode of binding of AZ82 **9** to KifC1 has also been explored. Based on its similarity to other kinesin inhibitors, AZ82 **9** was initially proposed to bind to the L5/α2/α3 binding site of KifC1. However, based on the crystal structure of KifC1, Park et al. hypothesized that AZ82 likely binds the α4/α6 cleft instead of the L5/α2/α3 pocket of KifC1 (Figure **1-24** C). Unfortunately, as most KifC1 inhibitors are proposed to bind to the KifC1-MT complex rather than the motor domain, currently there are no structural data available for any KifC1-inhibitor complexes due to the difficulty crystallising for KifC1-MT complex [91].
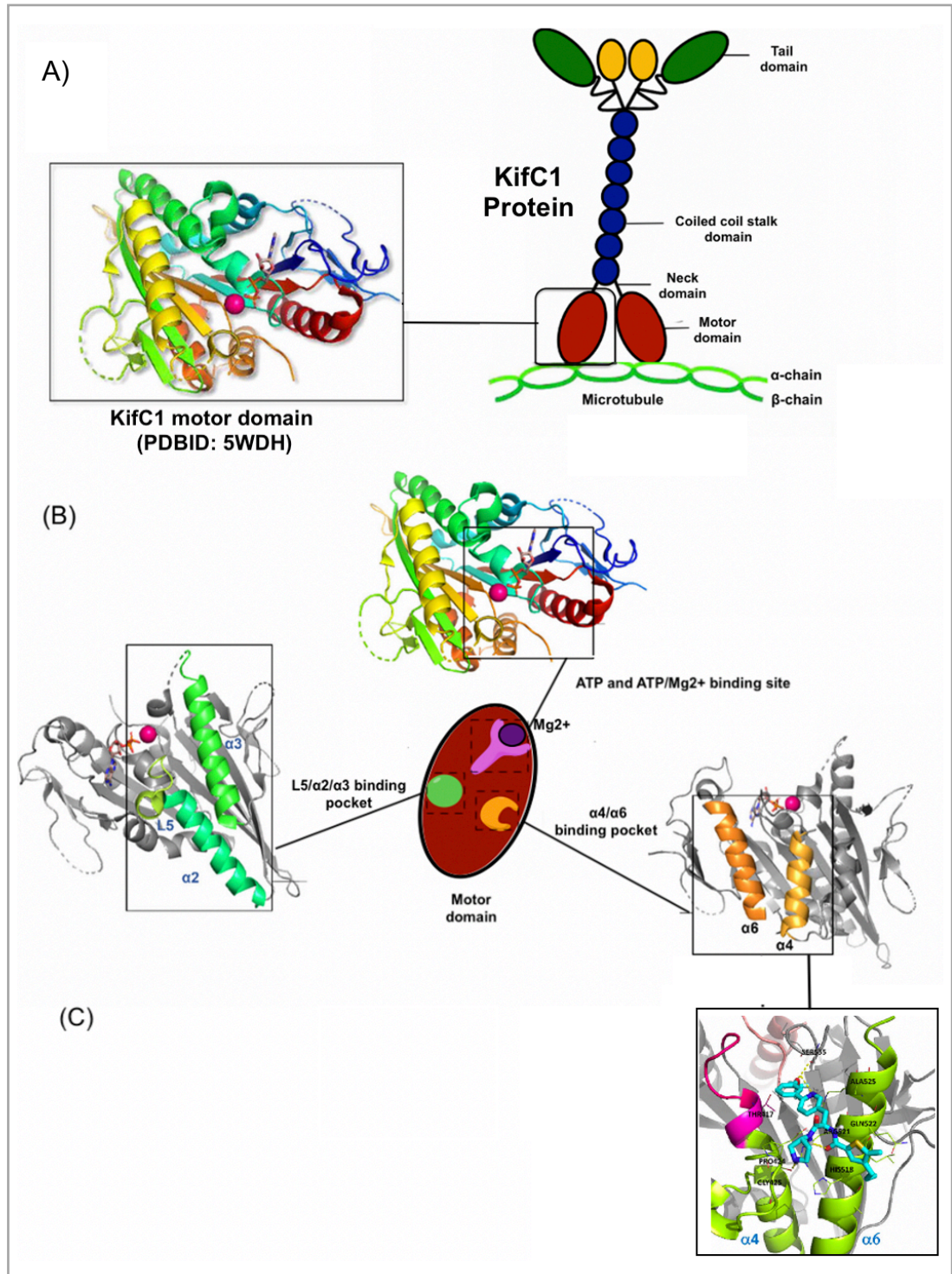
Figure 1-24 (A) KifC1 structural components include motor domain bound with Mg-ADP (PDBID: 5WDH) (B) KifC1 L5/α2/α3, α4/α6 inhibitor binding sites and ADP binding pocket. (C) AZ82 docked into the α4/α6 cleft of KifC1 (PDBID: 5WDH). Figure adapted from [91].

In normal cells, KifC1 plays a role in the formation and maintenance of mammalian meiotic and mitotic spindles, as well as spindle pole focusing [86]. It is also important in the formation of MT asters, structures composed of microtubules that radiate out from a central point. They are formed during cell division and are responsible for organizing the chromosomes and separating them into two daughter cells [85]. Furthermore, KifC1 transports bare double-stranded DNA, indicating its potential as a key transporter in gene therapy. KifC1 is highly expressed in the testis, spleen, and ovary and is responsible for acrosome biogenesis and nuclear reshaping, an important procedure in the formation of an acrosome, which is located in the front part of the sperm nucleus and is critical for sperm viability during spermatogenesis [86, 87]. Reduced KifC1 expression is reported to be a key factor in a rare male infertility disease characterized by defective acrosome formation and failure to elongate sperm heads [92].

1.5.2 KifC1 as an anti-cancer drug target

The nuclear envelope degrades during prometaphase, and the two centrosomes begin to separate, forming the bipolar spindle. Throughout mitosis, the centrosomes serve as the primary microtubule-organizing centre (MTOC). Before prometaphase, only two centrosomes emerge in normal cells. However, many solid and haematological cancers examined to date are reported to have supernumerary (more than two) centrosomes [93, 94]. Extra centrosomes may promote tumorigenesis by causing genetic instability via multipolar mitoses or by disrupting cell polarity and asymmetric cell division [58]. Extra centrosomes, on the other hand, can cause multipolar mitoses and genetic data mis-regulation, resulting in aneuploidy. While moderate levels of genetic instability contribute to tumorigenesis, high levels of genetic instability caused by multipolar mitoses are harmful to cancer cells and eventually result in apoptosis [90]. Cancer cells use a variety of mechanisms to avoid multipolar mitoses, including extrusion of extra centrosomes, inactivation of extra centrosomes, asymmetric segregation, and centrosome clustering [91]. Centrosome clustering is the most common and important mechanism. To avoid multipolar mitoses, cancer cells divide their extra

centrosomes into two groups and form a pseudo-bipolar spindle (Figure **1-25**).

Many cancer cells with extra centrosomes seem to rely on KifC1 to cluster centrosomes [95]. KifC1 is reported to use minus-end direct motility to bundle MTs at spindle poles and cluster multiple centrosomes into pseudo-bipolar spindles. Prolonged prometaphase and metaphase have also been reported when KifC1 maintains cancer cell bipolarity [86].
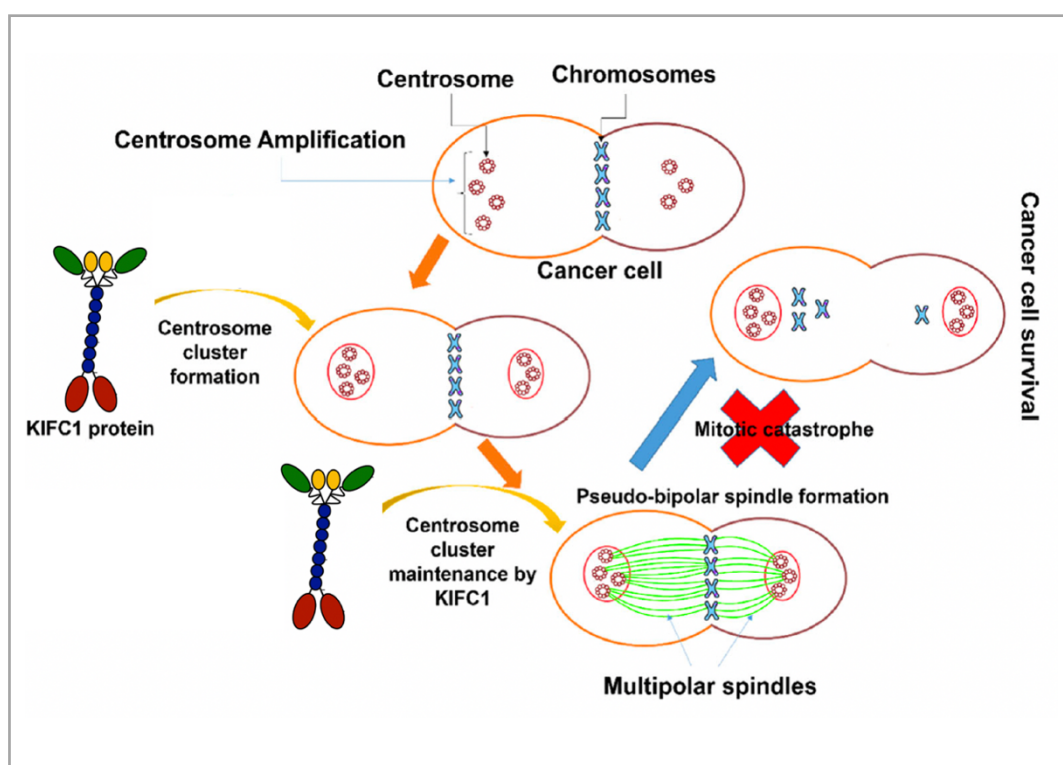
Figure 1-25 Representation of centrosomes amplification, cancer cells cluster extra centrosomes to form a pseudo-bipolar spindle to avoid multipolar mitoses [91] .

1.6 Heterocyclic compounds as small molecule in anticancer agents

The serious drawbacks of existing chemotherapeutics: nonspecific targeting, the lack of solubility, and the inability to enter to cancer cells [96] necessitate the requirement for continuous efforts to develop target anti-cancer drug-like candidates with minimal side effects and development in the area of anticancer agents is one of the key challenges in medicinal chemistry [97, 98]. Therefore,

these days research is focused on the introduction of new and safer therapeutic agents of clinical importance [99, 100]. Identifying special scaffolds of natural products having certain structural features responsible for their biological activities is of great interest to researchers [101].

Heterocyclic compounds play an essential role in medicinal chemistry [102] and are a significant source of biologically active compounds due to their diverse structures [103]. a class of important cyclic compounds which contains one or more non-carbon atoms in the ring, such as nitrogen, oxygen and sulphur [104, 105]. Heterocyclic compounds could be derived from organic synthesis or natural products and used in a variety of important medicinal and synthetic chemistry applications [106]. They are frequently found in various drugs, biomolecules, and biologically active compounds and exhibit a wide range of biological activities, including antifungal [107], anti-inflammatory [108], antibacterial [109], antiviral [110], and anti-cancer [111-113]. There have been different strategies used to discover small molecules inhibitors, including Rational drug design and High-throughput screening (HTS) Computer-aided drug design (CADD) and Virtual screening.

1.7 Drug design and development

Drug design is a process by which various techniques are used to create new chemical compounds that will bind to specific targets (usually proteins or nucleic acid) in the body, such as proteins or enzymes, to treat a disease or condition. The goal of drug design is to create a compound that is highly specific to its target, with minimal side effects and high effectiveness. There are several different techniques used in drug design, including: (1) Rational drug design which is a process by which scientists use knowledge of the three-dimensional structure of a target protein or enzyme to design a compound that will bind to it. This technique can be used to create new compounds that are similar in structure to existing drugs, but that have improved properties, such as increased efficacy or reduced side effects. (2) High-throughput screening (HTS); which is a process by which scientists use automated techniques to test large numbers of compounds

against a target protein or enzyme to identify those that bind to it. This technique can be used to identify new compounds that may have potential as drugs. (3) Computer-aided drug design (CADD); which is a process by which scientists use computer programs to predict how a compound will interact with a target protein or enzyme, and to optimize the properties of a compound to make it more effective as a drug. (4) Virtual screening: This is a process by which scientists use computer programs to predict how a compound will interact with a target protein or enzyme, and to identify compounds from large libraries of compounds that have the potential to bind to the target. The process of drug discovery and development is time-consuming and expensive, it takes typically more than 10 years to bring a new drug to the market. However, by using these techniques, scientists can create new compounds that have the potential to be used as drugs to treat a wide range of diseases and conditions.

1.7.1 Rational drug design

There are two types of techniques used in modern drug discovery to help design a drug: ligand-based drug design (LBDD) and structure-based drug design (SBDD) are both rational drug design approaches. LBDD involves designing drugs based on the knowledge of the activity of a ligand or set of ligands. This method involves analysing the physicochemical properties of the ligand and designing compounds that can mimic or improve upon the ligand's properties to achieve a desired biological effect. SBDD, on the other hand, involves designing drugs based on the knowledge of the three-dimensional (3D) structure of the target protein. This method involves analysing the protein-ligand interactions, identifying the binding site, and designing compounds that can specifically bind to the target protein with high affinity and selectivity [114]. SBDD has become more powerful than LBDD as the amount of experimental data about the protein's crystal structures has increased [115]. Both methods can be used alone or in combination to design drugs with specific properties that can effectively treat diseases.

1.7.1.1 Structure-based drug design (SBDD)

SBDD goes through several processes before the optimised lead enters clinical trials. The first step entails isolating, purifying, and determining the structure of the target protein using one of two key methods: X-ray crystallography or NMR [116]. Compounds obtained through virtual screening of various databases are placed in a specific region (active site) of the protein. These compounds are scored and ranked based on their steric, hydrophobic, and electrostatic interactions with the active site of the target protein [117]. Biochemical assays are used to test the top-ranked compounds. The structure of the protein in complex with the most promising lead compound(s), is determined to reveal positions on the compound that can be optimised to further increase potency. Following several additional steps including further synthesis and optimization, the refined compounds generally show increased target specificity and binding affinity [118].

1.7.1.1.1 Homology modelling

If there is no 3D structure information for the target, it may be possible to create a homology model (also known as homology modelling or comparative modelling) based on primary sequence similarity of the target to homologous proteins, of which 3D structure is empirically known. Homology modelling predicts the 3D structure of a query protein based on sequence alignment of template proteins [119]. Generally, the process of homology modelling consists of four steps: target identification, sequence alignment, model building, and model refinement. Models built with templates that exhibit over 70% identities are considered accurate enough for drug discovery applications [120]. Homology modelling can be used to predict the structure of a wide variety of proteins and enzymes. It is a powerful tool for drug design and can be used in combination with other techniques, such as molecular dynamics simulations and site-directed mutagenesis, to further improve the accuracy and reliability of the predicted structures.

1.7.1.1.2 Molecular Modelling

In the 1980s structure-based design using molecular docking studies became a new way to identify potential drug candidates. Studies involved the use of computational software to dock small chemical compounds into ligand-binding sites in protein structures. The availability of 3D structures of proteins determined by x-ray crystallography and nuclear magnetic resonance, have made molecular docking a common approach to novel drug design [80, 121]. A ligand can bind to its binding site as a result of various interactions: hydrogen bonding (H-B), ionic interaction, hydrophobic interactions and van der Waals forces. The hydrophobic interaction is often responsible for a large proportion of the total interaction energy, while hydrogen bonding is associated with specific molecular recognition between hydrogen bond donor-acceptor pairs. The presence of many potential translational and rotational degrees of freedom poses an obstacle to accurately determining the intermolecular force of interactions [122, 123]. A major factor in obtain useful results from molecular docking studies is access to high quality X-ray crystal structures of the protein of interest. It is suggested that the optimum resolution for an X-ray structure for such experiment is < 2.5 Å. The goals of using such docking programs include identifying a new lead compound, assessing outcomes of modifications and visualization of possible binding interactions with the target protein [123]. Two commonly used programs for molecular docking are AutoDock Vina (The Scripps Research Institute, La Jolla, CA) and LeDock. In order to evaluate the binding affinity (BA) of different ligand conformations, AutoDock Vina and LeDock predict the binding free energy (ΔG) and accordingly calculate the binding constant for simulated docking of a ligand to its binding site [124]. AutoDock Vina and LeDock have two advantages: high speed and high accuracy for prediction of mode of interaction. The software computes grid maps and groups the results in user-friendly format. By making use of Discovery Studio (BIOVIA, San Diego, CA), interactions between the protein and docked ligands can be visualised and evaluated [83, 124].

1.7.1.1.3 Structure-based virtual screening (SBVS).

The search for new chemical compounds as lead molecules is a critical step in the drug discovery process. Once the target has been determined, the small molecules database is chosen for virtual screening, and their binding interactions with the chosen drug target are investigated. The top-ranked compounds with the desired binding interactions are chosen as lead compounds for the next steps. Virtual screening is a computational method that evaluates large libraries of compounds and identifies putative hits (leads) by determining the fit of the ligands into the binding site. The affinity of the ligand to the target protein is estimated using molecular docking and a relevant scoring function. Virtual screening is a highly automated and quick method for identifying candidate compounds from a large dataset based on their docking interaction rank [125]. This allows researchers to concentrate their resources and efforts on compounds that are likely to have the desired activity.

1.7.1.2 Ligand-based drug design (LBDD)

In many cases, the 3D structure of a target protein or its homolog is not available for SBDD approach or the protein target is unknown. This is true in particular for proteins that are present on the cell surface or within cell membranes due to their inherent difficulties in protein crystallization. In some cases, the use of unreliable homologous proteins (for example, low sequence identity) for homology modelling can result in high rate of false positive hits. In such cases, the researcher can use LBDD. LBDD is based on knowledge of the structural and chemical properties that molecules must have in order to bind to the target of interest [126]. One of the LBDD approaches uses pharmacophore models built based on the on knowledge of such molecules binding to the target and then uses this model to design new drug candidates.

1.7.1.2.1 Pharmacophore Models

The term pharmacophore was defined as, "the ensemble of minimum, steric and electronic features required to ensure optimal supramolecular interactions with a

specific biological target structure and to trigger (or block) its biological response" in 1968 [127]. Since then, it has become a widely accepted standard definition for the pharmacophore concept. Pharmacophores are neither real molecules nor functional groups. They simply represent the essential points of drug molecules for an optimal interaction with the target protein, which interactions are hydrogen-bonding, charge transfer, electrostatic, and hydrophobic interactions [128]. All these interactions were combined in 3D space by the pharmacophore model. Pharmacophore models can be generated using various computational techniques such as 3D-QSAR (Three-dimensional quantitative structure-activity relationship), molecular dynamics simulations or machine learning. These models can then be used to screen large libraries of compounds to identify new lead compounds or optimize the binding of a drug candidate to a target protein or enzyme. Pharmacophore models can be used in various stages of drug discovery such as virtual screening, lead optimization and used to understand the mechanism of action of a drug. It can also be used to predict the potential side effects of a drug candidate by identifying potential interactions with other proteins or enzymes [129].

1.7.1.2.2 Ligand-based virtual screening (LBVS)

Once a pharmacophore model is built, it can be used to predict whether candidate ligands are likely to bind to the target by comparing them to the pharmacophore model. This is known as ligand-based virtual screening. This method has been shown to be most effective when scanning through candidate compounds with desired chemical properties from a large, diverse set of chemical libraries [130]. In effect, LBVS functions as a chemical database filter, drastically reducing the number of chemical compounds for *in vivo* and *in vitro* studies.

1.7.1.2.3 *De novo* ligand design (DnLD) and Fragment-based drug design (FBDD)

De novo ligand design is also known as the fragment-based drug design approach. Because of the benefit of tailoring the new compounds, FBDD has been effectively employed in both SBDD and LBDD approaches. In SBDD, the

chemical features of the target's active site are used to design novel compounds, whereas in LBDD, the chemical features derived from the pharmacophore are used to design novel compounds [131]. The FBDD approach is a technique for novel ligand design that starts with libraries of small ligands or specifically very small molecules called "fragments" with low affinity to the target protein of clinical relevance. The most promising ones are then grown, merged, or linked with other fragments or functional groups that bind to other places in the target protein to increase the potency of the binding or to enhance the binding affinity. These strategies, which are key approaches for fragment-based drug design [132].

The following chapters describe the development of MPP1 (Chapter 2) and KifC1 (Chapter 3) inhibitors. The aims and objectives for the work are discussed at the start of each chapter. These are followed by chapters describing the conclusions of the project (Chapter 4) and the experimental methods and analytical data for the synthesised compounds (Chapter 5).

2 Small molecule inhibitors of MPP1

2.1 Background

2.1.1 MPP1 inhibitors

Several MPP1 inhibitors have been identified, including 2-phenylquinoxaline **4** (Figure **2-1** A), however the patent describing these structures was later withdrawn by the applicants [133]. Also in a previous study, our collaboration partner from Prof Frank Kozielski's research group at UCL School of Pharmacy has reported two structurally related naturally occurring depsidone compounds from Lichens, physodic acid **11** and norlobaridone **12** (Figure **2-1** B), as inhibitors of MPP1 [133, 134].

Physodic acid was found to inhibit the basal ATPase activity of MPP1 with an IC_{50} of 9.9 ± 1.1 μM and norlobaridone with an IC_{50} of 18.7 ± 2.6 μM [135]. Physodic acid is not competitive with ATP, indicating the presence of an allosteric inhibitor-binding pocket on MPP1. The lower IC_{50} value for physodic acid may indicate that the carboxylic acid substituent is important to the binding behaviour of the molecule [135].
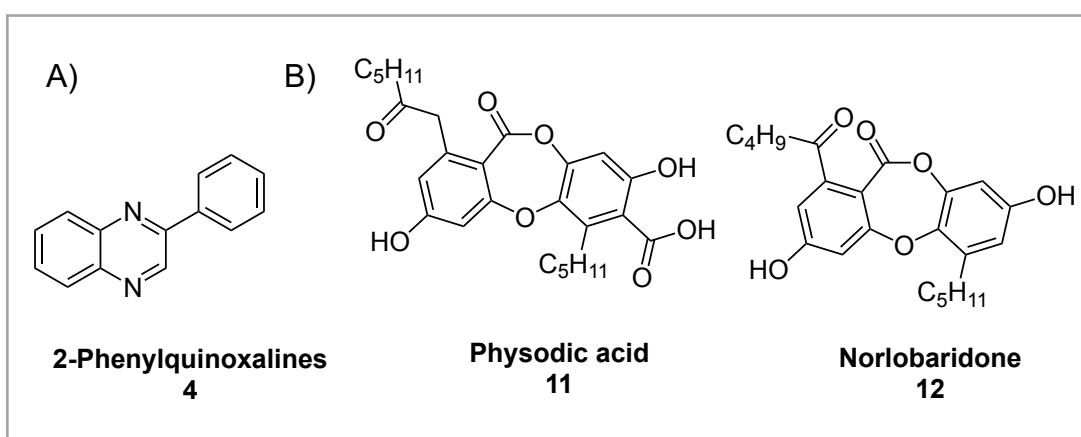
Figure 2-1 Chemical structures of A) 2-Phenylquinoxaline an example of a quinoxaline MPP1 inhibitor, (patent withdrawn). B) Physodic acid and norlobaridone as depsidones are inhibitors of MPP1 ATPase activity [135].

43

2.1.1.1 Ascochitine

Ascochitine is a toxin produced by the fungus *Ascochyta rabiei*, which is a plant pathogen that can cause serious damage to a variety of crops, including chickpeas, lentils, and peas. The toxin can cause a range of symptoms, including reduced growth and yield, and can also make the affected crops unmarketable [136] .

The initial focus of this chapter has been R-ascochitine **14** (Figure **2-2**) that is a hit compound identified from a screen of potential MPP1 inhibitors. It was also found to have cytotoxic activity against a panel of bladder cancer cell lines with an average IC$_{50}$ of 17 µM [unpublished data from Prof Frank Kozielski].
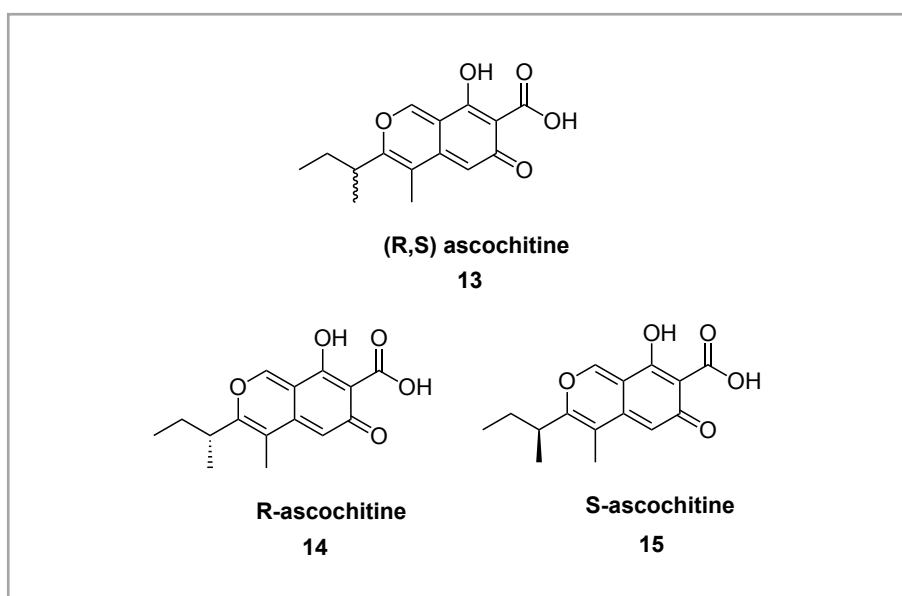
Figure 2-2 Chemical structures of (R,S) ascochitine, R-ascochitine and S-ascochitine.

The aim of this chapter is to identify novel ascochitine-based inhibitors by synthesising compounds that incorporate similar pharmacophores. Such molecules may be used as chemical probes for studying MPP1 biology and as potential lead compounds for drug development.

2.1.1.1.1 Ascochitine as azaphilone metabolites

Ascochitine is a natural product that belongs to a class of compounds called azaphilones, compounds that have a high affinity for ammonia, and that are characterized by a pyrone-quinone skeleton [137]. Azaphilones are a diverse class of compounds that can be found in various organisms such as fungi, lichens, and plants. They are known to have a wide range of biological activities including antimicrobial, antifungal, antiviral, antioxidant, cytotoxic, nematocidal and anti-inflammatory properties [95].

 The ascochitine structure incorporates an azaphilonoid scaffold [138], that contains a cyclohexenone moiety, a common structural motif in compounds developed within the research group. Ascochitine also has structural similarities to the previously described depsidone MPP1 inhibitors (physodic acid **11**) in that it incorporates a motif that mimics the *ortho*-hydroxybenzoate in the latter compound (Figure **2-3**).
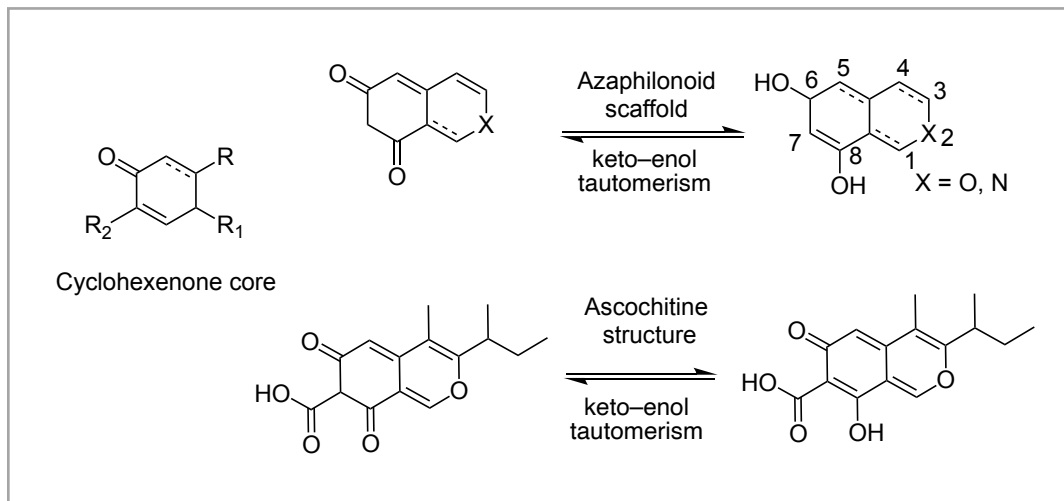
Figure 2-3 Azaphilonoid scaffold and ascochitine structure with the fused cyclohexenone motif.

The broad spectrum of biological activities indicates the potential of azaphilones as a basis for new drugs. However, this potential should be contrasted with the lack of selectivity exhibited by azaphilones in their reactions with various amines such as those found in amino acids, proteins and nucleic acids, resulting in the formation of vinylogous γ-pyridones (Figure **2-4**) [139]. This prompted the

exploration of alternative scaffolds as bioisosteres of ascochitine as potential MPP1 inhibitors.
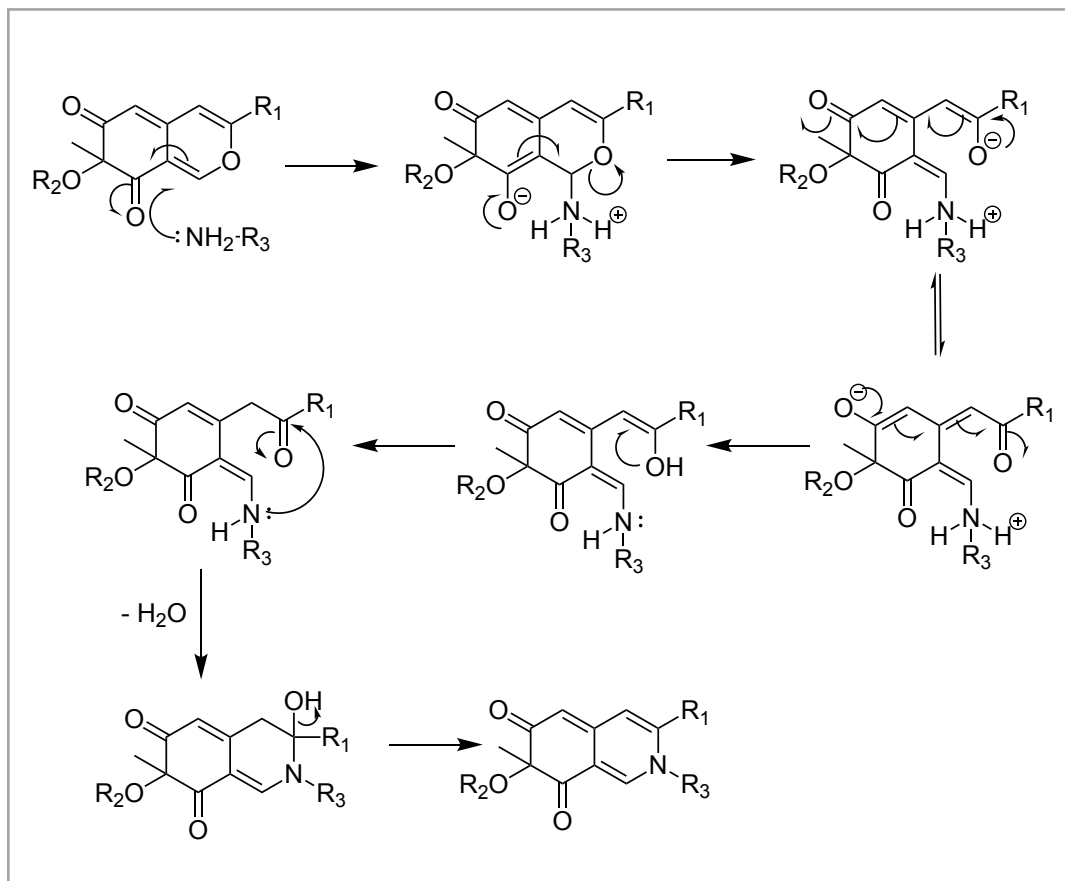
Figure 2-4 Reaction mechanism of azaphilones with amines.

2.1.1.1.2 Synthesis of novel ascochitine-based inhibitors targeting MPP1

The synthesis of ascochitine and analogues that contain the azaphilone scaffold is challenging. The synthetic route is relatively long, requiring up to 11 steps for some analogues and a difficult final cyclisation step. In some of the preliminary work on the project Sai Life Sciences (a contract synthesis company) successfully synthesised several ascochitine analogues (Figure **2-5** A) including six ascochitine derivatives (**16** ,**17**, **18**, **19**, **23** and **24**) and seven intermediate compounds. The synthesis of some analogues failed at the last cyclisation step of the synthetic route (**20**, **21** and **22**) (Figure **2-5** B).
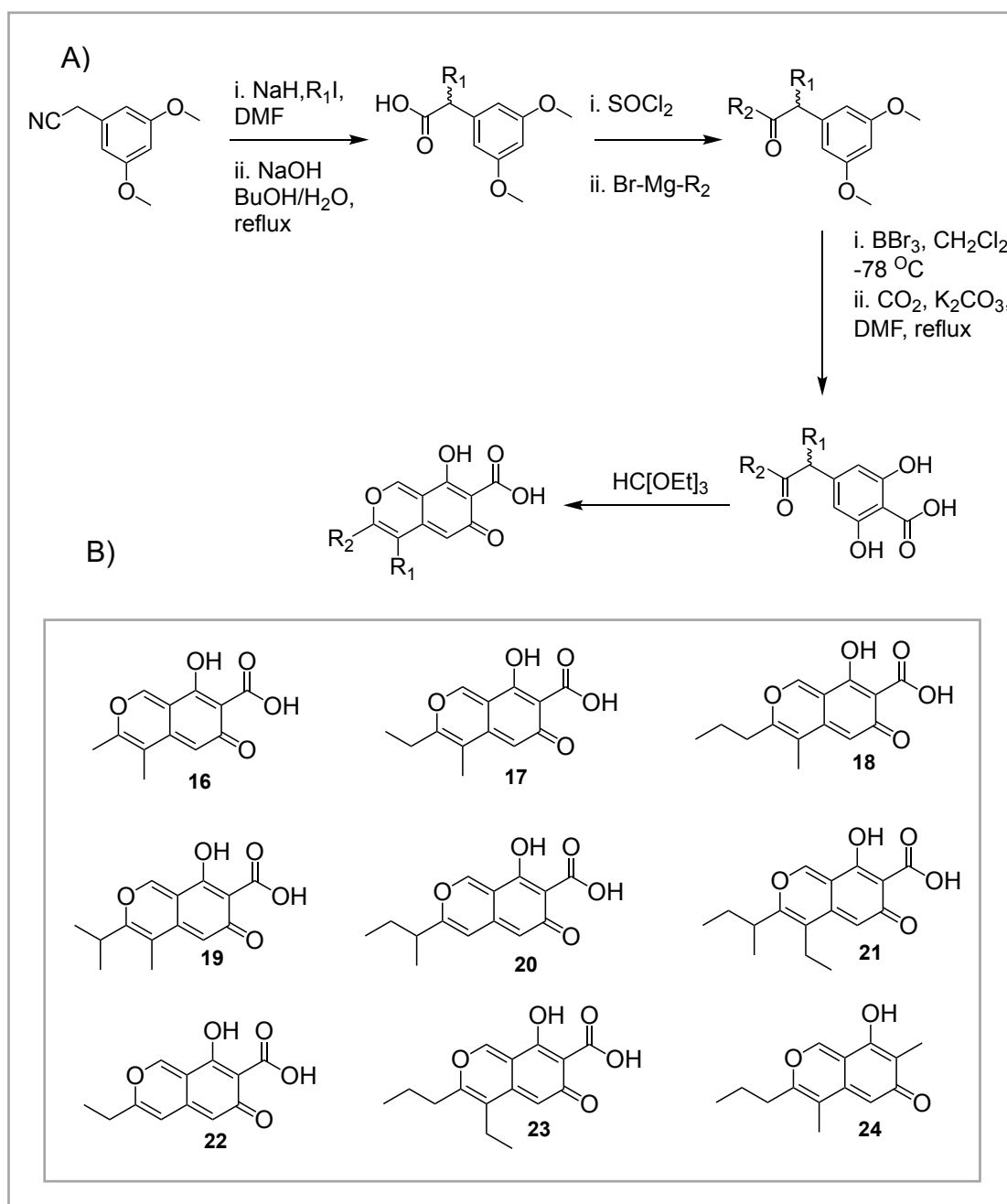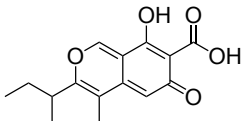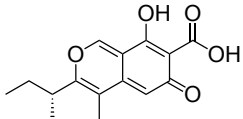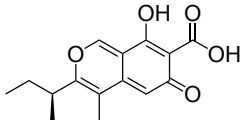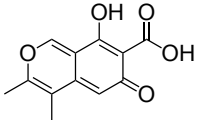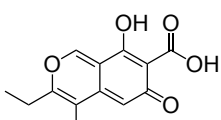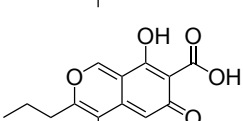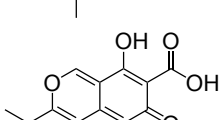
Figure 2-5 (A) Synthetic route for MPP1 inhibitor analogues.(B) Chemical structure of the nine ascochitine analogues which successfully synthesised by the company Sai Life Sciences.

Dr Jiazhi Tang at UCL School of Pharmacy conducted tests on the novel ascochitine-based analogues to determine their ability to inhibit MPP1 enzymatic activity. The basal ATPase activity revealed that none of the intermediate compounds (prior to the final cyclisation step) had any activity, indicating that the two-ring system is essential for inhibition. This indicated that the difficult final

cyclisation step, which is very challenging, cannot be avoided for this scaffold. Furthermore, it was also observed that analogue **16** with the methyl substituent is a weak inhibitor of MPP1 (IC_{50} = 53 µM), whereas the analogue **17** with the ethyl substituent has an IC_{50} value of 26.8 µM. The most active analogue **18** of this series with an n-propyl group has an IC_{50} of 6.6 µM and is slightly more active than the iso-propyl containing analogue **19**; IC_{50} = 11.9 µM. Compound **18** is approximately 2-fold more active than the parent compound ascochitine **13**, with an IC_{50} of 16 µM (Table **2-1**).

Table 2-1 Inhibition of MPP1 basal ATPase activity by ascochitine and ascochitine analogues with alkyl substitutions, synthesised by the Sai Life Sciences and tested by Dr. Jiazhi Tang.

Compound	Structure	Inhibition of MPP1 basal ATPase activity with IC_{50} (µM)
(R,S) ascochitine **13**		16.0 ± 1.8
R-ascochitine **14**		19.8 ± 3.3
S-ascochitine **15**		14.9 ± 3.4
16		68.7 ± 12.5
17		26.8 ± 6.5
18		6.6 ± 0.3
19		11.9 ± 2.0

The most active compounds **18** and **19** were further characterised using the MT-stimulated ATPase assay and demonstrated similar potencies (Table **2-2**).

Table 2-2 Inhibition of the MT-stimulated MPP1 ATPase activity by ascochitine and the most active analogues **18** and **19**, synthesised by the Sai Life Sciences and tested by Dr. Jiazhi Tang.

Compound	Structure	Inhibition of MT-stimulated MPP1 ATPase activity with IC$_{50}$ (µM)
(R,S) ascochitine 13		16.0 ± 1.8
18		5.5 ± 0.6
19		10.3 ± 1.0

Overall, the available structure-activity relationships for ascochitine indicate that the two-ring system is important for activity and that the n-propyl substituent is at least as active as the chiral s-butyl substituent (Figure **2-6**). This suggests that substitutions of the alkyl group could be pursued, but that alternative heterocyclic scaffolds should be considered to speed up the synthesis and increase the range of analogues that can be explored.
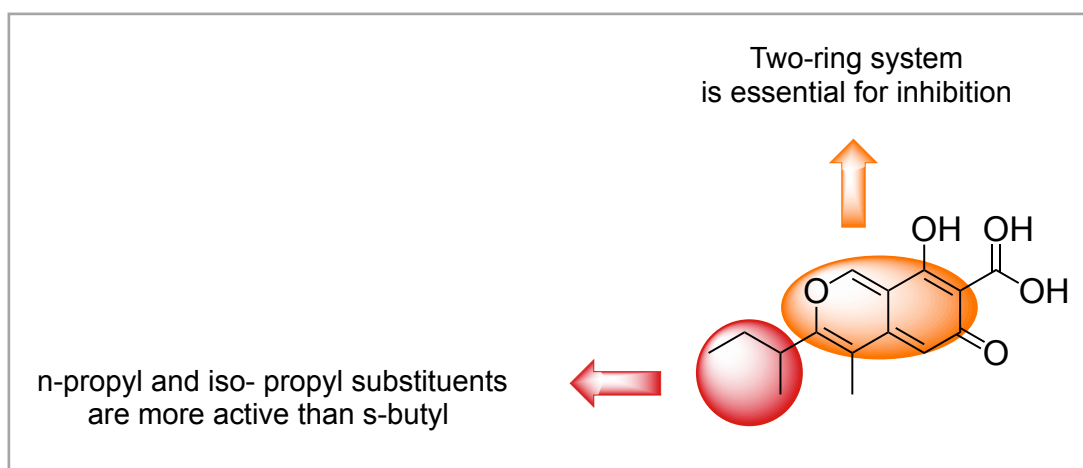
Figure 2-6 Structure activity relationship of R-ascochitine.

2.2 Aim and Objectives

This chapter focuses on a hit compound, R-ascochitine that is an inhibitor of MPP1.The aim of this chapter is to identify novel MPP1 kinesin inhibitors by synthesising compounds that incorporate similar pharmacophores. Such molecules may act as chemical probes for studying MPP1 biology and as potential lead compounds for drug development.

One of the objectives of the chapter is to identify new analogues related to these structures which may improve their biological activity (inhibition of the target protein, cytotoxicity, target, or cell line selectivity) and physicochemical properties (drug-like properties, solubility). Using pharmacophore-based searches we have identified structures with an O-substituted or N-substituted heterocyclic ring (i.e., chromenone-3-carboxylic acid and quinolone-3-carboxylic acid core structures) which have similar shapes and substitution patterns to that of ascochitine (see *2.3.2 Searching for ascochitine analogues using a pharmacophore-based approach*). They retain the enone carboxylic acid motif, of the right-hand ring and have a variable R_2 group in the left-hand ring in an equivalent position to the *s*-butyl substituent of ascochitine (Figure **2-7**).
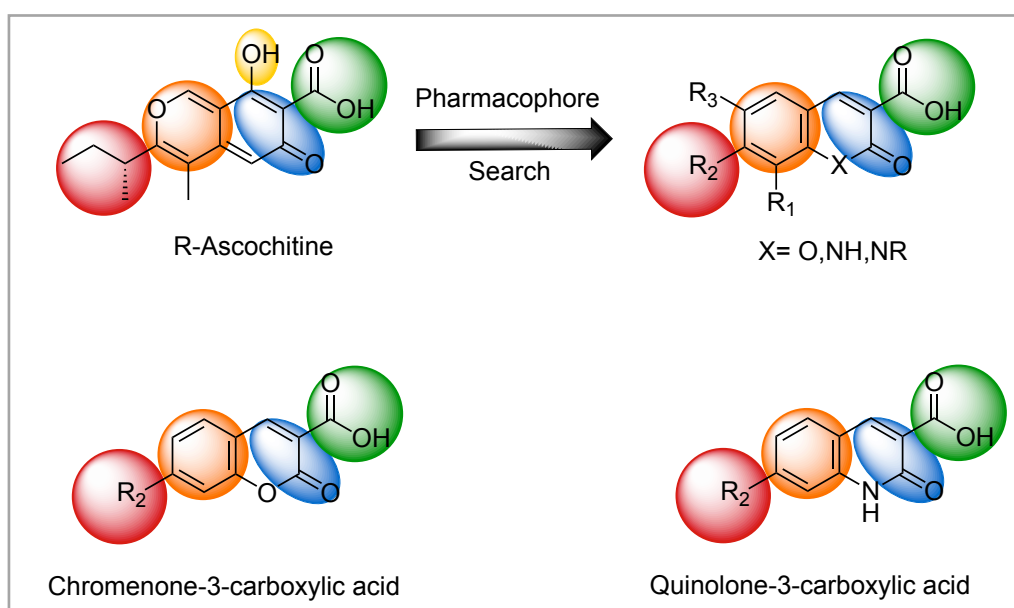
Figure 2-7 R-ascochitine and compounds with related pharmacophore features.

The synthesis of novel ascochitine-based inhibitors is challenging, requiring several synthetic steps to obtain analogues. To speed up the generation of novel inhibitor analogues, it is therefore desirable to simplify and shorten their synthesis. Thus, we are looking for small molecules that have the potential to be more synthetically accessible and more easily derivatised than the ascochitine, which should assist with the rapid development of structure-activity relationships.

In this chapter, we will provide answers to these questions:

1. How can coumarin and quinoline type compounds be synthesized? What method(s) can be applied and what reagents and reaction conditions can be applied to make compounds with the desired substitution patterns?
2. With a knowledge of the reactions used to make coumarin and quinoline type compounds, which analogues could be made using commercially available starting materials?
3. Can we make compounds with substituents that are closely related to ascochitine, and compounds that are different and more diverse in structure?

Additionally, the crystal structure of the MPP1 protein has not been determined, so in order to carry out molecular modelling and docking studies *in silico* we constructed a homology model of the protein and evaluated AlphaFold2 models of the MPP1 motor domain to predict the binding of ligands using LeDock, rDock, DOCK and Autodock Vina for docking calculations and AMBER software for molecular dynamics studies.

2.3 Result and Discussion

2.3.1 Development of additional synthetically accessible MPP1 analogues

As discussed, the synthesis of novel ascochitine-based inhibitors is challenging, with up to 11 steps required for certain analogues (see *2.1.1.1.2 Synthesis of novel ascochitine-based inhibitors targeting MPP1*), which makes the exploration of SARs with this scaffold a time consuming and resource intensive process. In order to speed up the generation of novel inhibitor analogues, it is therefore desirable to have simple and short synthetic routes to the target compounds.

Therefore, the focus was on finding isosteres of ascochitine that have a similar structure and biological activity but can be synthesised using simpler and shorter routes from commercially available starting materials.

2.3.2 Searching for ascochitine analogues using a pharmacophore-based approach
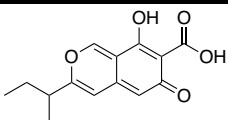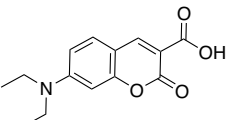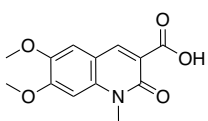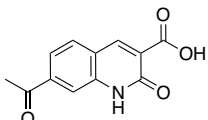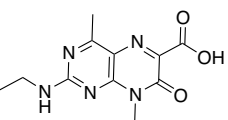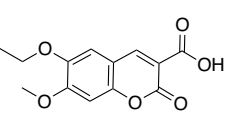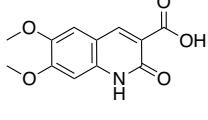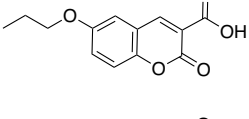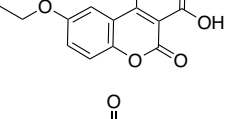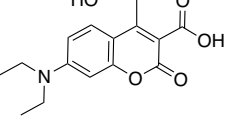
We used the online tool Zinc Pharmer (http://zincpharmer.csb.pitt.edu/) to identify potential lead compounds for synthesis based on the pharmacophore features of ascochitine.

The ascochitine features included two aryl/hydrophobic motifs, two hydrophobic centres on the *s*-butyl substituent, hydrogen bond acceptors associated with the ring oxygens, carbonyl, hydroxyl and carboxylate groups, a hydrogen bond donor (hydroxyl group) and a negatively charged site (carboxylate) (Figure **2-8** A). Based on the ascochitine structure-activity relationships (SAR), we chose the carboxylate anion, carbonyl hydrogen bond acceptor, the hydrophobic sites associated with the bicyclic ring system and the extended alkyl substituent as key features to be reproduced in the pharmacophore-based search (Figure **2-8** B).
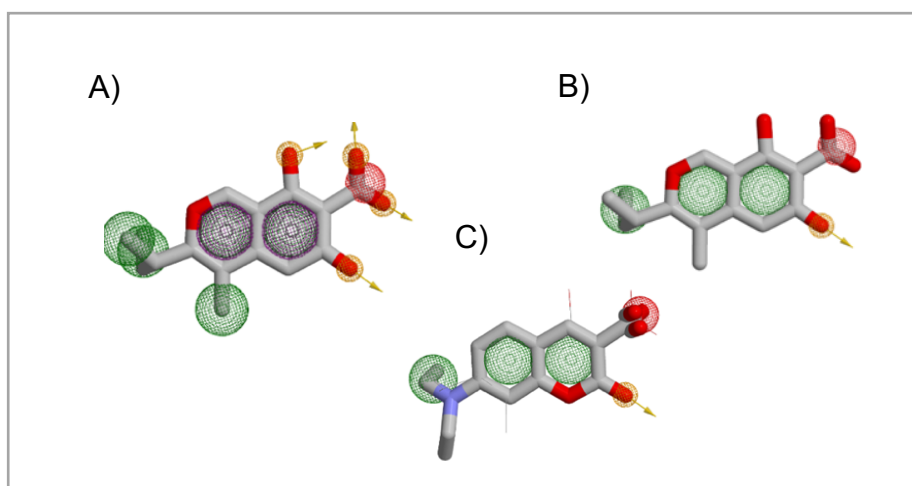
Figure 2-8 A) The pharmacophore features of ascochitine. Hydrophobic substituents are shown in (green), aryl groups (black), H-bond acceptors (yellow) and the negative charge (red); B) The features selected for the pharmacophore-based search of the ZINC database; and C) Example of a hit compound (sticks) overlaid on the ascochitine structure (line representation).

Table 2-3 Pharmacophore-based hits with structural similarity to ascochitine

Compound	Structure	RMSD (Å)[a]
(R,S) ascochitine **13**		0.140
25		0.162
26		0.220
27		0.222
28		0.232
29		0.234
30		0.254
31		0.271
32		0.272
33		0.295

a. RMSD relative to the ascochitine pharmacophore features in Figure 6B.

The top nine unique hits are shown in (Table **2-3**). The best overlap was established with ascochitine (RMSD = 0.140 Å). It was noteworthy that four of the next eight hits had a coumarin scaffold and four were quinolin-2-ones.

The pharmacophore-based search suggested that chromenone-3-carboxylic acid and quinolone-3-carboxylic acid core structures would act as potential isosteres by virtue of having similar shapes and substitution patterns to that of ascochitine, which can then be used as starting points for the design of novel inhibitors. These isosteric compounds have the potential to be more synthetically accessible and more easily derivatized than ascochitine, with a significantly reduced number of synthesis steps (between 2 and 3 in most cases), which should assist with the rapid development and optimization of structure-activity relationships (SAR), and were selected as starting points for the design and synthesis of novel MPP1 inhibitors.

The core structures of chromenone-3-carboxylic acid and 2-quinolone-3-carboxylic acid (Figure **2-9** A, B) can be modified with substituents related to ascochitine (Figure **2-9** C) or related structures such as 4-quinolone-3-carboxylic acid (Figure **2-9** D) to create new derivatives. This diversification of the structure has the potential to lead to the discovery of compounds with improved biological activities.

Chromenone-3-carboxylic acids and 4-hydroxychromen-2-one-3-carboxylic acids are compounds that share structural similarities with flavanones and coumarins (Figure **2-10** A), respectively. Flavanones are a class of flavonoids that are commonly found in plants and are known for their antioxidant and anti-inflammatory properties, while coumarins are organic compounds found in many plants and are known for their anticoagulant and vasodilatory effects. On the other hand, quinolone-3-carboxylic acids are aza-analogues of flavanones and analogues of quinolines (Figure **2-10** B).
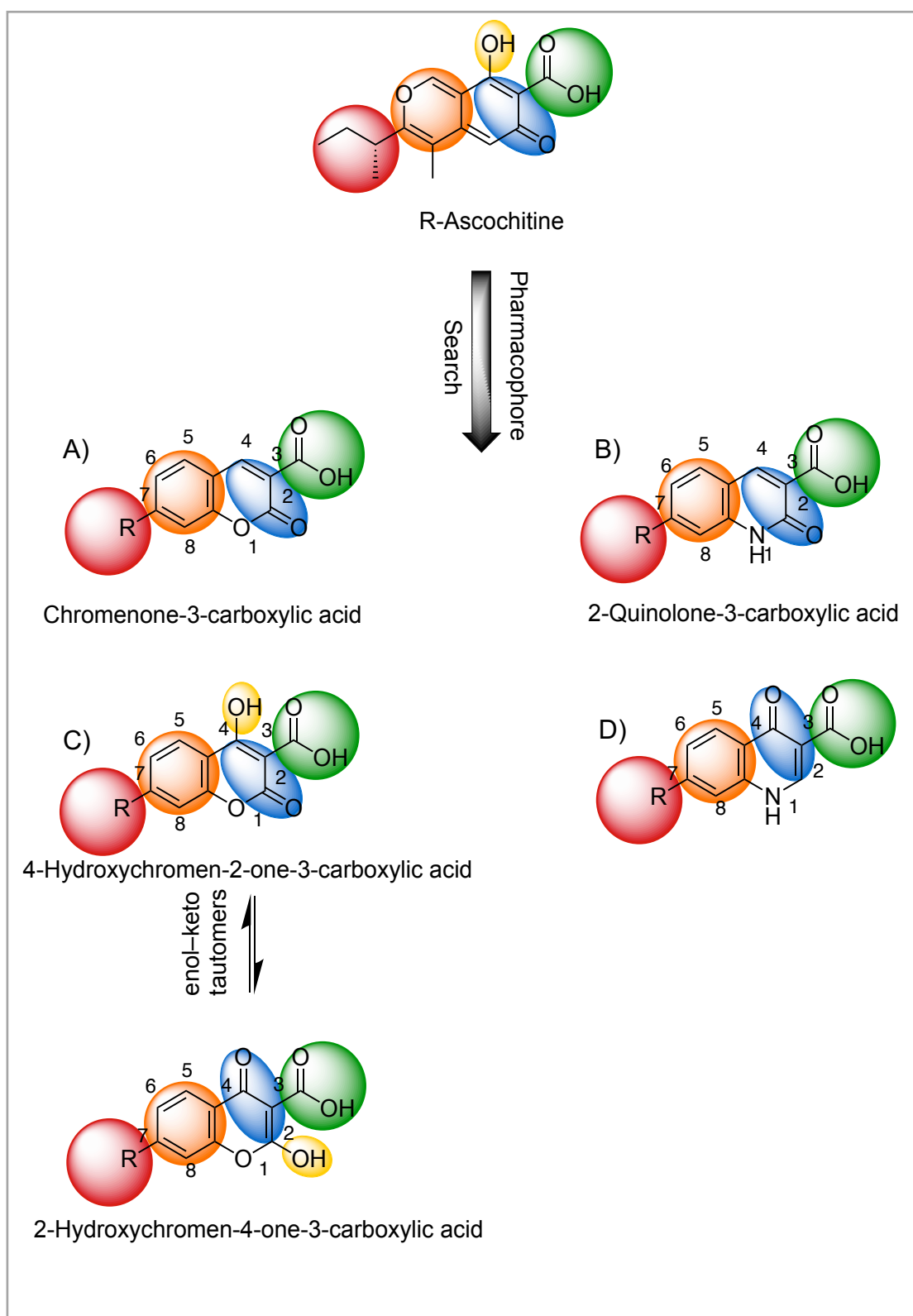
Figure 2-9 Chromenone-3-carboxylic acid and 2-quinolone-3-carboxylic acid core and alternative structures.
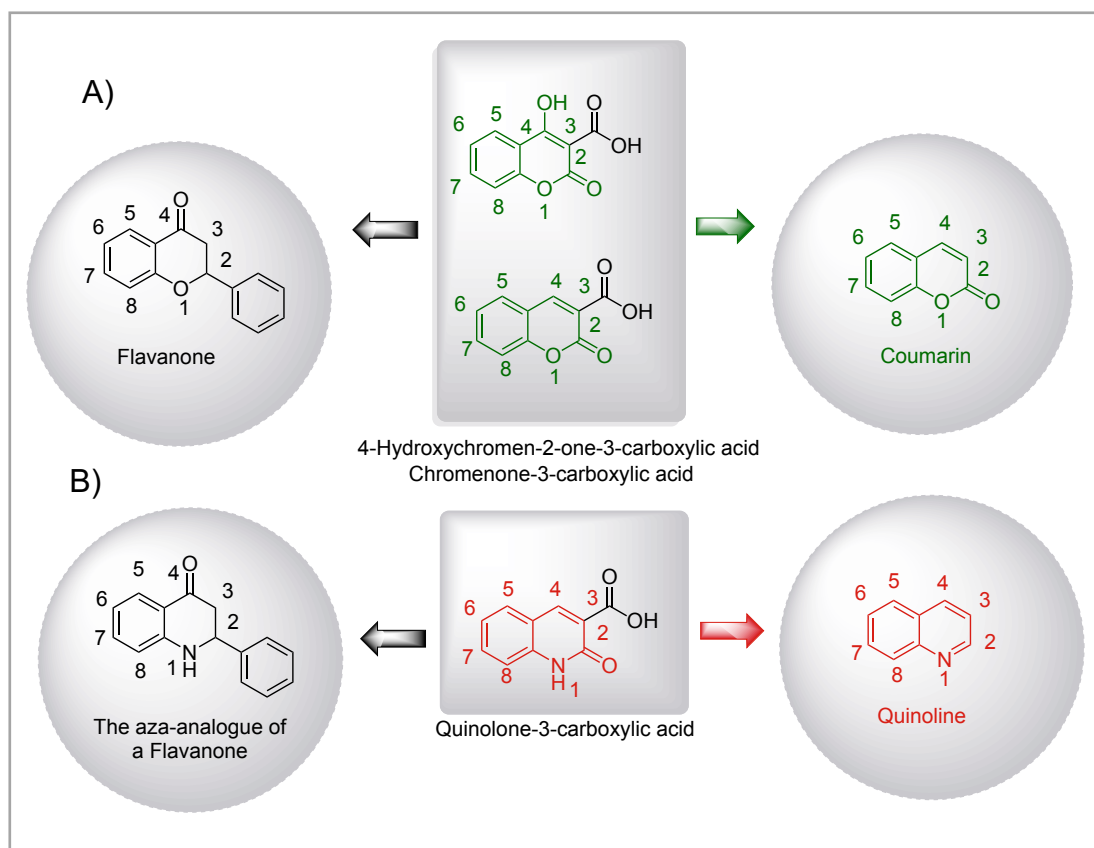
Figure 2-10 Chromenone-3-carboxylic acid, quinolone-3-carboxylic acid, and 4-Hydroxychromen-2-one-3-carboxylic acid as coumarin, quinoline, Flavanone and aza-analogue of a Flavanone analogues structures.

2.3.3 Design and synthesis of coumarins

The initial compounds were designed with a carboxylate ester or a carboxylic acid at C-3 position and the commercially available substitutions including alkyl and alkoxy groups at the C-7 position of the coumarin core (Figure **2-11** A). Eight analogues were synthesised to evaluate their activity as MPP1 inhibitors (Figure **2-11** B).
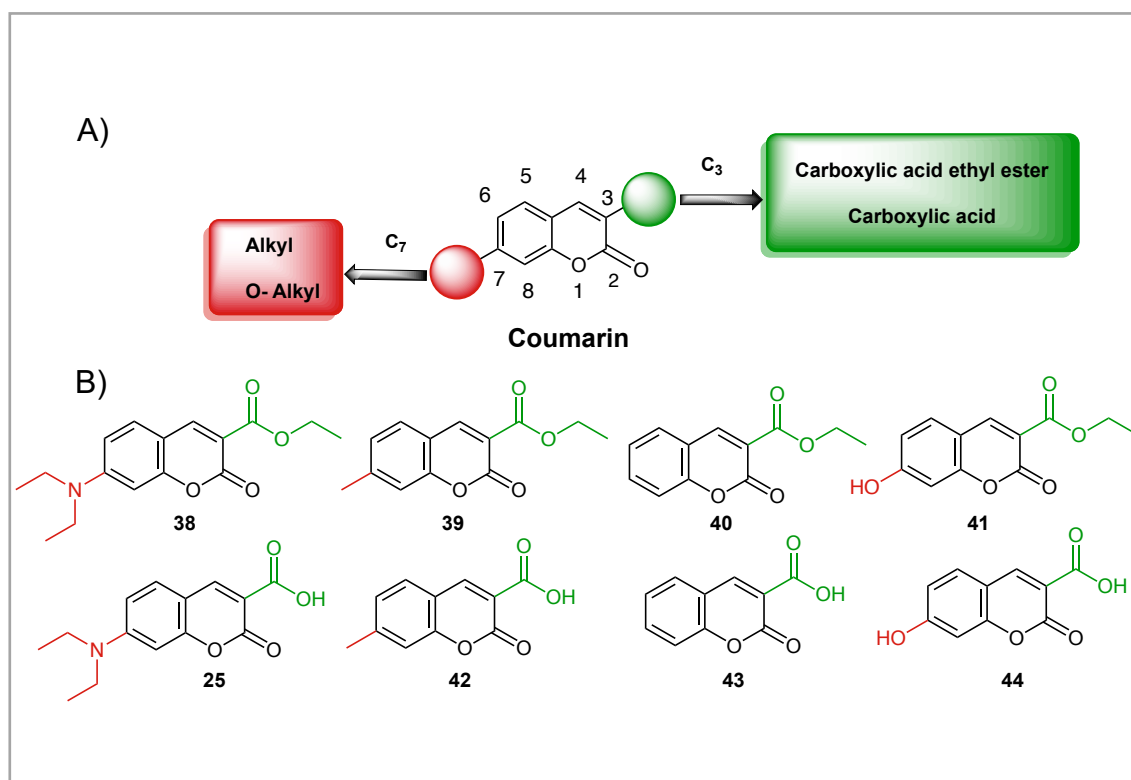
Figure 2-11 Modification on coumarin to identify new analogues.

2.3.3.1 Synthesis of chromenone-3-carboxylic acid ethyl esters and chromenone-3-carboxylic acids

In order to synthesise this small series of chromenone-3-carboxylic acid derivatives we chose a short synthetic route that allowed us to react commercially available salicylaldehydes under Claisen-Schmidt condensations with diethyl malonate. Piperidine was used as the catalyst and ethanol as a solvent. In this reaction, the carbonyl group of the salicylaldehyde undergoes nucleophilic attack by the deprotonated methylene group of diethyl malonate to give the chromenone-3-carboxylic acid ethyl esters with yields in the range 44-77% (Table **2-4**). The structures of the compounds were confirmed by their ^{1}H NMR spectra and comparison with analytical data from the literature. The presence of a triplet corresponding to three hydrogens at δ 1.0-1.6 and a quartet (two hydrogens) at δ (4.2-4.4) in the compounds, confirming the presence of the ethyl ester, in addition to the other expected resonances confirmed that the desired condensation-cyclization reaction has occurred. The yield of analogue **30** under

these reaction conditions was 44%. The yield of this compound was increased considerably by replacing ethanol as a solvent with piperidine, which functioned as both catalyst and solvent, a shorter reaction time (1 hr vs 24 hrs) and lower temperature (RT cf. reflux) which afforded the 7-hydroxy-2-oxo-2H-chromene-3-carboxylic acid ethyl ester in 90% yield after recrystallization from ethanol (Table **2-4**). The ethyl esters were then hydrolysed to the corresponding free acids using aqueous sodium hydroxide solution*.* Subsequent analysis of the ^{1}H NMR spectrum of chromenone-3-carboxylic acids established that the ethyl protons were no longer present and a broad single peak at δ 12.0 was consistent with the presence of a carboxylic acid.

Table 2-4 General scheme for synthesis of chromenone-3-carboxylic acid ethyl esters, chromenone-3-carboxylic acids, and percentage yield products.
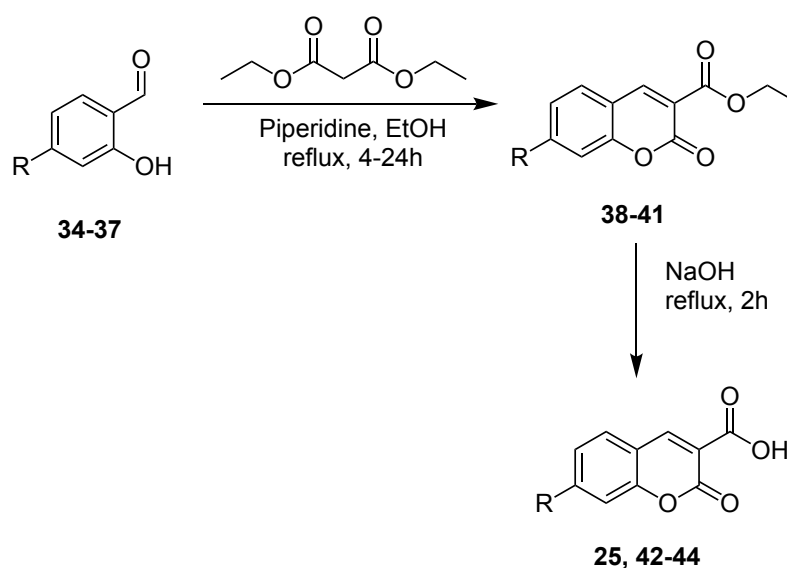
R	Chromone-3-carboxylic acid ethyl esters	Yield %	Chromone-3-carboxylic acid	Yield %
–ξ–N(CH₂CH₃)₂	38	63	25	43
-ξ–CH₃	39	77	42	
H	40	76	43	75
-ξ–OH	41	44-(90)[a]	44	53

a. Synthesis using piperidine as catalyst and solvent.

2.3.4 Biological evaluation of coumarins

2.3.4.1 Basal ATPase measurements of chromenone-3-carboxylic acid ethyl esters and chromenone-3-carboxylic acids

The compounds were tested for their ability to inhibit MPP1 enzymatic activity by Dr Jiazhi Tang at UCL School of Pharmacy. The inhibition of basal ATPase activity was measured in the absence of salt at a fixed concentration of inhibitor (200 µM) and the percentage inhibition was determined at this concentration (Table **2-5**). The most active compound in this experiment was analogue **44** which has a C3-carboxylic acid and C7- hydroxyl substituent. The corresponding ester compound **41** was less active, and compounds with other C-7 substituents were relatively inactivate at the test concentration.

Analogue **44** was tested for its ability to inhibit MPP1 enzymatic activity in a dose-response assay. The inhibition of basal ATPase activity was measured in the absence of salt using inhibitor concentrations up to a maximum of 200 µM. The concentration response profile suggests that the IC_{50} of the compound is close to 200 µM.

The inhibitory activity of this compound is lower than ascochitine but suggests that it may be possible to optimise the substitution pattern of the chromenone-3-carboxylic acids in order to improve their MPP1 inhibitory activity.

Table 2-5 Inhibition of MPP1 by chromenone-3-carboxylic acid ethyl esters and chromenone-3-carboxylic acids.

Compound	Structure	Percentage inhibition (%)[a]
38		12
39		20
40		7
41		31
25		3
42		12
43		9
44		68

a. Inhibition of MPP1 basal ATPase activity by chromenone-3-carboxylic acids at a fixed concentration of 200 µM. Data obtained by Dr. Jiazhi Tang

2.3.5 Further investigation of C-7 and C-3 positions of coumarins

In order to study the influence of substituent effects on the inhibitory activity and expand the structure-activity relationship library of carboxycoumarin derivatives, it was decided to keep the core coumarin heterocycle unchanged and explore modifications to the C-3 position by synthesising a series of carboxamides derived from primary (benzylamine and aniline) or secondary amines (piperidine and diethyl amine). At the C-7 position a hydroxy substituent, or methoxy or benzyloxy ethers were included to evaluate their activity as MPP1 inhibitors

(Figure **2-12** A). In total, 14 derivative compounds as a new series of coumarins (Figure **2-12** B).
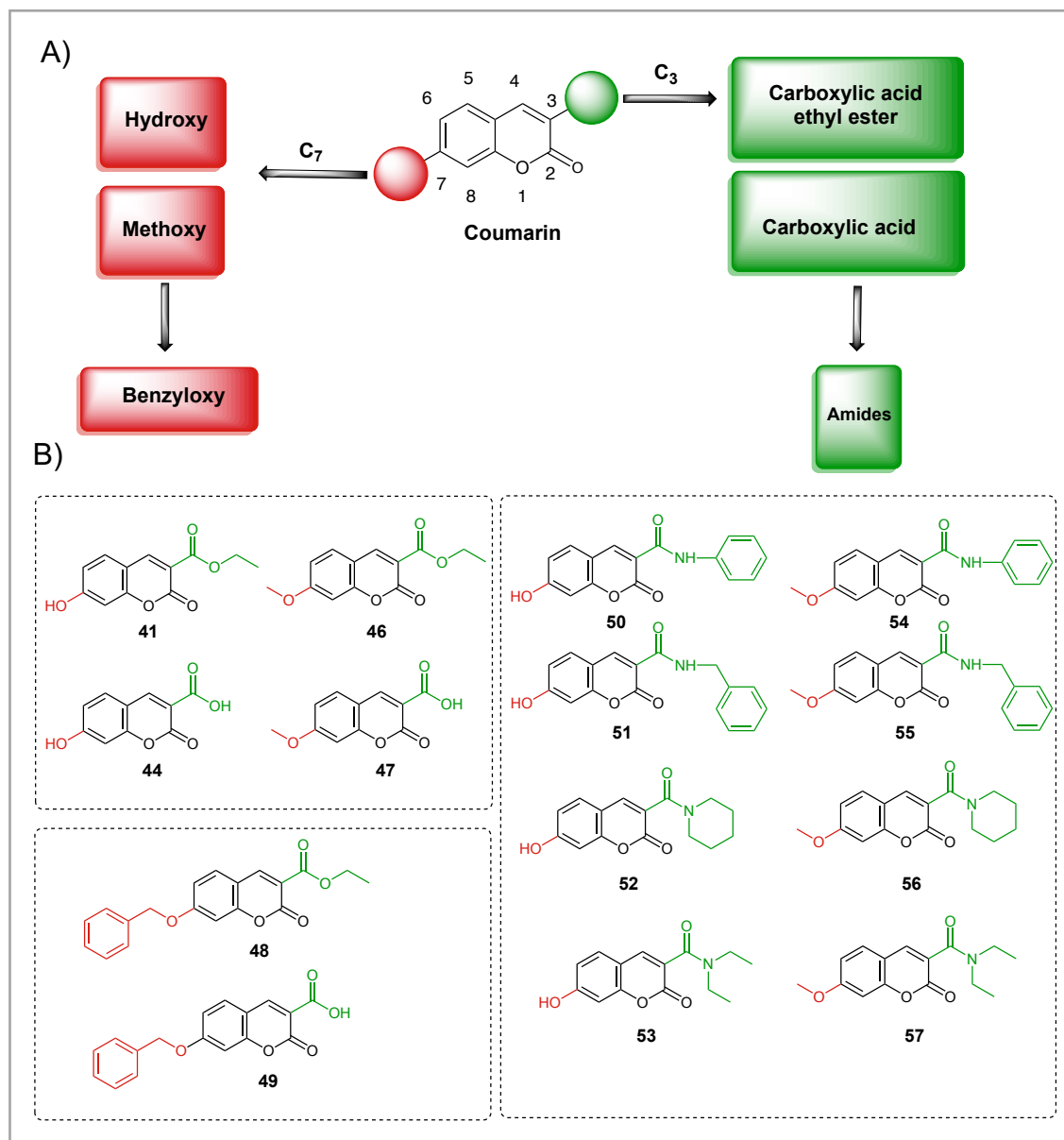
Figure 2-12 Modification on C-7 and C-3 positions of coumarin to identify new analogues.

2.3.5.1 Synthesis of 7-alkoxy-chromenone-3-carboxylic acid ethyl esters 7-alkoxy-chromenone-3-carboxylic acids

Claisen-Schmidt condensation of 2,4-dihydroxybenzaldehyde with diethyl malonate in the presence of piperidine as a catalyst and solvent gave the 7-hydroxy-chromenone-3-carboxylic acid ethyl ester **41** in 90% yield *(Figure **2-13**)*. The condensation of 2-hydroxy-4-methoxybenzaldehyde with diethyl malonate in the presence of piperidine as a catalyst and solvent gave the 7-methoxy-chromenone-3-carboxylic acid ethyl ester **46** in 92% yield *(Figure **2-13***). The structures of the compounds were confirmed by their ^{1}H NMR spectra and comparison with analytical data from the literature. The presence of a triplet corresponding to three hydrogens at δ 1.30 and a quartet (two hydrogens) at δ 4.27 in the compounds in addition to the other expected resonances confirmed that the desired condensation-cyclization reaction has occurred.

The 7-hydroxy-chromenone-3-carboxylic acid ethyl ester **41** and the 7-methoxy-chromenone-3-carboxylic acid ethyl ester **46** were hydrolysed using sodium hydroxide to give the corresponding 7-hydroxychromenone-3-carboxylic acid **44** and 7-methoxychromenone-3-carboxylic acid **47** in 53% and 57% yields, respectively. Subsequent analysis of the ^{1}H NMR spectrum of 7-substituted-chromenone-3-carboxylic acids established that the ethyl protons were not present, and a broad single peak appeared at around δ 12 ppm was consistent with the presence of a carboxylic acid.
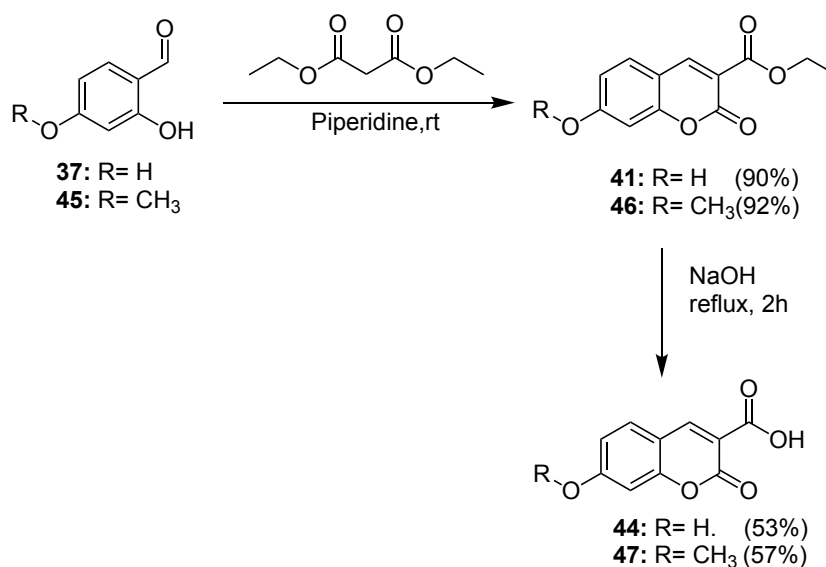
Figure 2-13 General scheme for synthesis of 7-alkoxy-chromenone-3-carboxylic acid ethyl esters, 7-alkoxy-chromenone-3-carboxylic acids.

2.3.5.2 Synthesis of 7-benzyloxy-chromene-3-carboxylic acid ethyl ester and 7-benzyloxy-chromene-3-carboxylic acids

The previously synthesised 7-hydroxy-chromene-3-carboxylic acid ethyl ester **41** was alkylated using benzyl bromide in the presence of potassium carbonate in DMF to give the corresponding 7-benzyloxychromene-3-carboxylic acid ethyl ester **48** in 88% yield (Figure **2-14**). Subsequent analysis of the ^{1}H NMR spectrum of 7-benzyloxy-chromene-3-carboxylic acid ethyl ester **48** revealed the absence of the C7 hydroxyl proton, consistent with the formation of the required ether. The 7-benzyloxychromene-3-carboxylic acid ethyl ester was hydrolysed under basic conditions such as sodium hydroxide to give the corresponding 7-benzyloxy-chromene-3-carboxylic acid **49** in a 54% yield (Figure **2-14**). The ^{1}H NMR spectrum of 7-benzyloxy-chromene-3-carboxylic acid confirmed that the ethyl protons were absent and that a proton associated with the carboxylic acid appeared at around δ 13.
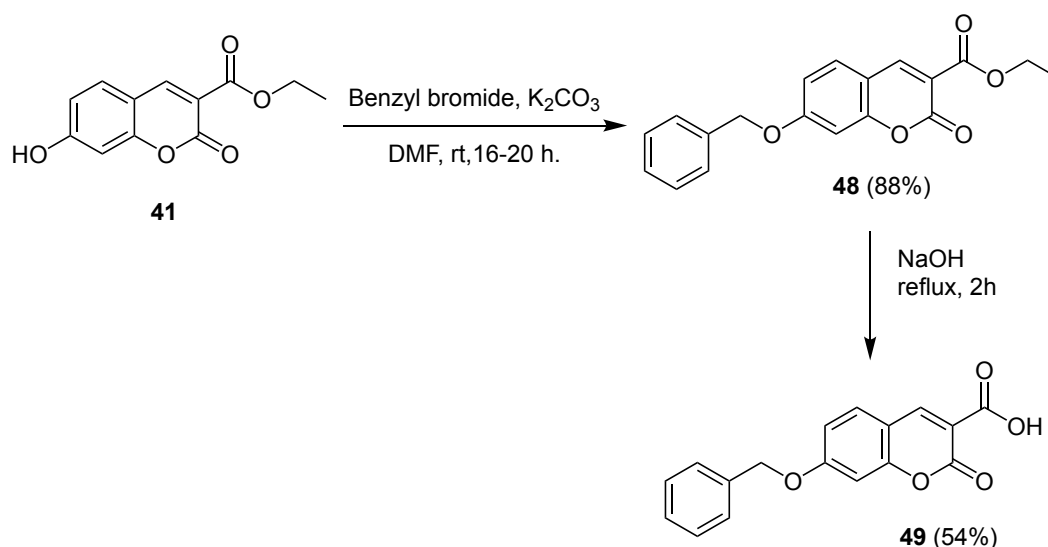
Figure 2-14 General scheme for synthesis of 7-benzyloxy-chromene-3-carboxylic acids.

2.3.5.3 Synthesis of 7-Alkoxy-chromene-3-carboxamides

The previously described 7-substituted-chromene-3-carboxylic acids were used to synthesise a series of amide derivatives by coupling with either aniline, benzylamine, piperidine or diethyl amine (1eq) using 1-(3-dimethylaminopropyl)-3-ethylcarodiimide hydrochloride (EDCI) (1.5eq) in the presence of a catalytic quantity of 4-(dimethyl amino) pyridine (DMAP) and N,N-diisopropylethylamine (DIPEA) (1eq) as a base. The reactions were quite slow, typically taking up to 72 hours. This time was reduced by increasing the equivalence of EDCI from 1.5 to 2 and replacing the DIPEA with DMAP (2.5 equivalents) as both base and catalyst. The products were formed in 63-79% isolated yields (Table **2-6**) and the structures of the compounds was confirmed by ^{1}H and ^{13}C NMR spectra and LCMS were consistent with the expected amides.

Table 2-6 General scheme for synthesis of 7-alkoxy-chromene-3-carboxamides and percentage yield products.

44: R= H.
47: R= CH₃
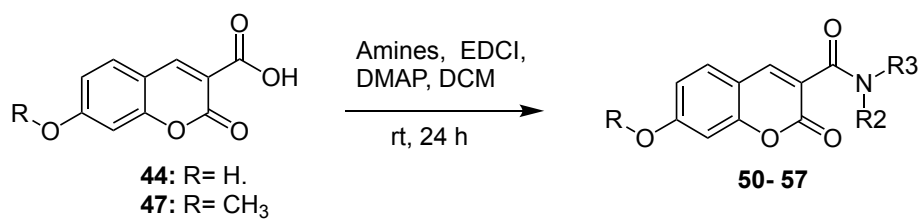
R	R₂	R₃	7-Alkoxy-chromene-3-carboxamides	Yield %
H	H		**50**	71
H	H		**51**	64
H			**52**	73
H	-ξ-CH₂CH₃	-ξ-CH₂CH₃	**53**	74
-ξ-CH₃	H		**54**	79
-ξ-CH₃	H		**55**	63
-ξ-CH₃			**56**	63
-ξ-CH₃	-ξ-CH₂CH₃	-ξ-CH₂CH₃	**57**	66

2.3.6 Molecular docking of compounds to MPP1

2.3.6.1 Human MPP1 Homology Model

Molecular docking is used to predict the binding mode of a small molecule to a protein target. In the case of human MPP1, for which there is no published crystal structure, a homology model of the protein can be created using one or more known structures of related proteins as a template. This homology model can then be used in molecular docking studies to predict the binding of potential inhibitors, such as physodic acid, norlobaridone, R-ascochitine and chromenone-3-carboxylic acid derivatives, to the protein. The binding energy and binding mode of the compounds can be predicted using molecular docking software. This information can be used to guide further optimization of the compound for improved binding and potential as an anti-cancer drug. We uploaded the FASTA sequence of the MPP1 motor domain to the Protein Model Portal (https://www.proteinmodelportal.org/). The M4T server produced three models of which the first (Cluster1) had the best overall scores. The templates selected by the server were from the human Eg5 kinesin in complex with Mg-ADP (PDB entry 1II6 https://www.rcsb.org/structure/1ii6) and kinesin-6 from *Caenorhabditis elegans* (PDB entry 5X3E https://www.rcsb.org/structure/5X3E), the latter structure incorporates a region that has similarities to the long L6 loop of MPP1. The sequence similarity with the best template was 34.4%. In (Figure **2-15**).
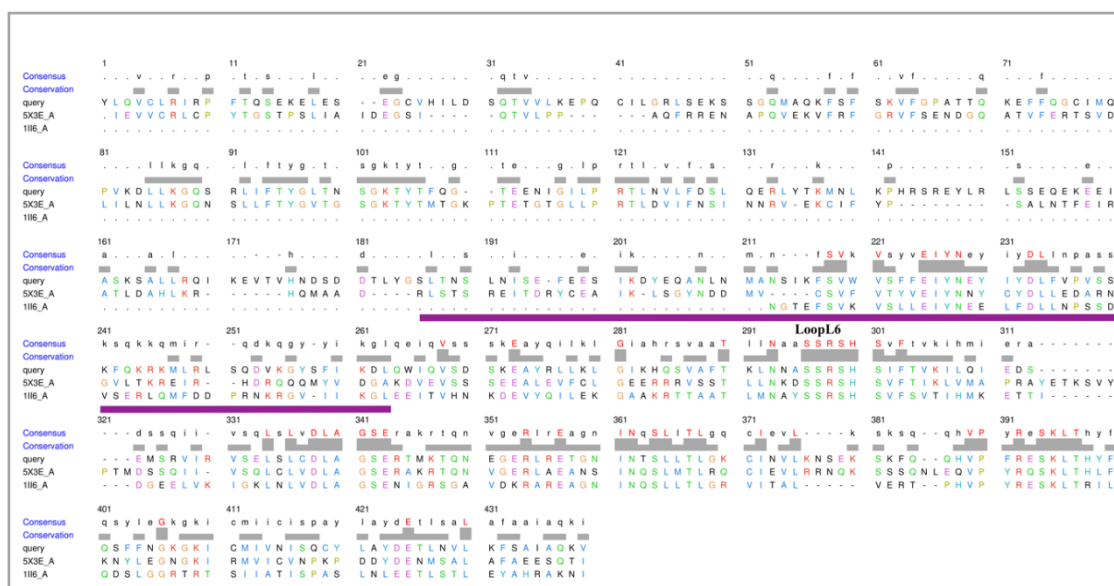
Figure 2-15 Sequence alignment of the human Eg5 kinesin motor domain (PDB entry 1II6) for which the crystal structure is available with kinesin 6 from *Caenorhabditis elegans* (PDB entry 5X3E). The alignment shows the characteristic long inserting in the motor domain of MPP1 inserted in the loop L6 region (aa186-262) (marked in purple) of the motor domain with unknown function. The structure alignment was performed using UCSF Chimera 1.13.1.

This homology model was compared with the widely studied crystal structure of the Eg5 kinesin and was used for subsequent docking experiments. The individual structures of human Eg5 (Figure **2-16** A) and homology model of human MPP1 (Figure **2-16** B) and the superimposed structures illustrates the similarity between these two motor domains (RMSD = 0.763 Å). By analogy to the Eg5 motor, one of the potential binding pockets on the MPP1 homology model is an allosteric site adjacent to the Mg-ADP binding site in (Figure **2-16** C).
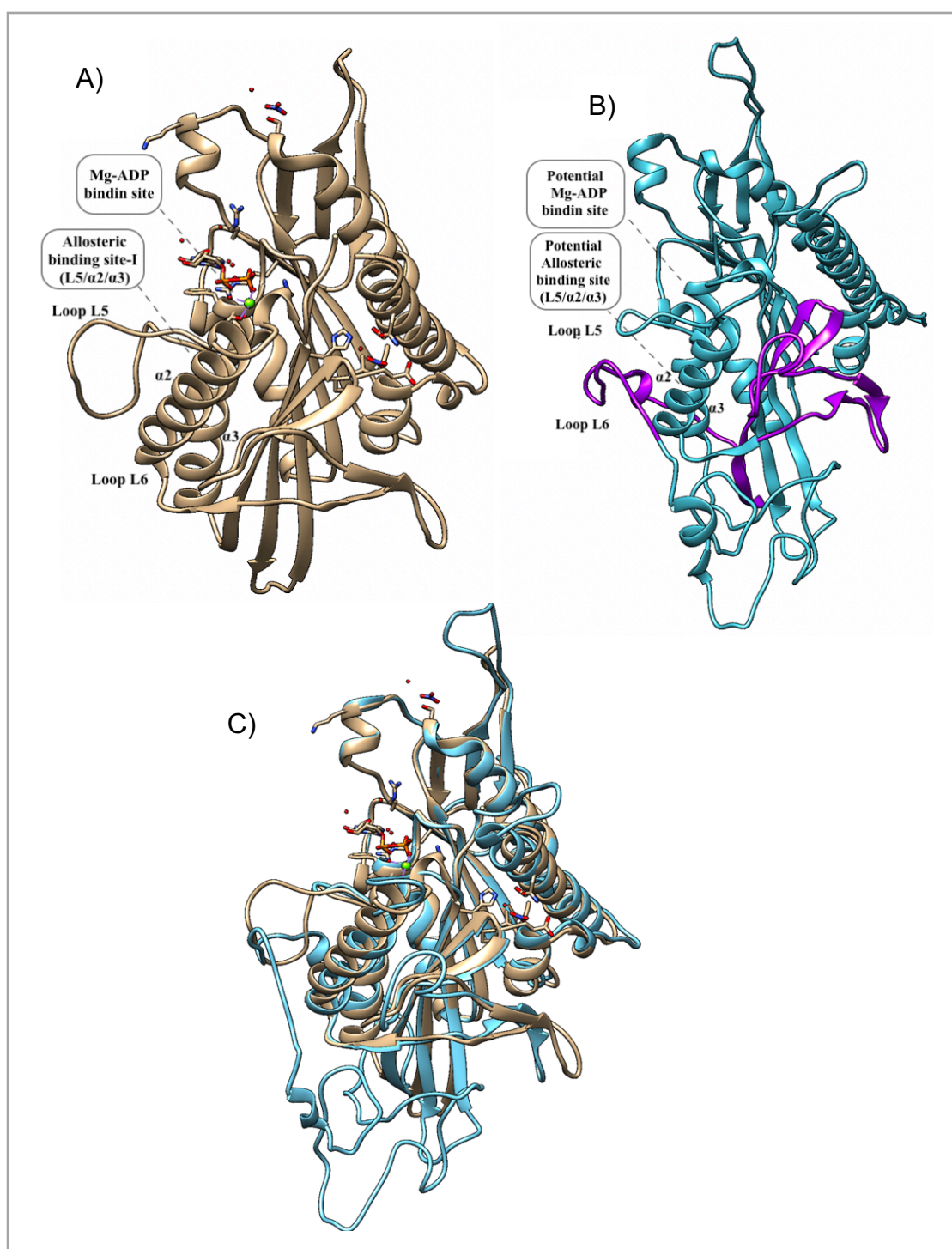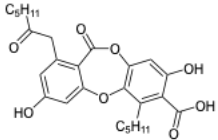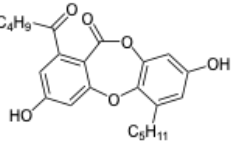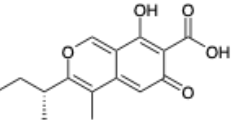
Figure 2-16 Superimposed crystal structure of human Eg5 kinesin motor domain with Mg-ADP (PDB entry 1II6) and the human MPP1 motor domain homology model. A) Crystal structure of human Eg5 kinesin motor domain in ribbons (beige) (PDB entry1II6) represent allosteric binding site and ADP binding site. B) Human MPP1 motor domain homology model structure in ribbons (blue) represent of the predicted or corresponding binding site and the loop L6 region in (purple). C) Superimposition of the human Eg5 kinesin motor domain in ribbons (beige) and human MPP1 motor domain homology model structure in ribbons (blue) (Image prepared using UCSF Chimera).

2.3.6.2 Docking of depsidones and R-ascochitine to the MPP1 homology model

Using the homology model of MPP1, a series of compounds, including the known depsidone inhibitors physodic acid, norlobaridone and R-ascochitine, were docked into the allosteric pocket adjacent to the Mg-ADP binding site. We used AutoDock Vina and LeDock to run the docking calculations. AutoDock Vina [124] and LeDock [140] are software programs that can be used to dock small molecules to the predicted 3D structure of human MPP1 and predict the binding affinity of potential inhibitors. These programs use different algorithms and strategies for predicting the binding pose and affinity of ligands to a protein, so using both can provide a more comprehensive analysis of potential inhibitors. The results are shown in (Table **2-7** and Figure **2-17** to Figure **2-22**).

Table 2-7 Binding affinity and interactions of depsidones and r-ascochitine with the human MPP1 motor domain homology model.

Compound	structure	H-B	BA LeDock kcal/mol	H- B	BA AutoDock Vina kcal/mol
Physodic acid **11**		3	-6.56	1	-7.4
Norlobaridone **12**		2	-5.86	0	-7.1
R-ascochitine **14**		5	-4.24	0	-6.1

The docking scores represent the predicted binding energy of the higher ranked protein ligand complex. The hydrogen bonds count between the ligand and protein was calculated using UCSF Chimera.

Using LeDock, the docked conformation of physodic acid forms hydrogen bond interactions with Asn190, Ser197 and Lys276 of MPP1, the latter interaction is also reproduced in the AutoDock Vina structure (Figure **2-17** and Figure **2-18**).

2.3.6.2.1 Docking of Physodic acid to the MPP1 homology model
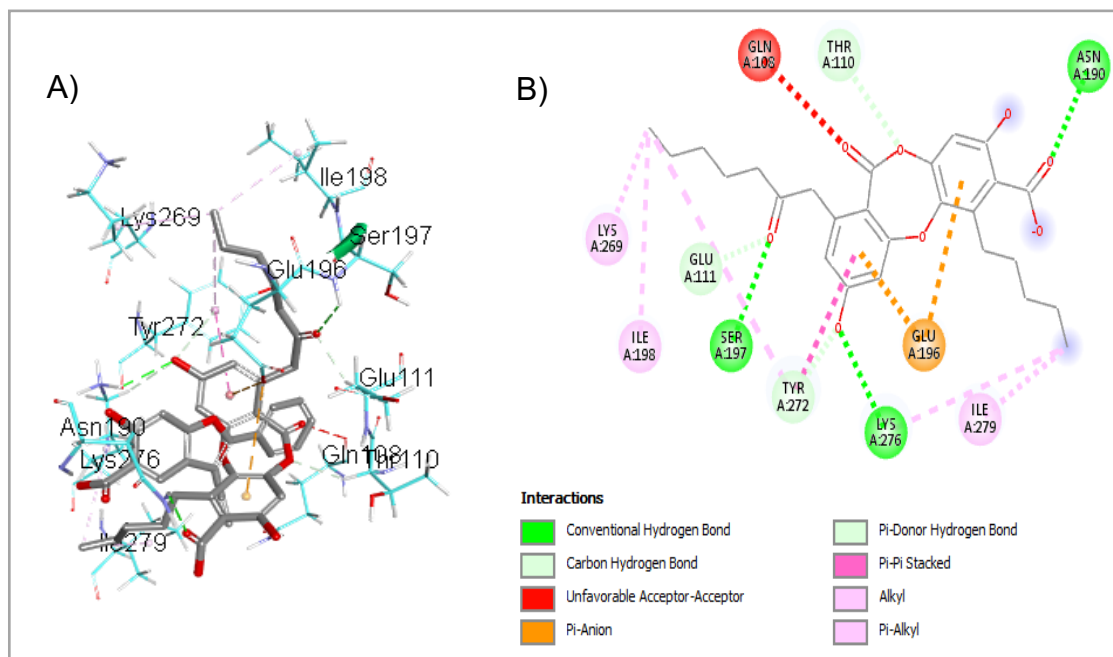
Figure 2-17 The best pose of physodic acid docked into allosteric site of the MPP1 homology model using LeDock: A) 3D protein and B) 2D protein - ligand interaction plots. Amino acids residues are represented as cyan thin sticks, while the ligand is shown as thick sticks with carbon atoms coloured in grey.
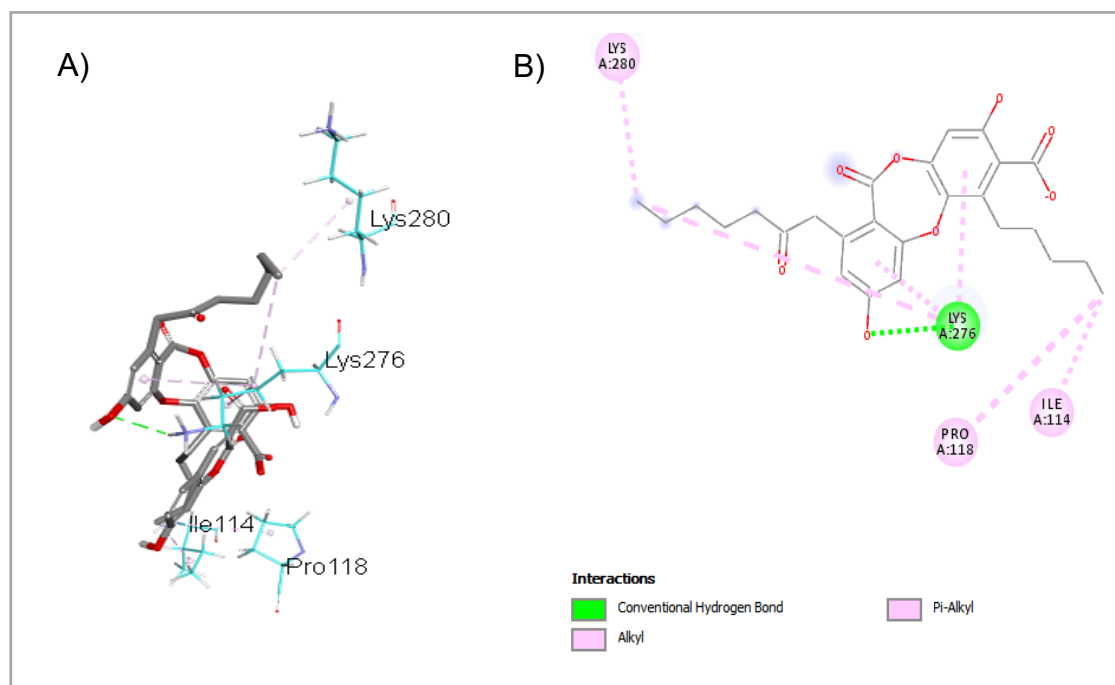
Figure 2-18 The best pose of physodic acid docked into allosteric site of the MPP1 homology model using AutoDock Vina: A) 3D protein and B) 2D protein - ligand interaction plots. Amino acids residues are represented as cyan thin sticks, while the ligand is shown as thick sticks with carbon atoms coloured in grey.

2.3.6.2.2 Docking of Norlobaridone to the MPP1 homology model
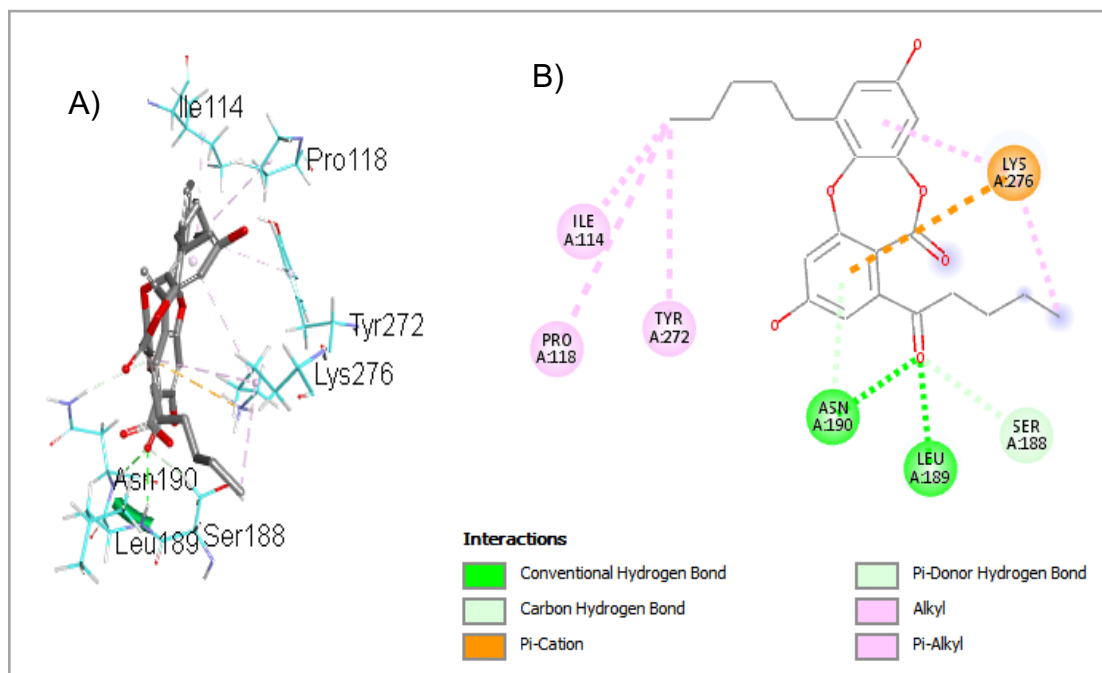
Figure 2-19 The best pose of norlobaridone docked into allosteric site of the MPP1 homology model using LeDock: A) 3D protein and B) 2D protein - ligand interaction plots. Amino acids residues are represented as cyan thin sticks, while the ligand is shown as thick sticks with carbon atoms coloured in grey.
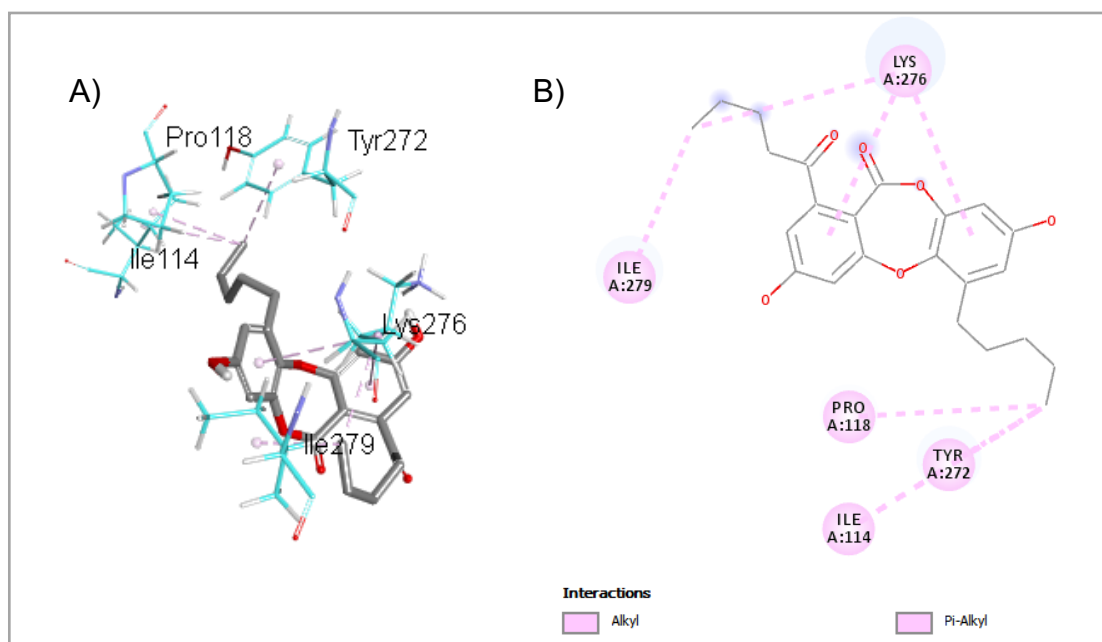
Figure 2-20 The best pose of norlobaridone docked into allosteric site of the MPP1 homology model using AutoDock Vina: A) 3D protein and B) 2D protein - ligand interaction plots. Amino acids residues are represented as cyan thin sticks, while the ligand is shown as thick sticks with carbon atoms coloured in grey.

In the case of norlobaridone, hydrogen bond interactions are only observed in the LeDock complex (via MPP1 residues Leu189 and Asn190) (Figure **2-19** and Figure **2-20**).

The calculated binding affinities for the two compounds are in the same order as the measured binding affinities (Table **2-7**).

2.3.6.2.3 Docking of R-ascochitine to the MPP1 homology model

The hydrogen bond interactions of R-ascochitine are only observed in the LeDock complex (via MPP1 residues Ser192, Leu189 and Asn190) illustrated in (Figure **2-21** and Figure **2-22**)
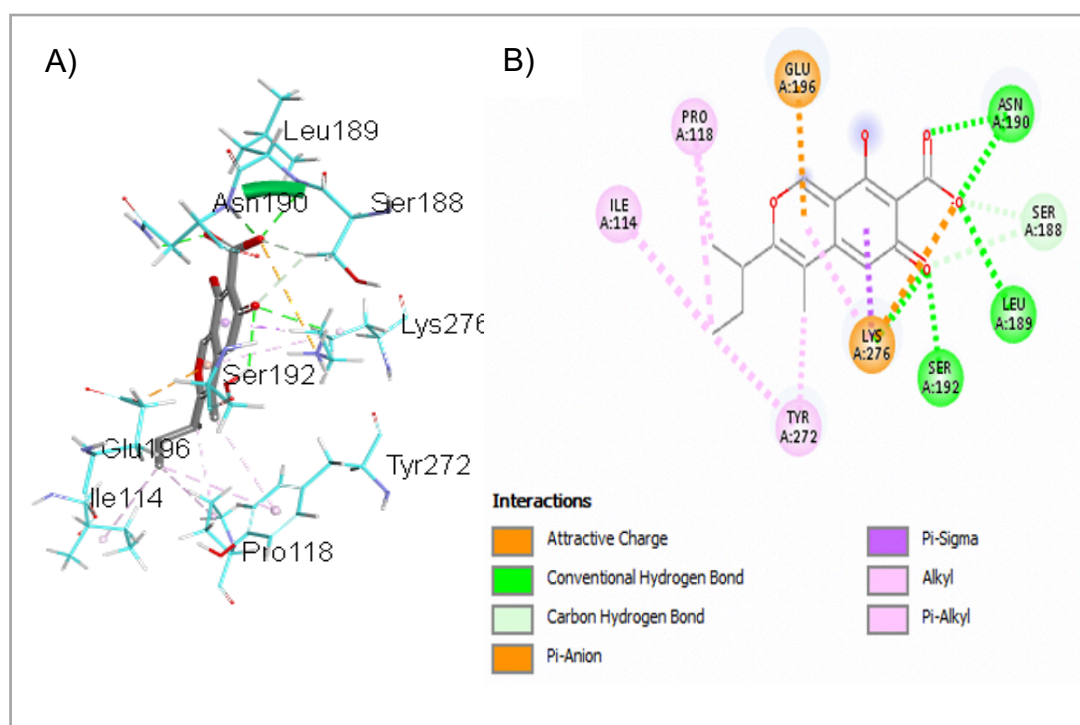
Figure 2-21 The best pose of R-ascochitine docked into allosteric site of the MPP1 homology model using LeDock: A) 3D protein and B) 2D protein - ligand interaction plots. Amino acids residues are represented as cyan thin sticks, while the ligand is shown as thick sticks with carbon atoms coloured in grey.
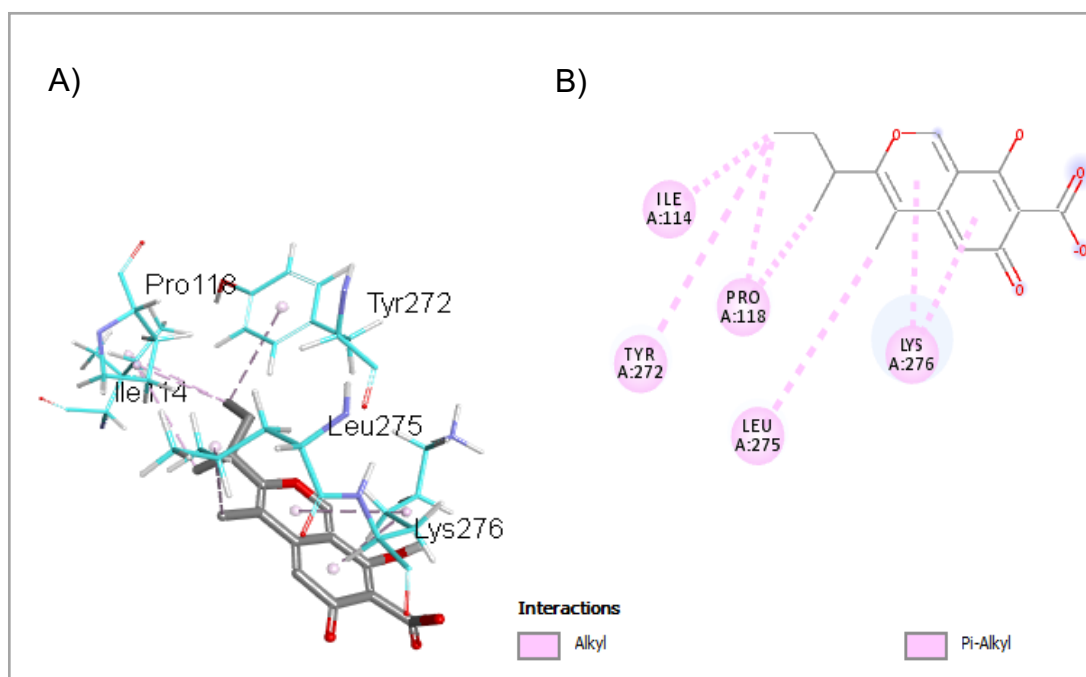
Figure 2-22 The best pose of R-ascochitine docked into allosteric site of the MPP1 homology model using AutoDock Vina.: A) 3D protein and B) 2D protein - ligand interaction plots. Amino acids residues are represented as cyan thin sticks, while the ligand is shown as thick sticks with carbon atoms coloured in grey.
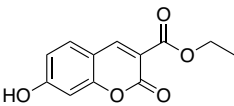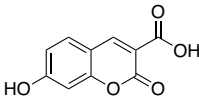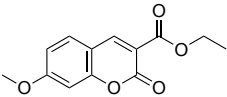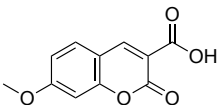
Furthermore, molecular docking with our available homology model of MPP1 studies suggested that physodic acid, norlobaridone and R-ascochitine may not be competitive with ATP and interact with a potential allosteric binding site adjacent to the Mg-ADP binding pocket which is located on the L5/α2/α3 regions illustrated in (Figure **2-23** A-B).
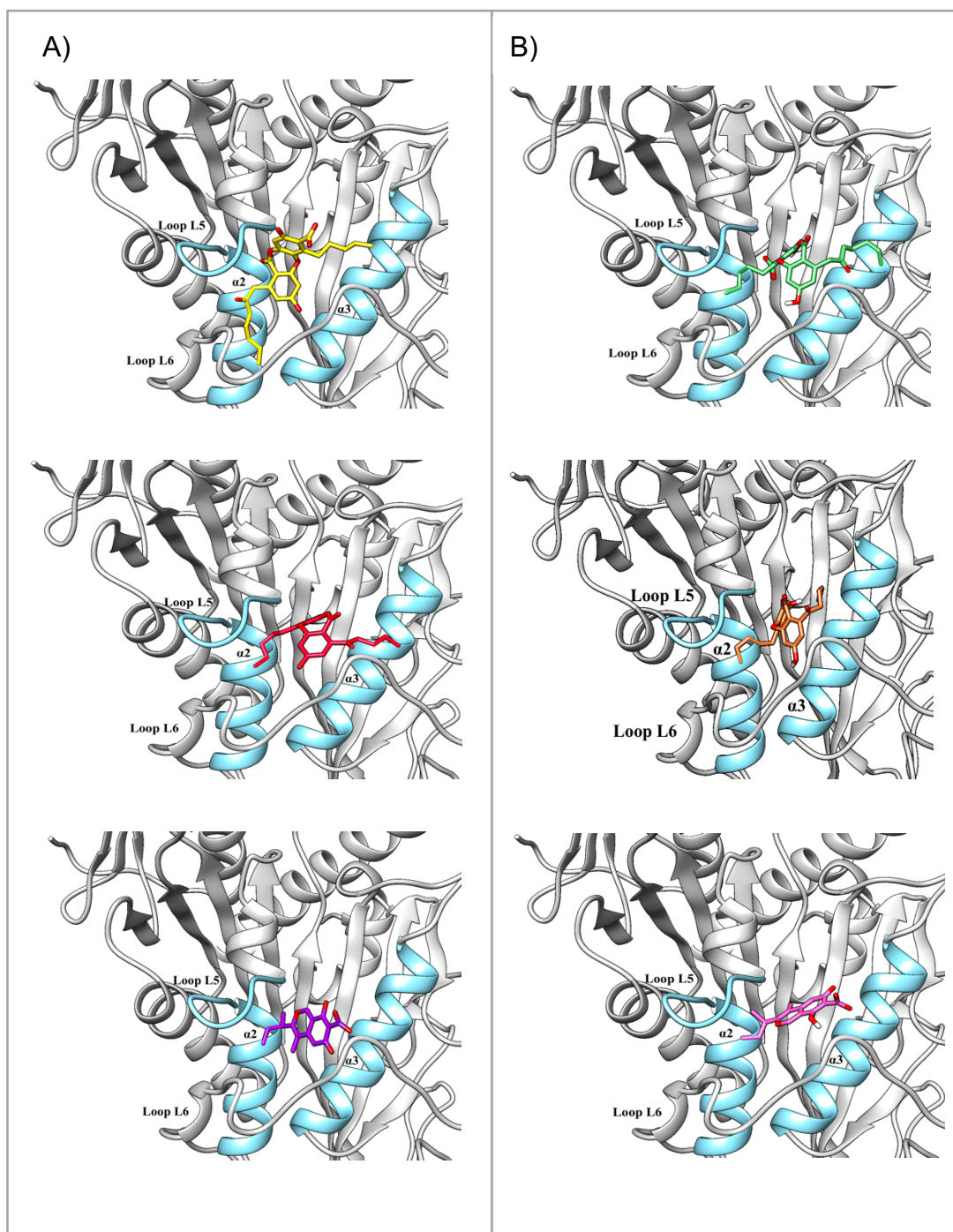
Figure 2-23 A) L5/α2/α3 binding pocket of homology model of MPP1 with physodic acid (yellow), norlobaridone (red) and R-ascochitine ligands (purple) overlaid to illustrate how they occupy the site using LeDock B) L5/α2/α3 binding pocket of homology model of MPP1 with physodic acid (green), norlobaridone (orange) and R-ascochitine ligands (pink) overlaid to illustrate how they occupy the site using AutoDock Vina.
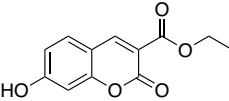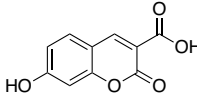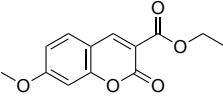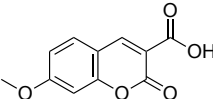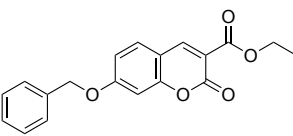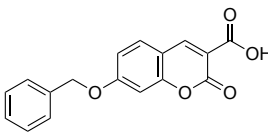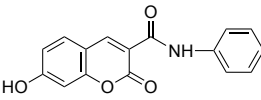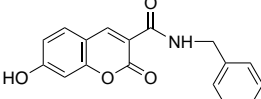
2.3.6.3 Docking of coumarins to MPP1 homology model
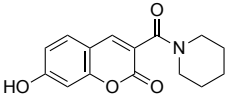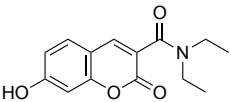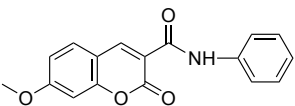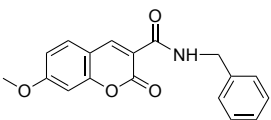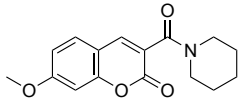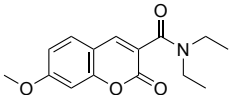
Prior to synthesizing the compounds, they were docked as described previously into the proposed MPP1 binding pocket.

2.3.6.3.1 Docking of coumarins using LeDock

We found that compounds showed a range of predicted binding affinities to the MPP1 homology model, with **51** and **55** (-5.87 kcal/mol and -5.92 kcal/mol) respectively giving the lowest scores (Table **2-8**). The docked conformations of these two compounds are shown in Figure **2-24** and Figure **2-25**.

Table 2-8 Binding affinity and interactions of coumarin derivative compounds with human MPP1 motor domain homology model using LeDock.

| Compound	Structure	H-B	BA (kcal/mol)
41		1	-4.87
44		2	-4.25
46		1	-4.74
47		2	-3.92
48		1	-5.71
49		2	-5.42
50		1	-5.83
51		1	-5.87

Compound	Structure	H-B	BA (kcal/mol)
52		1	-4.77
53		1	-4.69
54		2	-5.79
55		0	-5.92
56		1	-4.86
57		1	-4.79

The hydrogen-bonds and docking scores represent the predicted binding energy of the higher ranked protein ligand complex. The hydrogen bonds count between the ligand and protein was calculated using UCSF Chimera.

The docked conformation for compound **55** with human MPP1 homology model showed the amide nitrogen substituent forming a conventional hydrogen bond interaction with Glu196 illustrated in Figure **2-24**. On the other hand, Figure **2-25**, the docked conformation for compound **50** with human MPP1 homology model showed that the C2 carbonyl substituent formed a hydrogen bond interaction with Lys276 and the amide formed a hydrogen bond interaction with Glu196
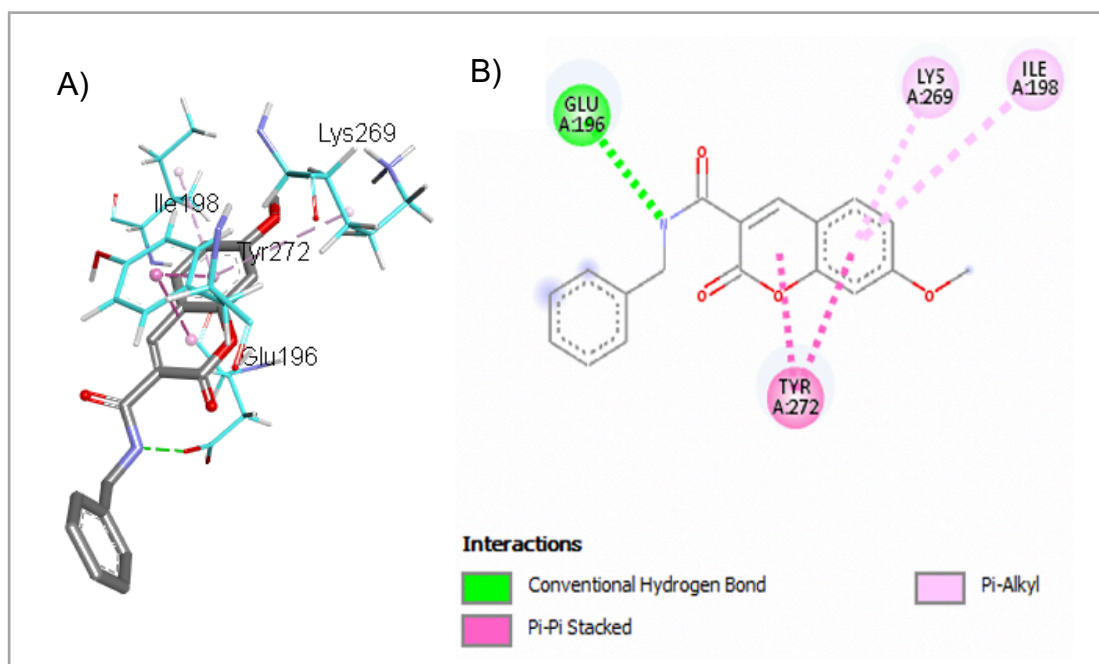
Figure 2-24 The best pose of compound **55** docked into allosteric site of the MPP1 homology model using LeDock: A) 3D protein and B) 2D protein - ligand interaction plots. Amino acids residues are represented as cyan thin sticks, while the ligand is shown as thick sticks with carbon atoms coloured in grey.
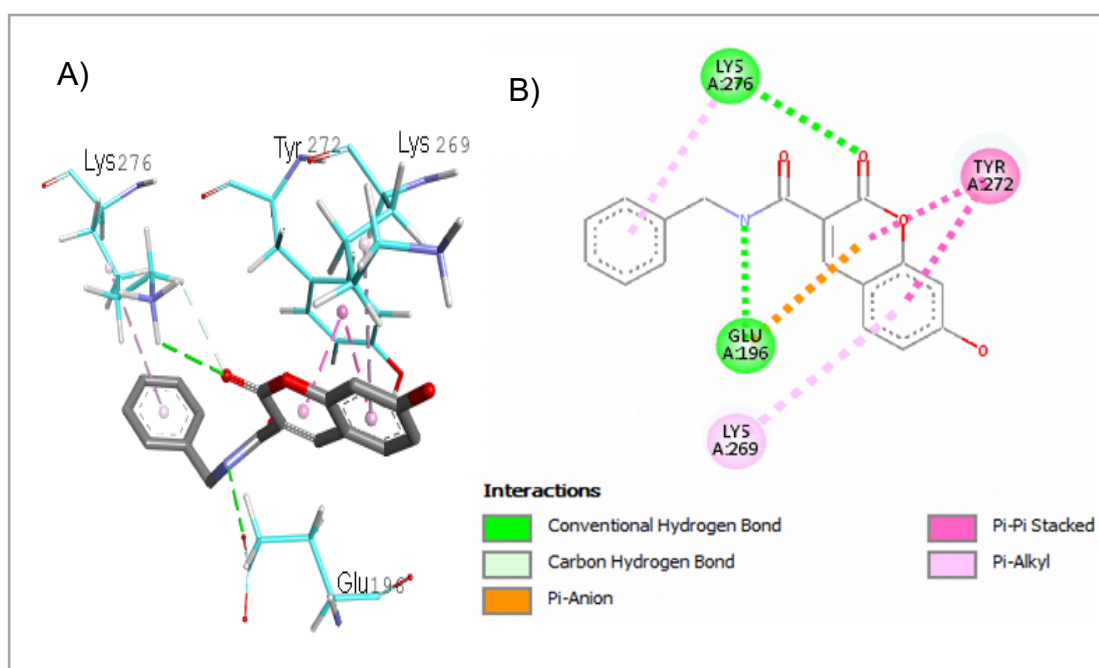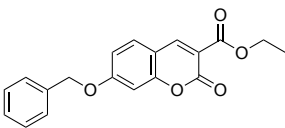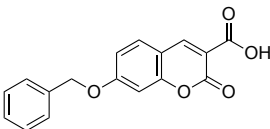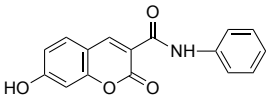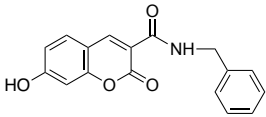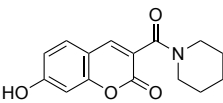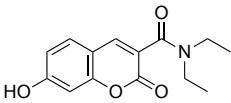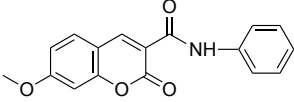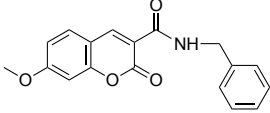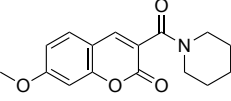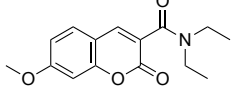
Figure 2-25. The best pose of compound **51** docked into allosteric site of the MPP1 homology model using LeDock: A) 3D protein and B) 2D protein - ligand interaction plots. Amino acids residues are represented as cyan thin sticks, while the ligand is shown as thick sticks with carbon atoms coloured in grey.

2.3.6.3.2 Docking of coumarins using AutoDock Vina

We found that compounds showed a range of predicted binding affinities to the MPP1 homology model, with **49** and **51** (-7.8 kcal/mol and -8.1 kcal/mol) giving the lowest scores (Table **2-9**). The docked conformations of these two compounds and the structure of the docked complexes are shown in Figure **2-26** and Figure **2-27**.

Table 2-9 Binding affinity and interactions of coumarin derivative compounds with human MPP1 motor domain homology model using AutoDock Vina.

Compound	Structure	H-B	BA (kcal/mol)
41		1	-6.3
44		2	-6.4
46		1	-6.3
47		2	-6.5
48		1	-6.9
49		2	-7.8
50		1	-7.4
51		1	-8.1
52		1	-7.5

Compound	Structure	H-B	BA (kcal/mol)
53		1	-6.7
54		2	-7.5
55		0	-7.1
56		1	-7.4
57		1	-6.5

The hydrogen-bonds and docking scores represent the predicted binding energy of the higher ranked protein ligand complex. The hydrogen bonds count between the ligand and protein was calculated using UCSF Chimera.

The docked conformation for compound **51** with human MPP1 homology model showed the C7 hydroxy substituent formed a hydrogen bond interaction with Tyr272 illustrated in Figure **2-26** Additionally, the docked conformation for compound **49** with human MPP1 homology model showed the C3 carboxylic acid substituent formed a conventional hydrogen bond interaction with Ser197 and Tyr272 while it also formed a carbon hydrogen bond interaction with Glu111 illustrated in Figure **2-27**.

Based on the molecular docking using the homology model of MPP1, it was suggested that the coumarin compounds may not be competitive with ATP, by virtue of interacting with a potential allosteric binding site adjacent to the Mg-ADP binding pocket which is located on the L5/α2/α3 regions illustrated in Figure **2-28** A-B. However, these predictions will require experimental verification as part of the future work on this project.
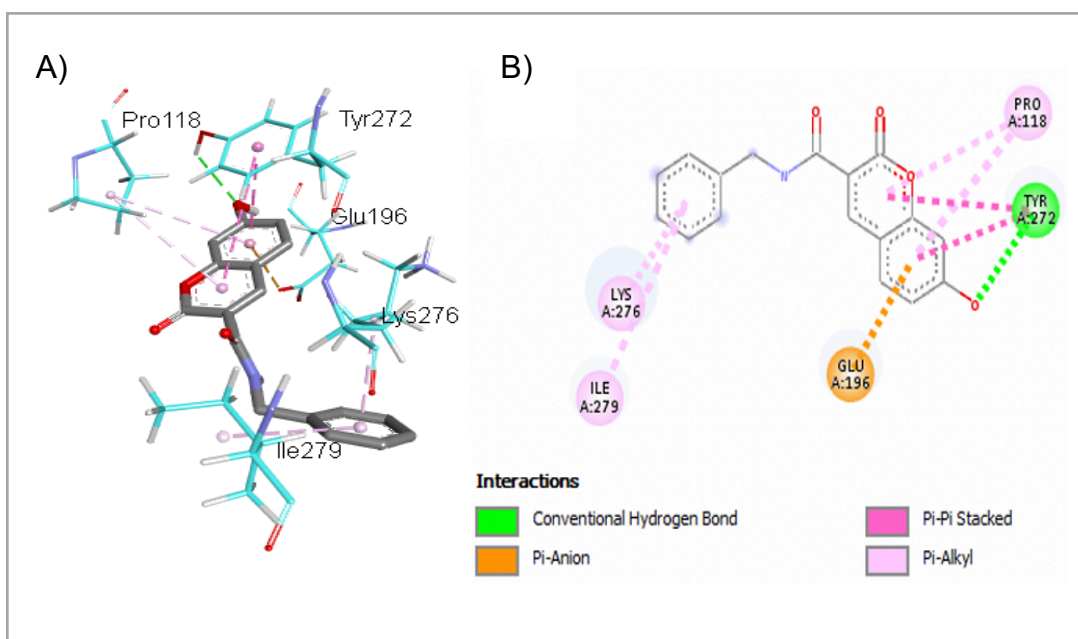
Figure2-26 The best pose of compound **51** docked into allosteric site of the MPP1 homology model using AutoDock Vina: A) 3D protein and B) 2D protein - ligand interaction plots. Amino acids residues are represented as cyan thin sticks, while the ligand is shown as thick sticks with carbon atoms coloured in grey.
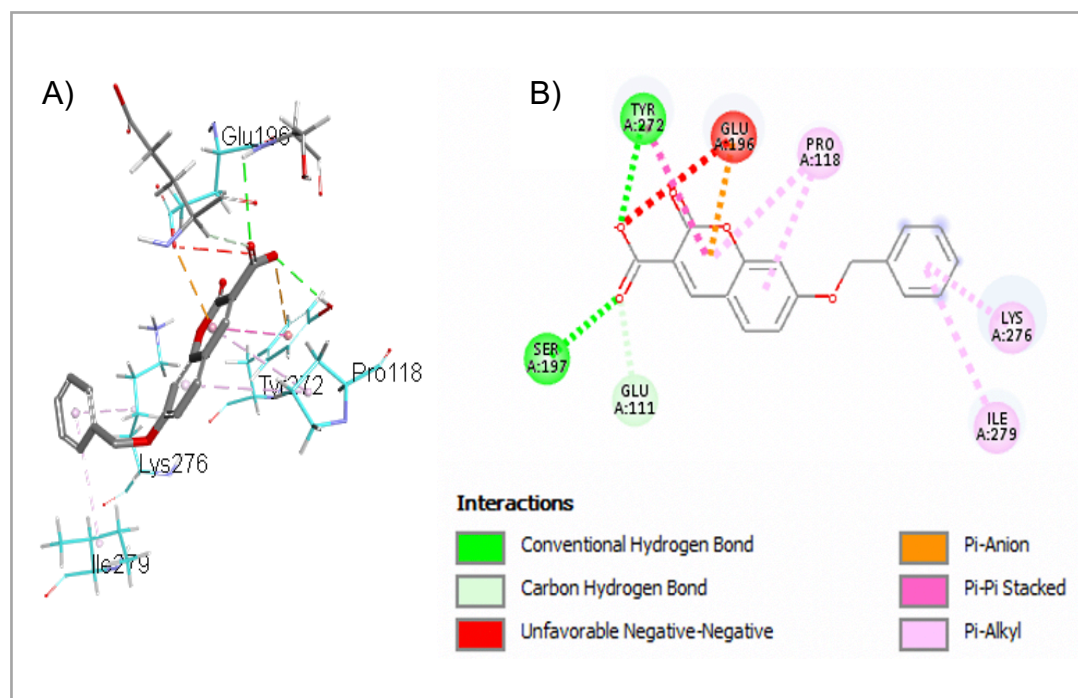

Figure 2-27 A) The best pose of compound **49** docked into allosteric site of the MPP1 homology model using AutoDock Vina: A) 3D protein and B) 2D protein - ligand interaction plots. Amino acids residues are represented as cyan thin sticks, while the ligand is shown as thick sticks with carbon atoms coloured in grey.
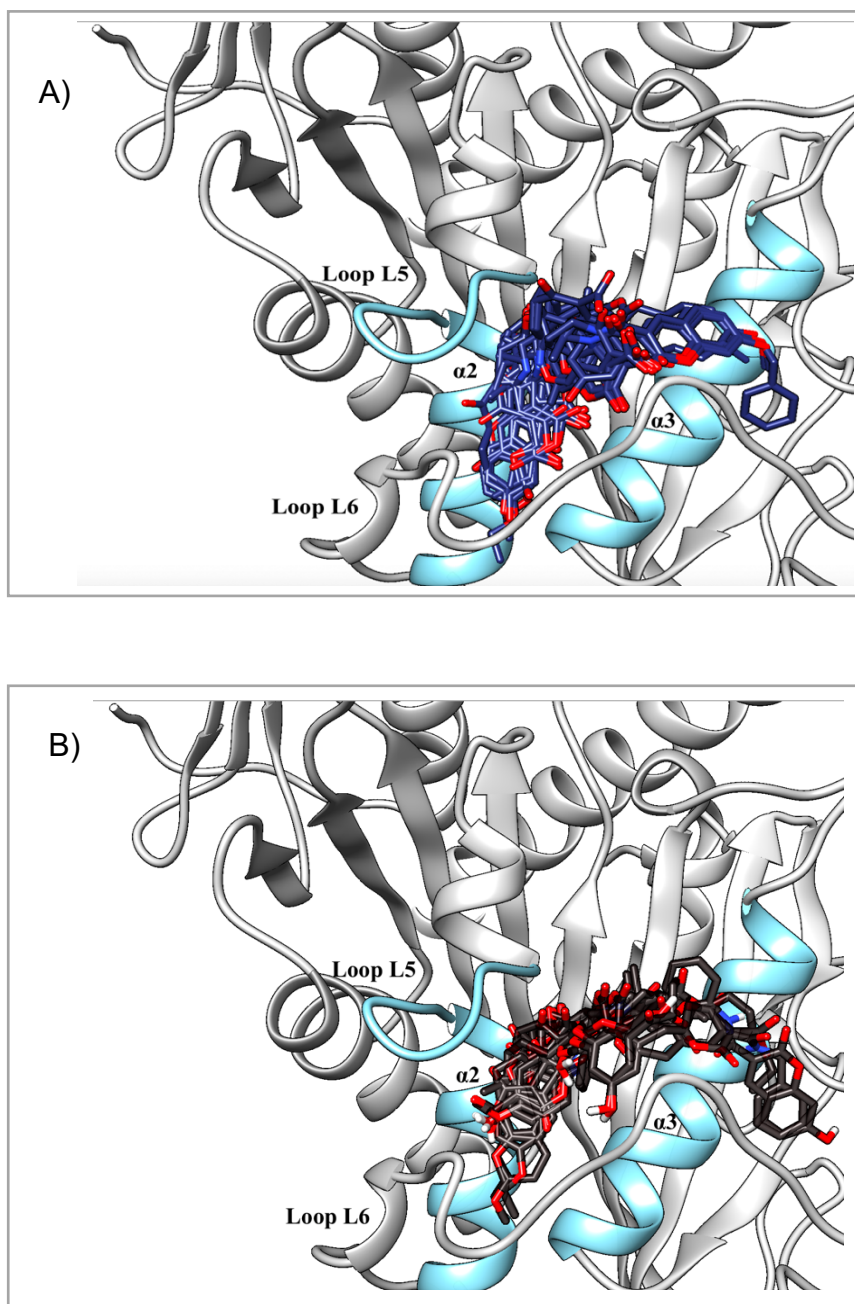
Figure 2-28 A) L5/α2/α3 binding pocket of homology model of MPP1 with coumarin ligands (Navy blue) overlaid to illustrate how they occupy the site using LeDock B) L5/α2/α3 binding pocket of human MPP1 with coumarin compound ligands (black) overlaid to illustrate how they occupy the site using AutoDock Vina.

2.3.6.4 Human MPP1 Alphafold structure

In order to carry out molecular modelling and docking studies we initially built a homology model of the protein based on the structures of human Eg5 and *C. elegans* kinesin-6 (Figure **2-29** A) and later we used the Alphafold [141] structure prediction for human MPP1 (Figure **2-29** B). Alphafold uses artificial intelligence and machine learning approaches to predict protein structures from their sequence. The initial structures built by the algorithm are energy minimised using AMBER and made available online through webservers such as the Uniprot site (www.uniprot.org). In many cases, the predictions can be more accurate than standard homology models [142].

Initially the original homology model and the Alphafold structure were compared. The superimposition of the two structures (Figure **2-29** C) illustrates the high degree of similarity between these two motor domains (RMSD = 1.152 Å).The L6 loop is more structured in the Alphafold model, having a greater alpha-helical composition. The equivalent potential binding pocket in Alphafold model corresponding to allosteric site-I adjacent to the Mg-ADP (L5/α2/α3) was selected for the docking studies to provide a comparison with the previous work.
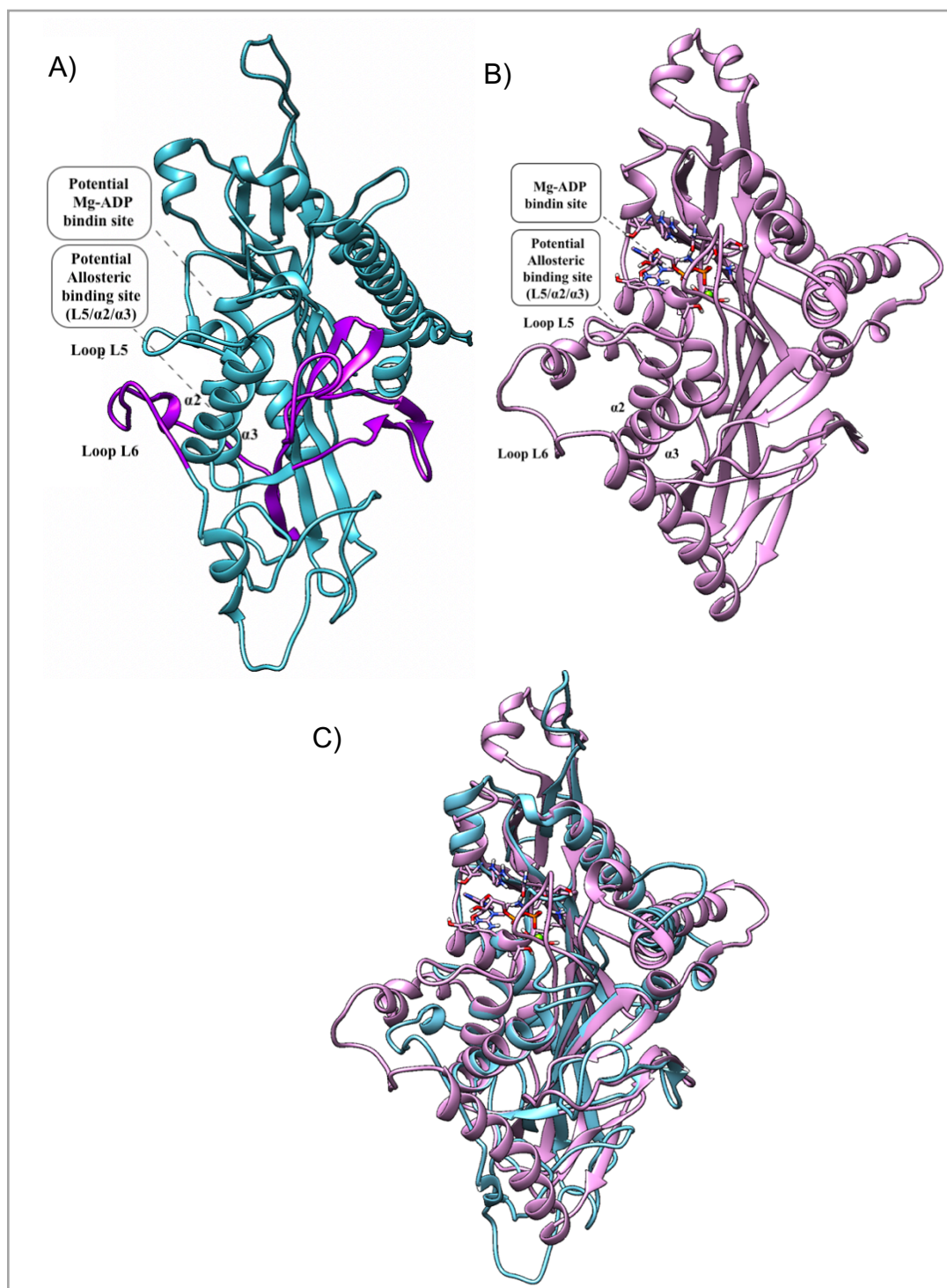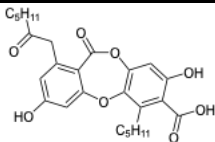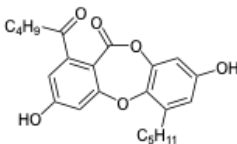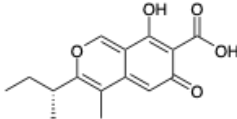
Figure 2-29 Superimposition of the human MPP1 motor domain homology model structure and the human MPP1 Alphafold structure complex with bound Mg-ADP. A) Human MPP1 motor domain homology model structure in ribbons (blue) B) Human MPP1 Alphafold structure in ribbons (pink) C) Superimposition of the human MPP1 motor domain homology model structure in ribbons (blue) and the human MPP1 Alphafold structure complex with bound Mg-ADP in ribbons (pink) (Image prepared using UCSF Chimera).

2.3.6.5 Docking of Depsidones and R-ascochitine to MPP1 Alphafold structure

Using the Alphafold structural prediction for MPP1, the known depsidone inhibitors physodic acid, norlobaridone and R-ascochitine were docked into the allosteric pocket adjacent to the Mg-ADP binding site. AutoDock Vina was used to dock the ligands. The results are shown in (Table **2-10** and Figure **2-30** to Figure **2-32**).

Table 2-10 Binding affinity and interactions of depsidones and R-ascochitine with the human MPP1 Alphafold structure using AutoDock Vina.

Compound	Structure	H-B	Hydrophobic contacts	BA (kcal /mol)
Physodic acid **11**		2	16	-7.24
Norlobaridone **12**		3	11	-6.52
R-ascochitine **14**		2	5	-6.18

The docking scores represent the predicted binding energy of the higher ranked protein ligand complex. The hydrophobic contacts were calculated using Open Drug Discovery Toolkit and hydrogen bonds count between the ligand and protein were calculated using UCSF Chimera.

Using AutoDock Vina, the docked conformation of physodic acid forms hydrogen bond interactions Gln282 and Gly109 and Ser294 of the MPP1 Alphafold structure illustrated in Figure **2-30**. Similarly, in the case of norlobaridone, hydrogen bond interactions are observed in the AutoDock Vina, complex via MPP1 residue Asn290 and the bound ADP (Figure **2-31**). Furthermore, for R-ascochitine, AutoDock Vina result displayed hydrogen bond interactions in the complex via MPP1 residues Gln282 and Thr104 illustrated in Figure **2-32**.
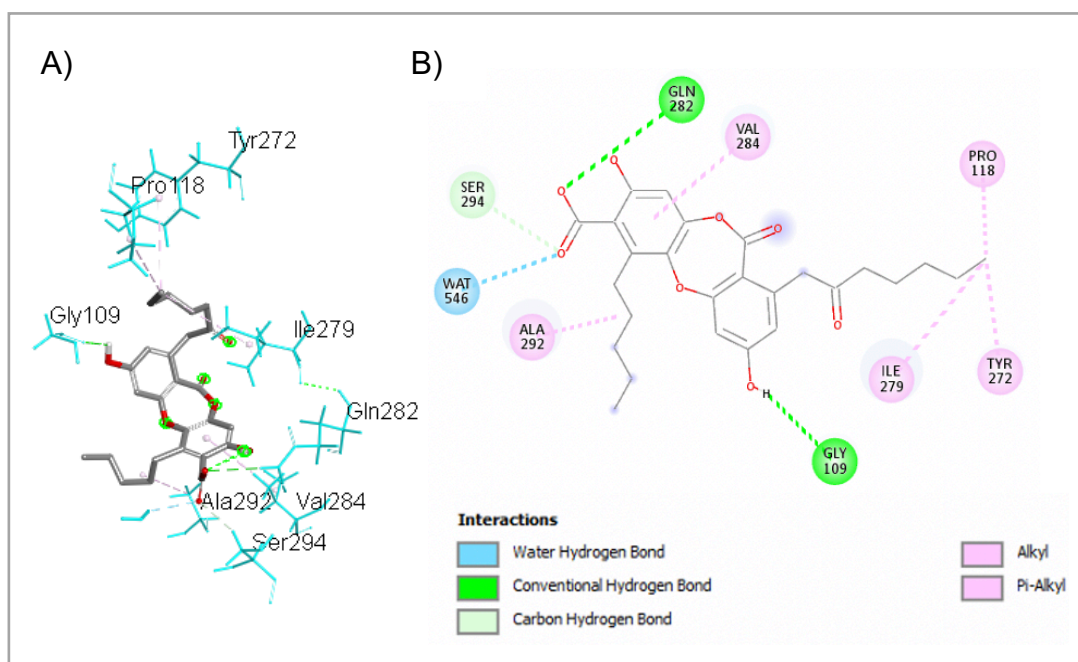
Figure 2-30 The best pose of physodic acid docked into allosteric site of the MPP1 Alphafold structure using AutoDock Vina: A) 3D protein and B) 2D protein - ligand interaction plots. Amino acids residues are represented as cyan thin sticks, while the ligand is shown as thick sticks with carbon atoms coloured in grey.
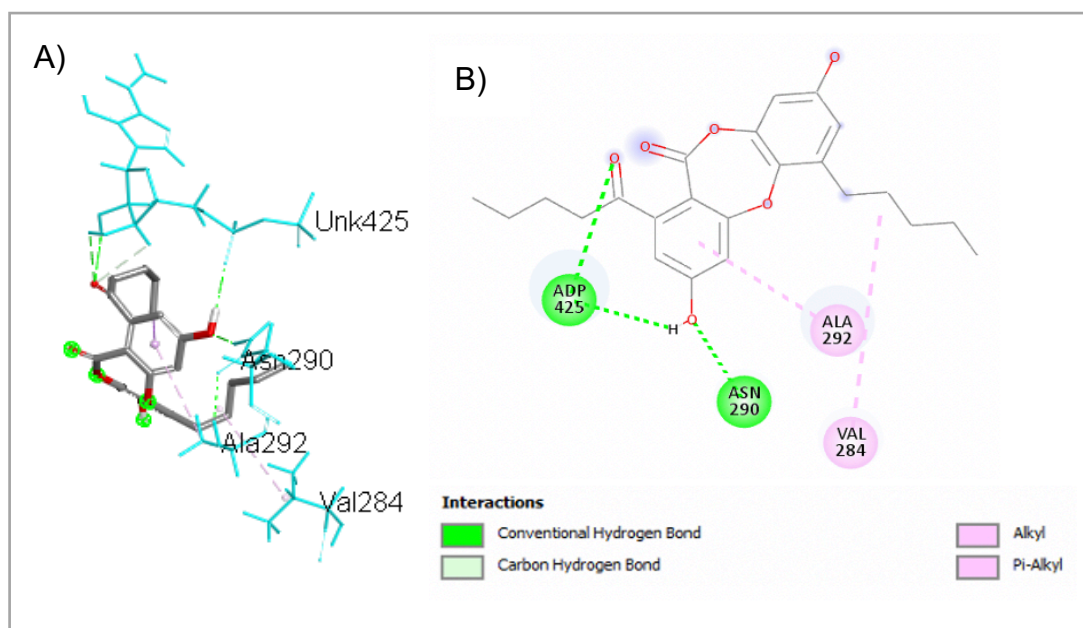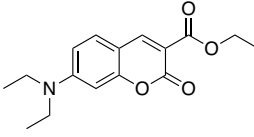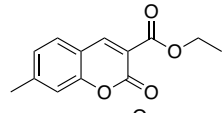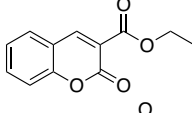

Figure 2-31 The best pose of norlobaridone docked into allosteric site of the MPP1 Alphafold structure using AutoDock Vina: A) 3D protein and B) 2D protein - ligand interaction plots. Amino acids residues are represented as cyan thin sticks, while the ligand is shown as thick sticks with carbon atoms coloured in grey.
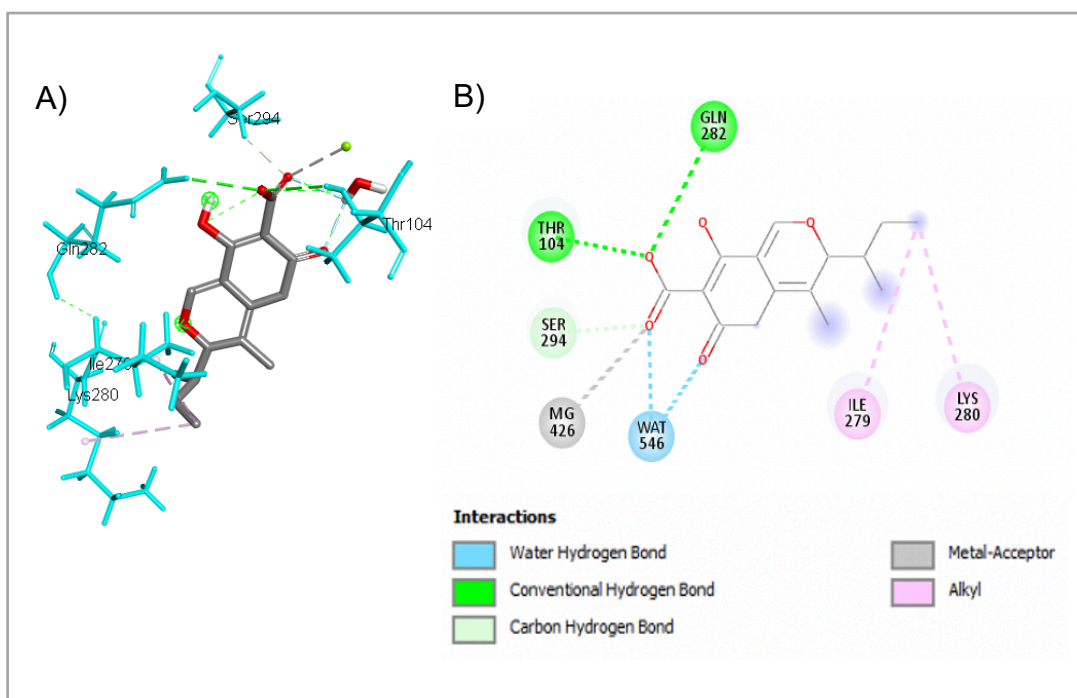
Figure 2-32 The best pose of R-ascochitine docked into allosteric site of the MPP1 Alphafold structure using AutoDock Vina: A) 3D protein and B) 2D protein - ligand interaction plots. Amino acids residues are represented as cyan thin sticks, while the ligand is shown as thick sticks with carbon atoms coloured in grey.
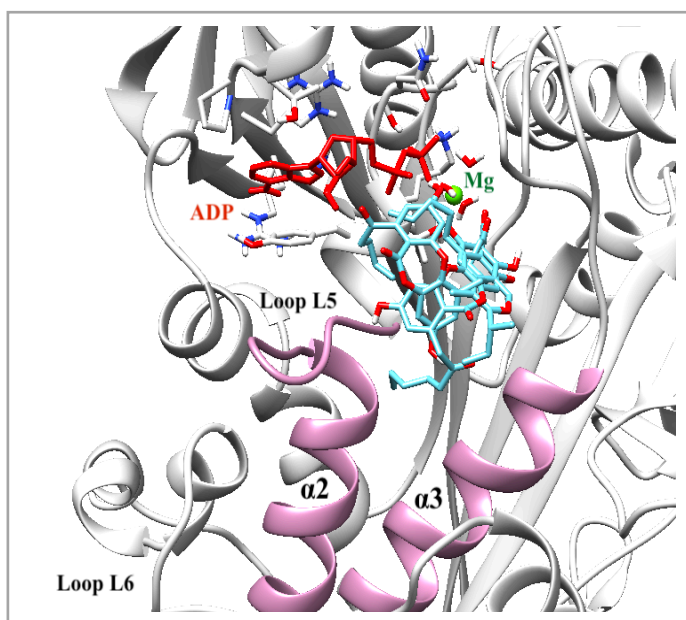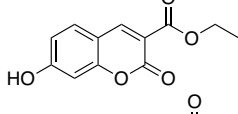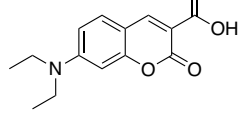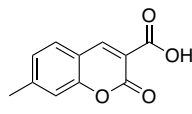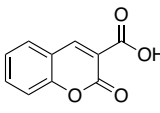

Figure 2-33 L5/α2/α3 binding pocket of human MPP1 Alphafold structure with ADP-Mg (red) and physodic acid, norlobaridone and R-ascochitine ligands (light blue) overlaid to illustrate how they occupy the site when docked using AutoDock Vina.
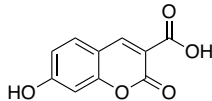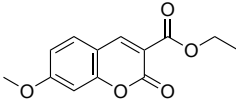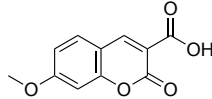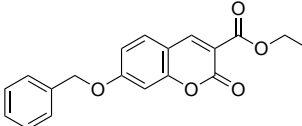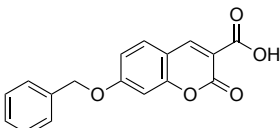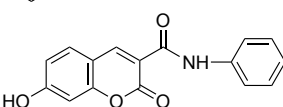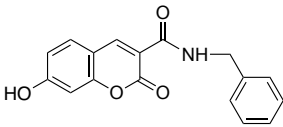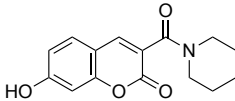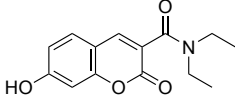
Molecular docking with the Alphafold structure of MPP1 studies suggested that physodic acid, norlobaridone and R-ascochitine may interact with a potential allosteric binding site adjacent to the Mg-ADP binding pocket which is located on the L5/α2/α3 regions illustrated in (Figure **2-33**). However, this prediction requires experimental validation as part of the future work on the project.

2.3.6.6 Docking of coumarins to the MPP1 Alphafold structure

We found that the coumarin compounds showed a range of predicted binding affinities to the Alphafold MPP1 model, with **52** and **49** (-7.27 kcal/mol and -7.41 kcal/mol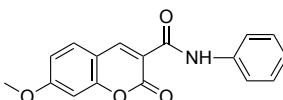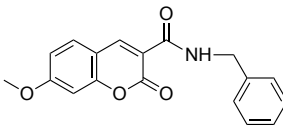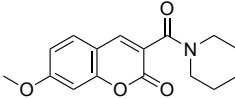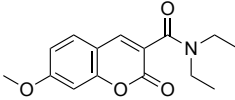) giving the lowest scores (Table **2-11**). The docked conformations of these two compounds and the 3D structure of the docked complexes are shown in Figure **2-34** and Figure **2-35**.

Table 2-11 Binding affinity and interactions of coumarin derivative compounds with MPP1 Alphafold structure using AutoDock Vina.

Compound	Structure	H-B	Hydrophobic contacts	BA (kcal /mol)
38		1	4	-5.53
39		3	8	-6.12
40		1	8	-5.60
41		1	5	-5.48
25		2	9	-6.27
42		3	10	-6.71
43		3	9	-6.47

Compound	Structure	H-B	Hydrophobic contacts	BA (kcal /mol)
44		2	8	-6.38
46		3	5	-5.49
47		1	8	-6.37
48		2	15	-6.68
49		3	16	-7.41
50		4	6	-7.10
51		1	10	-7.23
52		11	11	-7.27
53		1	2	-5.78
54		1	9	-6.84
55		1	13	-7.14
56		0	11	-6.82
57		3	4	-5.46

The hydrogen bonds, hydrophobic contacts and docking scores represent the predicted binding energy of the higher ranked protein ligand complex. The hydrogen bonds count between the ligand and protein was calculated using UCSF Chimera.

The docked conformation for compound **52** with the human MPP1 Alphafold structural showed that the C3 amide carbonyl substituent formed a hydrogen bond interaction with a water residue coordinated to the ADP-Mg, while the C7 hydroxyl substituent formed a hydrogen bond interaction with Gln282 and Ile279 in (Figure **2-34**). Whereas the docked conformation for compound **49** with the MPP1 Alphafold structure showed that the C3 carboxylic acid substituent formed a hydrogen bond interactions with Ala292 and Ser294 and formed a hydrogen bond interaction with a water residue coordinated to the ADP-Mg. Additionally, the C2 carbonyl substituent formed a hydrogen bond interaction with the same water residue and the O1 coumarin oxygen formed a hydrogen bond interaction with Gln108 (Figure **2-35**).Furthermore, molecular docking with the Alphafold structure of MPP1 studies suggested that the coumarin compounds may not be competitive with ATP and may interact with a potential allosteric binding site adjacent to the Mg-ADP binding pocket which is located on the L5/α2/α3 regions illustrated in (Figure **2-36**). These predictions will require experimental validation.
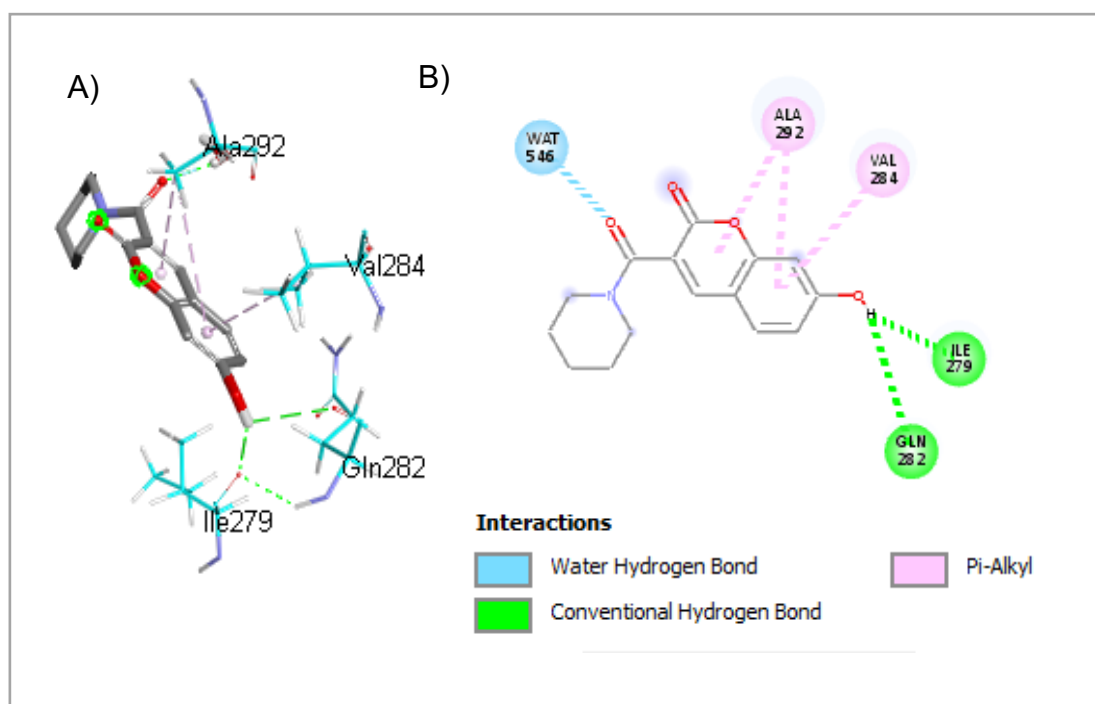
Figure 2-34 The best pose of compound **52** docked into allosteric site of the MPP1 Alphafold structure using AutoDock Vina: A) 3D protein and B) 2D protein - ligand interaction plots. Amino acids residues are represented as cyan thin sticks, while the ligand is shown as thick sticks with carbon atoms coloured in grey.
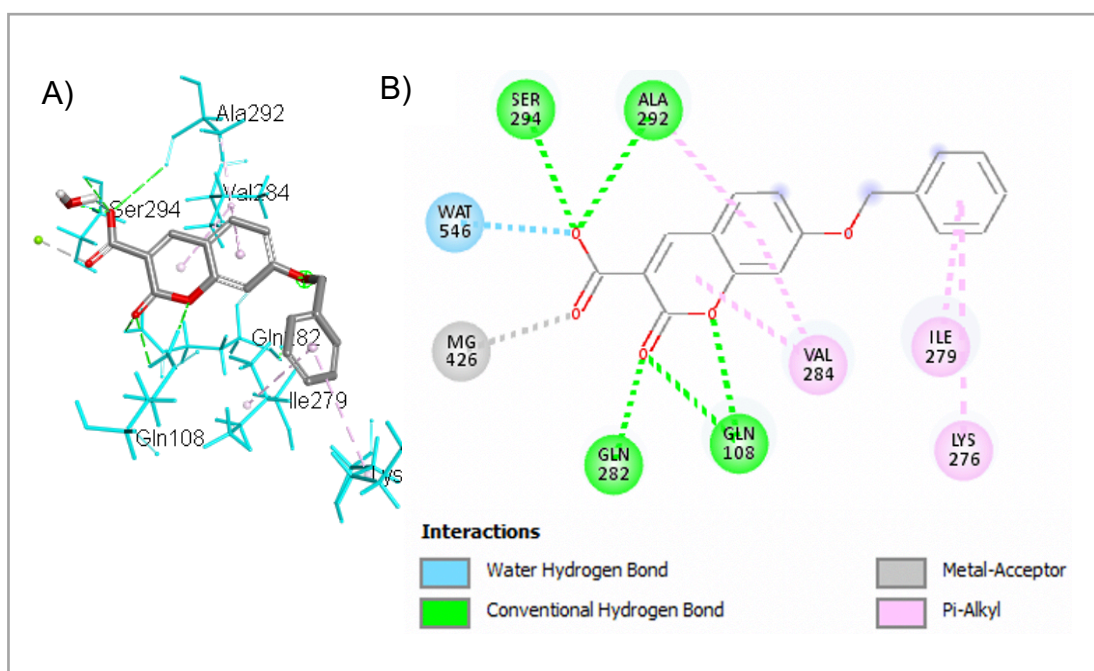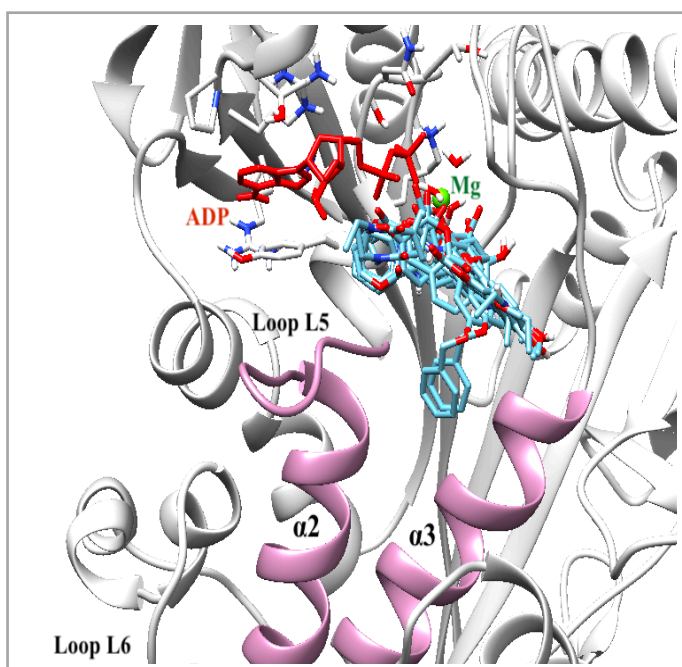
Figure 2-35 The best pose of compound **49** docked into allosteric site of the MPP1 Alphafold structure using AutoDock Vina: A) 3D protein and B) 2D protein - ligand interaction plots. Amino acids residues are represented as cyan thin sticks, while the ligand is shown as thick sticks with carbon atoms coloured in grey.


Figure 2-36 L5/α2/α3 binding pocket of human MPP1 Alphafold structure with ADP-Mg (red) and coumarin ligands (light blue) overlaid to illustrate how they occupy the site using AutoDock Vina.

90

2.3.7 Biological evolution of a new series of coumarins

2.3.7.1 Basal ATPase measurements of a new series coumarins

Dr Jiazhi Tang at UCL School of Pharmacy conducted tests on coumarin derivatives to determine their ability to inhibit MPP1 enzymatic activity. The inhibition of basal ATPase activity was measured in the absence of salt, using different concentrations of inhibitors to determine the IC_{50} for the inhibition of basal MPP1 ATPase activity.
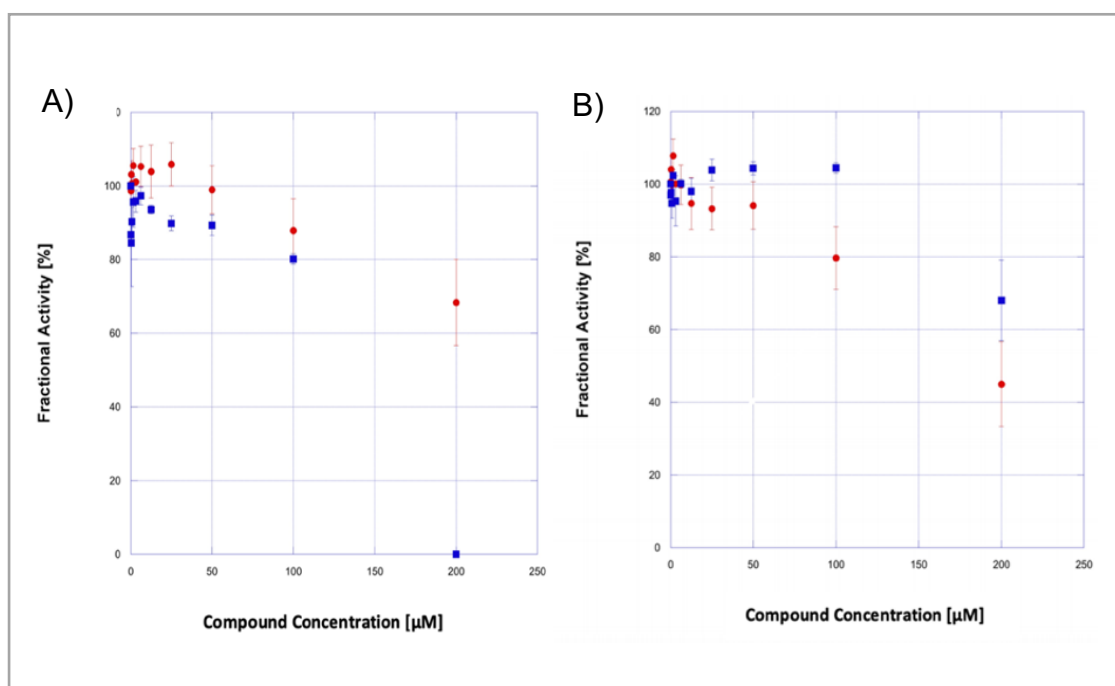
Figure 2-37 Inhibition of the basal MPP1 ATPase activity by chromene-3-carboxylic acids. A) Compound **41** (red), compound **46** (blue). Partial inhibition was observed for both compounds. B) Compound **44** (red), compound **47** (blue). Partial inhibition was observed for both compounds. Data obtained by Dr. Jiazhi Tang.
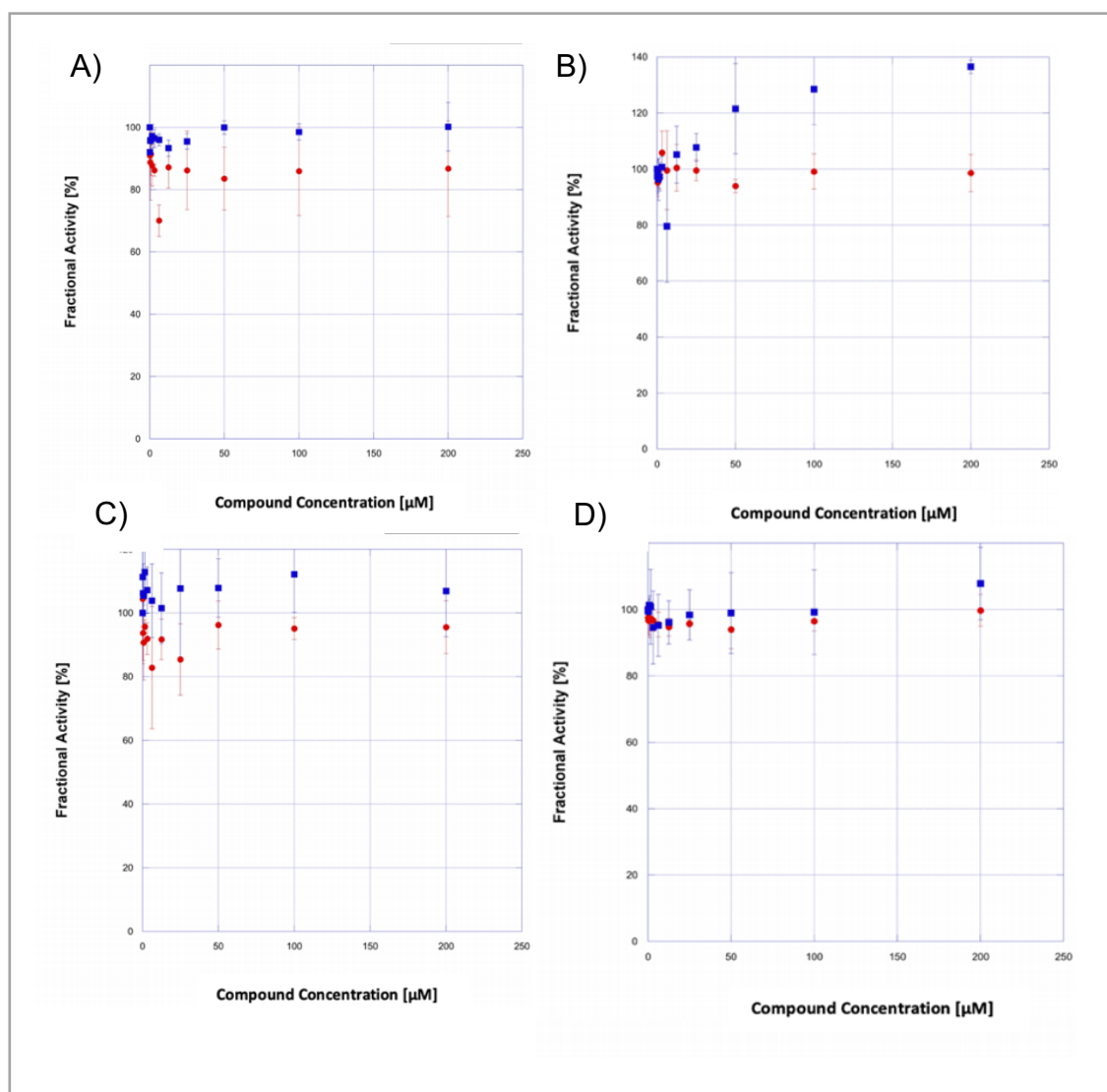
Figure 2-38 Inhibition of the basal MPP1 ATPase activity by 7-alkoxy-chromene-3-carboxamides. A) Compound **50** (red), compound **54** (blue). No inhibition was observed for both compounds. B) Compound **51** (red), compound **55** (blue), No inhibition was observed for compound **51** and weak activation was observed for compound. C) Compound **52** (red), compound **56** (blue). No inhibition was observed. D) Compound **53** (red), compound **57** (blue). No inhibition was observed. Data obtained by Dr. Jiazhi Tang.
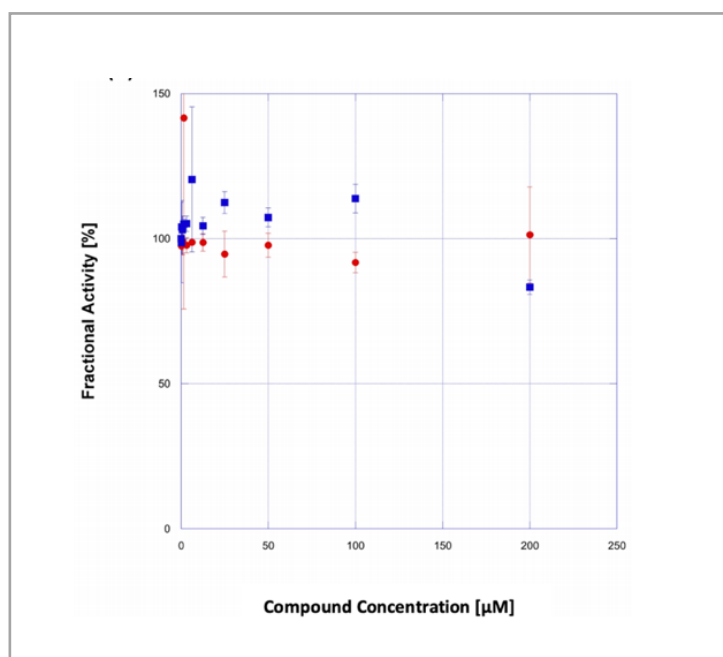
Figure 2-39 Inhibition of the basal MPP1 ATPase activity by 7-alkoxy-chromene-3-carboxylic acids alignment of compound **48** (red), compound **49** (blue). No inhibition was observed for both compounds. Data obtained by Dr. Jiazhi Tang.

In the experiment, compounds **41**, **44**, **46**, and **47** showed partial inhibitory activity against MPP1 (Figure **2-37**), while weak or no inhibition was observed for other derivatives, including compounds **49**, **51**, and **55**, which had the best docking scores in the LeDock and AutoDock Vina experiments (Figure **2-38** and Figure **2-39**). These results suggest that the affinity of the compounds from the docking experiments was not supported by the experimental data on the inhibition of basal ATPase activity. Therefore, the docking studies using both the available homology model and Alphafold structure of MPP1with do not necessarily predict MPP1 binding activity in a consistent manner.

Based on the information provided, compound **44** that has a chromenone-3-carboxylic acid core scaffold with a 7-hydroxy substituent had the best activity of the series, with an IC_{50} of approximately 200 μM.

The comparison with other derivatives suggests that the presence of a 7-alkoxy substituent, such as methoxy or benzyloxy, does not provide as strong inhibitory

activity as the 7-hydroxy substituent present in compound **44**. Similarly, the presence of a 3-carboxamide substituent in other derivatives also does not provide as strong inhibitory activity as the 7-hydroxy substituent in compound **44**.

Despite having only partial to weak inhibitory activity compared to ascochitine, coumarin derivatives are still valuable analogues that can be optimized to enhance their biological activity and investigate structure-activity relationships (SAR) with respect to MPP1. Following on from this study, molecular modelling and pharmacophore-based searches were conducted to identify alternative heterocycles and scaffolds for further exploration.

2.3.8 Design, synthesis of 4-hydroxychromen-2-one-3-carboxylic acids

We explored alternative heterocycles and scaffolds identified through our molecular modelling and pharmacophore-based searches such as 4-hydroxychromen-2-one-3-carboxylic acids, these compounds are closer analogues of the ascochitine core structure and incorporate an equivalent of the ascochitine hydroxyl group (Figure **2-40** A). In total, eight analogue compounds were designed and synthesised to evaluate their potential activity as MPP1 inhibitors (Figure **2-40** B).
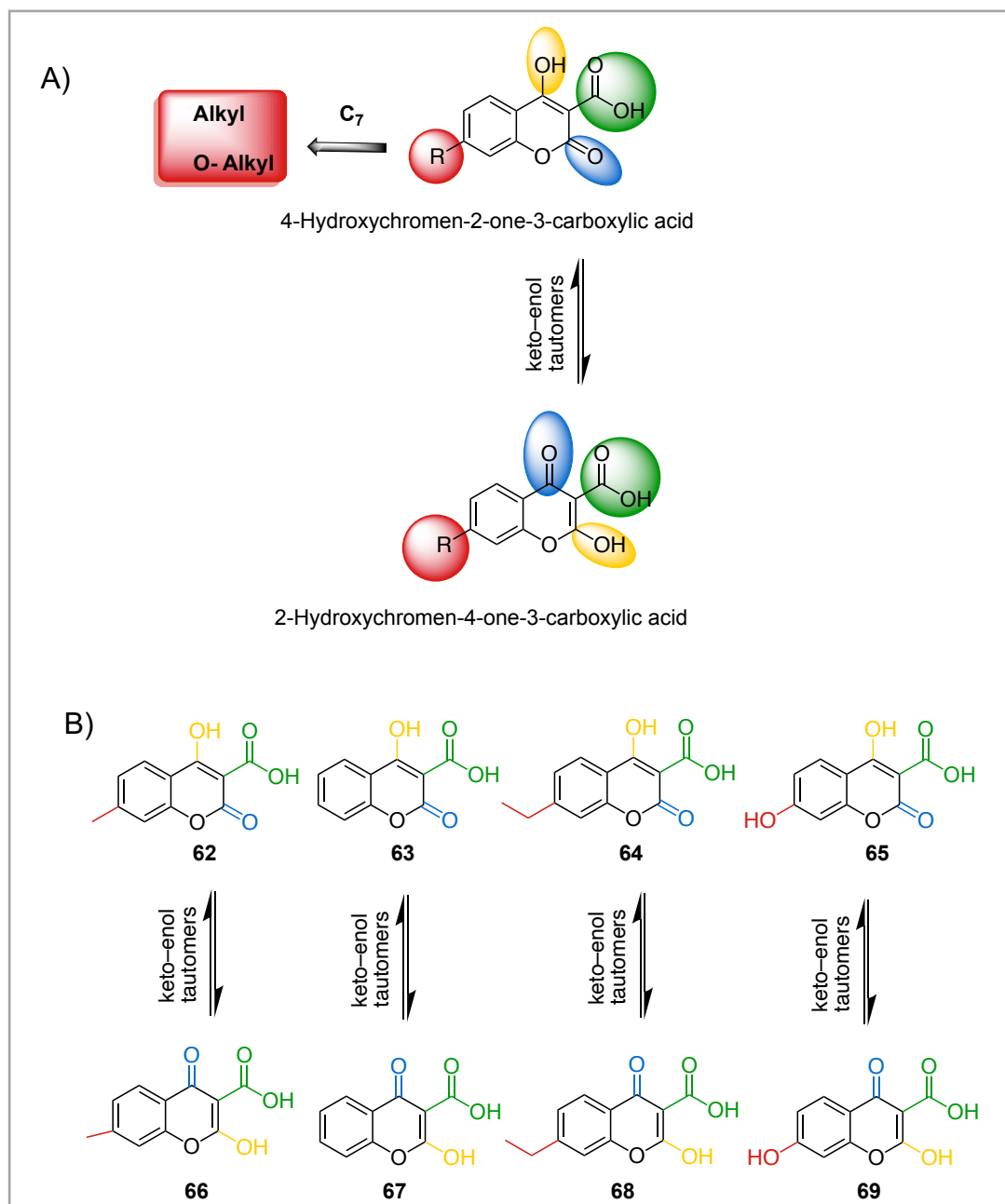
**Figure 2-40** Keto-enol tautomers of 4-hydroxychromen-2-one-3-carboxylic acid analogues for synthesis.

In order to synthesise a small series of 4-hydroxychromen-2-one-3-carboxylic acid we chose a short synthetic route that allowed us to use commercially available salicylic acid as starting material. According to the literature procedure [143, 144], the condensation of the substituted salicylic acids with malonic acid

in the presence of trifluoroacetic acid as a solvent and the cyclisation process to form the desired compounds. However, in each reaction (Table **2-12**), no conversion of the starting material to the product could be detected by TLC or LCMS and the ^{1}H NMR spectra of the crude products after work up confirmed the presence of the starting materials.

Table 2-12 General scheme for synthesis of 2-hydroxychromen-2-one-3-carboxylic acids and percentage yield products.
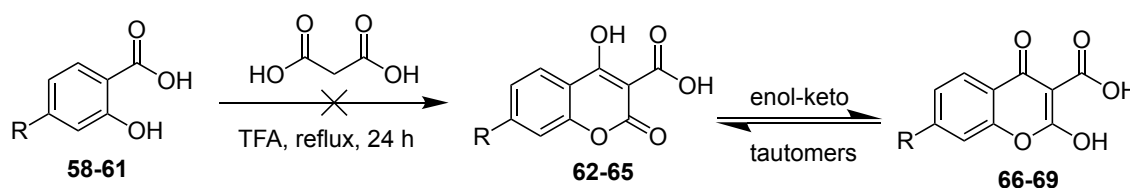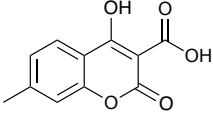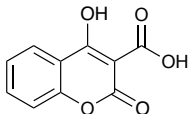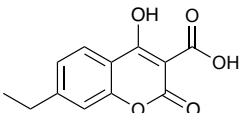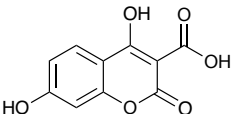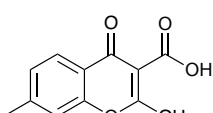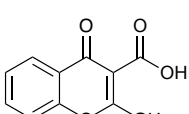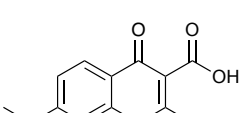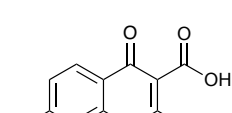

R	4-hydroxychromen-2-one-3-carboxylic acids	Yield %
—CH₃	**62/66**	Not detected
H	**63/67**	Not detected
—CH₂CH₃	**64/68**	Not detected
—OH	**65/69**	Not detected

2.3.9 Docking of 4-hydroxychromen-2-one-3-carboxylic acids

Prior to synthesizing the compounds, they were docked as described previously into the proposed MPP1 binding pocket. We found that the compounds showed a range of predicted binding affinities to the Alphafold model of MPP1, with **66** and **62** (-6.50 kcal/mol and -6.52 kcal/mol) giving the lowest scores (Table **2-13**). The docked conformations of these two compounds are shown in Figure **2-41** and Figure **2-42**.

Table 2-13 Binding affinity and interactions of 4-hydroxychromen-2-one-3-carboxylic acid analogues with human MPP1 motor domain Alphafold using AutoDock Vina.

Compound	Structure	H-B	Hydrophobic contacts	BA (kcal/mol)
62		3	4	-6.52
63		3	4	-6.23
64		4	2	-5.99
65		2	4	-6.19
66		3	4	-6.50
67		3	4	-6.38
68		1	13	-6.19
69		1	1	-5.78

The hydrogen bond, hydrophobic contacts and docking scores represent the predicted binding energy of the higher ranked protein ligand complex. The hydrogen bonds count between the ligand and protein was calculated using UCSF Chimera.

The docked conformation for compound **62** with the Alphafold MPP1 structure showed that the C3 carboxylic acid substituent formed an ionic interaction with the magnesium ion from the ADP-Mg and a hydrogen bond interaction with Gln282, Gln108 while the C2 carbonyl substituent formed a hydrogen bond interaction with water (Figure **2-41**). Whereas the docked conformation for

compound **66** showed that the C3 carboxylic acid substituent formed interactions with the magnesium ion from the ADP-Mg and formed hydrogen bond interactions with Gln282 and Gln108 while the C2 hydroxyl substituent formed a hydrogen bond with a bound water residue (Figure **2-42**). Furthermore, molecular docking with the Alphafold structure of MPP1 studies suggested that the 4-hydroxychromen-2-one-3-carboxylic acids may not be competitive with ATP, may interact with a potential allosteric binding site adjacent to the Mg-ADP binding pocket which is located on the L5/α2/α3 regions illustrated in (Figure **2-43**).
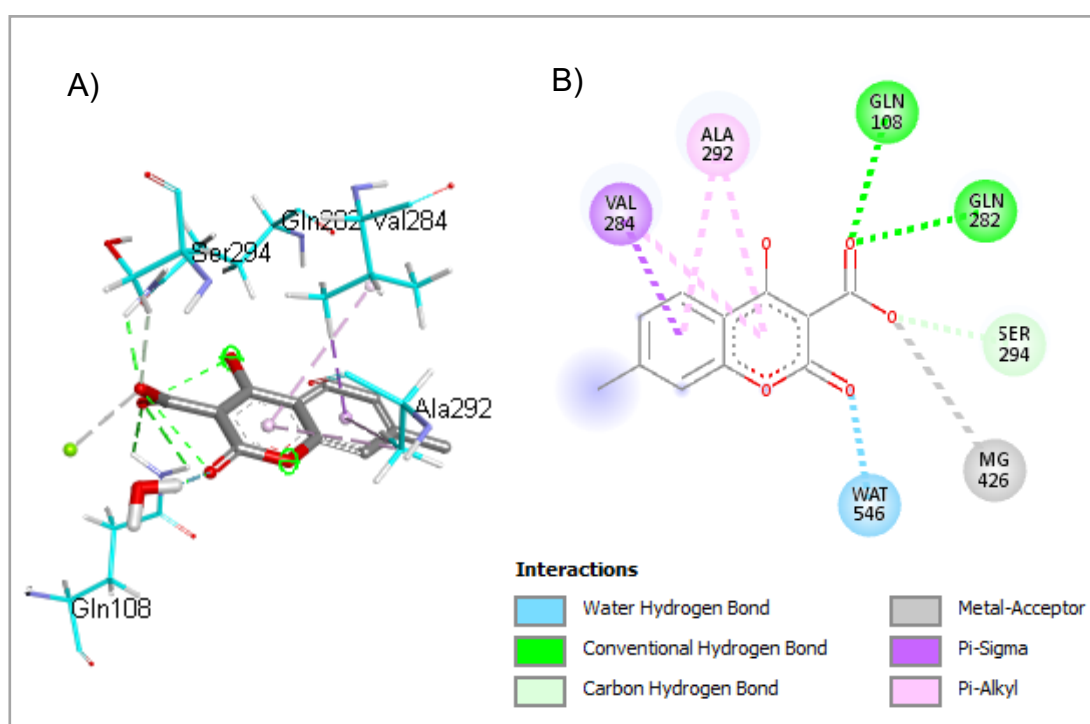
Figure 2-41 The best pose of compound **62** docked into allosteric site of the MPP1 Alphafold structure using AutoDock Vina: A) 3D protein and B) 2D protein - ligand interaction plots. Amino acids residues are represented as cyan thin sticks, while the ligand is shown as thick sticks with carbon atoms coloured in grey.
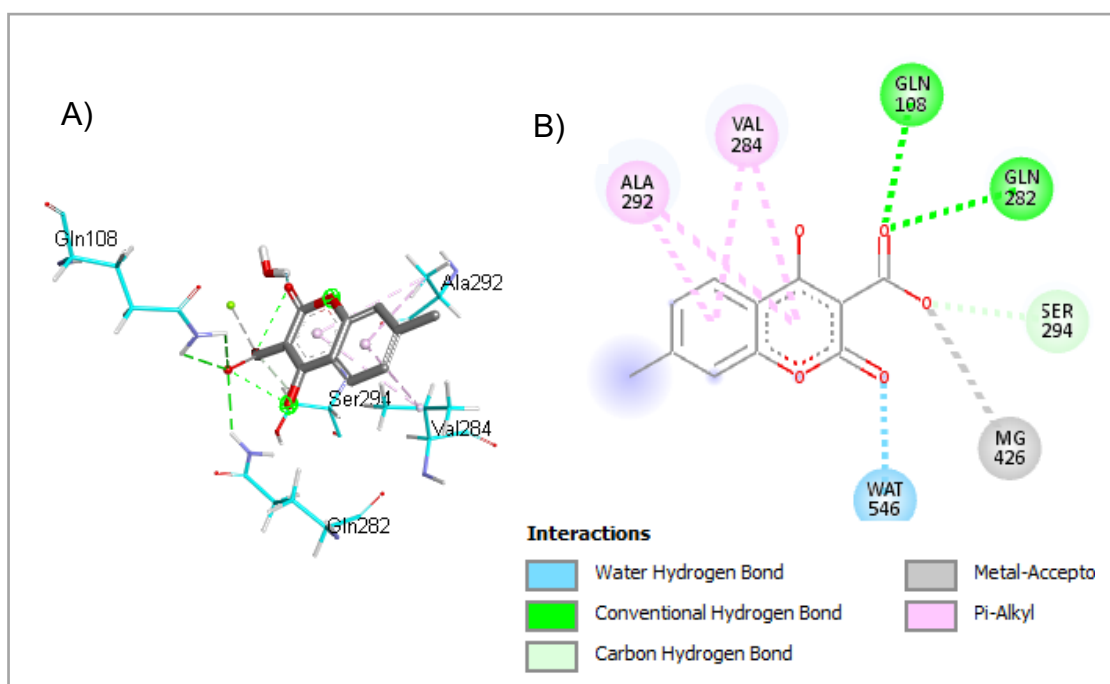
Figure 2-42 The best pose of compound **66** docked into allosteric site of the MPP1 Alphafold structure using AutoDock Vina: A) 3D protein and B) 2D protein - ligand interaction plots. Amino acids residues are represented as cyan thin sticks, while the ligand is shown as thick sticks with carbon atoms coloured in grey.
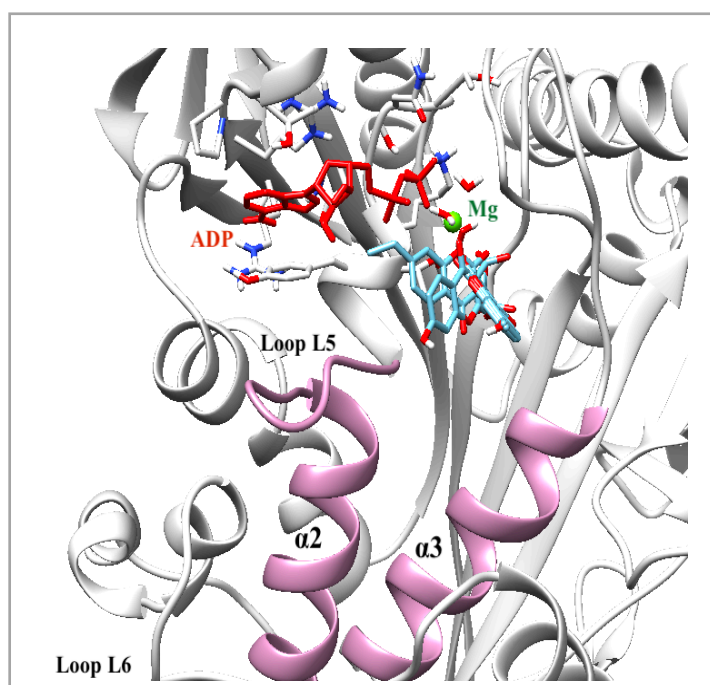
Figure 2-43 L5/α2/α3 binding pocket of human MPP1 Alphafold structure with ADP-Mg (red) and 4-hydroxychromen-2-one-3-carboxylic acid (light blue) ligands overlaid to illustrate how they occupy the site using AutoDock Vina.

2.3.10 Design, synthesis of quinolone-3-carboxylic acids

A series of 2-quinolone-3-carboxylic acids with alkyl or alkoxy groups at the C-7 position were designed as our third synthetic target compounds (this scaffold was also identified in our initial pharmacophore searches). As our aim is to synthesise small compound libraries to rapidly evaluate potential inhibitor scaffolds, the alternative 4-quinolone-3-carboxylic acids were also evaluated (Figure **2-44** A). In total nine compounds were synthesised (Figure **2-44** B) with different substituents at the C-7 positions of the quinolone scaffolds to evaluate their activity as MPP1 inhibitors.
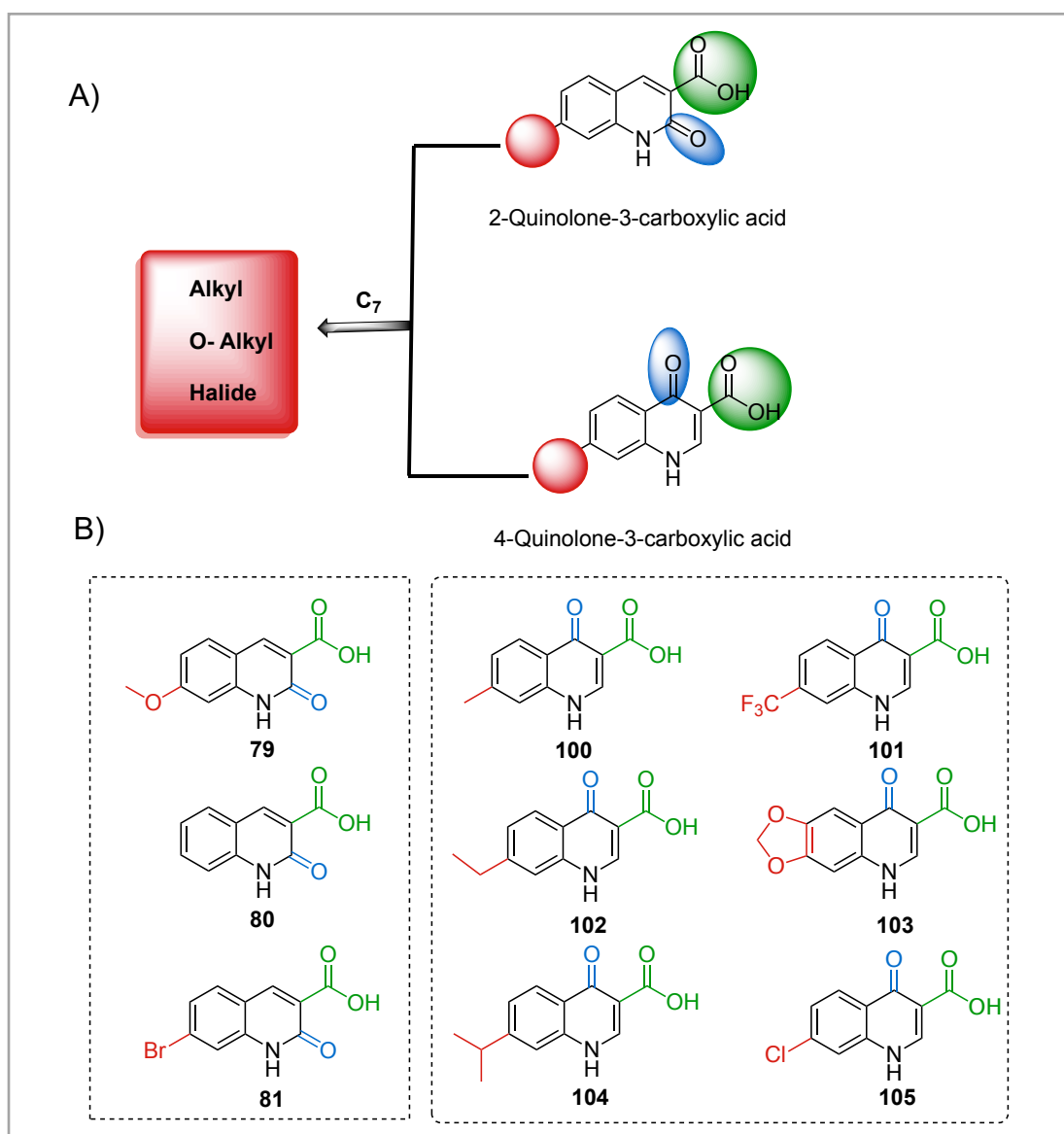
Figure 2-44 Design of 2-quinolone-3-carboxylic acid and 4-quinolone-3-carboxylic acid to identify new analogues.

2.3.10.1 Synthesis of 2-quinolone-3-carboxylic acids

The synthesis of the 2-quinolone-3-carboxylic acids could be achieved by a three-step procedure. In the first step a Knoevenagel condensation of 2-nitrobenzaldehydes with diethyl malonate in the presence of a catalyst such as piperidine was performed. The reaction is typically carried out in an aqueous or polar solvent such as ethanol or methanol. The resulting diethyl 2-(2-nitrobenzylidene) malonates were isolated in 17-50% yields (Table **2-14**). The structures of the compounds were confirmed by their ^{1}H NMR spectra and comparison with analytical data from the literature. The presence of a triplet corresponding to six hydrogens at δ 1.20-1.40 and a two quartets at δ 4.27-4.45 indicated the presence of the two ethyl esters. The nitro group reduction and cyclization were achieved using iron in acetic acid as the reducing agent. The iron undergoes oxidation during the nitro group reduction, while the acetic acid acts as a proton source for the cyclization of the molecule to form the 2-quinolone-3-carboxylic acid ethyl esters in 52-91% yields (Table **2-14**). The structures of the compounds were confirmed by their ^{1}H NMR spectra and comparison with analytical data from the literature. The presence of a triplet corresponding to three hydrogens at δ 1.30 and a quartet (two hydrogens) at δ 4.27 and a singlet at δ ~12 for the quinoline N-H proton, in addition to the other expected resonances confirmed that the desired condensation-cyclization reaction had occurred. This reaction typically took place under reflux (118°C) for two hours. The 2-quinolone-3-carboxylic acid ethyl esters were hydrolysed under basic conditions to obtain the corresponding 2-quinolone-3-carboxylic acid compounds in 28-56% yields (Table **2-14**). Subsequent analysis of the ^{1}H NMR spectrum of 2-quinolone-3-carboxylic acids established that the ethyl protons were not present, and a broad single peak appeared at around δ 14 was consistent with the presence of a carboxylic acid.

Table 2-14 General scheme for synthesis of 2-quinolone-3-carboxylic acids and percentage yield products.

R	Diethyl 2-(2-nitrobenzylidene) malonates	Yield %	2-Quinolone-3-carboxylic acid ethyl esters	Yield %	2-Quinolone-3-carboxylic acid	Yield %
$-OCH_3$	**73**	17	**76**	52	**79**	52
H	**74**	25	**77**	91	**80**	56
$-Br$	**75**	50	**78**	55	**81**	28

2.3.10.2 Synthesis of 4-quinolone-3-carboxylic acids

In order to synthesis a small series of 4-quinolone-3-carboxylic acids we chose a three-step synthetic route that allowed us to use commercially available anilines as starting materials. Knoevenagel condensation of the anilines with diethyl ethoxy methylene malonate, followed by cyclization provided 4-quinolone-3-carboxylic acid ethyl esters, which were hydrolysed to give 4-quinolone-3-carboxylic acid. The diethyl 2-amino methylene malonates with yields in the range

16-34% (Table **2-15**). The structures of the compounds were confirmed by their ^{1}H NMR spectra and comparison with analytical data from the literature. The Knoevenagel condensation of anilines with diethyl ethoxy methylene malonate in the presence of ethanol as a solvent gave the diethyl 2-amino methylene malonates in 40-73% yields (Table **2-15**). The structures of the compounds were confirmed by their ^{1}H NMR spectra and comparison with analytical data from the literature. A triplet corresponding to six hydrogens at δ 1.20-1.40 and two quartets at δ 4.27-4.45 indicated the presence of two ethyl groups, in addition to a singlet (one hydrogen) for the secondary amine around δ 11. Followed by reduction successive cyclization provided 4-quinolone-3-carboxylic acid ethyl esters, which was hydrolysed to give 4-quinolone-3-carboxylic acid in 43-75% yields. The structures of the compounds were confirmed by their ^{1}H NMR spectra and comparison with analytical data from the literature. The presence of a triplet corresponding to (three hydrogens) at δ 1.30 and a quartet (two hydrogens) at δ 4.27 and a singlet (one hydrogen) at around δ 12 for the secondary amine of quinoline compounds in the compounds in addition to the other expected resonances confirmed that the desired condensation-cyclization reaction has occurred. The esters were hydrolysed using sodium hydroxide to give the corresponding 4-quinolone-3-carboxylic acids and in 43-75% yields (Table **2-15**). Subsequent analysis of the ^{1}H NMR spectrum of 4-quinolone-3-carboxylic acids established that the ethyl protons were not present, and a broad single peak appeared at around δ 15.0 was consistent with the presence of a carboxylic acid.
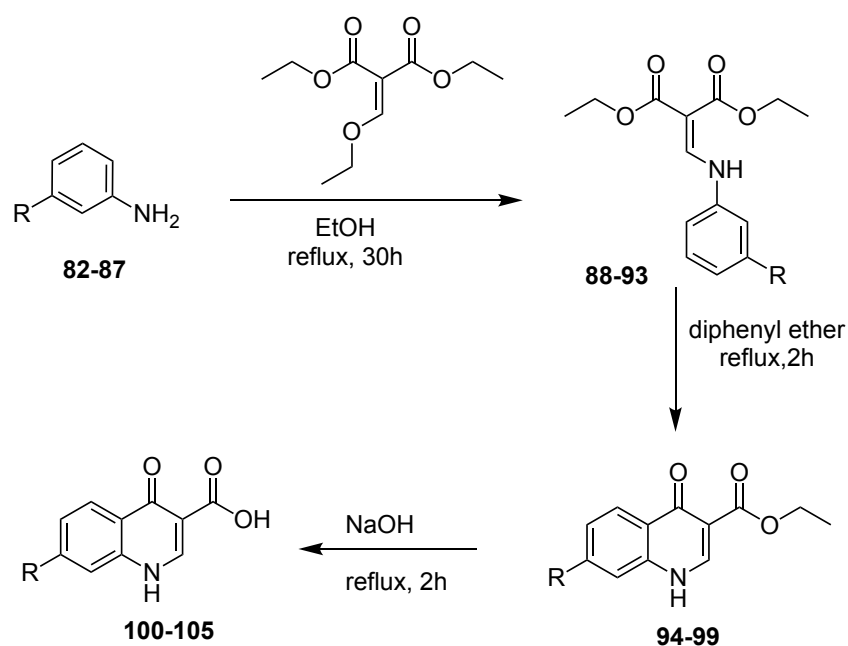
Table 2-15 General scheme for synthesis of 4-quinolone-3-carboxylic acid derivatives and percentage yield products.

R	Diethyl 2-amino methylene malonates	Yield %	4-Quinolone-3-carboxylic acid ethyl esters	Yield %	4-Quinolone-3-carboxylic acid	Yield %
-CH₃	88	23	94	40	100	58
-CH₂C	89	16	95	70	101	51
(isopropyl)	90	21	96	68	102	48
CF₃	91	27	97	62	103	57
Dioxol	92	34	98	73	104	65
Cl	93	23	99	66	105	52
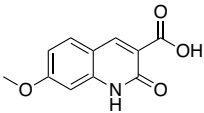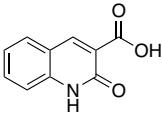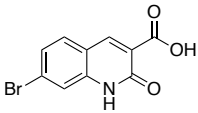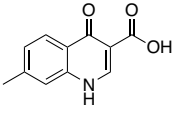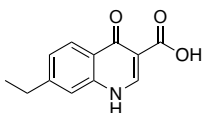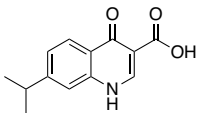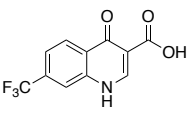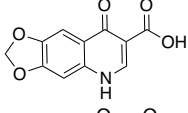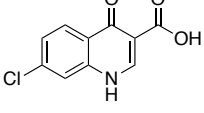
2.3.11 Docking of quinolone-3-carboxylic acids

Prior to synthesizing the compounds, they were docked as described previously

into the proposed MPP1 binding pocket.

We found that compounds showed a range of predicted binding affinities to Alphafold MPP1 model, with **81** and **104** and (-6.76 kcal /mol and -6.90 kcal /mol) giving the lowest scores (Table **2-16**). The docked conformations of these two compounds are shown in Figure **2-45** and Figure **2-46**.

Table 2-16 Binding affinity and interactions of quinolone-3-carboxylic acid derivative compounds with the MPP1 Alphafold structure using AutoDock Vina.

Compound	Structure	H-B	Hydrophobic contacts	BA (kcal /mol)
79		2	8	-6.52
80		2	8	-6.59
81		3	8	-6.76
100		3	5	-6.73
101		3	6	-6.54
102		3	6	-6.75
103		3	7	-6.74
104		3	5	-6.90
105		3	5	-6.55

The hydrogen bonds, hydrophobic contacts and docking scores represent the predicted binding energy of the higher ranked protein ligand complex. The hydrogen bonds count between the ligand and protein was calculated using UCSF Chimera.

The docked conformation for compound **81** with the Alphafold MPP1 model showed that the compound was predicted to form a range of hydrogen bond and ionic interactions with the protein (Figure **2-45**).
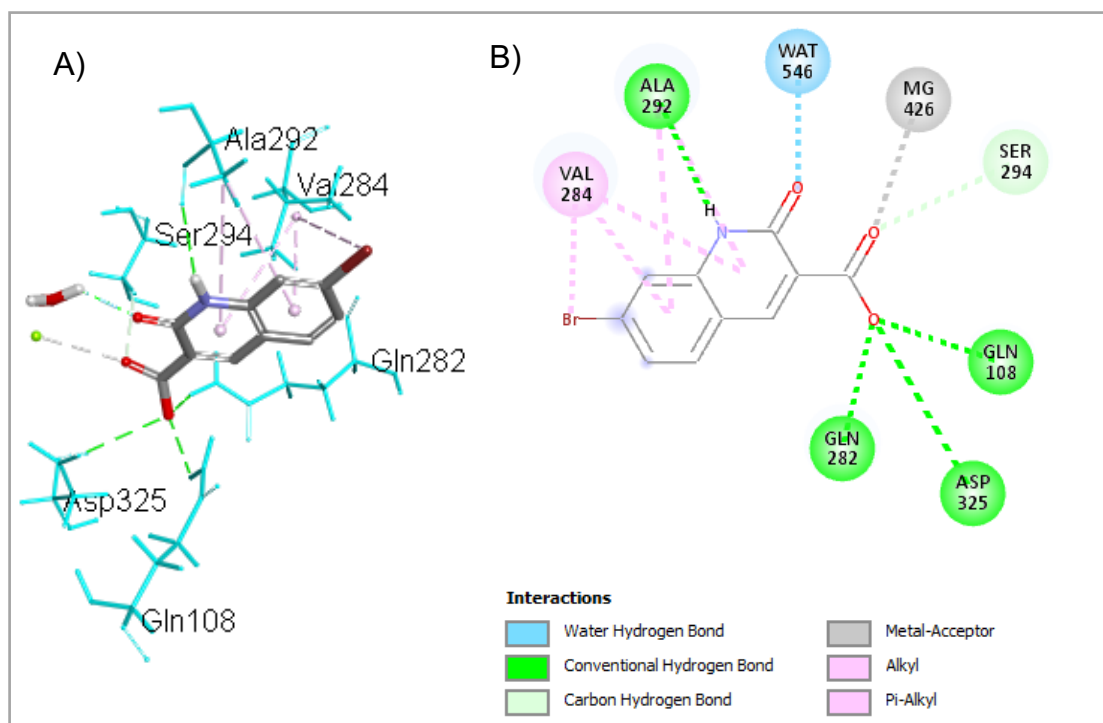
Figure 2-45 The best pose of compound **81** docked into allosteric site of the MPP1 Alphafold structure using AutoDock Vina: A) 3D protein and B) 2D protein - ligand interaction plots. Amino acids residues are represented as cyan thin sticks, while the ligand is shown as thick sticks with carbon atoms coloured in grey.

The docked conformation for compound **104** with the Alphafold MPP1 model showed that the compound was predicted to form a range of hydrogen bond and ionic interactions with the protein (Figure **2-46**).

Figure 2-46 The best pose of compound **104** docked into allosteric site of the MPP1 Alphafold structure using AutoDock Vina: A) 3D protein and B) 2D protein - ligand interaction plots. Amino acids residues are represented as cyan thin sticks, while the ligand is shown as thick sticks with carbon atoms coloured in grey.
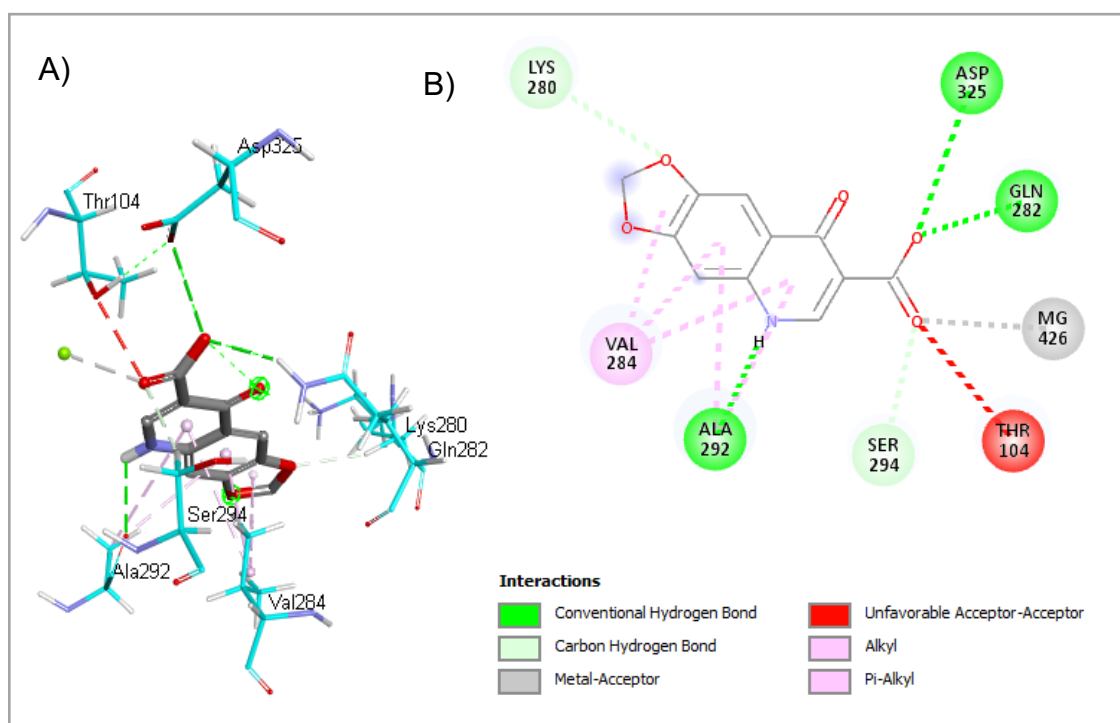
2.3.12 Biological evaluation of quinolone-3-carboxylic acids

2.3.12.1 Basal ATPase measurements of quinolone-3-carboxylic acids

Small molecule compounds synthesised based on the quinolone-3-carboxylic acid core structures were tested for their ability to inhibit MPP1 enzymatic activity by Dr Jiazhi Tang at UCL School of Pharmacy. The inhibition of the basal ATPase activity was measured in the absence of salt with different concentration of inhibitor and the IC_{50} for the inhibition of basal MPP1 ATPase activity was determined. However, eight quinolone-3-carboxylic acid analogues illustrated atypical basal ATPase curves **80**, **81**, **100**, **101**, **102**, **103**, **104** and **105**, which showed partial inhibitory activity against MPP1 this is may be due to the low solubility of some of the compounds at the test concentrations (Figure **2-47** A-B).
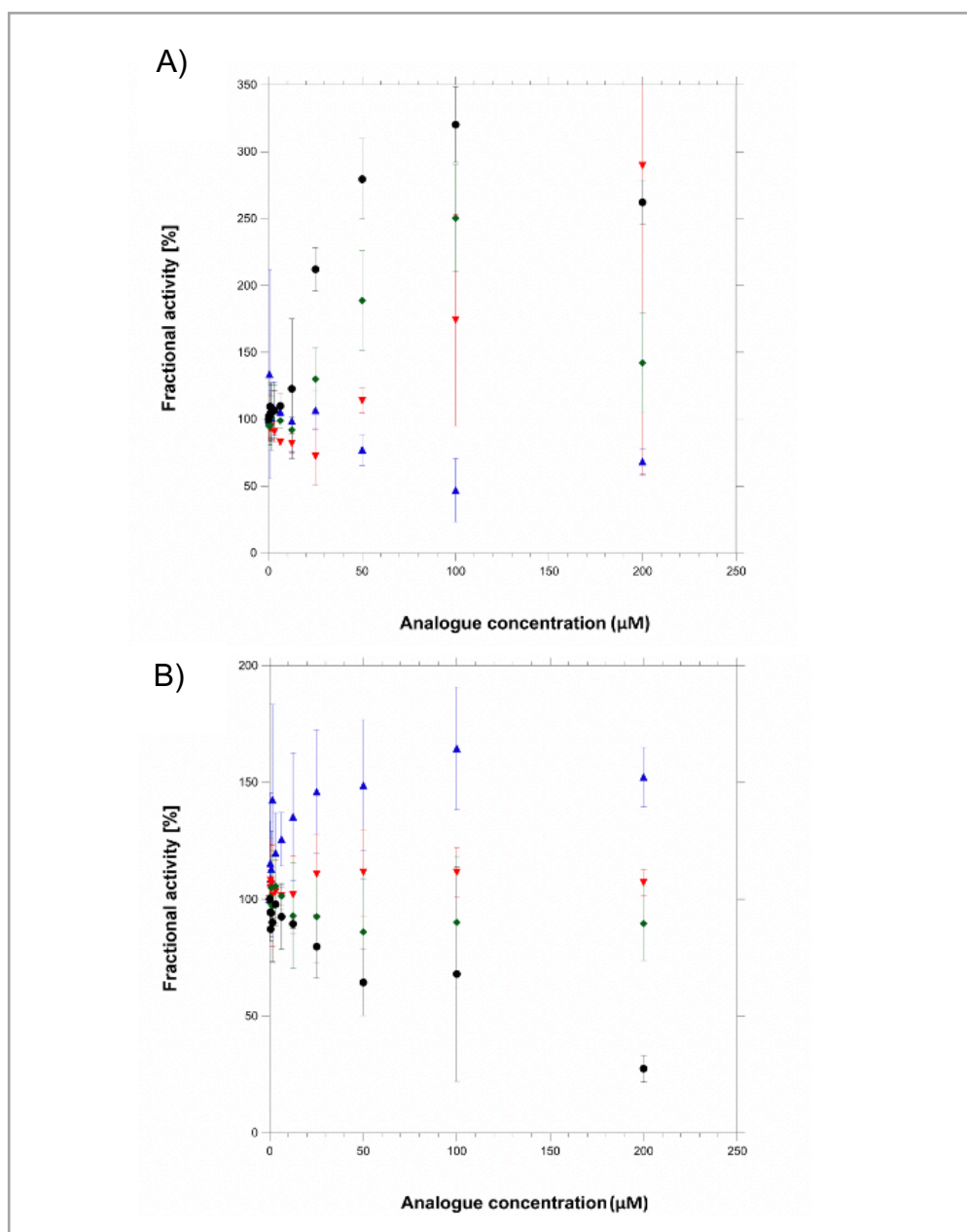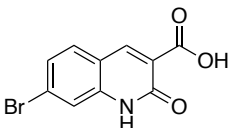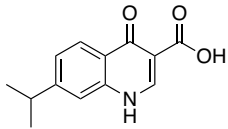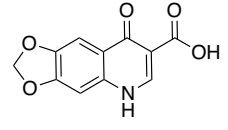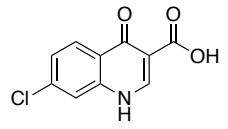
Figure 2-47 Basal Inhibition of the basal MPP1 ATPase activity by quinolone-3-carboxylic acids (A) Compound **80** (blue), **81** (red), **100** (green) and **101** (black). (B) Compound **101** (blue), **102** (red), **104** (green) and **105** (black). Data obtained by Dr. Jiazhi Tang.

2.3.12.2 MT-stimulated ATPase measurements of quinolone-3-carboxylic acids

The analogues **80**, **81** and **100** - **105** were also measured using a MT-stimulated ATPase assay (performed by Dr Jiazhi Tang at UCL School of Pharmacy). Finally, four hits were active in the MT-stimulated ATPase assay, analogues **81, 102, 104** and **105.**

Analogue **81** reduced the MT-stimulated ATPase activity of MPP1 by up to 98% at the maximum test concentration with an IC_{50} value of 42.53 ± 17.64 μM. Meanwhile, analogue **102** reduced the MT-stimulated ATPase activity of MPP1 by up to 84% with an IC_{50} value of 59.67 ± 16.07 μM. The other two hits, analogues **104** and **105**, illustrate inhibition of MPP1with IC_{50} values of 58.16 ± 16.07 μM and 33.33 ± 15.76 μM (Table **2-17**).

Table 2-17 Inhibition of the MT-stimulated MPP1 ATPase activity by four analogues.

Compound	Structure	Inhibition of MT-stimulatedMPP1 ATPase activity with IC_{50} (μM)[a]
81		42.53 ± 17.64
102		59.67 ± 16.07
104		58.16 ± 16.07
105		33.33 ± 15.76

a. Data obtained by Dr. Jiazhi Tang.

However, analogues **81** and **102** illustrated higher percentage inhibitions of MPP1 at the maximum test concentration compared to analogues **104** and **105**. The inhibition curves for **104** and **105** did not reach plateaus (Figure **2-48**), these data suggesting that their IC_{50} values are higher than the measured values.
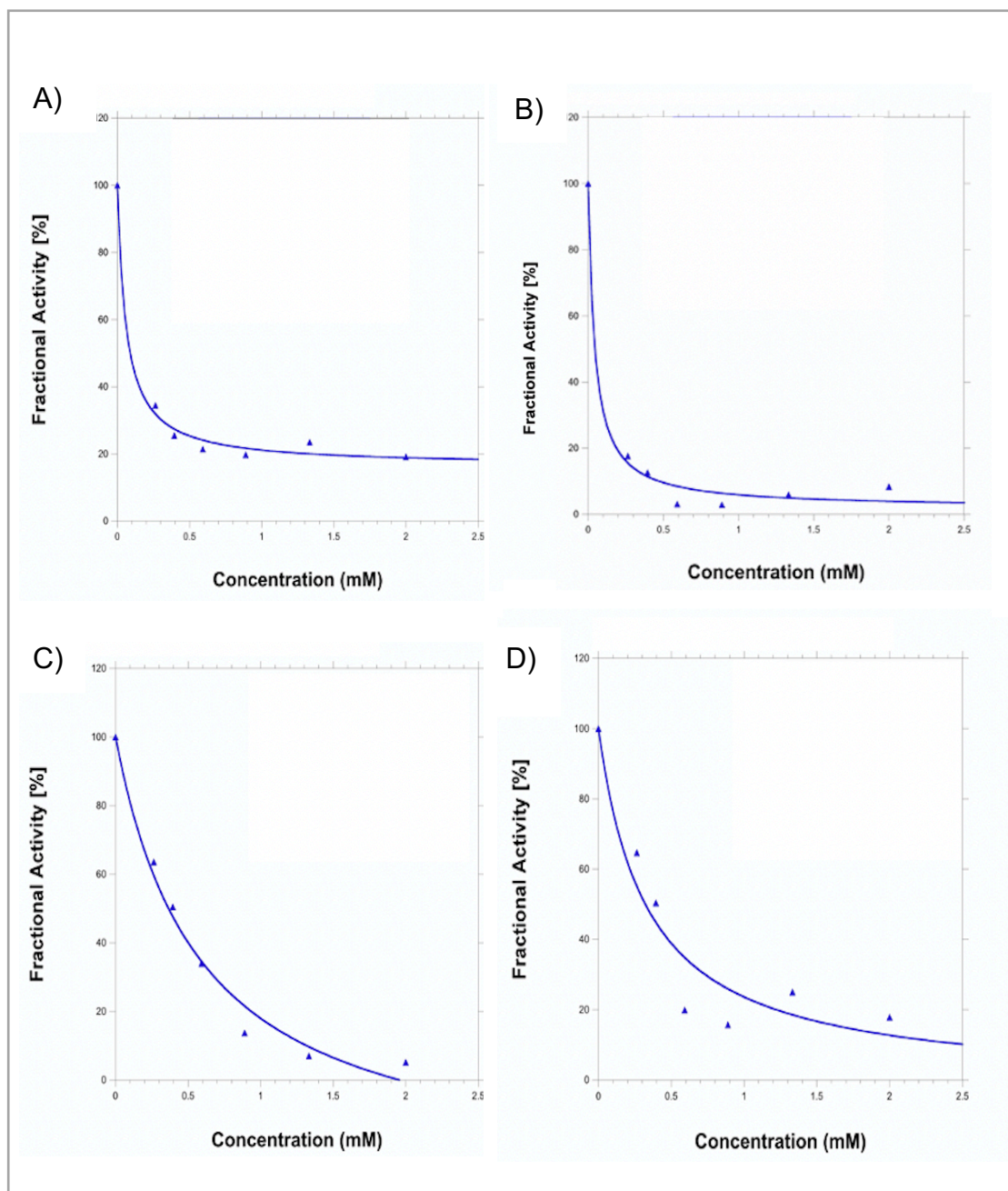
Figure 2-48 Compound A) **81**, B) **102**, C) **104** and D) **105** inhibition of the MT-stimulated MPP1 ATPase activity. Data obtained by Dr. Jiazhi Tang.

In summary, analogue **81**, which was synthesized based on the 2-quinolone-3-carboxylic acid scaffold, is slightly more active than the 4-quinolinone-3-carboxylic acid derivatives, although the inhibition values are similar and require further validation (Figure **2-49**). In terms of the 4-quinolinone-3-carboxylic acid derivatives, replacement of the isopropyl substituent at the C-7 position (similar to that present in the earlier ascochitine analogues) with halogens appears to be tolerated.
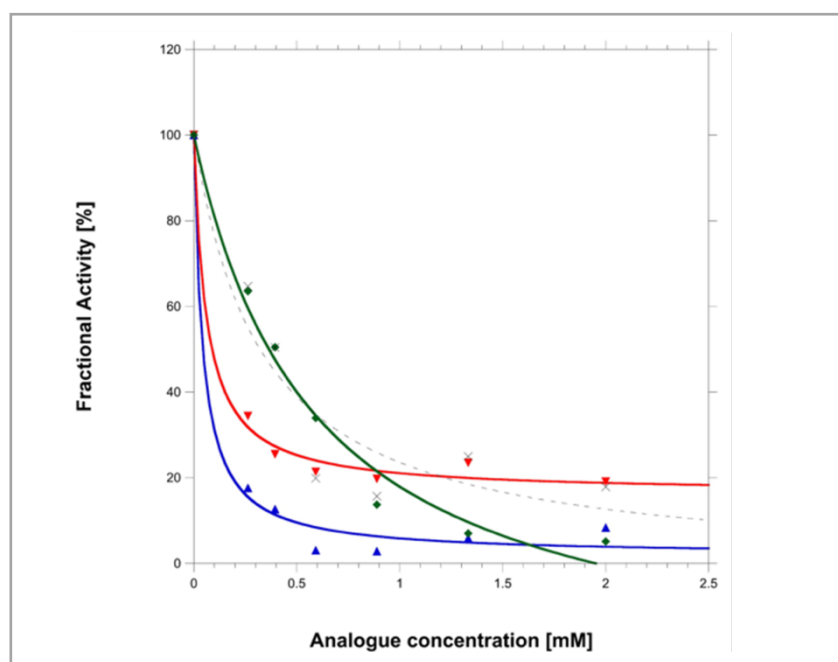
Figure 2-49 Inhibition of the MT-stimulated MPP1 ATPase activity by compound **70** (blue), **91** (red), **93** (green), **94** (black dot)**.** Data obtained by Dr. Jiazhi Tang.

According to the data, analogue **81** has a higher inhibitory activity than the other analogues studied (42.53 ± 17.64 µM), but it is still considered lower than ascochitine **13** (19.8 ± 3.3 µM) in MT-stimulated ATPase assay, showing approximately 2.5 -fold less potency. These findings suggest that it may be feasible to enhance the MPP1 inhibitory activity by optimizing the substitution pattern of the 2-quinolone-3-carboxylic acid. Therefore, we investigated the effect of substituents on the C-7 position of 2-quinolone-3-carboxylic acids in order to explore the structure-activity relationships (SAR).

2.3.13 Further investigation of the C-7 position of the 2-quinolone-3-carboxylic acids

To investigate the effect of the substituents on C-7 position of the 2-quinolone-3-carboxylic acids, four derivatives were synthesised according to previously described scheme (Table **2-16**) these compounds contain dimethylamino which is electron donating substituents and various electron withdrawing substituents of different size: fluoro (-F), trifluoromethyl (-CF$_3$), and chloro (-Cl) groups respectively (Figure **2-50**). The synthesis of a 7-amino derivate was also attempted, starting from the corresponding dinitro starting material, however this reaction failed to yield an isolatable product.
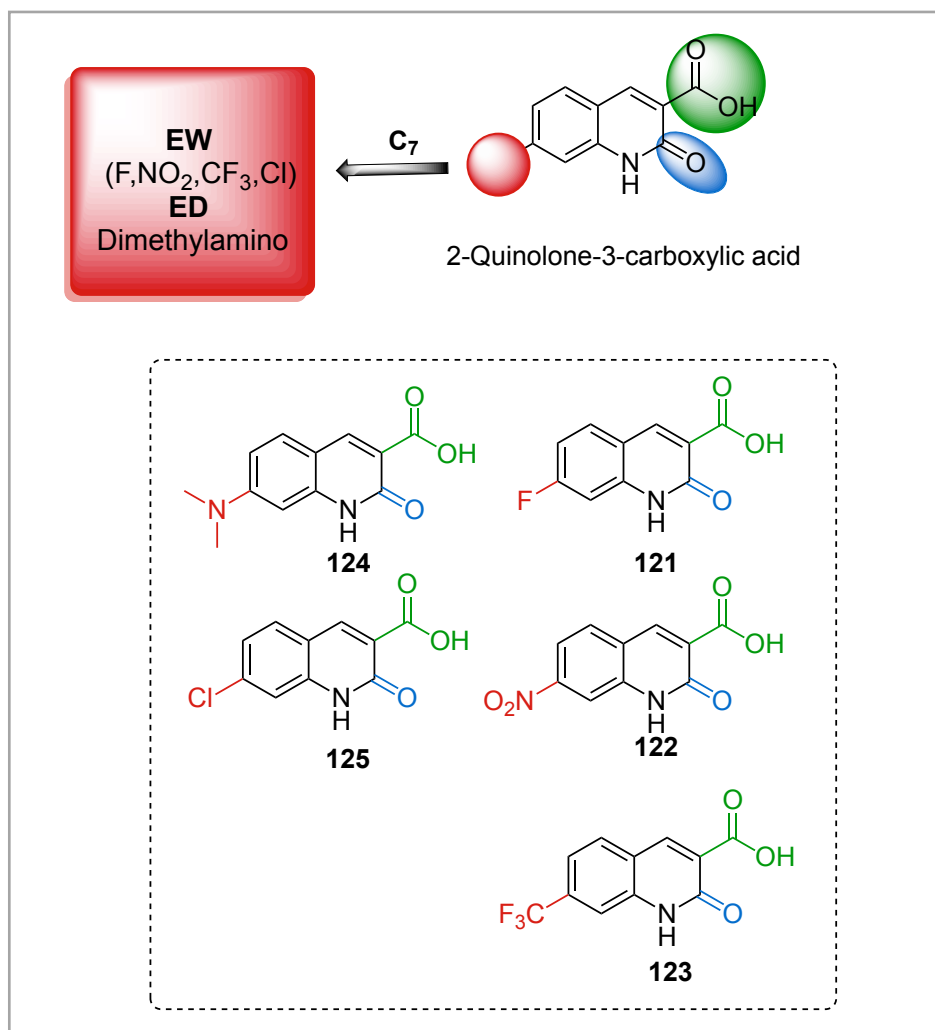
Figure 2-50 Modifications at the C-7 position of 2-quinolone-3-carboxylic acid to identify new analogues.

2.3.13.1 Synthesis of a new series of 2-quinolone-3-carboxylic acids

The same general scheme for synthesis of 2-quinolone-3-carboxylic acid derivatives was followed (*2.3.10.1 synthesis of 2-quinolone-3-carboxilic acids*) Table **2-14** that allowed us to use commercially available 2-nitrobenzaldehydes as starting materials. Knoevenagel condensation with diethyl malonate, followed by reduction of the nitro group and successive cyclization provided 2-quinolone-3-carboxylic acid ethyl esters, which was hydrolysed to give 2-quinolone-3-carboxylic acid. The Knoevenagel condensation of 2-nitrobenzaldehydes with diethyl malonate in the presence of ethanol as a solvent gave the diethyl 2-(2-nitrobenzylidene) malonate in 17-27% (Table **2-18**). The structures of the compounds were confirmed by their ^{1}H NMR spectra and comparison with analytical data from the literature. The presence of a triplet corresponding to six hydrogens at δ 1.0-1.6 and two quartets at δ 4.2-4.4 indicated the presence of two ethyl substituents. Reduction of the nitro group and successive cyclization provided 2-quinolone-3-carboxylic acid ethyl esters in the range 66-83% (Table **2-18**). The structures of the compounds were confirmed by their ^{1}H NMR spectra and comparison with analytical data from the literature. The presence of a triplet corresponding to three hydrogens at δ 1.30 and a quartet (two hydrogens) at δ 4.27 and a singlet (one hydrogen) at around δ 12 for the secondary amine of quinoline compounds in addition to the other expected resonances confirmed that the desired condensation-cyclization reaction has occurred. The esters were hydrolysed using sodium hydroxide to give the corresponding 2-quinolone-3-carboxylic acids in 58-61% yields (Table **2-18**). Subsequent analysis of the ^{1}H NMR spectrum of 2-quinolone-3-carboxylic acids established that the ethyl protons were not present, and a broad single peak appeared at around δ 15 was consistent with the presence of a carboxylic acid.

Table 2-18 Products of the reaction of substituted 2-nitrobenzaldehyde with diethyl malonate, nitro group cyclization to 2-quinolone-3-carboxylic acid ethyl esters and hydrolysis.

R	Diethyl 2-(2-nitrobenzylidene) malonates	Yield %	2-Quinolone-3-carboxylic acid ethyl esters	Yield %	2-Quinolone-3-carboxylic acid	Yield %
F	**111**	17	**116**	83	**121**	58
NO$_2$	**112**	20	**-**	-	**122**	Not detected
NH$_2$	**-**	-	**117**	Failed isolated	**-**	-
CF$_3$	**113**	25	**118**	75	**123**	59
-§-N<	**114**	22	**119**	66	**124**	58
Cl	**115**	27	**120**	70	**125**	61
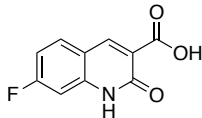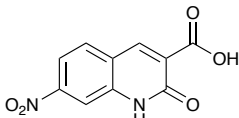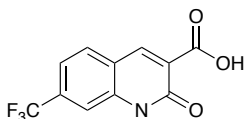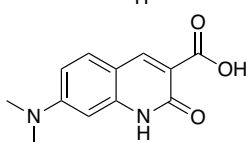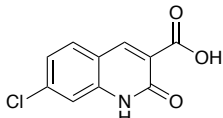
2.3.13.2 Docking a new series of 2-quinolone-3-carboxylic acids

Prior to synthesizing the compounds, they were docked as described previously into the proposed MPP1 binding pocket.

We found that compounds showed a range of predicted binding affinities to the MPP1 Alphafold model, with **123** and **125** and (-6.71 kcal /mol and -6.91 kcal /mol) respectively giving the lowest scores (Table **2-19**). The docked conformations of these two compounds are shown in (Figure **2-51** and Figure **2-52**).

Table 2-19 Binding affinity and interactions of 2-quinolone-3-carboxylic acid derivative compounds with MPP1 Alphafold structure using AutoDock Vina.

Compound	Structure	H-B	Hydrophobic contacts	BA (kcal /mol)
121		2	8	-6.63
122		2	8	-6.58
123		2	10	-6.91
124		2	8	-6.67
125		3	8	-6.71

The hydrogen bonds, hydrophobic contacts and docking scores represent the predicted binding energy of the higher ranked protein ligand complex. The hydrogen bonds count between the ligand and protein was calculated using UCSF Chimera.

The docked conformation for compound **123** with the Alphafold MPP1 model showed that the C3 carboxylic acid substituent formed a hydrogen bond interaction with Gln282, Gln108, Asp325 and an ionic interaction with the magnesium ion in the ADP binding pocket. The C2 carbonyl substituent formed a hydrogen bond interaction with a bound water residue and the quinoline NH formed a hydrogen bond interaction with Ala292 (Figure **2-51**). Whereas the docked conformation for compound **125** formed similar interactions with MPP1 (Figure **2-52**).
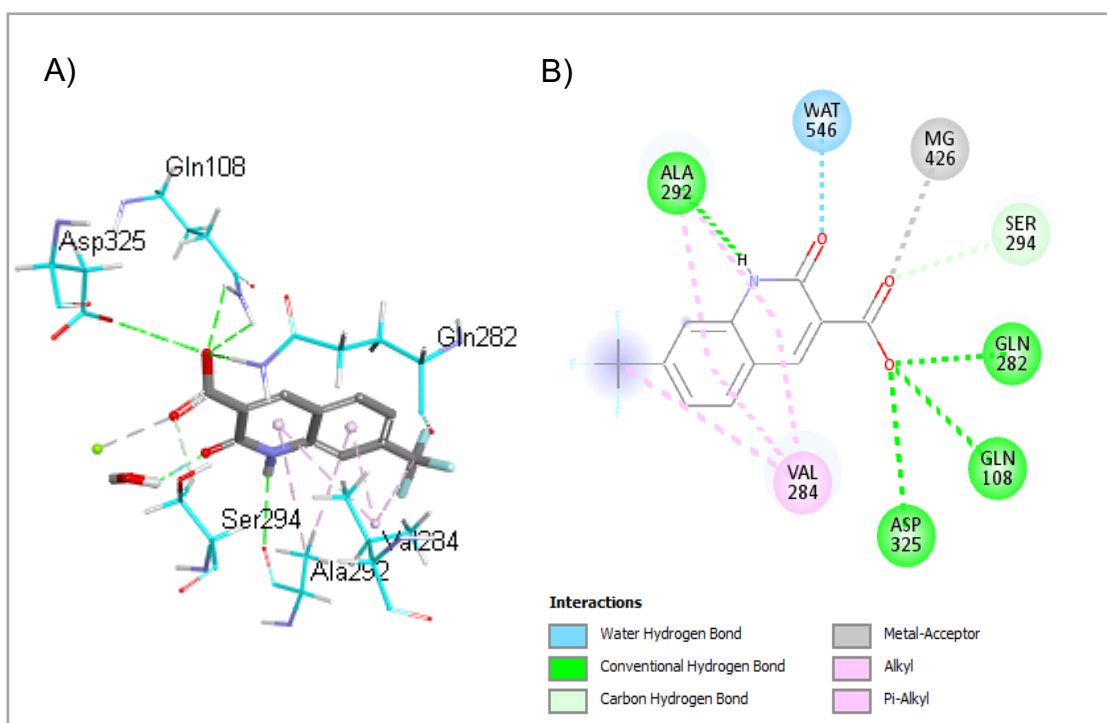
Figure 2-51 The best pose of compound **123** docked into allosteric site of the MPP1 Alphafold structure using AutoDock Vina: A) 3D protein and B) 2D protein - ligand interaction plots. Amino acids residues are represented as cyan thin sticks, while the ligand is shown as thick sticks with carbon atoms coloured in grey.
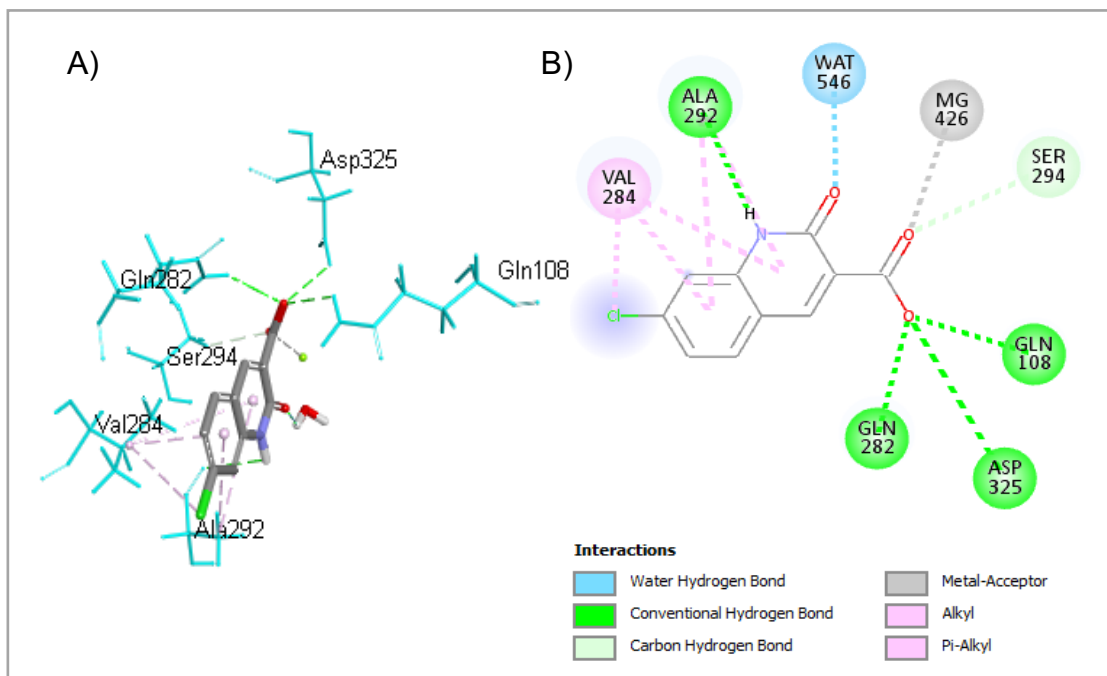
Figure 2-52 The best pose of compound **125** docked into allosteric site of the MPP1 Alphafold structure using AutoDock Vina: A) 3D protein and B) 2D protein - ligand interaction plots. Amino acids residues are represented as cyan thin sticks, while the ligand is shown as thick sticks with carbon atoms coloured in grey.

Molecular docking with the Alphafold structure of MPP1 studies suggested that the quinolones compounds may not be competitive with ATP, and may interact with a potential allosteric binding site adjacent to the Mg-ADP binding pocket which is located on the L5/α2/α3 regions illustrated in (Figure **2-53**). These predictions will require experimental validation as part of the future work on the project.
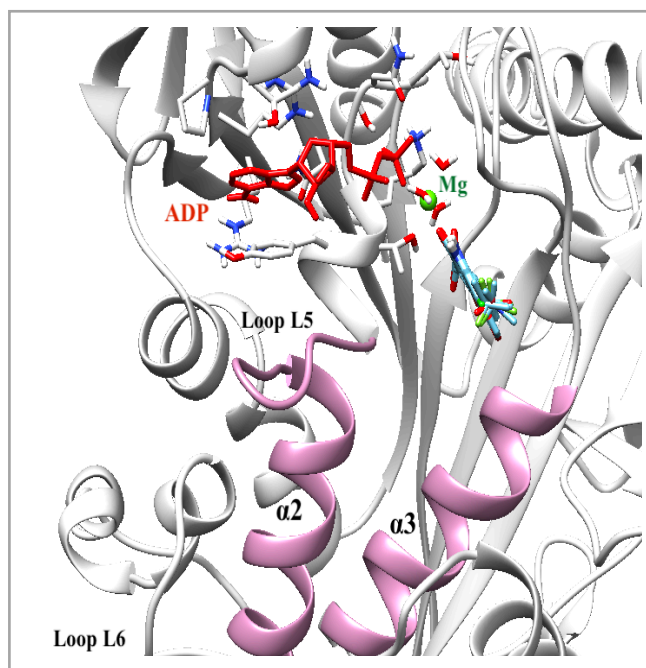
Figure 2-53 L5/α2/α3 binding pocket of human MPP1 Alphafold structure with ADP-Mg (red) and quinolone ligands (light blue) overlaid to illustrate how they occupy the site using AutoDock Vina.

2.3.14 Biological evaluation of a new series of 2-quinolone-3-carboxylic acids

2.3.14.1 MT-stimulated ATPase measurements of a new series of 2-quinolone-3-carboxylic acids

Due to time constraints, and the availability of MPP1 protein, the compounds could not be tested during the project.

2.4 Conclusions

Depsidones and ascochitine are known inhibitors of MPP1 enzymatic activity. We chose to use a pharmacophore and molecular modelling-based approach to identify new chemotypes of MPP1 inhibitors. Pharmacophore modelling suggested that chromenone-3-carboxylic acids and quinolone-3-carboxylic acids would be potential isosteres of the less synthetically accessible ascochitine. Molecular docking studies suggested that these compounds may interact with a potential allosteric binding site adjacent to the Mg-ADP binding pocket.

We designed a small library of coumarins to explore structure-activity relationships (SAR) in relation to the C3- and C7-positions of the heterocycle. The compounds were successfully synthesised from commercially available starting materials via condensation/cyclisation and hydrolysis. Amides were synthesised by coupling of the coumarin-3-carboxylic acids with various amines and 7-benzyloxy-chromene-3-carboxylic acid was synthesised by alkylating of the 7-hydroxy-chromene-3-carboxylic acid ethyl ester followed by hydrolysis of the ester. In addition to a small library of quinolones to explore the SAR in relation to the C7-positions of the heterocycle. The compounds were synthesised from commercially available starting materials via condensation/cyclisation and hydrolysis and were characterised by ^{1}H and ^{13}C NMR, LC-MS, and comparison with the literature. They were tested for their ability to inhibit MPP1 ATPase activity.

The coumarin analogues, which were synthesized based on the chromenone-3-carboxylic acid scaffold, showed weak inhibition of basal MPP1 ATPase assay activity with compound **44** having an IC$_{50}$ ~200 µM. The quinolone analogues were synthesized based on a quinolone-3-carboxylic acid scaffold and illustrated weak inhibition of the MT-stimulated MPP1 ATPase assay, with analogues **81**, **102**, **104**, and **105** having IC$_{50}$s in the range ~33-59 µM (around 2.5 to 3-fold less active than ascochitine, IC$_{50}$ 16 ± 1.8 µM).

118

The basal and MT-stimulated ATPase assays suggest that coumarin and quinolone analogues are weak inhibitors of MPP1 that could be further derivatised and optimised to improve their biological activity.

3 Fragment-based drug design (FBDD) of KifC1 inhibitors

3.1 Background

3.1.1 Small molecule inhibitors of KifC1

Though KifC1 is essential and indispensable in some cancer cell lines and functions in reproductive cells, its activity is not required for most somatic cells, making it a desirable target for cancer chemotherapy [145]. Up to now, two KifC1 inhibitors, AZ82 **9** and CW069 **10** (Figure **3-1**), have been identified. However, their mechanisms of action remain unknown due to the challenge of obtaining structural information and their exclusive binding to the MT-KifC1 complex rather than KifC1 alone. AZ82 specifically targets the KifC1-MT complex, inhibiting MT-stimulated KifC1 ATPase activity with an IC_{50} of 0.3 μM. Nevertheless, its non-specific cytotoxic effects at higher concentrations and the difficulty in solving the KifC1-AZ82 complex have hindered further development. CW069 binds directly to KifC1 but exhibits limited efficacy with an IC_{50} value of 75 ± 20 μM and lacks selectivity for KifC1 over Eg5. Consequently, neither of these inhibitors is suitable for further clinical development [146, 147].
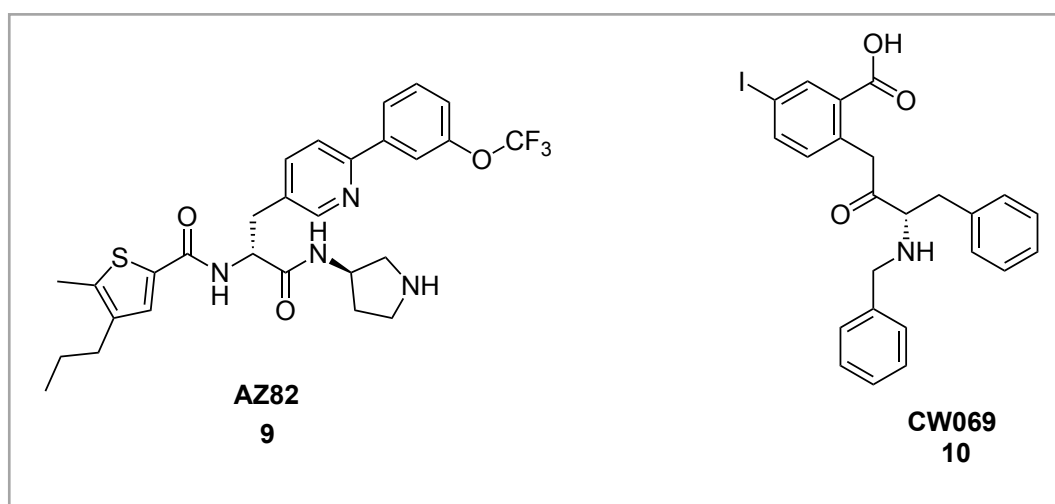

Figure 3-1 Chemical structures of known KifC1 inhibitors.

3.1.2 Fragment-based drug design (FBDD) of KifC1 strategy

Fragment-based drug design (FBDD) is a strategy used in drug discovery to identify small, low molecular weight compounds (fragments, <300 Da) that bind to a specific target protein. It enables the identification of potential drug candidates at an early stage of the discovery process, reducing the time and resources required for drug development.

In FBDD, there are three main strategies for improving fragment hits: fragment growing, fragment merging, and fragment linking. However, in the context of developing KifC1 inhibitors, the fragment merging, and fragment linking approaches rely on the crystal structures of protein-ligand complexes, which are not currently available for the development of KifC1 inhibitors. Therefore, the development of KifC1 fragments can only be conducted by fragment growing based on SAR analysis.

In this project, small fragment KifC1 ligands had previously been identified by NMR-based screening. These fragments form the starting point for the design, synthesis, and evaluation of fragment analogues with improved KifC1 binding properties and inhibitory activities.

3.1.3 Evaluation of KifC1 fragments

Prof. Frank Kozielski's research group at UCL School of Pharmacy in collaboration with Monash University conducted a study to identify potential inhibitors of KifC1. They used complementary NMR fragment screens techniques and identified twenty fragment hits of KifC1.Out of these twenty hits, ten fragments were selected for further analysis based on their identification via multiple NMR methods, including STD (Saturation Transfer Difference), CPMG (Carr-Purcell-Meiboom-Gill), and Water Logsy (Figure **3-2**). These multiple identification methods increase the confidence in the binding interactions between the fragments and KifC1. To evaluate the potential of these ten fragments, TSA (Thermal Shift Assay) and ATPase assays were conducted to study the thermal stability and potential inhibition of the basal KifC1 ATP activity

of KifC1 proteins. These fragments were evaluated using TSA and ATPase assays to study the thermal stability and potential inhibition of the basal KifC1 ATP activity of KifC1 proteins.
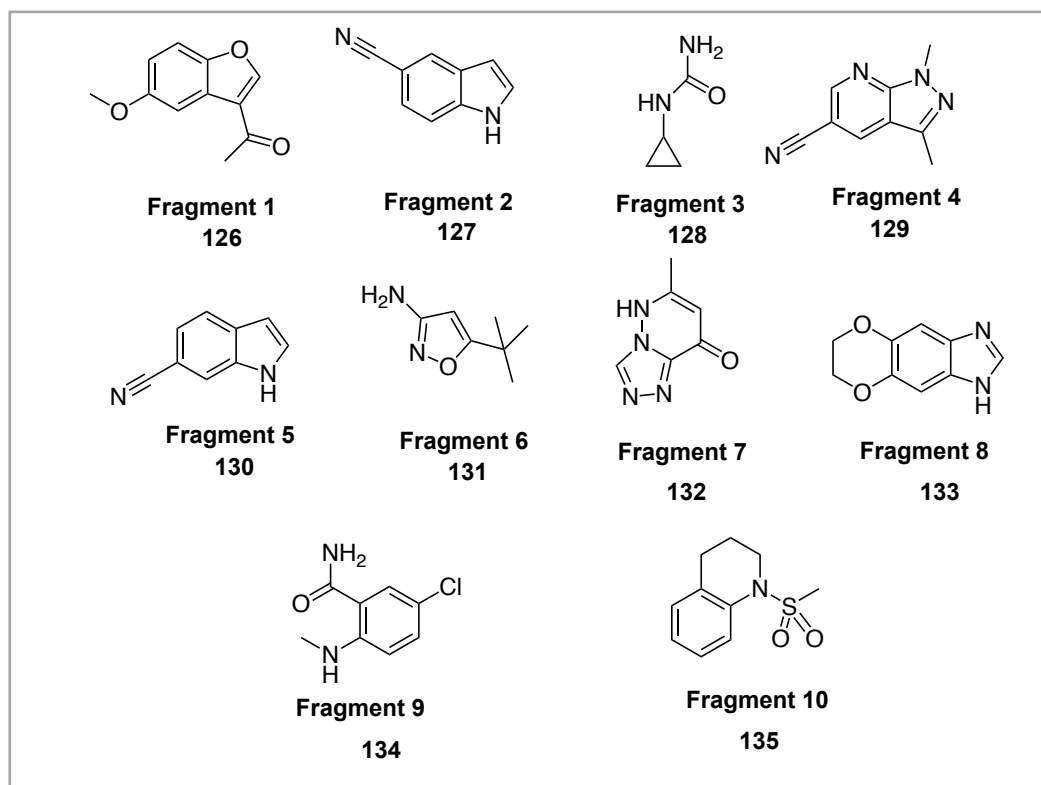
Figure 3-2 Ten fragments that bind to KifC1, which selected for further analyses that identified via more than one NMR method.

3.1.3.1 Thermal shift analyses of KifC1 fragments

The TSA of KifC1 fragments was conducted by monitoring the changes in fluorescence intensity ratio with increasing temperature for nine of the ten fragments (**1** to **9**). If the fragments bind to the protein, there should be a change in the temperature at which the KifC1 protein unfolds and undergoes a change in fluorescence ratio (350 nm/330 nm) due to the formation of additional protein-ligand interactions. In most cases this should result in an increase in the inflection temperature of the protein (T_i), the temperature at which the change in fluorescence ratio vs. temperature is at its steepest. However, the TSA measurements of KifC1 in the presence of the fragments illustrated decreased T_i values. The T_i values of fragments are below the DMSO blank group (KifC1 in

the assay buffer with DMSO but without fragments), T_i value 53.6 ± 0.25°C (data from Dr. Jiazhi Tang) (Table **3-1**). Several fragments also generate atypical binding profiles, which could not always be improved by reducing the fragment concentration in the experiments. This suggests that TSA may not be a suitable assay for measuring fragment binding to KifC1 but may be applicable to more potent fragment analogues.

Table 3-1 TSA measurements of KifC1 fragments.

Measurements[a]	T_i (5 mM) [°C]	T_i (2.5 mM) [°C]	T_i (1.25 mM) [°C]	T_i (0.625 mM) [°C]
KifC1 blank without DMSO	53.6 ± 0.25			
Control (10%, 5%, 2.5%, 1.25% DMSO)	51.3 ± 0.14	52.2 ± 0.15	52.7 ± 0.17	53.6 ± 0.18
Fragment **1** 126	50.7 ± 0.42	51.3 ± 0.25	52.2 ± 0.23	53.1 ± 0.09
Fragment **2** 127	39.7 ± 0.07	39.6 ± 0.22	40.6 ± 0.10	41.9 ± 0.19
Fragment **3** 128	50.7 ± 0.35	52.2 ± 0.11	atypical curve	53.3 ± 0.15
Fragment **4** 129	41.3 ± 0.19	41.8 ± 0.13	42.2 ± 0.14	43.1 ± 0.14
Fragment **5** 130	atypical curve	atypical curve	atypical curve	atypical curve
Fragment **6** 131	atypical curve	50.0 ± 0.09	51.8 ± 0.18	53.0 ± 0.41
Fragment **7** 132	atypical curve	atypical curve	atypical curve	atypical curve
Fragment **8** 133	None*	None*	None*	None*
Fragment **9** 134	atypical curve	atypical curve	52.3 ± 0.31	52.9 ± 0.25

a. Binding measurements carried out at different fragment concentrations.
*Fragment **8** could not be measured due to intrinsic fluorescence. Data obtained by Dr. Jiazhi Tang.

3.1.3.2 Basal ATPase measurements of KifC1 fragments

The basal ATPase inhibition assay gives an indication of the extent to which fragments inhibit the enzymatic activity of KifC1. The measurements were conducted in the presence of the fragments by Dr. Jiazhi Tang in Prof. Frank Kozielski's research group at UCL School of Pharmacy.

Fragment **1** was not subjected to ATPase measurements due to its limited availability. Among fragments **2** to **10**, fragments **4** and **9** showed inhibition of the basal KifC1 ATPase activity, while the remaining fragments illustrated very weak or no inhibition. The IC_{50} values are 0.99 ± 0.04 mM and 0.91 ± 0.02 mM for fragments **4** and **9**, respectively. Fragment **4** reduced the basal ATPase activity of KifC1 by 48% at the highest test concentration while fragment **9** reduced the basal ATPase activity by 84%. Furthermore fragments **4** and **9** showed perfectly fitted sigmoidal curves. illustrated in (Figure **3-3**).
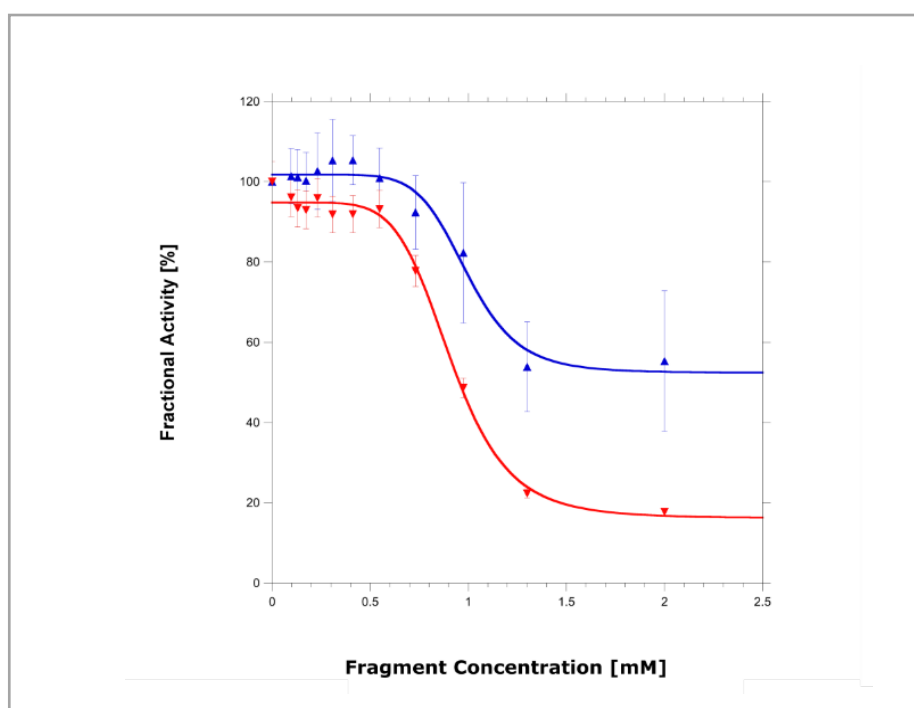
Figure 3-3 Dose-response curves of the inhibition of the basal KIfC1 ATPase activity of fragments **4** (blue) and **9** (red). Data obtained by Dr. Jiazhi Tang.

Whereas TSA experiments are not yet useful for the evaluation of fragments binding to KifC1, the inhibition of the basal KifC1 ATPase activity seems to provide an indication of inhibition for at least two of the ten fragments.

3.2 Aim and Objectives

The work described in this chapter focuses on fragment-based drug development with the purpose of developing more potent fragment analogues for the KifC1

protein. As a starting point, a set of active fragments have been identified by fragment screening, followed by an initial SAR analysis. The goal is to identify novel KifC1 fragment analogues through the design, synthesis and molecular modelling of a series of analogues using fragment growing strategies. Such molecules may be used as chemical probes for studying KifC1 function and as potential lead compounds for drug development.

The objectives of this part of the project included:

1- Identifying new fragment analogues with binding affinity for the target.
2- Determining the optimal binding mode and orientation of the fragment on the target using computational modelling (molecular docking and molecular dynamics).
3- Optimizing the fragment analogues for physicochemical properties (drug-like properties, solubility).
4- Providing fragment analogues for evaluation *in vitro* (inhibition of the target protein, cytotoxicity, target, or cell line selectivity).

3.3 Results and Discussion

3.3.1 Human KifC1 Alphafold structure

The crystal structure of the human KifC1 motor domain (PDBID:5WDH) protein was determined with Mg-ADP bound [58] (Figure **3-4** A). In order to carry out molecular modelling and docking studies we used the Alphafold structure prediction for human KifC1 that included some of the loop regions that were missing from the crystal structure (Figure **3-4** B). The superimposition of the two structures (Figure **3-4** C) illustrates the extent of the similarity between these two motor domains (RMSD = 0.961 Å). By analogy to the crystal structure of the human KifC1 motor domain (PDBID:5WDH), one of the potential binding pockets on the human KifC1 Alphafold structure is the allosteric site-I (L5/α2/α3) adjacent to the Mg-ADP binding pocket.
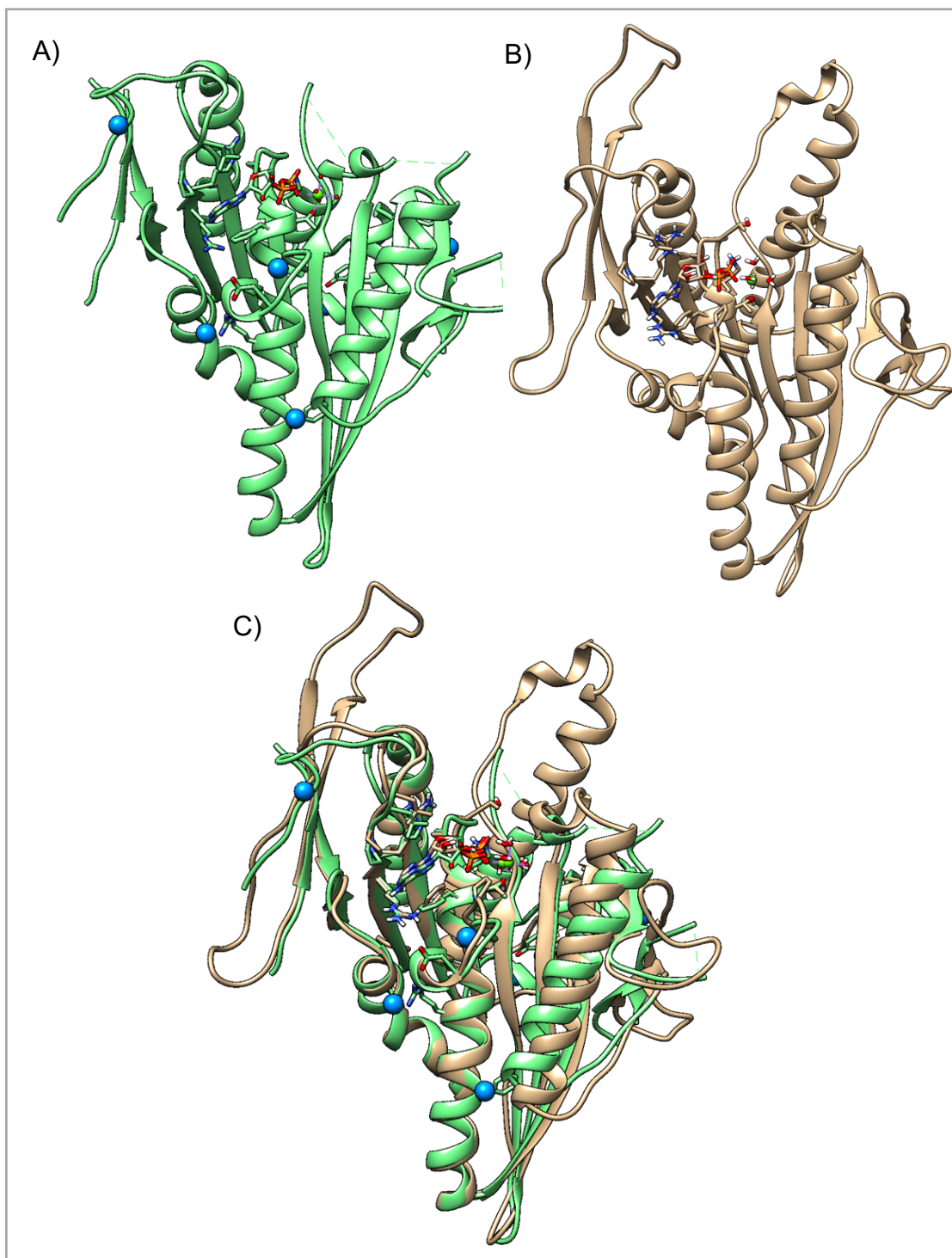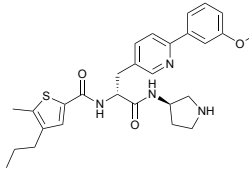
Figure 3-4 Superimposition of the crystal structure of the KifC1 motor domain complex with bound Mg-ADP (PDB entry: 5WDH) and and Alphafold model of KifC1 that included the missing sequence A) crystal structure of the KifC1 motor domain complex with bound Mg-ADP (PDBID: 5WDH) in ribbons (green) B) KifC1 Alphafold Structure complex with 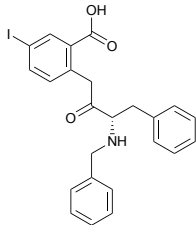bound Mg-ADP of that included the missing sequence of crystal structure in ribbons (beige C) Superimposition of the) crystal structure of the KifC1 motor domain complex with bound Mg-ADP (PDB entry: 5WDH) in ribbons (green)and and KIfC1 Alphafold model of KifC1 in ribbons (beige (Image prepared using UCSF Chimera).

3.3.2 Molecular docking of fragment analogues to KifC1

### 3.3.2.1 Docking of the fragment inhibitors of KifC1

AutoDock Vina was used to predict the binding mode of two known inhibitors, AZ82 and CW069 to the Alphafold model, the results are presented in Table **3-2**. In this study, the compounds were docked into the L5/α2/α3 pocket adjacent to the ADP-Mg binding site. This is consistent with our previous studies on MPP1, although it is possible that the compounds may bind elsewhere on the protein as the binding site(s) for these inhibitors has not yet been determined experimentally.

Table 3-2 Binding affinity and interactions of AZ82 and CW069 with human kifc1 using AutoDock Vina.

Compound	Structure	Molecular Wight (g/mol)	H-B	Hydrophobic contacts	BA (kcal/mol)
AZ82 **9**		560.64	2	1	-6.19
CW069 **10**		499.35	1	3	-5.15

The docking scores represent the predicted binding energy of the higher ranked protein ligand complex. The hydrophobic contacts were calculated using Open Drug Discovery Toolkit and hydrogen bonds count between the ligand and protein were calculated using UCSF Chimera.

In a molecular docking study of the Alphafold structure prediction for human KifC1 that included the missing sequence of crystal structure the KifC1 motor domain (PDBID: 5WDH), The analysis indicates that the allosteric L5/α2/α3 binding pocket has a slightly reduced volume compared to the MPP1 protein, but it remains accessible for current KifC1 inhibitors including AZ82 and CW069, as shown in (Figure **3-5** A) Additionally, the α4/α6 binding pocket appears to be spacious enough to harbour AZ82, as illustrated in Figure **3-5** B.
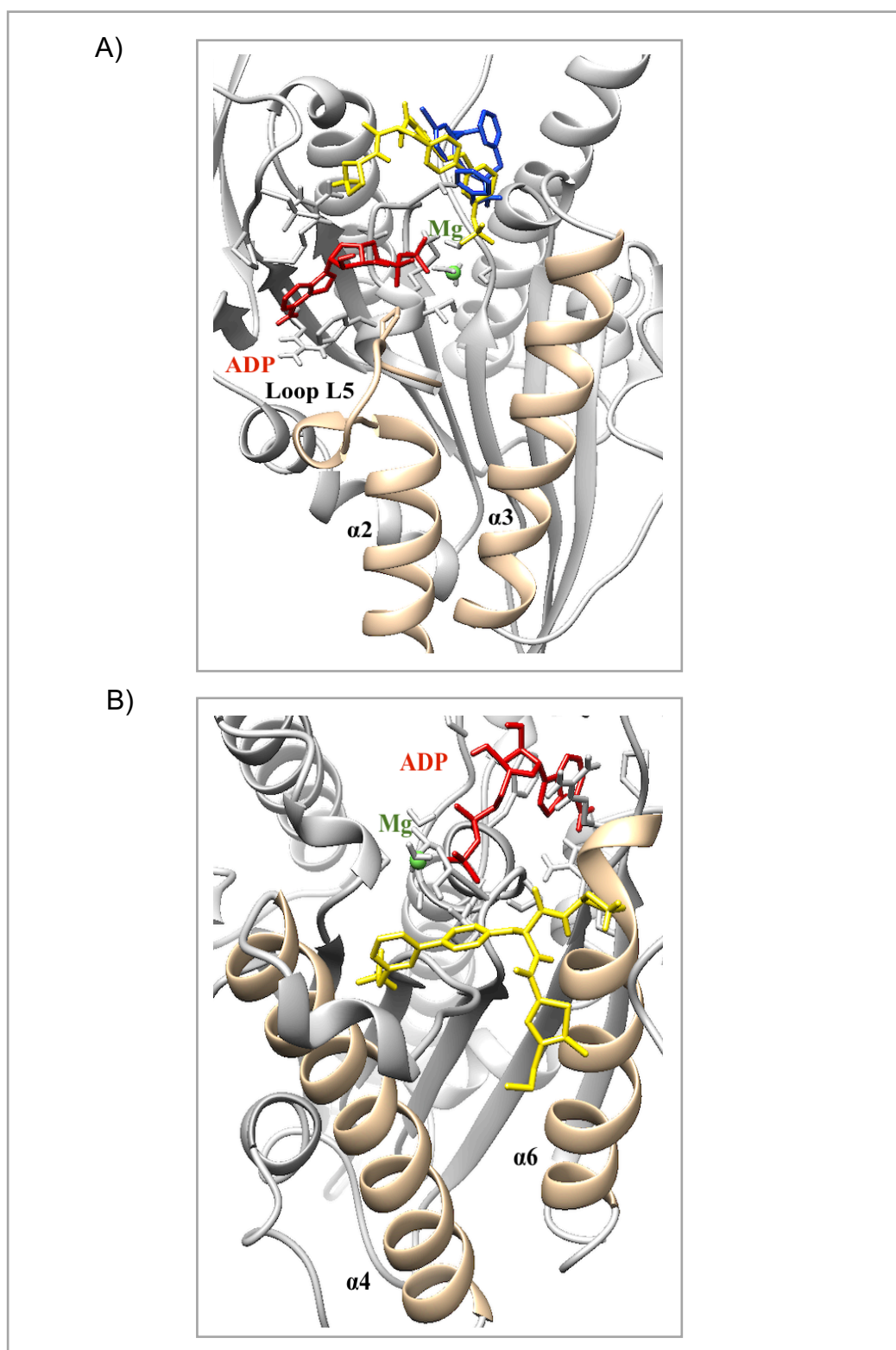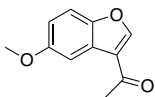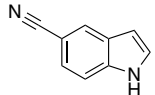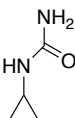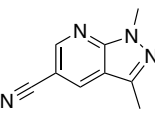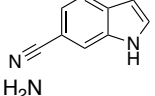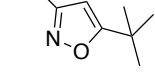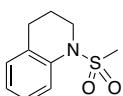
127

Figure 3-5 A) L5/α2/α3 binding pocket of human KifC1 Alphafold structure with ADP-Mg (red) and AZ82 (yellow) and CW069 (blue) ligands overlaid to illustrate how they occupy the site using AutoDock Vina. B) α4/α6 binding pocket of human KifC1 Alphafold structure with ADP-Mg (red) and AZ82 (yellow) ligand overlaid to illustrate how they occupy the site using AutoDock Vina.

3.3.2.2 Docking of KifC1 fragments

We used AutoDock Vina to dock the ten fragments that were identified by the NMR screening methods into the same allosteric pocket adjacent to Mg-ADP pocket. The results are shown in Table **3-3**.

Table 3-3 Binding affinity and interactions of fragments with human KifC1 using AutoDock Vina.

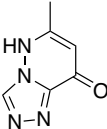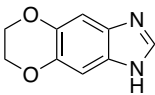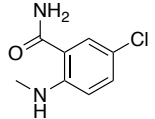| Compound	Structure	Molecular Wight (g/mol)	H-B	Hydrophobic contacts	BA (kcal/mol)
Fragment **1** 126		190.20	2	1	-4.68
Fragment **2** 127		142.16	1	0	-3.93
Fragment **3** 128		100.12	2	7	-3.90
Fragment **4** 129		172.19	1	0	-4.47
Fragment **5** 130		142.16	2	1	-4.12
Fragment **6** 131		140.19	6	1	-4.34
Fragment **7** 132		150.14	1	1	-4.72
Fragment **8** 133		176.17	2	0	-4.52
Fragment **9** 134		184.62	2	2	-4.66
Fragment **10** 135		211.28	1	2	-4.39

The docking scores represent the predicted binding energy of the higher ranked protein ligand complex. The hydrophobic contacts were calculated using Open Drug Discovery Toolkit and hydrogen bonds count between the ligand and protein were calculated using UCSF Chimera.

The data show how the fragments and the AZ82 and CW069 may bind to the L5/α2/α3 site, and what interactions may be formed between the inhibitors and the protein (Figure **3-6**). In the absence of other structural data, they provide predictions of what changes could be made to the fragments to improve their binding activity. It is conceivable that the fragments may bind elsewhere on the protein, further structural studies would be required to confirm the binding site(s) as part of the future work on this project.
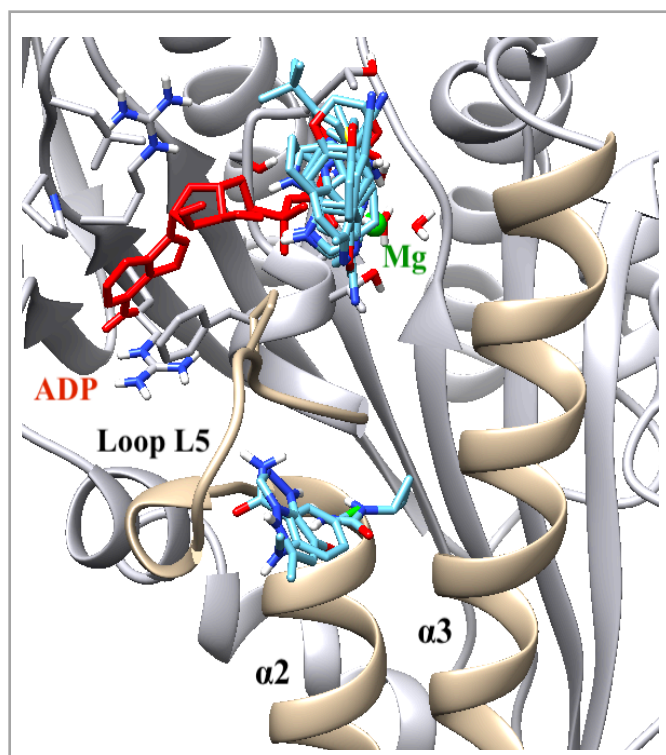
Figure 3-6 L5/α2/α3 binding pocket of human KifC1 Alphafold structure with ADP-Mg (red) and fragments ligands **1-10** (light blue) overlaid to illustrate how they occupy the site using AutoDock Vina.

3.3.3 Identifying fragment analogue inhibitors of human KifC1 using FBDD

As discussed previously in (*see Fragment-based drug design (FBDD) of KifC1 strategy*), the fragment merging and fragment linking approaches are highly dependent on structural data from X-ray crystallography of protein-ligand complexes, that are not currently available. Therefore, the development of KifC1 fragments can only be accomplished through fragment growth approaches based on SAR analysis of the available binding affinity data.

Our primary objective is to synthesis fragment analogues that have improved binding affinities to KifC1. To achieve this, fragment growth and modification approaches were adopted to explore the structure-activity relationships associated with the fragments.

Initially, molecular modelling techniques were used to predict the binding affinities of the analogues to KifC1. This approach was used to identify and select compounds for synthesis and testing in KifC1 binding and ATPase inhibition assays.

3.3.4 Design, synthesis, modelling, and biological evaluation of fragment 10 analogues

3.3.4.1 Design of sulphonyl 1,2,3,4-tetrahydroquinolines

The initial work on KifC1 inhibitors began with fragment 10 (compound **124**), methylsulphonyl-1,2,3,4-tetrahydroquinoline (Figure **3-7** A). Several small molecules were designed as fragment analogues by replacing the methyl sulphonamide substitution with different alkyl sulphonamide substitutions such as ethyl and cyclopropyl or aryl sulphonamides including 4-methoxyphenyl and phenyl (Figure **3-7** B).
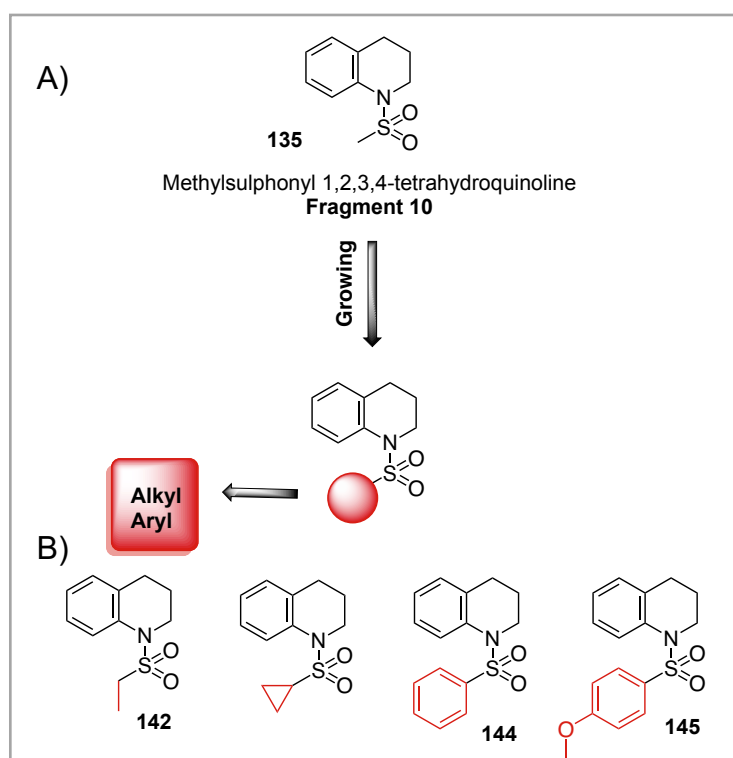
Figure 3-7 Design of sulphonyl 1,2,3,4-tetrahydroquinolines as fragment 10 analogues.

3.3.4.2 Design of sulphonyl 1,2,3,4-tetrahydroisoquinolines

Several tetrahydroisoquinoline (THIQ) analogues were also designed to explore the effect of moving position of the sulphonamide substituent on the core heterocycle. Under some circumstances THIQs can behave as bioisosteres of tetrahydroquinolines (Figure **3-7** A) [148]. Bioisosteres are molecular structures that are similar in their properties, including their physical, chemical, and biological properties, despite having different chemical structures. These similarities make bioisosteres useful in drug design, as they can mimic the activity of a target molecule while having potentially reduced toxicity and improved pharmacokinetic properties [149].

We utilized a short synthetic route to produce a small series of compounds derived from methylsulphonyl-1,2,3,4-tetrahydroisoquinoline compound **141**, comparable to that used for the tetrahydroquinoline analogues. A similar choice of alkyl and aryl sulphonamide substituents were chosen so that direct comparisons could be made between the two series (Figure **3-8** B).
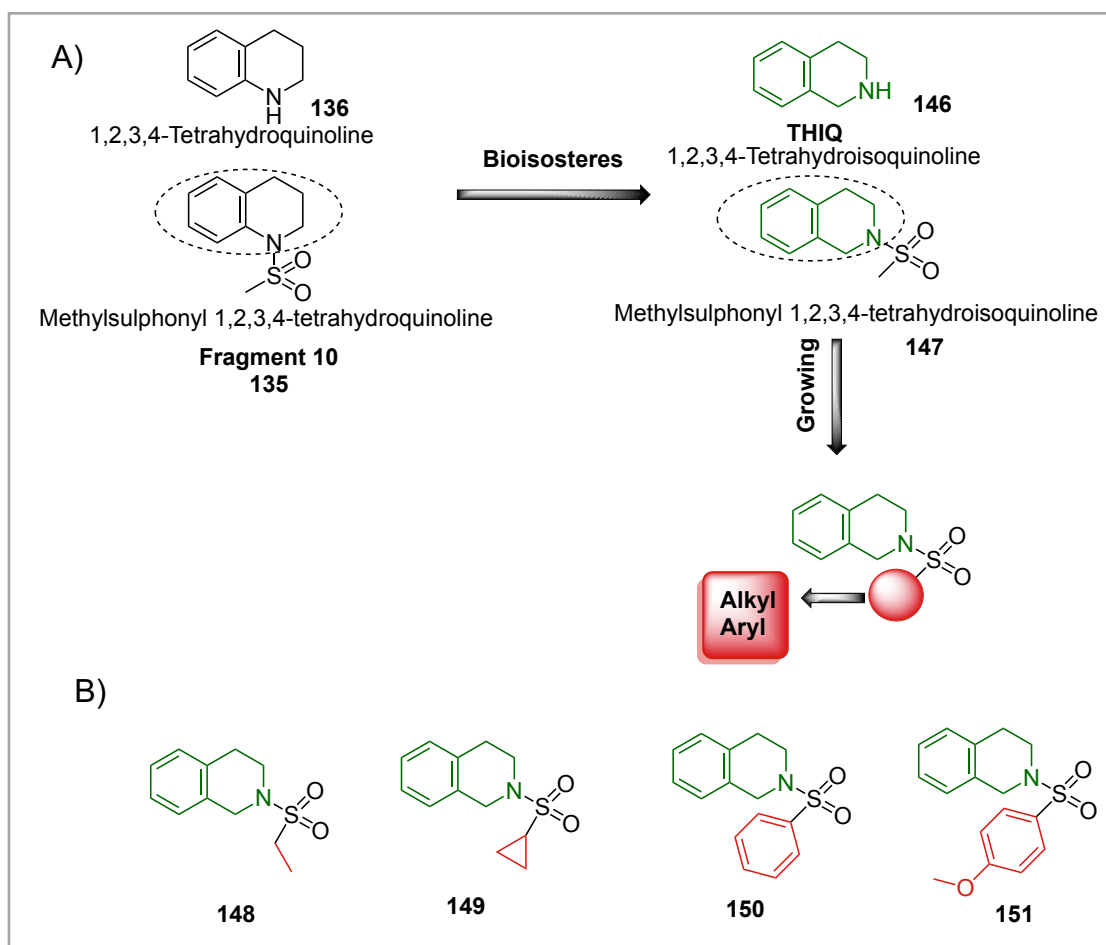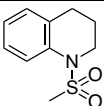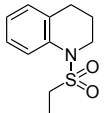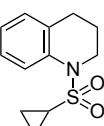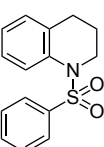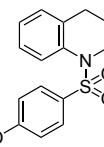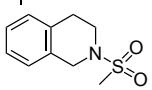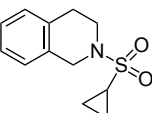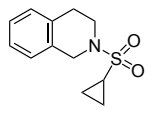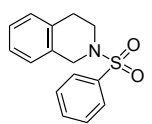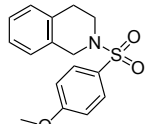
Figure 3-8 Design of sulphonyl 1,2,3,4-tetrahydroisoquinolines as fragment 10 analogues.

3.3.4.3 Docking of sulphonyl 1,2,3,4-tetrahydroquinolines and sulphonyl 1,2,3,4-tetrahydroisoquinolines

When the compounds were docked to the KifC1 protein a range of predicted binding affinities were observed from -4.43 kcal/mol to -6.53 kcal/mol. Notably, these affinities were lower (more negative) than that of methylsulphonyl-1,2,3,4-tetrahydroquinoline **135** (fragment **10**) starting point that had a calculated binding energy of -4.39 kcal/mol.

Compound **150** exhibited the most promising predicted binding affinity for KifC1, with a score of -6.53 kcal/mol (Table **3-4**). The docked conformations of **135** and **150** are shown in Figure **3-9** and Figure **3-10**.

Table 3-4 Binding affinity and interactions of fragment **10** analogue compounds with human KifC1 using AutoDock Vina.

Compound	Structure	Molecular Wight (g/mol)	H-B	Hydrophobic contacts	BA (kcal/mol)
Fragment **10** **135**		211.28	1	2	-4.39
142		225.31	2	3	-4.43
143		273.35	2	3	-5.43
144		303.38	2	2	-5.48
145		237.32	3	3	-4.84
147		225.31	2	1	-4.63
148		273.35	3	2	-4.81
149		303.38	3	1	-5.90
150		237.32	3	10	-6.53
151		211.28	3	4	-5.14

The docking scores represent the predicted binding energy of the higher ranked protein ligand complex. The hydrophobic contacts were calculated using Open Drug Discovery Toolkit and hydrogen bonds count between the ligand and protein were calculated using UCSF Chimera.

The docked conformation for compound **135** in the allosteric pocket in human KifC1 from Alphafold showed that a sulphonamide oxygen formed a hydrogen bond interaction with a water residue and the remaining sulphonamide oxygen formed a hydrogen bond interaction with Ser227 (Figure **3-9**). Additionally, the docked conformation for compound **150** with the human KifC1 Alphafold model showed that both sulphonamide oxygens formed a hydrogen bond interaction with Arg220. The nitrogen of 1,2,3,4-tetrahydroisoquinoline formed a hydrogen bond interaction with a water residue (Figure **3-10**).

The docking study was performed using the L5/α2/α3 regions of KifC1 illustrated in Figure **3-11**. Binding at this site would be uncompetitive with ATP, however the details of the binding mode will require further experimental validation.
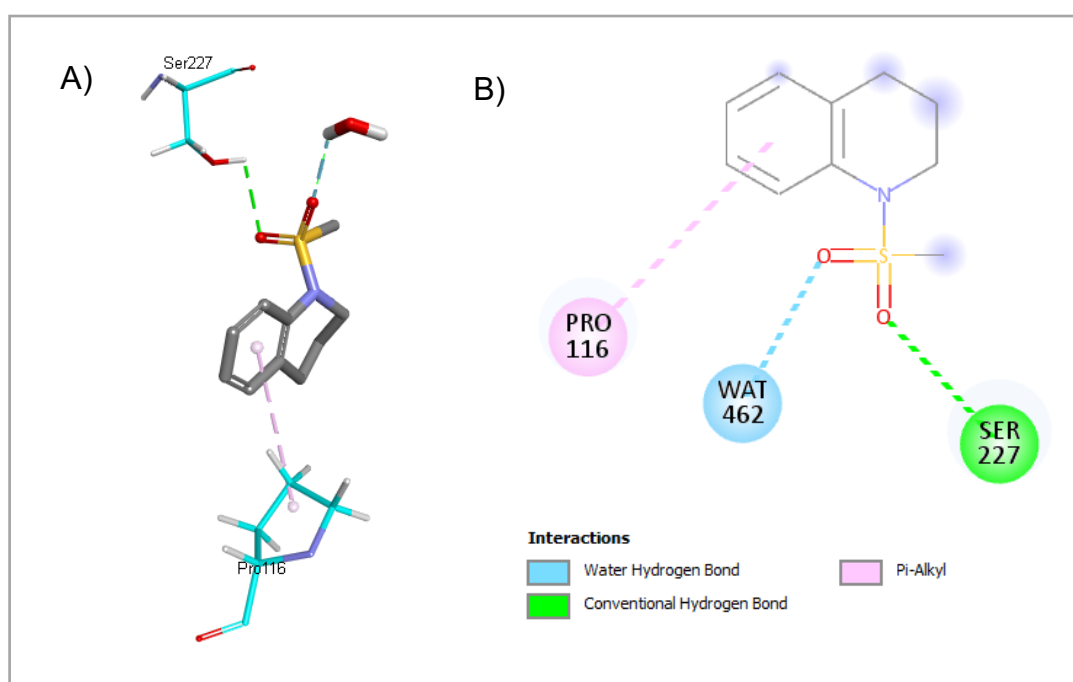
Figure 3-9 The best pose of compound **135** docked into allosteric site of the human KifC1 using AutoDock Vina: A) 3D protein and B) 2D protein - ligand interaction plots. Amino acids residues are represented as cyan thin sticks, while the ligand is shown as thick sticks with carbon atoms coloured in grey
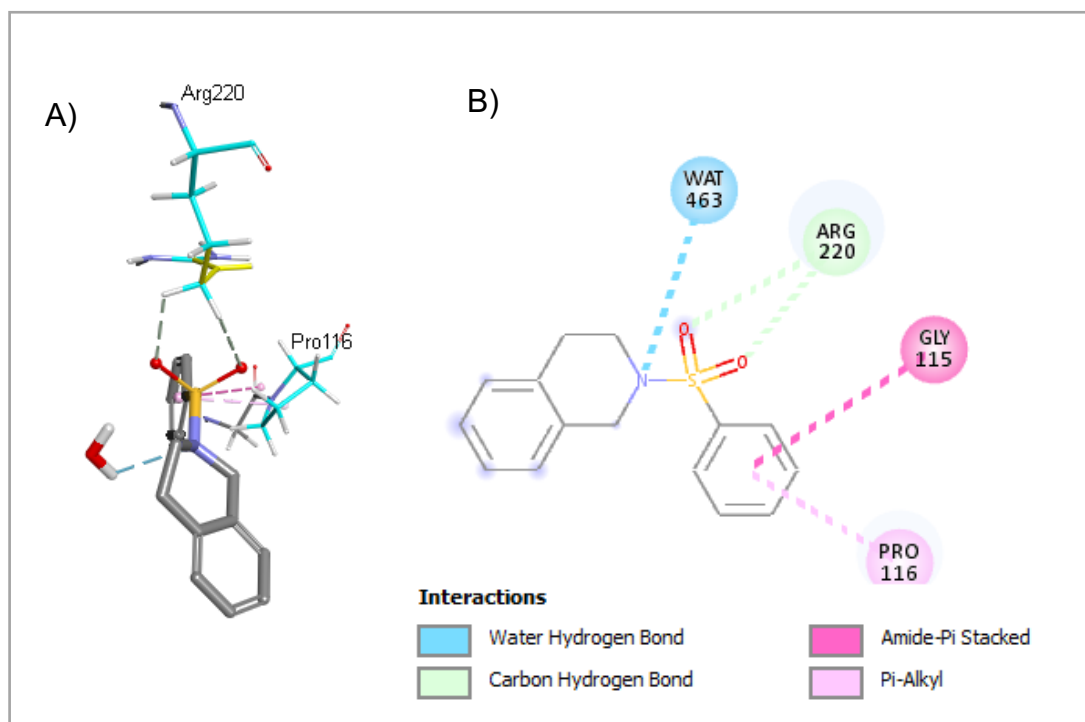
Figure 3-10 The best pose of compound **150** docked into allosteric site of the human KifC1 using AutoDock Vina: A) 3D protein and B) 2D protein - ligand interaction plots. Amino acids residues are represented as cyan thin sticks, while the ligand is shown as thick sticks with carbon atoms coloured in grey
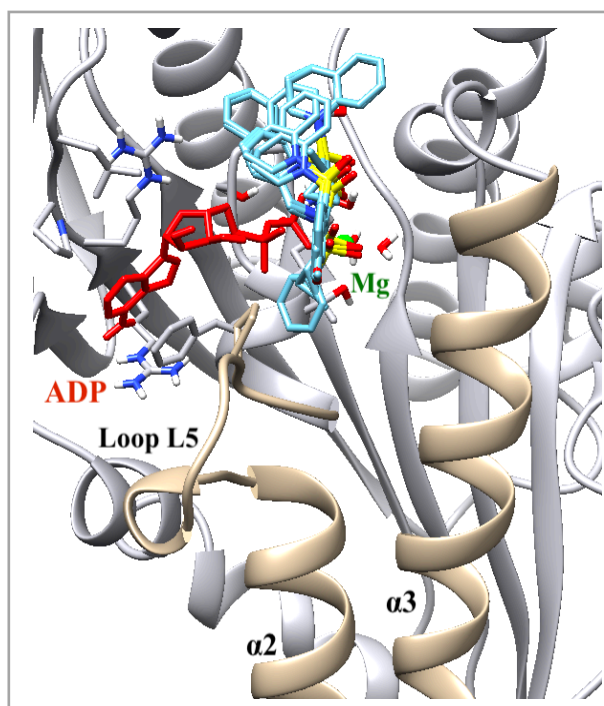
Figure 3-11 L5/α2/α3 binding pocket of human KifC1 Alphafold structure with ADP-Mg (red) and fragment **10** analogue ligands (light blue) overlaid to illustrate how they occupy the site using AutoDock Vina.

136

3.3.4.3.1 Sulfonamide synthesis of sulphonyl 1,2,3,4-tetrahydroquinolines

In order to synthesise the series of sulphonyl 1,2,3,4-tetrahydroquinolines we chose a short synthetic route that allowed us to use commercially available tetrahydroquinolines as starting materials. The reaction of 1,2,3,4-tetrahydroquinoline **135** with alkyl or aryl sulphonyl chlorides in the presence of dry pyridine at room temperature results in the formation of sulphonyl 1,2,3,4-tetrahydroquinolines in acceptable yield (26-84%) (Table **3-5**). The structures of the compounds were confirmed by ^{1}H and ^{13}C NMR spectra and LCMS, and were consistent with the expected alkyl or aryl sulphonyl 1,2,3,4-tetrahydroquinolines.

Table 3-5 General scheme for synthesis of sulphonyl 1,2,3,4 tetrahydroquinolines and percentage yield products.

R	Sulphonyl 1,2,3,4-tetrahydroquinolines	Yield %
-CH₃	**(Fragment 10)** **135**	84
-CH₂CH₃	**142**	57
(cyclopropyl)	**143**	86
(phenyl)	**144**	64
(methoxyphenyl)	**145**	26

This reaction is an addition-elimination process in which the nitrogen atom in the 1,2,3,4-tetrahydroquinoline acts as a nucleophile and reacts with the aryl or alkyl sulfonyl chloride to form a new sulphur-nitrogen bond, followed by loss of the chloride leaving group. The pyridine acts as a base, that neutralises the hydrogen chloride produced during the reaction. The reaction takes place at room temperature, although the exact reaction time and conditions can vary depending on the specific reactants and conditions used.

3.3.4.3.2 Sulfonamide synthesis of sulphonyl 1,2,3,4-tetrahydroisoquinolines

The series of sulphonyl 1,2,3,4-tetrahydroisoquinolines were synthesised using the same synthetic route that we used for the corresponding tetrahydroquinolines. The commercially availability of 1,2,3,4-tetrahydroisoquinoline makes it feasible to carry out this synthesis.

Table 3-6 General scheme for synthesis of sulphonyl 1,2,3,4-tetrahydroisoquinolines and percentage yield products.

R	Sulphonyl 1,2,3,4-tetrahydroisoquinoline	Yield %
-CH_3	**147**	89
-CH_2CH_3	**148**	40
(cyclopropyl)	**149**	61
(phenyl)	**150**	74
(4-methoxyphenyl)	**151**	42

The reaction of 1,2,3,4-tetrahydroisoquinoline with an aryl or alkyl sulphonyl chlorides in the presence of dry pyridine at room temperature results in the formation of aryl or alkyl 1,2,3,4-tetrahydroisoquinolines in acceptable yields (40-89%) (Table **3-6**) and the structures of the compounds confirmed by ^{1}H and ^{13}C NMR spectra and LCMS were consistent with the expected aryl or alkyl sulphonyl 1,2,3,4-tetrahydroisoquinolines.

3.3.4.4 Basal ATPase measurements of sulphonyl 1,2,3,4-tetrahydroquinolines and sulphonyl 1,2,3,4-tetrahydroisoquinolines
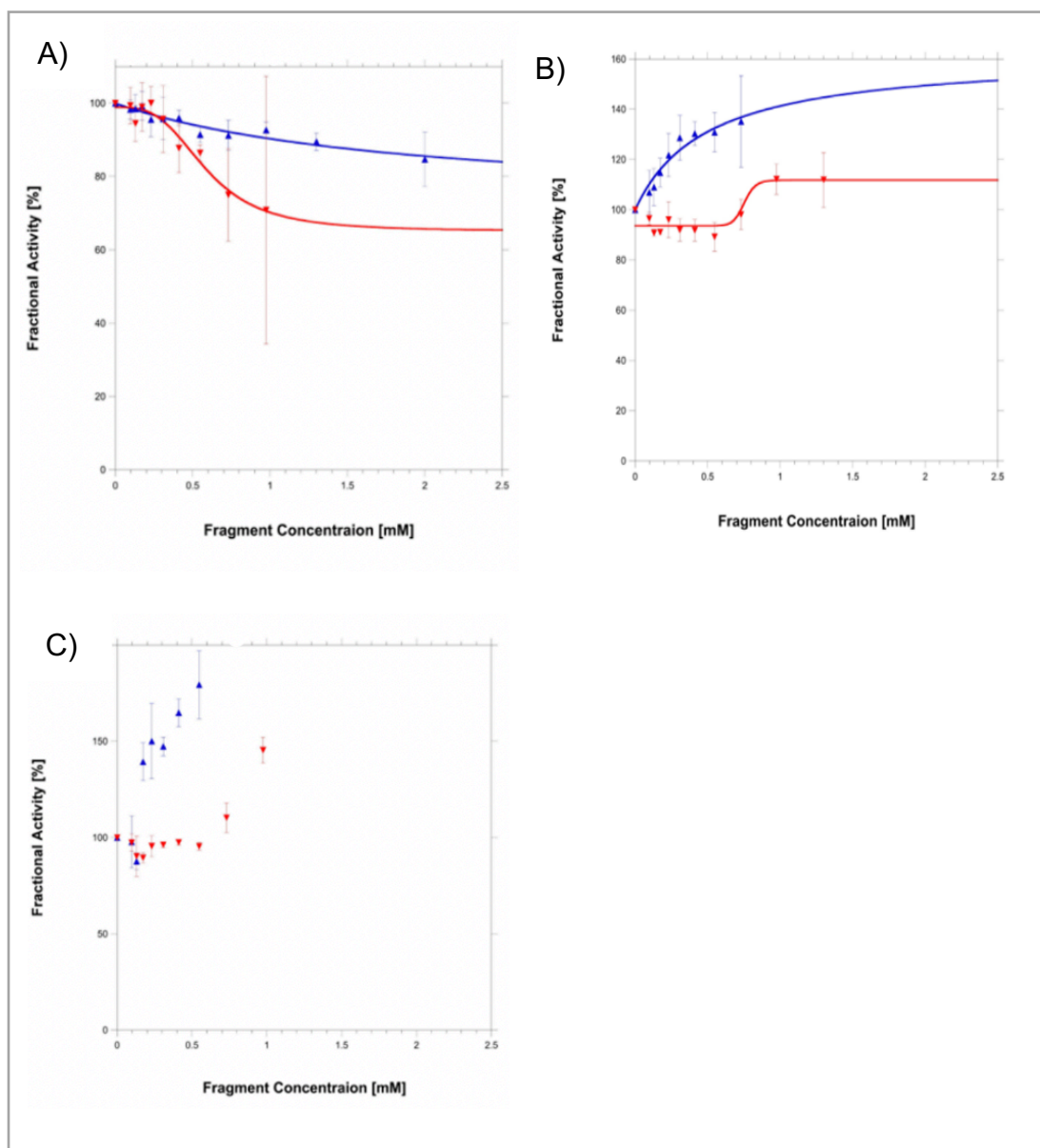
Figure 3-12 Basal ATPase activities in the presence of analogues of fragment **10**. (A) Analogues **147** (blue) and **150** (red). (B) Analogues **149** (blue) and **151** (red) show either weak inhibition or weak activation effects on KifC1.(C) Analogues **144** (blue) and *145* (red) act as agonists. Data obtained by Dr. Jiazhi Tang.

The nine KifC1 fragment analogues that were synthesised were tested by measuring the inhibition of basal KifC1 ATPase activity by Dr. Jiazhi Tang in Prof Frank Kozielski's research group. The experiments require repetition, however the preliminary data suggested that the compounds had mixed effects on the ATPase activity of KifC1. Analogues **147** and **150** appeared to marginally inhibit the basal ATPase activity of KifC1 with IC_{50} values of 1.93 ± 0.88 mM and 0.59 ± 0.13 mM, respectively (Figure **3-12** A). In contrast, analogues **149, 151, 144** and **145** analogues appeared to exert some agonist activity although the data are unclear (Figure **3-12** B-C). The poor solubility of **144** and **145**, meant that some of the higher fragment concentrations could not be measured.

3.3.5 Design, modelling, synthesis, and biological evaluation of fragment 2 and 5 analogues

3.3.5.1 Design of sulphonyl-1*H*-indole-5-carbonitriles and sulphonyl-1*H*-indole-6-carbonitriles

We designed a small series of compounds as fragment analogues based on the structure of 1H-indole-5-carbonitrile **127** (fragment **2**) and 1H-indole-6-carbonitrile **130** (fragment **5**) to synthesise (Figure **3-13** A). Using a similar approach to the previous tetrahydroisoquinoline and tetrahydroisoquinoline derivatives, the compounds were reacted with a range of alkyl or aryl sulphonyl chlorides (Figure **3 13** B). These compounds allowed the comparison of a common functionalisation route to different heterocyclic fragments discovered during the NMR screening exercise.
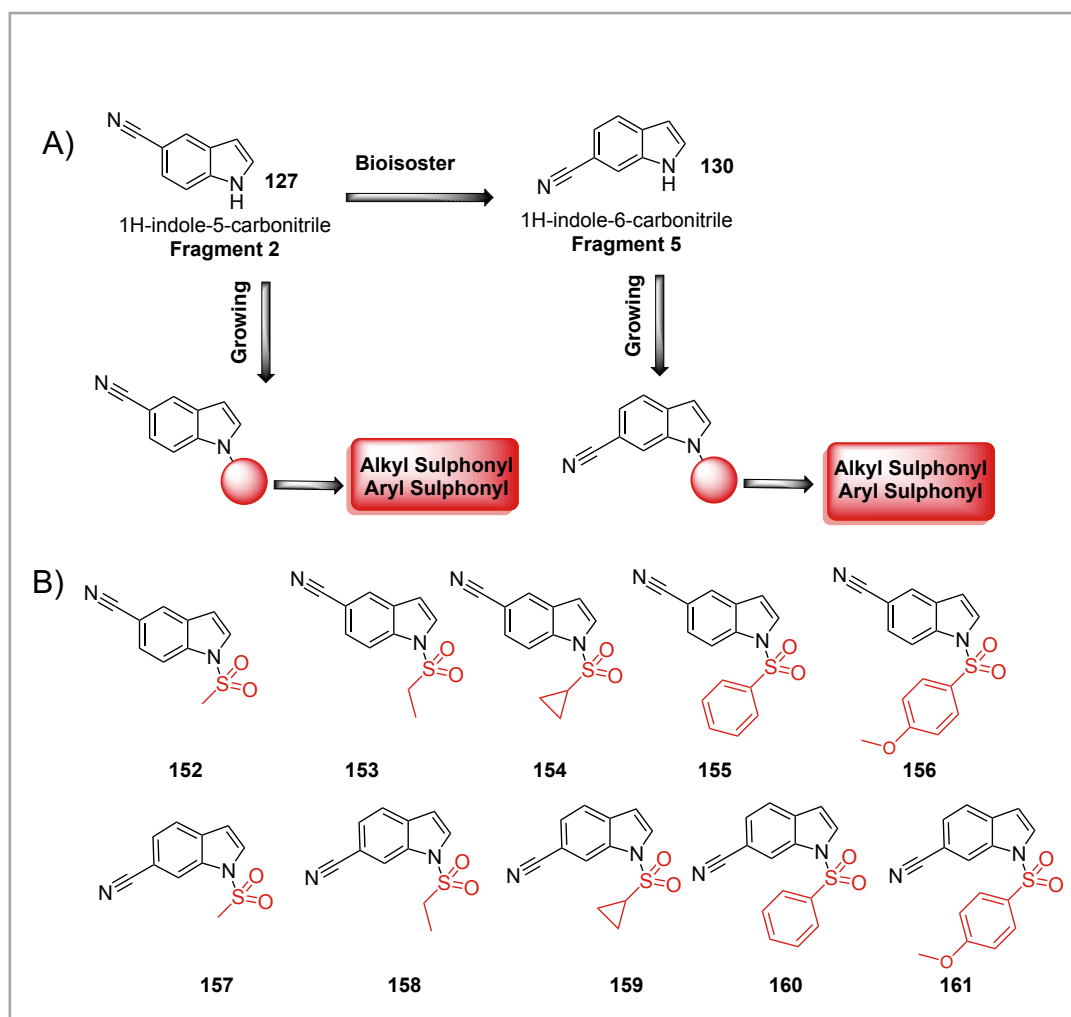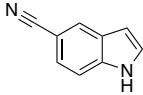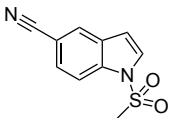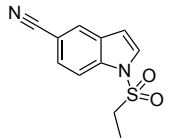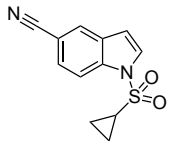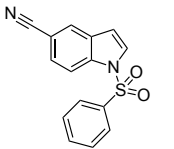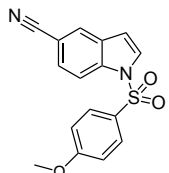
Figure 3-13 Design of sulphonyl-1H-indole-5-carbonitriles and sulphonyl-1H-indole-6-carbonitriles as fragment 2 and 5 analogues.

3.3.5.2 Docking of sulphonyl-1*H*-indole-5-carbonitriles and sulphonyl-1*H*-indole-6-carbonitriles

In the docking experiments the fragment analogues exhibited a range of predicted binding affinities to KifC1, ranging from -4.98 kcal/mol to -5.73 kcal/mol (Table **3-7**). These affinities were lower than the docking score for 1*H*-indole-5-carbonitrile **127** (fragment **2**, -3.93 kcal/mol). Compound **156** had the lowest predicted binding affinity to KifC1, with a score of -5.73 kcal/mol. The structures of the docked complexes and the docked conformations of compounds **127** and **156** are displayed in Figure **3-14** and Figure **3-15** respectively.
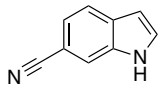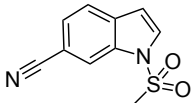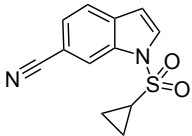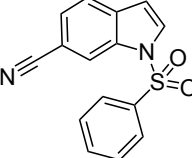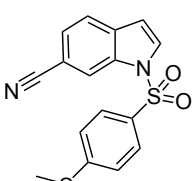
Table 3-7 Binding affinity and interactions of fragment **2** analogues with human KifC1 using AutoDock Vina.

Compound	Structure	Molecular Wight (g/mol)	H-B	Hydrophobic contacts	BE (kcal/mol)
Fragment **2** **127**		142.16	1	0	-3.93
152		220.25	2	0	-4.98
153		234.27	2	2	-5.04
154		246.28	0	0	-5.11
155		282.32	3	1	-5.44
156		312.34	3	5	-5.73

The docking scores represent the predicted binding energy of the higher ranked protein ligand complex. The hydrophobic contacts were calculated using Open Drug Discovery Toolkit and hydrogen bonds count between the ligand and protein were calculated using UCSF Chimera.

Similarly, upon docking the sulphonyl-1*H*-indole-6-carbonitriles, the fragment analogues exhibited a range of predicted binding affinities to KifC1 between -4.80 kcal/mol to -5.45 kcal/mol (Table **3-8**). These are lower scores than 1*H*-indole-6-carbonitrile **130** (fragment **5**), which had a docking score of -4.12 kCal/mol. Compound **161** displayed the lowest docking score of -5.45 kcal/mol, indicating a favourable predicted binding affinity to KifC1. The docked conformations of compounds **130** and **161** are shown in Figure **3-16** and Figure **3-17** respectively.

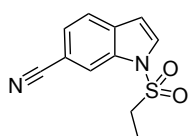**Table 3-8** Binding affinity and interactions of fragment **5** analogue*s* with human KifC1 using AutoDock Vina.

Compound	Structure	Molecular Wight (g/mol)	H-B	Hydrophobic contacts	BA (kcal/mol)
Fragment **5** **130**		142.16	2	1	-4.12
157		220.25	2	0	-4.98
158		234.27	0	0	-4.80
159		246.28	0	0	-5.13
160		282.32	2	3	-5.42
161		312.34	4	1	-5.45

The docking scores represent the predicted binding energy of the higher ranked protein ligand complex. The hydrophobic contacts were calculated using Open Drug Discovery Toolkit and hydrogen bonds count between the ligand and protein were calculated using UCSF Chimera.

The docked conformation for compound **127** with human KifC1 from Alphafold showed that the carbonitrile nitrogen formed a hydrogen bond interaction with Asn224 (Figure **3-14**).In addition, the docked conformation for compound **156** with human KifC1 from Alphafold showed that the carbonitrile nitrogen formed a hydrogen bond interaction with Glu225 and the sulphonamide oxygens formed a

hydrogen bond interaction with ADP. The oxygen of methoxyphenyl moiety formed a hydrogen bond interaction with Arg220 (Figure **3-15**).
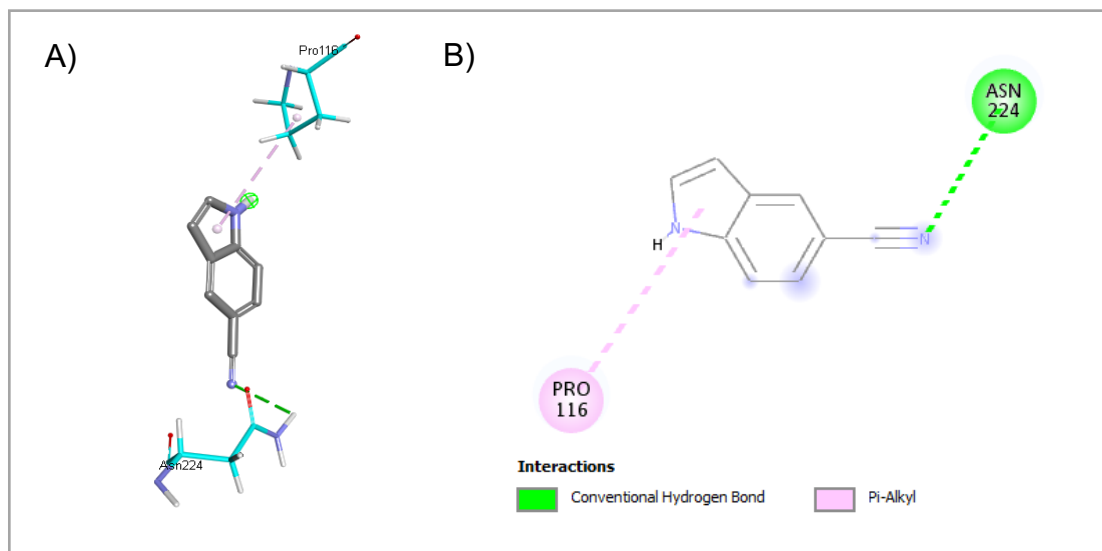
Figure 3-14 The best pose of compound **127** docked into allosteric site of the human KifC1 using AutoDock Vina: A) 3D protein and B) 2D protein - ligand interaction plots. Amino acids residues are represented as cyan thin sticks, while the ligand is shown as thick sticks with carbon atoms coloured in grey.
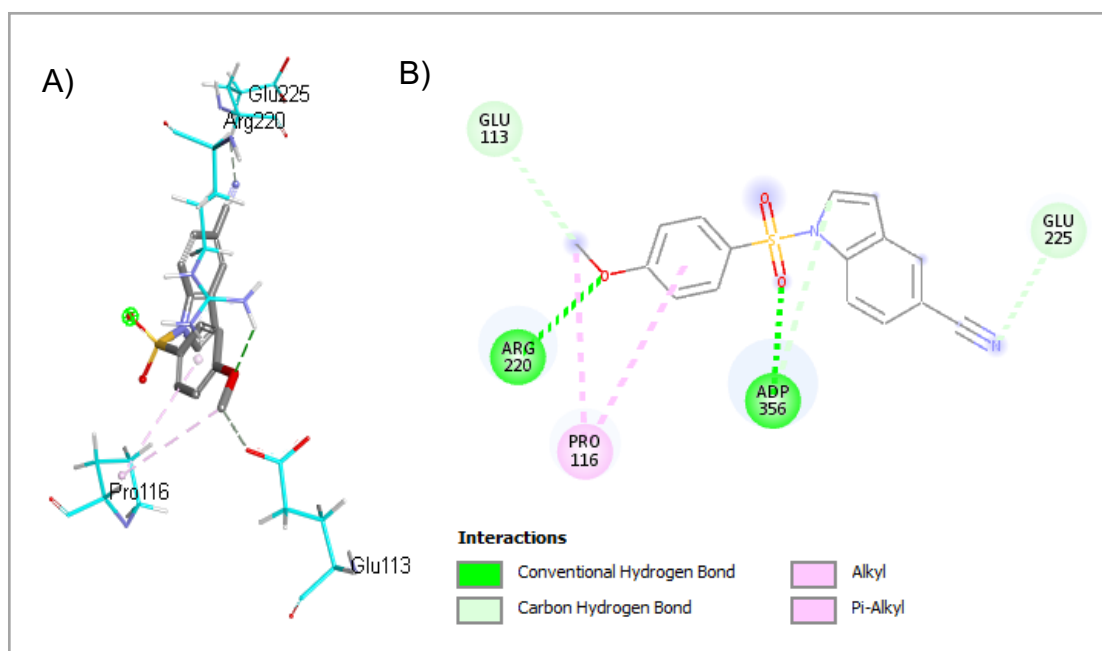
Figure 3-15 The best pose of compound **156** docked into allosteric site of the human KifC1 using AutoDock Vina: A) 3D protein and B) 2D protein - ligand interaction plots.

Amino acids residues are represented as cyan thin sticks, while the ligand is shown as thick sticks with carbon atoms coloured in grey

The docked conformation for compound **130** with human KifC1 from Alphafold showed that the indole nitrogen N1 formed a hydrogen bond interaction with Glu123 and that the indole carbon C2 formed a hydrogen bond interaction with Asp206 (Figure **3-16**). Additionally, the docked conformation for compound 161 with human KifC1 from Alphafold showed that the carbonitrile nitrogen formed a hydrogen bond interaction with ADP and the sulphonamide oxygens formed hydrogen bond interactions with Asn 224 (Figure **3-17**).
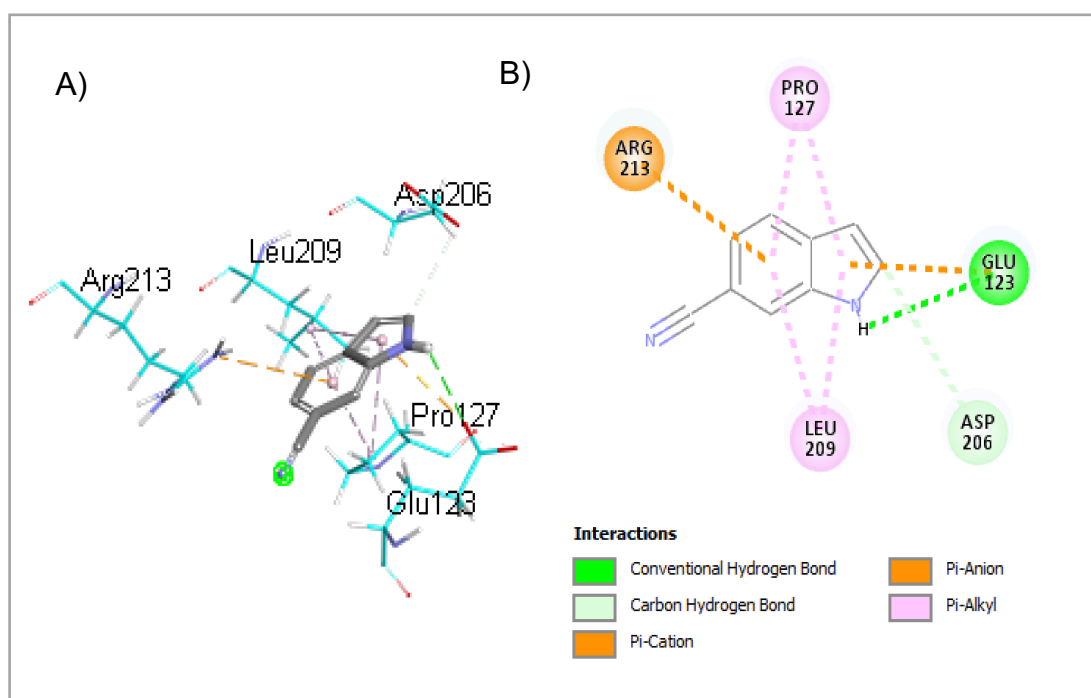
Figure 3-16 The best pose of compound **130** docked into allosteric site of the human KifC1 using AutoDock Vina: A) 3D protein and B) 2D protein - ligand interaction plots. Amino acids residues are represented as cyan thin sticks, while the ligand is shown as thick sticks with carbon atoms coloured in grey
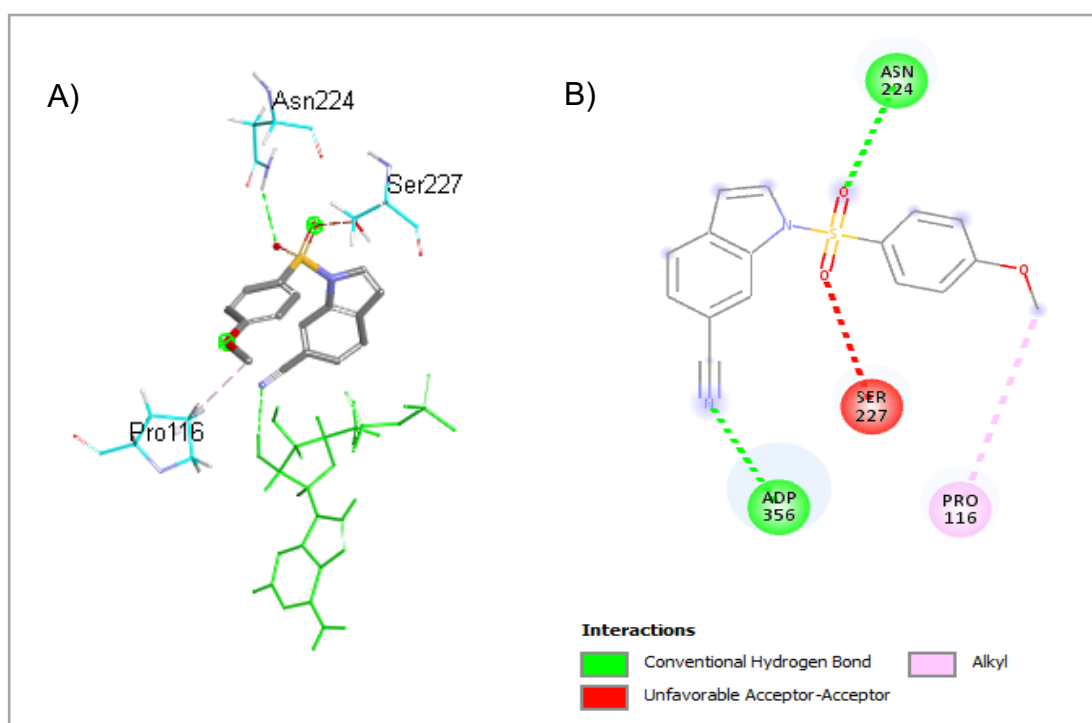
Figure 3-17 The best pose of compound **161** docked into allosteric site of the human KifC1 using AutoDock Vina: A) 3D protein and B) 2D protein - ligand interaction plots. Amino acids residues are represented as cyan thin sticks, while the ligand is shown as thick sticks with carbon atoms coloured in grey

The docking study was performed using the L5/α2/α3 regions of KifC1 illustrated in (Figure **3-18**). As noted previously, binding at this site would be uncompetitive with ATP, however the details of the binding mode will require further experimental validation.

.
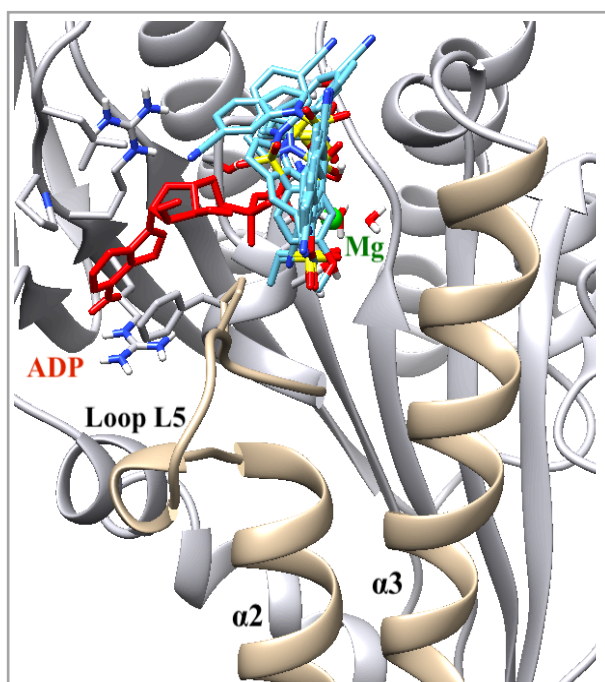
Figure 3-18 L5/α2/α3 binding pocket of human KifC1 Alphafold structure with ADP-Mg (red) fragment **2** and **5** analogue ligands (light blue) overlaid to illustrate how they occupy the site using AutoDock Vina.

3.3.5.3 Sulfonamide synthesis of sulphonyl-1*H*-indole-5-carbonitriles and sulfonyl-1*H*-indole-6-carbonitriles

The reaction of carbonitrile indoles (1H-indole-5-carbonitrile or 1H-indole-6-carbonitrile) with substituted sulphonyl chlorides was carried out under phase transfer conditions using a toluene and aqueous sodium hydroxide solvent mixture and tetrabutylammonium hydrogen sulphate (TBAHS) as the phase transfer catalyst. The substituted sulphonyl carbonitrile indoles were isolated in low to moderate yields (19-44%). Substantial amounts of unreacted starting material remained at the end of each reaction. Attempts to vary the conditions of the reaction (e.g., reaction temperature, order of addition of reagents) did not lead to improved yields (Table **3-9** and Table **3-10**). The structures of the compounds confirmed by ^{1}H and ^{13}C NMR spectra and LCMS were consistent with the expected substituted sulphonyl carbonitrile indoles.

Table 3-9 General scheme for synthesis of sulphonyl-1*H*-indole-5-carbonitriles and percentage yield products.

R	Sulphonyl-1*H*-indole-5-carbonitrile	Yield %
$-CH_3$	152	24
$-CH_2CH_3$	153	20
(cyclopropyl)	154	23
(phenyl)	155	24
(4-methoxyphenyl)	156	41

Table 3-10 General scheme for synthesis of sulphonyl-1*H*-indole-6-carbonitriles and percentage yield products.

R	Sulphonyl-1*H*-indole-6-carbonitrile	Yield %
$-CH_3$	157	28
$-CH_2CH_3$	158	24
(cyclopropyl)	159	19
(phenyl)	160	29
(4-methoxyphenyl)	161	44

3.3.5.4 Basal ATPase measurements of sulphonyl-1*H*-indole-5-carbonitriles and sulphonyl-1*H*-indole-6-carbonitriles as fragment 2 and 5 analogues
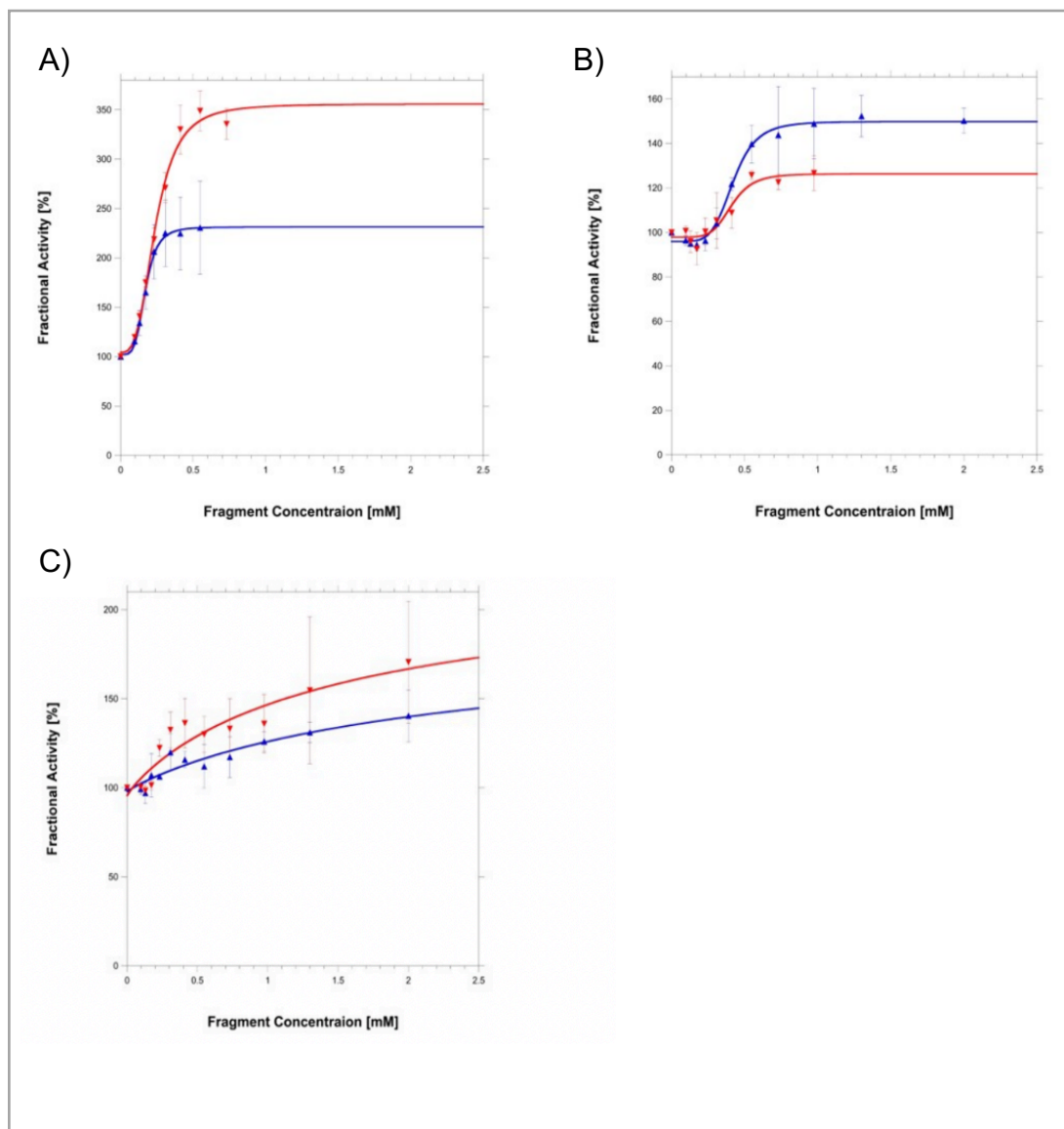
Figure 3-19 Basal ATPase activities in the presence of analogues of fragment **2** and **5**. Six analogues demonstrated activation effects on KifC1 **152**,**155** and**156** are isomers of **157**,**160** and**161** and thus separated into three panels (A), (B) and (C) for comparison (A), (B) Analogues **152** (blue) ,**155** (red) , **157** (blue) and **160** (red) increased the basal ATPase activity of KifC1 in a sigmoidal pattern. (C) The ATPase curves of **156** (blue) and **161** (red) are atypical, indicating that their IC50 values are questionable. Data obtained by Dr. Jiazhi Tang.

Both fragments **2** and **5** did not illustrate inhibition in the basal ATPase measurements. However, there were six KifC1 analogues that illustrated agonist activities in the basal ATPase assay. Analogues **152** and **157** increased the basal ATPase activity of KifC1 by more than 200%, with EC_{50}s of 0.17 ± 0.01 mM and 0.24 ± 0.01 mM, respectively (Figure **3-19** A). Analogues **155** and **160** increased the basal ATPase activity of KifC1 to a lesser extent (120-140% of control activity) with EC_{50}s of 0.42 ± 0.01 mM and 0.41 ± 0.04 mM, respectively (Figure **3-19** B). Analogues **156** and **161** showed a trend towards increasing the basal ATPase activity of KifC1, however the relatively large errors in the data indicate that the ATPase activity curves are atypical (Figure **3-19** C). The ATPase data of the analogues indicated that adding 1-sulphonyl substituents to the 1H-indole-5-carbonitrile and 1H-indole-6-carbonitrile (fragments **2** and **5**) scaffolds increases the binding affinities of the analogues **152** and **157**. However, any large sulphonyl substituents, for example, benzenesulphonyl **155** and **160**, appear to compromise the binding activity.

3.3.6 Design, synthesis, modelling, and biological evaluation of fragment 6 analogues

3.3.6.1 Design of 5-arylisoxazol-3-amines

5-(*tert*-Butyl)isoxazol-3-amine, fragment **6**, is a chemical compound that belongs to the class of isoxazole derivatives. Isoxazole is a type of heterocyclic compound that contains a five-member ring with three carbons atoms and one oxygen and one nitrogen atom (Figure **3-20** A). We developed a set of analogues using the structure of 5-(*tert*-butyl)isoxazol-3-amine **131** (fragment **6**), as a starting point. Our initial goal was to synthesize compounds with substituents that replaced the t-butyl group in the molecule. To achieve this, we utilized an approach to synthesise the isoxazole heterocycle starting from hydroxylamine sulphate and a range of commercially available aryl acetonitriles (Figure **3-20** B).

150
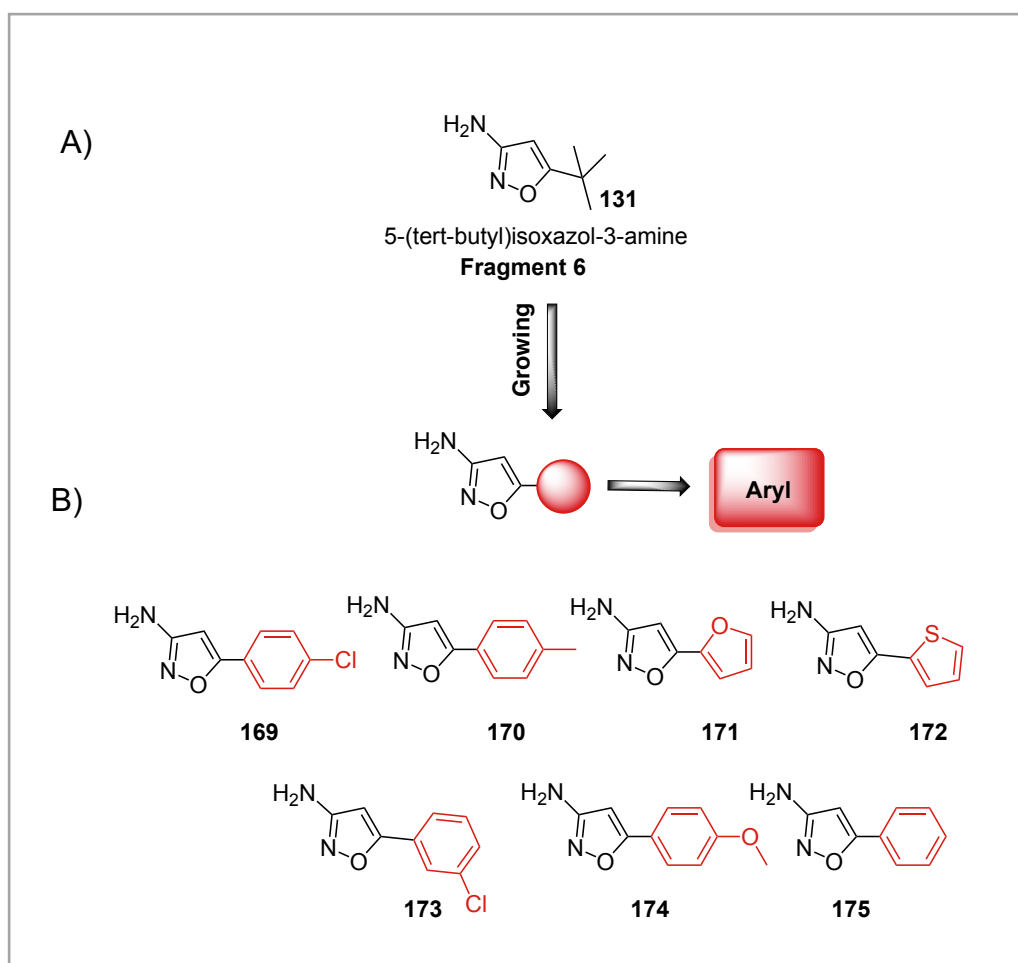
Figure 3-20 Design of 5-arylisoxazol-3-amines as fragment **6** analogues.

3.3.6.2 Design and synthesis of 5-arylpyrazol-3-amines

Due to the similarity of pyrazole and isoxazole, both are five-membered nitrogen-containing heterocyclic compounds, with similar molecular formulas and structural features, we also synthesised several pyrazole derivatives of fragment **6** with the same array of *tert*-butyl replacements (Figure **3-21** A) [150]. A short synthetic route to 5-(*tert*-butyl)pyrazol-3-amine and its analogues was chosen that was similar to that used for the isoxazole derivatives (Figure **3-21** B).
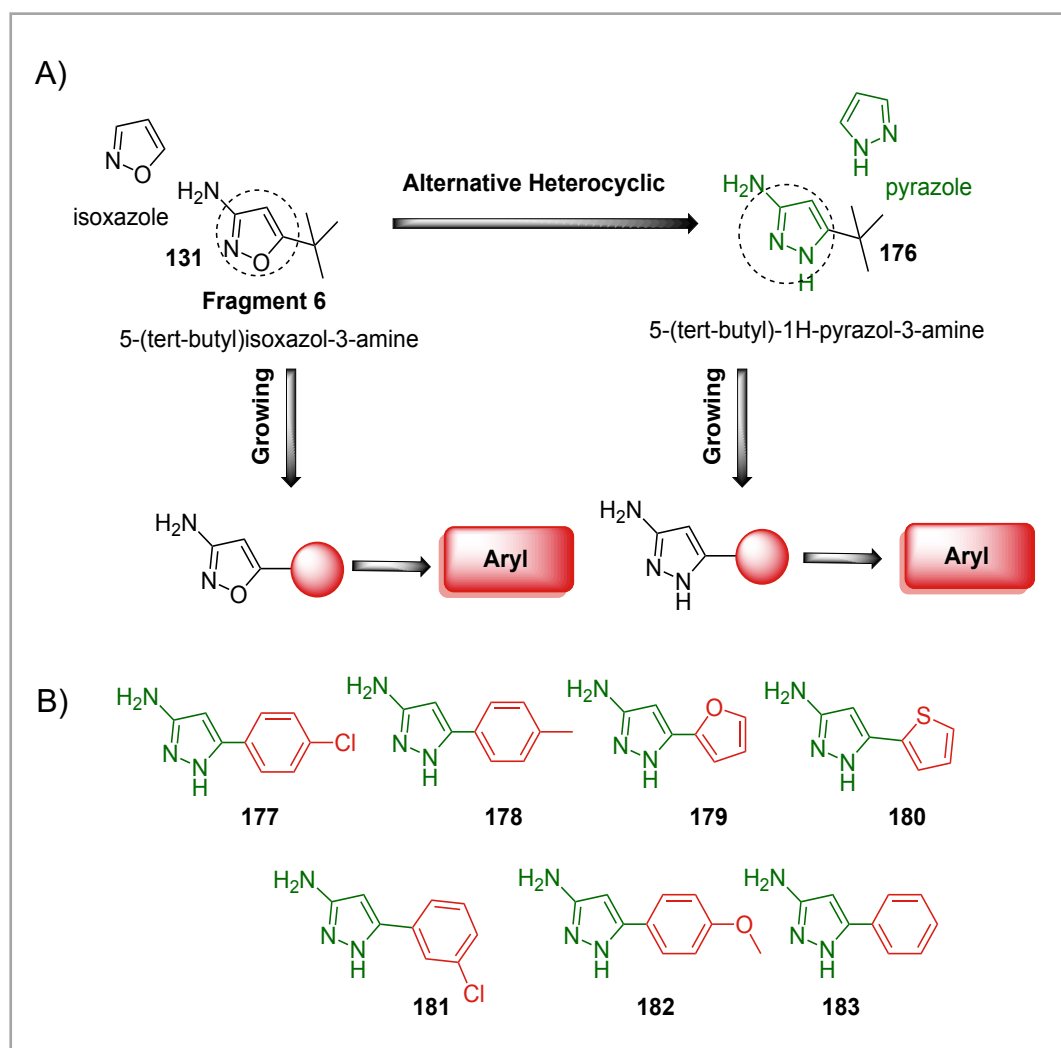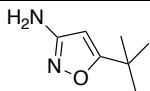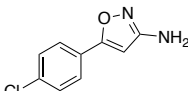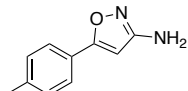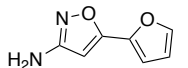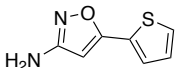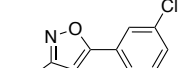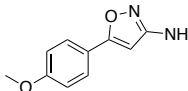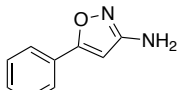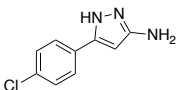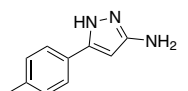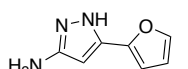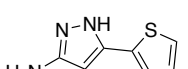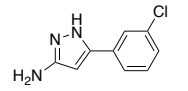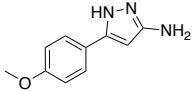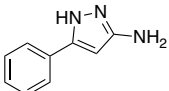
Figure 3-21 Design of 5-arylisoxazol-3-amines as fragment **6** analogues.

3.3.6.3 Docking of 5-arylisoxazol-3-amines and 5-arylpyrazole-3-amines

In the docking experiments fragment **6** analogues displayed a range of predicted binding affinities to KifC1, ranging from -4.37 kcal/mol to -5.04 kcal/mol (Table **3-11**). These affinities were lower than that of 5-(*tert*-butyl)isoxazol-3-amine **131** (fragment **6**), which had a docking score of -4.34 kcal/mol. Notably, compound **181** exhibited the lowest BE score with a predicted binding affinity to KifC1 of -5.04 kcal/mol. The docked docked conformations of compounds **131** and **181** are shown in Figure **3-22** and Figure **3-23** respectively.

Table 3-11 Binding affinity and interactions of fragment **6** analogue compounds with human KifC1 using AutoDock Vina.

Compound	Structure	Molecular Wight (g/mol)	H-B	Hydrophobic contacts	BA (kcal/mol)
Fragment 6 131		140.19	6	1	-4.34
169		194.62	4	2	-4.93
170		174.20	4	2	-4.97
171		150.14	4	2	-4.73
172		166.20	2	0	-4.56
173		194.62	1	1	-4.98
174		190.20	3	4	-5.02
175		160.18	2	6	-4.86
177		193.63	3	2	-4.88
178		173.22	1	6	-4.83
179		149.15	3	2	-4.67
180		165.21	1	0	-4.37
181		193.63	3	1	-5.04

Compound	Structure	Molecular Wight (g/mol)	Hydrogen bond	Hydrophobic contacts	BA (kcal/mol)
182		189.22	4	2	-4.96
183		159.19	2	10	-5.03

The docking scores represent the predicted binding energy of the higher ranked protein ligand complex. The hydrophobic contacts were calculated using Open Drug Discovery Toolkit and hydrogen bonds count between the ligand and protein were calculated using UCSF Chimera.

As illustrated in (Figure **3-22**), the docking of compound **131** with KifC1 showed that the isoxazole oxygen O1 established a hydrogen bond interaction with Gly105, whereas the isoxazole N2 nitrogen was in close proximity to the bound ADP. When compound **181** was docked with KifC1, the resulting conformation indicated that the pyrazole N1 nitrogen established a hydrogen bond interaction with ADP, and the pyrazole nitrogen N2 formed a hydrogen bond interaction with a water residue (Figure **3-23**). Furthermore, the docking study was performed using the L5/α2/α3 regions of KifC1 illustrated in Figure **3-24**. As noted previously, binding at this site would be uncompetitive with ATP, however the details of the binding mode will require further experimental validation.
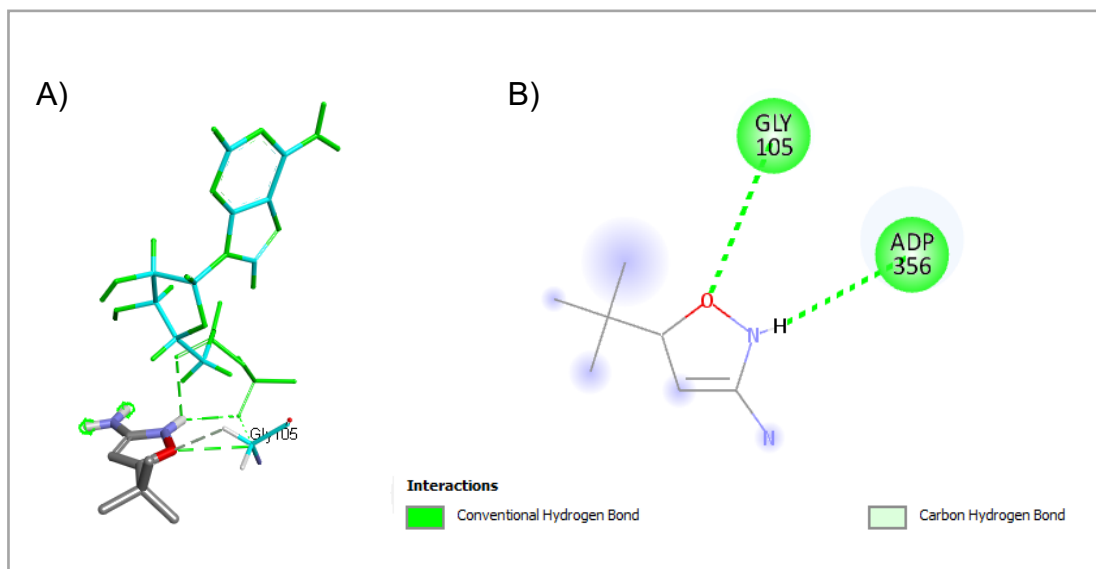
Figure 3-22 The best pose of compound 1**31** docked into allosteric site of the human KifC1 using AutoDock Vina: A) 3D protein and B) 2D protein - ligand interaction plots. Amino acids residues are represented as cyan thin sticks, while the ligand is shown as thick sticks with carbon atoms coloured in grey.
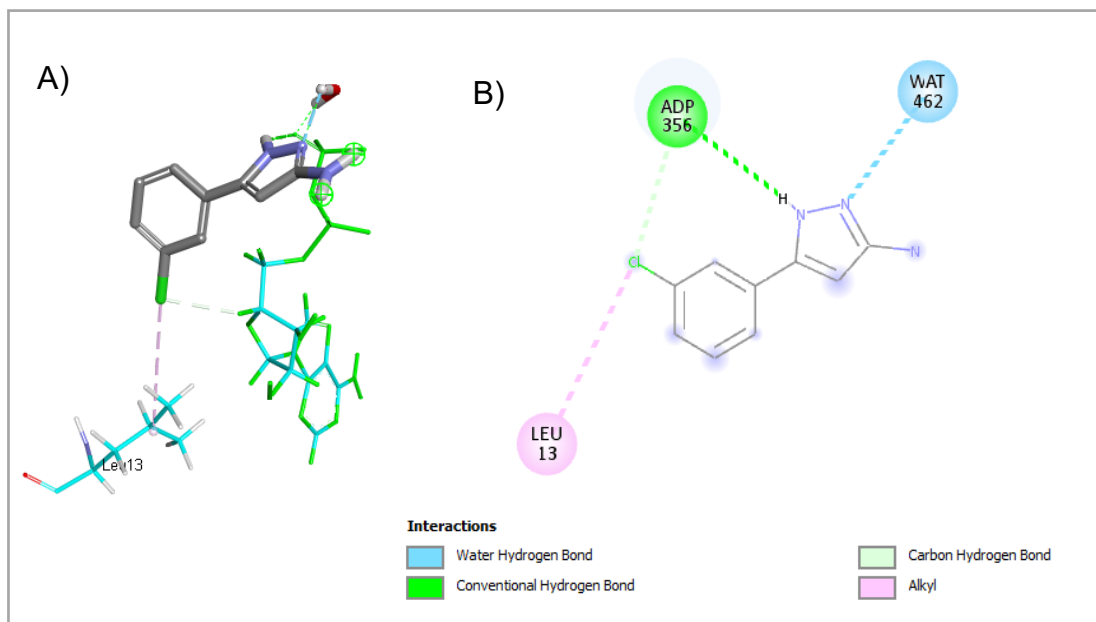
Figure 3-23 The best pose of compound **181** docked into allosteric site of the human KifC1 using AutoDock Vina: A) 3D protein and B) 2D protein - ligand interaction plots. Amino acids residues are represented as cyan thin sticks, while the ligand is shown as thick sticks with carbon atoms coloured in grey.
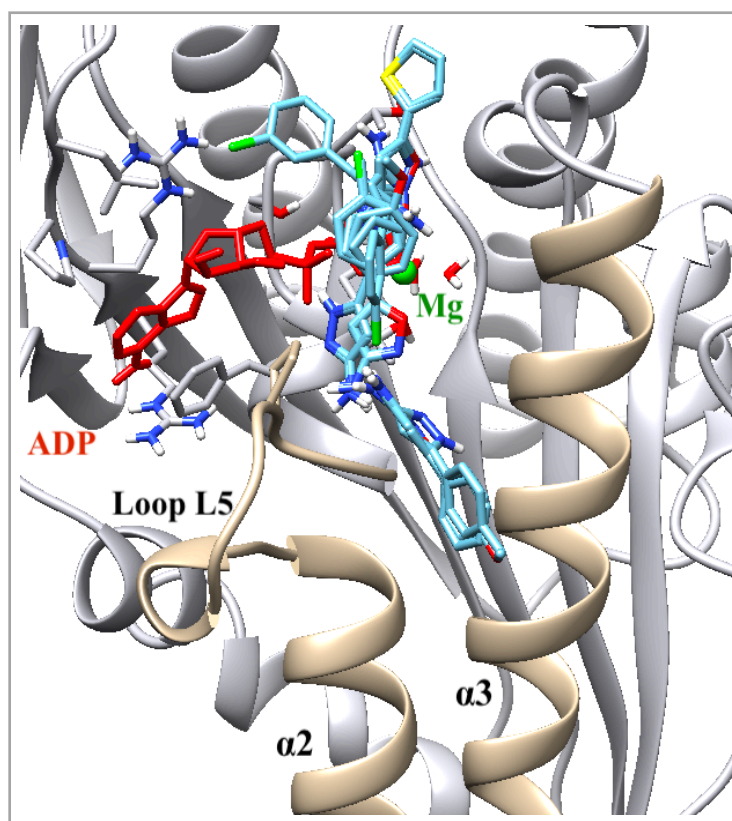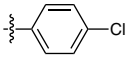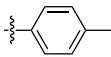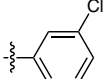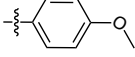
Figure 3-24 L5/α2/α3 binding pocket of human KifC1 Alphafold structure with ADP-Mg (red) and fragment **6** analogue (light blue) ligands overlaid to illustrate how they occupy the site using AutoDock Vina.

3.3.6.3.1 Isoxazole synthesis of 5-arylisoxazol-3-amines

To synthesize the 5-arylisoxazol-3-amines, acylacetonitriles were reacted with hydroxylamine sulphate in the presence of sodium hydroxide (NaOH). The reaction mechanism involves the nucleophilic attack of hydroxylamine on the acyl acetonitrile, leading to the formation of an intermediate N-hydroxyamidine, which then undergoes cyclization in the presence of HCl. This process yields substituted 5-aryl isoxazol-3-amines with a range of yields between 50-73% (Table **3-12**). Careful control of the reaction pH is required (pH < 8) because at pH values of ~9.5 and at higher temperatures (100°C cf. 45°C) the corresponding 5-aminoisoxazoles can be formed. The ^{1}H and ^{13}C NMR spectra and LCMS were used to confirm the structures of the compounds, which were consistent with the expected isoxazol-3-amines [151].
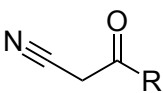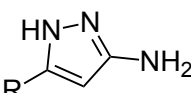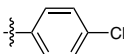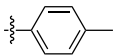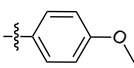
Table 3-12 General scheme for synthesis of 5-arylisoxazol-3-amines and percentage yield products.

R	Arylisoxazol-3-amines	Yield %
(4-Cl-phenyl)	169	57
(4-methyl-phenyl)	170	72
(furan-2-yl)	171	66
(thiophen-2-yl)	172	Product not isolated
(3-Cl-phenyl)	173	50
(4-methoxy-phenyl)	174	54
(phenyl)	175	73

3.3.6.3.2 Pyrazole synthesis of 5-arylpyrazol-3-amines

A group of 5-arylpyrazole-3-amine derivatives were synthesised by replacing the hydroxylamine sulphate with hydrazine sulfate in the reaction of the same aryl acetonitriles used to produce 5-arylisoxazol-3-amines. The substituted 5-arylpyrazole-3-amines were obtained using the pyrazole synthesis method, with yields ranging from 49-67% (Table **3-13**). The structures of the compounds were confirmed through ^{1}H and ^{13}C NMR spectra and LCMS, which were consistent with the expected 3-aminopyrazoles.

Table 3-13 General scheme for synthesis of 3-amino-5-arylisoxazoles and percentage yield products.

R	Arylpyrazol-3-amines	Yield %
	177	49
	178	74
	179	67
	180	Product not isolated
	181	62
	182	75
	183	68

3.5.6. Basal ATPase measurements of 5-arylisoxazol-3-amines and 5-arylpyrazole-3-amines as fragment 6 analogues

Due to time constraints, and the availability of KifC1 protein, the compounds could not be tested during the project.

3.3.7 Design, synthesis, modelling, and biological evaluation of fragment 9 analogues

3.3.7.1 Design of 2-amino-benzamides

Fragment **9**, 5-Chloro-2-(methylamino)benzamide **134**, is a chemical compound that belongs to the class of benzamide derivatives (Figure **3-25** A). Benzamides are a subclass of amides that contain a benzene ring and a nitrogen atom bonded

to a carbonyl group. Some benzamides have been studied for their potential anti-cancer properties. For example, some benzamides have been found to have anti-tumour effects by blocking the activity of enzymes involved in cell growth and division or by inducing cell death [152].

A series of fragment analogues based on 5-chloro-2-(methylamino)benzamide **143** (fragment **9**) were designed to explore the structure activity relationships relating to the amide, amine, and halogen substituents. The compounds could be made by forming amides of the corresponding 2-nitrobenzoic acids followed by reduction of the nitro group to make a range of derivatives of fragment **9** (Figure **3-25** B). Additional derivatives could be accessed by carrying out Suzuki coupling reactions on the bromobenzamide derivatives.
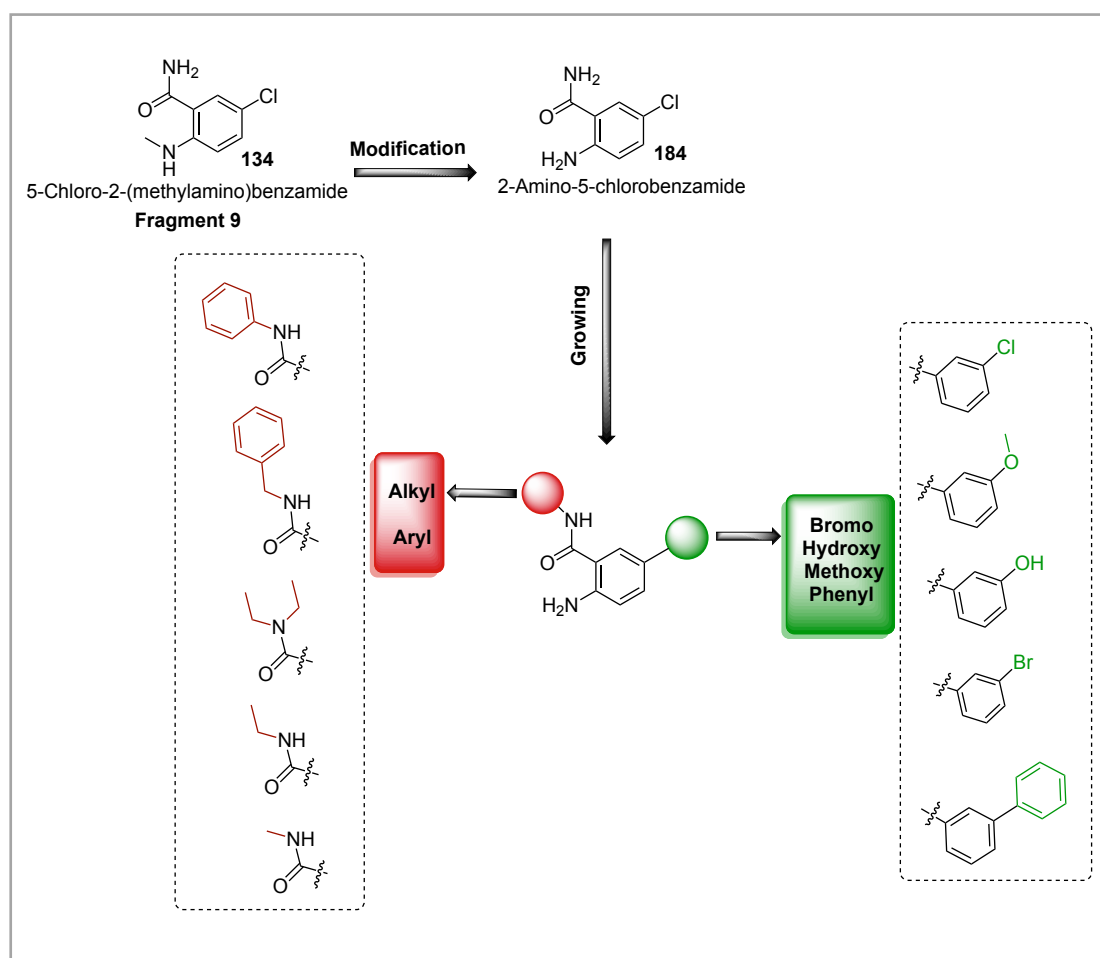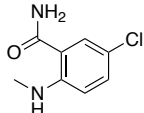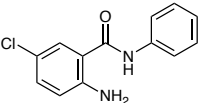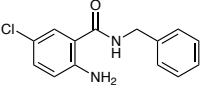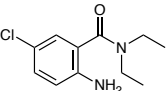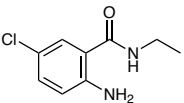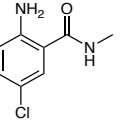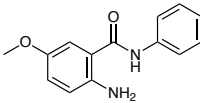
Figure 3-25 Design of 2-amino-benzamides as fragment **9** analogues

3.3.7.2 Docking of 2-amino-benzamides
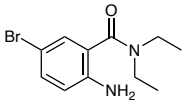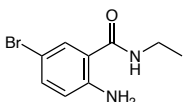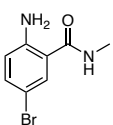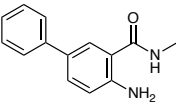
Molecular docking of the fragment analogues to KifC1 gave a range of predicted binding affinities from -4.61 kcal/mol to -6.26 kcal/mol (Table **3-14**). The scores were lower that for 5-chloro-2-(methylamino)benzamide **134** (Fragment **9**, -4.66 kcal/mol). Compound **226** had the lowest predicted binding affinity to KifC1 of -6.26 kcal/mol. The docked conformations of compounds **134** and **226** are shown in (Figure **3-27** and Figure **3-28**).

Table 3-14 Binding affinity and interactions of fragment **9** analogue compounds with human KifC1 using AutoDock Vina.

Compound	Structure	Molecular Wight (g/mol)	H-B	Hydrophobic contacts	BA (kcal/mol)
Fragment 9 **134**		184.62	2	2	-4.66
210		246.69	3	9	-6.14
211		260.72	3	12	-6.24
212		226.70	3	3	-4.77
213		198.65	4	2	-4.72
214		184.62	3	1	-4.61
215		242.28	3	9	-6.01

Compound	Structure	Molecular Wight (g/mol)	H-B	Hydrophobic contacts	BA (kcal/mol)
216		256.31	3	12	-6.20
217		222.29	3	3	-4.69
218		194.23	4	2	-4.78
219		180.21	2	1	-4.50
220		228.25	2	9	-6.19
221		242.28	3	12	-6.11
222		208.26	2	3	-4.61
223		180.21	4	1	-4.63
224		166.18	3	0	-4.33
225		291.15	3	9	-6.13
226		305.18	3	12	-6.26

Compound	Structure	Molecular Wight (g/mol)	H-B	Hydrophobic contacts	BA (kcal/mol)
227		271.16	2	3	-4.76
228		243.10	3	2	-4.84
229		229.08	3	1	-4.63
231		180.43	4	3	-5.60

The docking scores represent the predicted binding energy of the higher ranked protein ligand complex. The hydrophobic contacts were calculated using Open Drug Discovery Toolkit and hydrogen bonds count between the ligand and protein were calculated using UCSF Chimera.

The docked conformation of compound **134** with human KifC1 Alphafold model revealed that the benzamide nitrogen formed a hydrogen bond with Gly115. Additionally, the chloro group at C5 formed was in close proximity with Arg213 (Figure **3-26**). Upon docking compound **226** with human KifC1 Alphafold model, the benzamide oxygen formed a hydrogen bond interaction with Ser227 and a water residue, and the amino group at C2 formed a hydrogen bond interaction with ADP (Figure **3-27**).

Figure 3-26 The best pose of compound **134** docked into allosteric site of the human KifC1 using AutoDock Vina: A) 3D protein and B) 2D protein - ligand interaction plots. Amino acids residues are represented as cyan thin sticks, while the ligand is shown as thick sticks with carbon atoms coloured in grey.

Figure 3-27 The best pose of compound **226** docked into allosteric site of the human KifC1 using AutoDock Vina: A) 3D protein and B) 2D protein - ligand interaction plots. Amino acids residues are represented as cyan thin sticks, while the ligand is shown as thick sticks with carbon atoms coloured in grey.

The docking study was performed using the L5/α2/α3 regions of KifC1 illustrated in (Figure **3-28**). As noted previously, binding at this site would be uncompetitive with ATP, however the details of the binding mode will require further experimental validation.
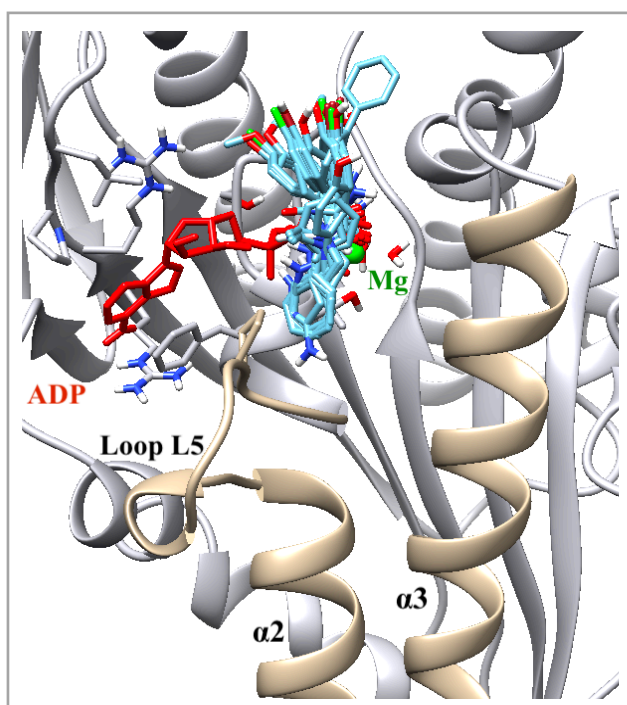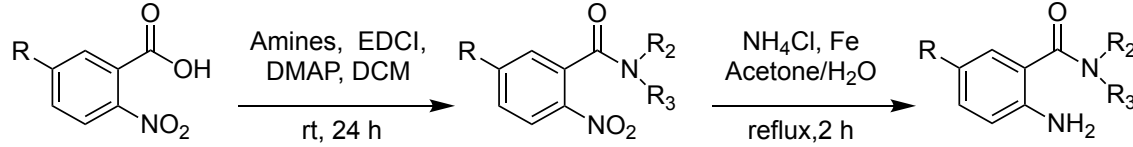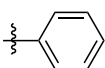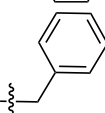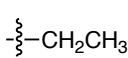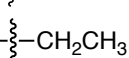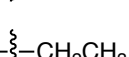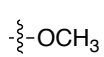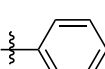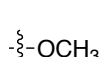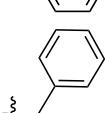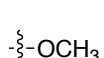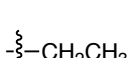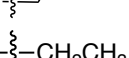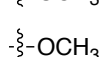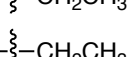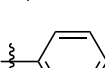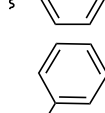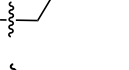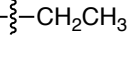
Figure 3-28 L5/α2/α3 binding pocket of human KifC1 Alphafold structure with ADP-Mg (red) and fragment **9** analogue ligands (light blue) overlaid to illustrate how they occupy the site using AutoDock Vina.

3.3.7.2.1 Synthesis of 2-aminobenzamides using amide derivatives of anthranilic acids

The synthesis of 2-aminobenzamides involves a two-step process starting from 2-nitrobenzoic acids. In the first step, the acids are coupled with amines, such as aniline, benzylamine, diethylamine, ethylamine hydrochloride, or methylamine hydrochloride, using 1-(3-dimethylaminopropyl)-3-ethylcarodiimide hydrochloride (EDCI) and 4-(dimethylamino)pyridine (DMAP) as a base. This reaction yielded a series of amide derivatives in 9-86% isolated yields and is compatible with a wide range of functional groups. The structures of the compounds were confirmed by ^{1}H and ^{13}C NMR spectra and LCMS. In the second step, the nitro

group in the 2-nitrobenzamides is reduced to an amino group using a combination of iron (Fe) and ammonium chloride (NH_4Cl), resulting in 2-aminobenzamides in 11-87% isolated yields in (Table **3-15**) . The structures of the compounds were confirmed by ^1H and ^{13}C NMR spectra and LCMS.

Table 3-15 General scheme for synthesis of 2-aminobenzamides.

R	R₂	R₃	2-Nitro benzamides	Yield %	2-Amino benzamides	Yield %
Cl	H	phenyl	**190**	69	**210**	25
Cl	H	benzyl	**191**	59	**211**	74
Cl	-CH₂CH₃	-CH₂CH₃	**192**	37	**212**	73
Cl	H	-CH₂CH₃	**193**	44	**213**	64
Cl	H	-CH₃	**194**	35	**214**	81
-OCH₃	H	phenyl	**195**	48	**215**	27
-OCH₃	H	benzyl	**196**	25	**216**	19
-OCH₃	-CH₂CH₃	-CH₂CH₃	**197**	28	**217**	73
-OCH₃	H	-CH₂CH₃	**198**	29	**218**	60
-OCH₃	H	-CH₃	**199**	43	**219**	73
-OH	H	phenyl	**200**	54	**220**	12
-OH	H	benzyl	**201**	23	**221**	19
-OH	-CH₂CH₃	-CH₂CH₃	**202**	12	**222**	20
-OH	H	-CH₂CH₃	**203**	9	**223**	11

R	R_2	R_3	2-Nitro benzamides	Yield %	2-Amino benzamides	Yield %
–OH	H	–CH$_3$	**204**	61	**224**	Product not isolated
Br	H	(phenyl)	**205**	59	**225**	33
Br	H	(benzyl)	**206**	52	**226**	33
Br	–CH$_2$CH$_3$	–CH$_2$CH$_3$	**207**	62	**227**	87
Br	H	–CH$_2$CH$_3$	**208**	65	**228**	82
Br	H	–CH$_3$	**209**	86	**229**	38

1.1.1.1.1 Synthesis of 4-amino-*N*-methyl-[1,1'-biphenyl]-3-carboxamide using Suzuki-Miyaura coupling

The Suzuki-Miyaura coupling reaction of the previously prepared 5-bromo-*N*-methyl-2-nitrobenzamide **209** with phenylboronic acid was investigated using potassium carbonate (K$_2$CO$_3$) as base and *tetrakis*(triphenylphosphine)palladium(0), Pd(PPh$_3$)$_4$ as a catalyst to give *N*-methyl-4-nitro-[1,1'-biphenyl]-3-carboxamide **230** in 53% yield (Figure **3-29**). The structure of the product was confirmed by ^{1}H and ^{13}C NMR spectroscopy and LCMS and were consistent with the formation of a biphenyl product. The reduction of the nitro group of *N*-methyl-4-nitro-[1,1'-biphenyl]-3-carboxamide **230** to give 4-amino-*N*-methyl-[1,1'-biphenyl]-3-carboxamide **231** proceeded in 52% yield (Figure **3-29**) and the structures of the compound was confirmed by ^{1}H and ^{13}C NMR spectroscopy and LCMS and was consistent with the expected amine product.
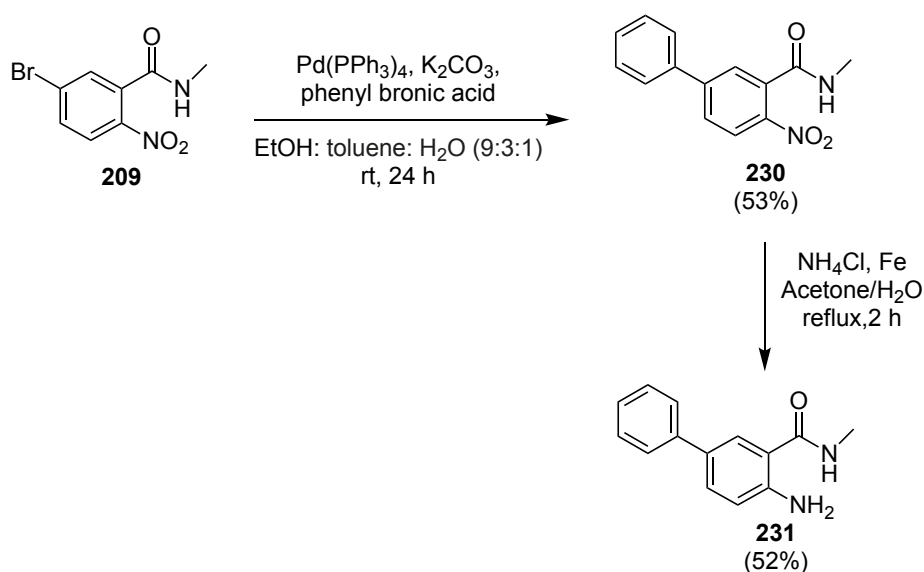
Figure 3-29 General scheme for synthesis of 4-amino-N-methyl-[1,1'-biphenyl]-3-carboxamide.

3.6.5. Basal ATPase measurements of 2-amino-benzamides

Due to time constraints, and the availability of KifC1 protein, the compounds could not be tested during the project.

3.4 Conclusions

Several previous attempts have been made to develop KifC1 inhibitors such as AZ82 and CW069, in the absence of structural data [147, 153]. However, none of these lead to KifC1 inhibitors that were suitable for clinical studies.

At the beginning of this project, from twenty hits that were identified through complementary NMR screens, ten fragments were selected for further analyses. However, following TSA measurement of the compounds in the presence of KifC1, none of the fragments were able to bind to the KifC1 motor domain in a way that increased its thermal stability. The measured Ti values in the presence of the fragments decreased compared with those in the control group, suggesting that TSA may not be suitable for measuring weak-binding KifC1 fragments. Interestingly, fragments **4** and **9** showed inhibitory effects during the

measurement of basal ATPase activity, which deviated from the typical inhibition curves observed in other kinesins. However, the inhibitory effects of these fragments remain uncertain and require further investigation.

Given the absence of solid structural data, we adopted a fragment-based drug design (FBDD) approach to enhance the KifC1 binding affinities of fragment hits through fragment growth and modification based on SAR analysis.

Molecular modelling techniques were utilised to predict the binding affinities of the analogues to KifC1. This approach aided in the identification, synthesis, and evaluation of compounds. We designed and synthesised a series of fragment analogues that were then tested in KifC1 binding and ATPase inhibition assays.

While some of the fragment analogues showed inhibitory effects in the basal ATPase assay, the experiments need to be repeated to produce more consistent binding profiles. Furthermore, certain fragment analogues acted as agonists rather than antagonists in the assay, indicating potential complexities to their interactions with KifC1. There are several types of compound that were not tested in the project due to time constraints and these should be tested as part of the future work.

Molecular docking studies using the Alphafold model of for human KifC1 that included sequences that were missing from the crystal structure of the KifC1 motor domain (PDBID: 5WDH), The analysis indicated that the allosteric L5/α2/α3 binding pocket has a slightly reduced volume compared to the MPP1 protein, but it remains accessible for current KifC1 inhibitors and fragment hits and their analogues. Docking using this potential allosteric L5/α2/α3 binding pocket adjacent to the Mg-ADP binding pocket suggested that it may be a potential binding site for the ligands, although the study did not rule out the possibility that the compounds may bind at other sites on the protein. In summary, the development of KifC1 inhibitors using fragment-based drug design (FBDD) approach though growing fragments without structural data is very challenging, with many unknowns still to be resolved. Most notably, KifC1-fragment crystal

structures and complete binding assay data are needed for the project to progress.

4 Conclusions

Several kinesins have been evaluated as potential cancer drug targets, and Eg5 inhibitors have reached the clinic. But there has been relatively little work on MPP1 and KifC1 despite their roles as mitotic kinesins that influence cell division. This project initially developed upon the first identified inhibitors of MPP1: depsidone natural products and the azaphilone ascochitine. The new derivatives aimed to mimic the key pharmacophoric features of ascochitine whilst significantly improving the synthetic accessibility of analogues. The use of coumarin and quinolone scaffolds provided compounds with comparable binding affinities to the natural products and identified some structural features that could be further optimised, particularly the equivalent of the ascochitine *s*-butyl substituent. Further binding assays are required with the compounds in order to identify the best structures to pursue in future work. It might be expected that the new scaffolds explored in this study would offer additional advantages beyond synthetic accessibility, including improved chemical and metabolic stability and physicochemical properties that are more easily tuned, although this requires further evaluation. The structure-activity studies would be greatly assisted by solving the crystal structure of MPP1, a task that has proved challenging to date, despite considerable efforts by the Kozielski group at UCL School of Pharmacy.

The KifC1 target also lacks structural data and bound conformations for the previously identified ligands. However, a fragment discovery approach identified a series of promising binders using NMR-based screening, some of which were validated using ATPase inhibition assays. These fragments formed the basis for a fragment analogue/fragment growth approach to identifying higher affinity binders. The approach adopted in this part of the project utilised a combination of fragment derivatisation, merging (via the synthesis of a range of indole sulfonamides) and growth. These approaches were combined with molecular modelling docking methods that were used to generate predictions for how the compounds might interact with KifC1. The efficacy of many of the structures remained untested due to time constraints and lack of access to the KifC1 protein. However, we anticipate that when the binding assays are completed the group of

compounds produced in this project will help to determine the future development of KifC1 inhibitors based on these fragments. Again, structural data would greatly assist in this endeavour.

Taken together this project has generated a series of testable hypotheses for how MPP1 and KifC1 inhibitors interact with their targets, it has initiated the synthesis of a range of chemotypes as potential inhibitors and provided preliminary data on structure-activity relationships that inform the future development of potential cancer therapeutic agents that target each protein. Taken together this represents a significant new contribution to the field that will help to shape the early stages of drug discovery for the two targets.

5 Future Work

The future work for the first part of the project related to MPP1 focuses on four main areas:

- Obtaining improved structural data for the MPP1 motor domain through X-ray crystallographic studies or refinement of the existing homology and Alphafold models. The latter activities could include molecular dynamics studies to explore protein flexibility and alternative protein conformations. The structural data is valuable for carrying out molecular docking studies of new potential inhibitors and for rationalising the structure activity relationships of compounds that have been tested as MPP1 inhibitors.

- The molecular docking studies in this project focussed on the analysis of binding interactions with the L5/α2/α3 pocket, adjacent to the ATP/ADP binding site using the Alphafold model of the MPP1 protein. During the project molecular dynamics simulations of the protein model were run (3 x 1 microsecond simulations) and docking was performed against structures separated by 100 ns in each simulation (a total of 30 MPP1 structures). Additionally, docking was performed across the whole protein using these 30 MPP1 structures. Docking was also performed using fragment libraries from the Enamine collection of purchasable compounds. These data sets were not extensively analysed during the project due to time constraints. However, they may provide insights into alternative binding modes for the fragments in the L5/α2/α3 pocket, alternative sites that may be occupied elsewhere on the protein, the presence of 'hidden' or 'cryptic' pockets that may emerge during molecular motions of the MPP1 protein, and alternative fragment leads from the Enamine fragment docking. Thus, analysis of these data should be a priority for the future work on the project.

- Based on the outcomes of the preceding work we will continue to design, synthesise, and characterise new potential ligands for MPP1, either based on scaffolds identified in our earlier work or from hits identified through *in silico* screening of small molecule libraries. Further testing of the compounds synthesised in the project should be carried out and the best

compounds should be evaluated to determine their cytotoxic activity against cancer cells.

- One of the specific aims in this respect is to synthesise a wider range of compounds that are related to the ascochitine scaffold to examine their structure-activity relationships (Figure **5-1**).
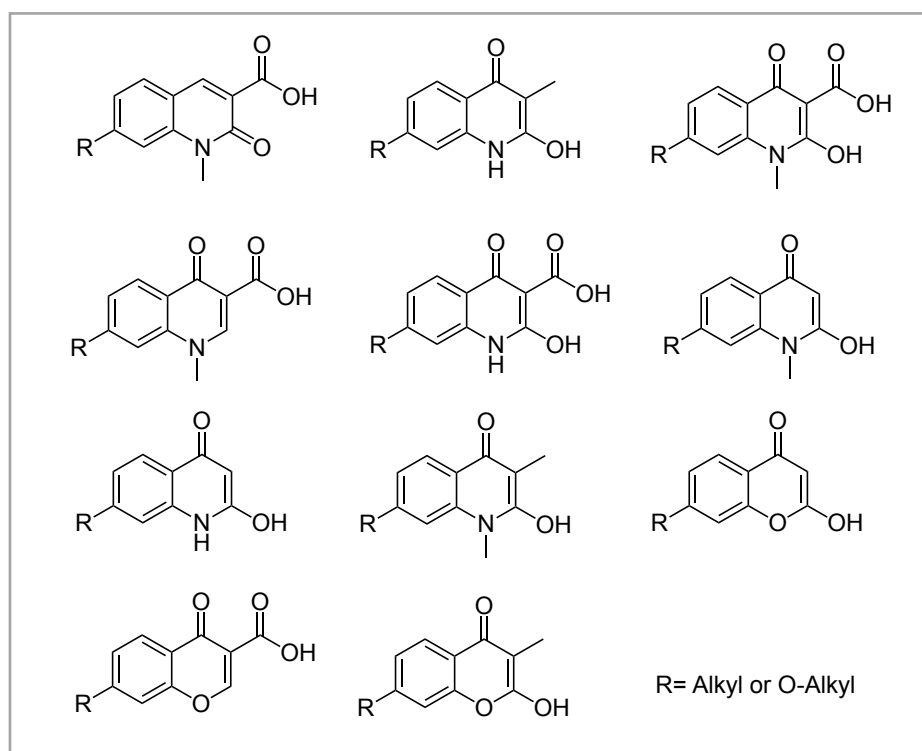
Figure 5-1 Quinolone-3-carboxylic acid and chromenone-3-carboxylic acid core alternative structures.

Regarding the second part of the project related to KifC1, the future work focuses on three main areas:

- Additional structural data for the KifC1 motor domain with bound ligands such as SR31527, a recently identified KifC1 inhibitor [153]. and the fragments and analogues identified in this study would be beneficial. Such studies would help to provide a structural basis for the development of improved KifC1 inhibitors.

- Several compounds in this work have not been tested for their binding and inhibitory activity with KifC1. Testing these compounds and validating the assay results of all of the compounds should be an early priority for future

work on the project. When compounds with low micromolar binding affinities are identified, cell-based assays to determine the cytotoxic activity of potential KifC1 inhibitors in cancer cells would be warranted.

- The molecular docking studies in this project focussed on the analysis of binding interactions with the L5/α2/α3 pocket, adjacent to the ATP/ADP binding site using the Alphafold model of the KifC1 protein. During the project molecular dynamics simulations of the protein model were run (3 x 1 microsecond simulations) and docking was performed against structures separated by 100 ns in each simulation (a total of 30 KifC1 structures). Additionally, docking was performed across the whole protein using these 30 KifC1 structures. Docking was also performed using fragment libraries from the Enamine collection of purchasable compounds. These data sets were not extensively analysed during the project due to time constraints. However, they may provide insights into alternative binding modes for the fragments in the L5/α2/α3 pocket, alternative sites that may be occupied elsewhere on the protein, the presence of 'hidden' or 'cryptic' pockets that may emerge during molecular motions of the KifC1 protein, and alternative fragment leads from the Enamine fragment docking. Thus, analysis of these data should be a priority for the future work on the project.

- Based on the outcomes of the preceding work, we will continue to design, synthesise and evaluation fragment analogues for KifC1 based on the scaffolds pursued in this chapter. The fragments that were not pursued as part of the current work should also be evaluated and derivatised further, specifically fragments **3**, **4**, **7** and **8** that were previously identified through NMR-based screening (Figure **5-2**).
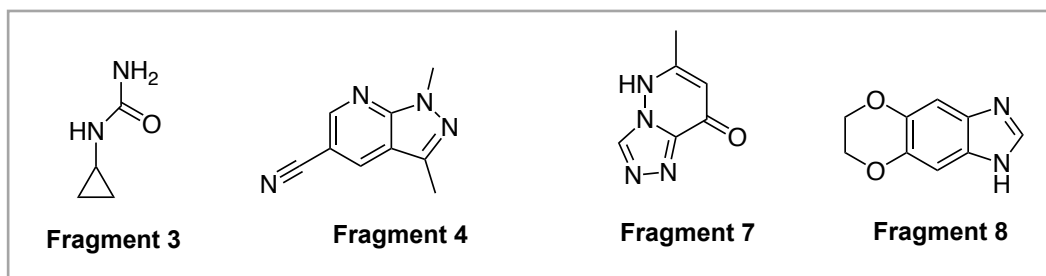
Figure 5-2 Fragments **3,4,7**and **8** which were previously identified through NMR-based screening.

6 Experimental section

6.1 General Experimental Details

All chemical reagents were purchased from Sigma Aldrich, Fisher Scientific, Merck and VWR. Unless specified in experimental protocols, reagents were used in their original form without further purification. Analytical thin layer chromatography was performed on TLC Silica gel 60 F_{254}, 20 × 20 cm aluminium sheets (Merck) and visualised under UV light (254 nm). Compound purification was performed on Flash Column Chromatography was performed using Merck Silica Gel 60, particle size 40-63 µm. and Biotage Selekt flash chromatography system. Normal phase purification was performed on Biotage Sfar Silica 60 µm 5 g/10 g/25 g/50 g columns. Reverse phase chromatography was performed on Biotage Sfar C18 Duo 100 Å 30 µm, 30 g columns. pH measurements were evaluated with pH-Fix 0-14 colour fixed indicator sticks, Fisher brand.

All reported yields refer to chromatographically and spectroscopically pure products.

6.2 General Spectroscopic Analysis

Structural product characterisation was performed on the following analytical instrumentation:

[1]H Nuclear Magnetic Resonance (NMR) spectra were recorded on a Bruker Advance 400 Spectrophotometer at 400.13 MHz or a Bruker Advance 500 Spectrophotometer at 500 MHz. Chemical shifts were measured in parts per million (ppm) relative to tetramethylsilane (TMS) (δ = 0) using the following internal reference: DMSO-d6 (δ 2.50). Multiplicities in ^{1}H NMR spectra are quoted as: s = singlet, d = doublet, t = triplet, q = quartet, m = multiplet, dd = double doublet, ddd = double double doublet. Complex splitting patterns were given as br (broad peaks) or m. Coupling constants (*J*) are determined by analysis using Bruker TopSpin 3.2 software and are quoted in Hz.

^{13}C Nuclear Magnetic Resonance (NMR) spectra were recorded on a Bruker Advance 400 Spectrophotometer at 100.61 MHz or a Bruker Advance 500 Spectrophotometer at 125 MHz. Chemical shifts were measured in parts per million (ppm) relative to tetramethylsilane (TMS) (δ = 0) using the following internal references: DMSO-d6 (δ 39.4). Multiplicities and Coupling constants (*J*) are determined by analysis using Bruker TopSpin 3.2 software and are quoted in Hz.

Liquid chromatography-Mass spectrometry (LC-MS) were recorded using an Agilent 1290 Infinity II system consisting of a quaternary pump (G7111A) and a diode array detector (WR(G7115A)coupled to a InfinityLab LC/MSD (G6125B) using ESI. An Agilent ZORBAX Eclipse XDB-C16 column , (5 µm, 4.6x 150 mm) was eluted at a flow rate of 1mL/min with mobile phase of 0.1% formic acid in H_2O and 0.1% formic acid in MeCN. Total run time = 12 min.

High-resolution mass spectrometry (HRMS) spectra were obtained on a Micromass Q-TOF Premier Tandem Mass Spectrometer using electrospray (ES) ionisation, coupled to an HPLC instrument. Calibration was performed with an internal standard: positive mode: [Glu]-fibrinopeptide B peptide which gives $[M+2H]^{2+}$ *m/z* = 785.8426, negative mode: taurocholic acid which gives $[M-H]^-$ *m/z* = 514.2839.

Infrared spectrometry (IR) was carried out on Agilent Cary 630 FTIR Spectrometer equipped with a single bounce diamond ATR sampling accessory. Solid samples were loaded directly onto the sample window. Spectra were recorded in the range 4,000 to 650 cm^{-1}, using 74 scans at a 4cm^{-1} resolution with a total measurement time of 30 seconds.

Melting points (m.p) were obtained on Stuart SMP10 Melting Point Apparatus using glass capillary tubes (ø = 1.8-1.9 mm, 100 mm).

Microwave specifications: All microwave assisted reactions were carried out in a Biotage initiator$^+$ Robot Eight (355380) microwave reactor.

6.3 Molecular modelling method

For small molecule docking studies, the MPP1 homology model and the Alphafold structural prediction and for Fragment-based drug design docking studies, the KifC1 crystal structure of motor domain (PDBID:5WDH) with Mg-ADP bound and the Alphafold structure prediction that included the missing sequence of crystal structure, ligand, and protein-ligand complex for use in subsequent analyses. The protein's PDB file were opened in AutoDock Tools (ADT) [154], the solvent and ions were removed, and the resulting structure was saved as a pdbqt file for use in AutoDock Vina [124] and LeDock [140]. The small molecule ligands were prepared by constructing the 2D structures in ChemBioDraw Ultra 14.0 (Perkin Elmer) which were saved in sdf format. The 2D representations were converted into 3D structures using an in-house script that used Balloon 1.6.1.1220 [155] to generate an initial 3D conformer, followed by Openbabel 2.3.4 [156] to add hydrogens appropriate for pH 7.4 and to perform a weighted conformer search (nconf = 1000, weighted, gasteiger partial charges). Energy mmunization was performed on the lowest energy conformer using obmimimize (n = 10000, c = 1e-30) followed by MOPAC2012 [157] using the semi-empirical PM7 paramters (keywords: PM7, MMOK, T=30000, PDBOUT). The compounds were saved in a mol2 file format and converted to pdb, pdbqt and mol2 files formats (the latter two containing partial charge information) using Openbabel 2.3.4. The properties of the compounds were determined using Openbabel 2.3.4 (molecular weight, number of non-hydrogen atoms, cLogP).

Molecular dynamics simulations of the MPP1 and KifC1 proteins were performed during the project using the Alphafold models of the motor domain of each protein. The structures of each protein complexed with ADP and Mg^{2+} were parameterised and prepared for simulation using the AMBER20 and AmberTools 20 software [158]. The protein was parameterised using the FF14SB forcefield and the structure was solvated with TIP3P water (10 Å truncated octahedral box) and neutralised with Cl- ions. The ion concentration was adjusted to 140 mM by the addition of K+ and Cl- ions to the solvent box. The complex was energy minimised and subject to 1 microsecond of molecular dynamics using pmemd.

The simulations were repeated three times. The trajectories were stripped of ions and solvent then centred and imaged using cpptraj. Snap shots from the simulation were saved every 100 nanoseconds and saved as pdb files for use in the docking calculations (total of 30 structures per protein).

AutoDock Vina was run using an Exhaustiveness setting of 9 and a binding site box centred on the proposed ligand binding pocket that was 24 x 20 x 20 Å in size. All other parameters were set to their default values. The lowest energy conformation of each docked ligand was extracted from the results file using a custom script and analysed in USCF Chimera 1.11.2 [159].

LeDock was run using the default parameters using receptor PDB file prepared using LePro. The receptor grid box has same coordinates as that for AutoDock Vina.

All images for the molecular docking study that illustrate the docked complex of our compounds bound to KifC1 and MPP1 were prepared using Discovery Studio 4.5 [160] and USCF Chimera 1.11.2.

6.4 Biological assays

The assays described in this section were performed by Dr. Jiazhi Tang, UCL School of Pharmacy.

6.4.1 Composition of ATPase buffers

Buffer 1: 25 mM ACES/KOH, pH 6.9, 2 mM magnesium acetate, 2 mM potassium EGTA, 0.1 mM potassium EDTA, and 1 mM 2-mercaptoethanol.

ATPase Buffer: 1 mM Mg^{2+}ATP, 2 mM PEP, 0.25 mM NADH, 3–10 µg/mL PK, and 3 µg/mL LDH, scaled to the required volume with **Buffer 1**. The prepared ATPase buffer was aliquoted, frozen in liquid nitrogen, and stored at -80 °C [161].

6.4.2 Basal ATPase assays to measurements of activities of MPP1 inhibitors

MPP1 inhibitors, were prepared for testing as stock solutions in DMSO. Diluted stocks were prepared in 96-well plates by serial dilution as outlined in Table **6-1**. All small molecules were characterized using ATPase assays in the presence of 710 nM MPP1. ATPase assays were carried out by mixing 96 µL of ATPase buffer with 2 µL of MPP1 and 2 µL of small molecule stocks in 96-well half-area µclear plates. All measurements were conducted in triplicate. Absorbance was read at 340 nm and 25 °C for 30 min using a Tecan Sunrise photometer [162].

Table 6-1 Small molecule concentrations in stocks and basal MPP1 ATPase activity measurement

Well number	1	2	3	4	5	6	7	8	9	10	11	12
Stock concentration (mM)	10	5	2.5	1.25	0.63	0.31	0.16	0.08	0.04	0.02	0.01	0.00
Final concentration (µM)	200	100	50	25	12.5	6.25	3.13	1.56	0.78	0.39	0.20	0.00

6.4.3 MT-stimulated ATPase assays to measurements of activities of MPP1 inhibitors

Small molecules were analysed via measurement of the MT-stimulated ATPase activity. Tubulin was polymerised into MTs before the measurements. The final concentration of MTs was optimised at 500 nM. For each measurement, a series of test comound concentrations was used. The mixture of ATPase buffer along with the specific comound dilution was added to each well. MPP1 was added just before the start of the experiment at a final concentration of 66 nM (Table **6-2**).

Table 6-2 Small molecule concentrations in stocks and MT-stimulated MPP1 ATPase activity measurement

Well number	1	2	3	4	5	6	7
Stock concentration (mM)	10	5	2.5	1.25	0.63	0.31	0.00
Final concentration measurement (µM)	200	100	50	25	12.5	6.25	0.00

6.4.4 Basal ATPase assays to measurements of activities of potential KifC1 fragments

ATPase activity was measured, in triplicate, using $Mg^{2+}ATP$ using a KifC1 concentration of 2.73 µM and 350 mM NaCl in 96-well half area plates. The mixture of ATPase Buffer together with increasing concentrations of inhibitor/salt/ATP was added to each well. The potential KifC1 fragments were dissolved in DMSO and transferred to 96-well plates in gradient dilution as outlined in Table **6-3**. The enzyme was added just before the start of each experiment. Absorbance was read at 340 nm and 25 °C for 30 min using a Tecan Sunrise photometer [162].

Table 6-3 fragment stock concentrations and final ATPase activity measurement.

Well number	1	2	3	4	5	6
Stock concentration (mM)	100.00	65 .00	42.25	27.46	17.85	11.60
Final concentration measurement (mM)	2.00	1.30	0.85	0.55	0.36	0.23

6.4.5 Thermal shift assays (TSA) in presence of potential KifC1 fragments

The Tycho NT.6 instrument (Nanotemper) was used to measure the intrinsic fluorescence ratio of tryptophan and tyrosine residues in KifC1 at 350 and 330

nm as a 30 °C/minute temperature ramp was applied from 35–95°C. This allowed the identification of the inflection temperature (Ti) that represented the unfolding transition for the protein.

KifC1 was concentrated to 8.4 mg/ml in the Assay Buffer (potassium phosphate monobasic pH 7.0, 150 mM NaCl, 5% glycerol, 1 mM DTT, and 1 mM Mg^{2+}ATP). All experiments were conducted in triplicate, and Ti values were calculated using the Tycho NT.6 software.

The fragments were measured at concentrations of 0.625, 1.25, 2.5, and 5.0 mM in triplicate in the presence of 8 µM KifC1 in the Assay Buffer. Simultaneously, 1.25%, 2.5%, 5.0%, and 10% DMSO were measured separately with 8 µM KifC1 as controls. Finally, 8 µM KifC1 alone was measured as a negative control [162].

6.5   General synthetic method

6.5.1 General method A1: Synthesis of chromenone-3-carboxylic acid ethyl esters

The substituted salicylaldehyde (10 mmol, 1equiv.) and diethyl malonate (10 mmol, 1 1equiv.) were placed into a round-bottomed flask equipped with a magnetic stirrer. Ethanol (4 mL) and piperidine (2 drops) were added to the mixture. The resulting solution was then refluxed for 4-24 hours with continuous stirring. The progress of the reaction was monitored by TLC. After the reaction was complete, the reaction mixture solution was cooled to room temperature then placed in an ice bath for 1 hour. The resulting crystals were collected by filtration and then recrystallised from ethanol [163].

6.5.2 General method A2: Synthesis of 7-hydroxy and 7-methoxy-chromenone-3-carboxylic acid ethyl esters

The substituted salicylaldehyde (7.23 mmol, 1equiv.) and diethyl malonate (7.23 mmol 1equiv.) were added to the flask on a magnetic stirrer and piperidine (7.38

mmol) was slowly added at room temperature. The reaction mixture became pale yellow and was stirred for a further 1 hour. The progress of the reaction was monitored by TLC. After the reaction was complete, the reaction mixture solution was cooled to room temperature then placed in an ice bath for 1 hour, then HCl 10% w/v (50 mL) was added. Then filtration and washing with H_2O to give the crystals which was recrystallised from ethanol [164].

Ethyl 7-methyl-2-oxo-2*H*-chromene-3-carboxylate (39)
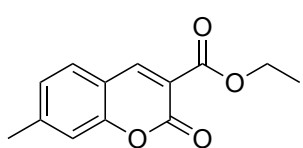
Synthesised according to general method **A**1 from 2-hydroxy-4-methylbenzaldehyde **35** (1.36 g, 10 mmol, 1equiv.) and diethyl malonate (1.52 mL, 10 mmol, 1equiv.) to give the title compound as a white solid (1.70 g, 80% yield). **m.p.** 102–104°C (no lit m.p.). **¹H NMR** (500 MHz, DMSO-d_6) δ 8.73 (s, 1H), 7.81 (d, *J* = 7.9 Hz, 1H), 7.30 – 7.22 (m, 2H), 4.29 (q, *J* = 7.1 Hz, 2H), 1.31 (t, *J* = 7.1 Hz, 3H). **¹³C NMR** (126 MHz, DMSO) δ 162.67, 156.15, 154.68, 148.79, 146.03, 129.97, 126.03, 116.26, 116.14, 115.42, 61.12, 21.47, 14.06. **LC-MS** *m/z* (ESI+) 233.3 ([M+H]⁺. Retention time: t_R = 3.94 min, >95%. Spectroscopic data matched those in the literature [163, 165].

Ethyl 2-oxo-2*H*-chromene-3-carboxylate (40)
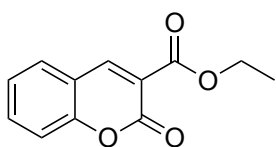
Synthesised according to general method **A**1 from salicylaldehyde **36** (1.22 g, 10 mmol, 1equiv.) and diethyl malonate (1.52 mL, 10 mmol, 1equiv.) to give the title compound as a white solid (1.66 g, 76% yield). **m.p.** 94–96°C (no lit m.p.). **¹H NMR** (500 MHz, DMSO-d_6) δ 8.77 (s, 1H), 7.93 (dd, *J* = 7.7, 1.6 Hz, 1H), 7.75 (ddd, *J* = 8.7, 7.3, 1.7 Hz, 1H), 7.51 – 7.37 (m, 2H), 4.31 (q, *J* = 7.1 Hz, 2H), 1.32 (t, *J* = 7.1 Hz, 3H). **¹³C NMR** (126 MHz, DMSO) δ 162.57, 156.01, 154.50, 148.66, 134.49, 130.25, 124.87, 117.77, 117.62, 116.11, 61.23, 14.02. **LC-MS** *m/z* (ESI+) 219.2 ([M+H]⁺. Retention time: t_R = 3.89 min, >95%. Spectroscopic data matched those in the literature [166].

Ethyl 7-(diethylamino)-2-oxo-2H-chromene-3-carboxylate (38)
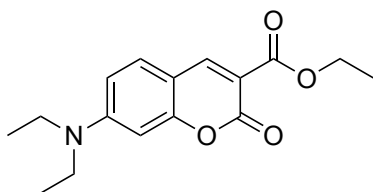
Synthesised according to general method **A**1 from 4-(diethylamino) salicylaldehyde **34** (0.5 g, 2.6 mmol, 1equiv.) and diethyl malonate (0.43 mL, 2.8 mmol, 1equiv.) to give the title compound as a yellow solid (0.47 g, 63% yield). **m.p.** 81–84°C (no lit m.p.). **¹H NMR** (500 MHz, DMSO-d_6) δ 8.55 (s, 1H), 7.63 (d, J = 9.0 Hz, 1H), 6.77 (dd, J = 9.0, 2.5 Hz, 1H), 6.54 (d, J = 2.4 Hz, 1H), 4.23 (q, J = 7.1 Hz, 2H), 3.48 (q, J = 7.0 Hz, 4H), 1.28 (t, J = 7.1 Hz, 3H), 1.14 (t, J = 7.0 Hz, 6H). **¹³C NMR** (126 MHz, DMSO) δ 163.36, 158.00, 156.97, 152.78, 149.21, 131.74, 109.76, 107.28, 106.94, 95.75, 60.31, 44.31, 40.02, 14.19, 12.27. **LC-MS** m/z (ESI+) 290.3 ([M+H]⁺. Retention time: t_R = 3.52 min, >95%. Spectroscopic data matched those in the literature [167].

Ethyl 7-hydroxy-2-oxo-2*H*-chromene-3-carboxylate (41)
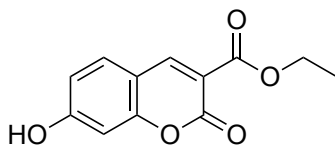
a) Synthesised according to general method **A**1 from 2,4-dihydroxybenzaldehyde **37** (1.38 g, 10 mmol, 1equiv.) and diethyl malonate (1.52 mL, 10 mmol, 1equiv.). Crystals were formation then isolated after added 2 mL of DCM and some of ethyl acetate to afford the title compound as a pink solid (1.03 g, 44% yield). **m.p.** 168–170°C (no lit m.p.). **¹H NMR** (400 MHz, DMSO-d_6) δ 8.67 (d, J = 0.6 Hz, 1H), 7.75 (d, J = 8.6 Hz, 1H), 6.84 (dd, J = 8.6, 2.3 Hz, 1H), 6.73 (dd, J = 2.2, 0.6 Hz, 1H), 4.26 (q, J = 7.1 Hz, 2H), 1.30 (t, J = 7.1 Hz, 3H). **LC-MS**: m/z (ESI)= 491 [2M+Na]⁺. Retention time: t_R = 3.79 min, >95%. Spectroscopic data matched those in the literature [163, 165]

b) Synthesised according to general method A2 from 2,4-dihydroxybenzaldehyde **37** (1.0 g, 7.24 mmol, 1equiv.), diethyl malonate (1.1 mL, 7.24 mmol, 1equiv.) and piperidine (0.7 mL, 7.38 mmol). The crude product was purified by recrystallisation from ethanol to afford the title compound as a pink solid (1.52 g, 90% yield). **m.p.** 168–170°C (no lit m.p.). **¹H NMR** (400 MHz, DMSO-d_6) δ 11.07 (s, 1H), 8.67 (d, J = 0.7 Hz, 2H), 7.76

(d, *J* = 8.6 Hz, 2H), 6.85 (dd, *J* = 8.6, 2.3 Hz, 2H), 6.73 (dd, *J* = 2.3, 0.7 Hz, 2H), 4.27 (q, *J* = 7.1 Hz, 4H), 1.30 (t, *J* = 7.1 Hz, 6H). **^{13}C NMR** (126 MHz, DMSO) δ 164.12, 162.93, 157.02, 156.40, 149.45, 132.07, 114.04, 111.99, 110.36, 101.77, 60.80, 14.10. **LC-MS** *m/z* (ESI+) 235.2 ([M+H] $^+$. Retention time: t_R = 3.86 min, >95%. Spectroscopic data matched those in the literature [164].

Ethyl 7-methoxy-2-oxo-2*H*-chromene-3-carboxylate (46)
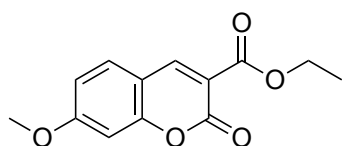
Synthesised according to general method **A**1 from 2-hydroxy-4-methoxybenzaldehyde **45** (1.1 g, 7.24 mmol, 1equiv.), diethyl malonate (1.1 mL, 7.24 mmol, 1equiv.) and piperidine (0.7 mL, 7.38 mmol). The crude product was purified by recrystallisation from ethanol to give title compound as a white solid (1.65 g, 92% yield). **m.p.** 131–132°C (no lit m.p.). **^{1}H NMR** (400 MHz, DMSO-d_6) δ 8.72 (d, *J* = 0.6 Hz, 1H), 7.84 (d, *J* = 8.6 Hz, 1H), 7.11 – 6.80 (m, 2H), 4.28 (q, *J* = 7.1 Hz, 2H), 3.90 (s, 3H), 1.31 (t, *J* = 7.1 Hz, 3H). **^{13}C NMR** (126 MHz, DMSO) δ 164.77, 156.97, 149.23, 133.13, 131.63, 129.53, 113.32, 106.15, 100.71, 100.25, 60.93, 56.24, 14.10. **LC-MS** *m/z* (ESI+) 249.3 [M+H]$^+$, t_R = 3.37 min, >95%. Spectroscopic data matched those in the literature [168].

6.5.3 General method B: Synthesis of chromenone-3-carboxylic acids

The chromenone-3-carboxylic acid ethyl ester (1 equiv.) and NaOH (2 equiv.) were dissolved in EtOH/H_2O (1:1 v/v) and added to the above reaction mixture, and the reaction was stirred under reflux at 60° C. for 2 h, and the progress of the reaction was detected by TLC (70% EtOAc in hexanes), which indicated that the reaction was complete. After the reaction was complete, the solution was cooled to room temperature, and hydrochloric acid was added dropwise to adjust the pH of the solution to 2-3. The solution was cooled over an ice bath for 2 hours, and a large amount of precipitate was generated. The precipitate was isolated via Buchner filtration and washed with H_2O, and then dried *in vacuo* to yield a crude product containing the titled compound as a solid without purification [163].

Ethyl 7-methyl-2-oxo-2*H*-chromene-3-carboxylate (42)
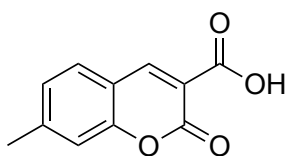
Synthesised according to general method **B** from 3-ethoxy carbonyl-7- methyl coumarin **39** (1.00 g, 4.3 mmol, 1 equiv.) and NaOH (0.34 g, 8.6 mmol, 2 equiv.) to give the title compound as a white solid (0.63 g, 72% yield).). **m.p.** 196–198°C (no lit m.p.). **^{1}H NMR** (500 MHz, DMSO-d_6) δ 13.14 (s, 1H), 8.73 (s, 1H), 7.79 (d, *J* = 8.0 Hz, 1H), 7.34 – 7.22 (m, 2H), 2.45 (s, 3H). **^{13}C NMR** (126 MHz, DMSO) δ 164.03, 156.90, 154.62, 148.56, 145.78, 129.89, 125.99, 116.85, 116.12, 115.59, 21.46. **LC-MS** *m/z* (ESI+) 205.2 ([M+H]$^+$. Retention time: t$_R$ = 2.65 min, >95%. Spectroscopic data matched those in the literature [165].

2-Oxo-2*H*-chromene-3-carboxylic acid (43)
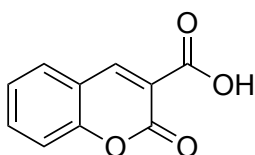
Synthesised according to general method **B** from ethyl coumarin-3-carboxylate **40** (1.00 g, 4.6 mmol, 1 equiv.) and NaOH (0.37 g, 9.2 mmol, 2 equiv.) to give title the compound as a white solid (0.69 g, 79% yield). **m.p.** 187–189°C (no lit m.p.). **^{1}H NMR** (500 MHz, DMSO-d_6) δ 8.76 (s, 1H), 7.92 (dd, *J* = 7.8, 1.6 Hz, 1H), 7.80 – 7.71 (m, 1H), 7.50 – 7.37 (m, 2H). **^{13}C NMR** (126 MHz, DMSO) δ 163.97, 156.65, 154.45, 148.36, 134.30, 134.49, 130.17, 124.80, 118.30, 117.95, 116.07. **LC-MS** *m/z* (ESI+) 191.2 ([M+H]$^+$. Retention time: t$_R$ = 2.54 min, >95%. Spectroscopic data matched those in the literature [169].

7-(Diethylamino)-2-oxo-2*H*-chromene-3-carboxylic acid (25)

Synthesised according to general method **B** from ethyl 7- diethyl amino coumarin-3-carboxylate **38** (0.2 g, 0.7 mmol, 1 equiv.) and NaOH (0.06 g, 1.4 mmol, 2 equiv.) to give the title compound as a yellow solid (0.08 g, 44% yield). **m.p.** 228–230°C (no lit m.p.). **^{1}H NMR** (500 MHz, DMSO-d_6) δ 7.25 (s, 1H), 6.23 – 6.18 (d, *J* = 9.0 Hz, 1H), 6.15 (dd, *J* = 9.1, 2.5 Hz, 1H), 6.54 (d, *J* = 2.3 Hz, 1H) (m, 1H), (d, *J* = 2.2 Hz, 1H), 3.32 (t, *J* = 7.0 Hz, 4H), 1.14 – 1.02 (m, 6H). **^{13}C NMR** (126 MHz, DMSO) δ 163.61, 158.12, 157.168, 152.92, 149.46, 131.84, 110.02, 108.15, 106.94, 95.87, 44.36, 44.02, 12.28,

12.26. **LC-MS** *m/z* (ESI+) 262.3 ([M+H]⁺. Retention time: t_R = 2.41 min, >95%. Spectroscopic data matched those in the literature [170] .

7-Hydroxy-2-oxo-2*H*-chromene-3-carboxylic acid (44)
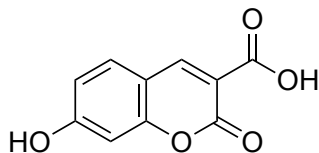
Synthesised according to general method **B** from 7-hydroxy-chromene-3-carboxylic acid ethyl ester **41** (0.2 g, 0.9 mmol, 1 equiv.) and NaOH (0.07 g, 1.7 mmol, 2 equiv.) to give the title compound as a brown solid (0.09 g, 51% yield). **m.p.** 253–255°C (no lit m.p.). **¹H NMR** (400 MHz, DMSO-*d*₆) δ 12.65 (s, 1H), 11.20 (s, 1H), 8.68 (s, 2H), 7.75 (d, *J* = 8.6 Hz, 2H), 6.85 (dd, *J* = 8.6, 2.3 Hz, 2H), 6.74 (d, *J* = 2.3 Hz, 2H). **¹³C NMR** (126 MHz, DMSO) δ 164.23, 163.92, 157.46, 156.92, 149.41, 132.03, 114.02, 112.45, 110.58, 101.77. **LC-MS** *m/z* (ESI+) 207.2 ([M+H] ⁺. Retention time: t_R = 2.52 min, >95%. Spectroscopic data matched those in the literature [171].

7-Methoxy-2-oxo-2*H*-chromene-3-carboxylic acid (47)
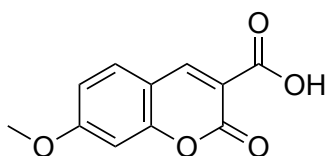
Synthesised according to general method **B** from 7-methoxy-chromene-3-carboxylic acid ethyl ester **46** (1.0 g, 4.0 mmol, 1 equiv.) and NaOH (0.33 g, 8.0 mmol, 2 equiv.) to give the title compound as a white solid (0.50g, 56% yield). **m.p.** 193–196°C (no lit m.p.). **¹H NMR** (400 MHz, DMSO-*d*₆) δ 12.65 (s, 1H), δ 8.72 (d, *J* = 0.6 Hz, 1H), 7.84 (d, *J* = 8.6 Hz, 1H), 7.11 – 6.80 (m, 2H), 3.90 (s, 3H). ¹³C NMR (126 MHz, DMSO) δ 164.64, 164.15, 157.14, 156.88, 149.10, 131.55, 113.76, 111.59, 106.14, 100.24, 56.22. **LC-MS** *m/z* (ESI+) 221.2 ([M+H]⁺. Retention time: t_R = 2.79 min, >95%. Spectroscopic data matched those in the literature [172].

6.5.4 General method C: Synthesis of chromene-3-carboxamides

The chromene-3-carboxylic acid (0.3 mmol, 1 equiv.) and amine (0.3 mmol, 1 equiv.) were dissolved in anhydrous CH₂Cl₂ (2 mL). After stirring the mixture at room temperature for several minutes EDCI (0.6 mmol, 2 equiv.) and DMAP (0.75

mmol, 2.5 equiv.). were added to the mixture. The reaction mixture was stirred at room temperature for 24 hours and monitored by TLC (60% EtOAc in hexanes), which indicated that the reaction was completed. The solvent was removed *in vacuo,* and the residue was diluted with EtOAc (25 mL) and washed with 1 M HCl solution (3 x 10 mL) and brine (10 mL) then saturated NaHCO$_3$ solution (3 x10 mL) only with methoxy substituted compounds and brine (10 mL). The organic fraction was dried over MgSO$_4$ and concentrated *in vacuo*, to yield a crude product containing the titled compound as a solid without purification [173].

7-Hydroxy-2-oxo-*N*-phenyl-2*H*-chromene-3-carboxamide (50)
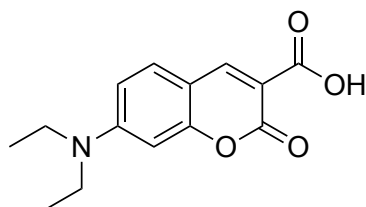
Synthesised according to general method **C** from 7-hydroxy-chromene-3-carboxylic acid **44** (62 mg, 0.3 mmol, 1 equiv.) and aniline (22 μL, 0.3 mmol, 1 equiv.), EDCI (116 mg, 0.6 mmol, 2 equiv.) and DMAP (92 mg, 0.75 mmol, 2.5 equiv.) to give the title compound as a yellow solid (0.06 g, 71%yield). **m.p.** 154–157°C (no lit m.p.). **¹H NMR** (400 MHz, DMSO-*d*$_6$) δ 11.39 (s, 1H), 10.67 (s, 2H), 8.87 (s, 2H), 7.86 (d, *J* = 8.6 Hz, 2H), 7.79 – 7.65 (m, 5H), 7.43 – 7.34 (m, 4H), 7.18 – 7.09 (m, 2H), 6.97 (dt, *J* = 8.6, 1.7 Hz, 2H), 6.92 (s, 3H). **¹³C NMR** (126 MHz, DMSO) δ 149.47, 148.38, 132.16, 132.11, 129.63, 129.01, 124.10, 119.79, 114.52, 114.31, 113.98, 110.38, 101.88, 101.76. **LC-MS** *m/z* (ESI+) 282.2 ([M+H]$^+$. Retention time: t$_R$ = 3.62 min, >95%. Spectroscopic data matched those in the literature [173]

***N*-Benzyl-7-methyl-2-oxo-2*H*-chromene-3-carboxamide (51)**
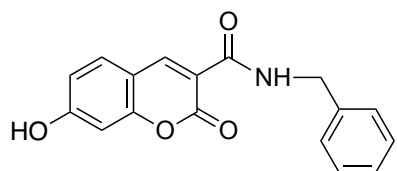
Synthesised according to general method **C** from 7-hydroxy-chromene-3-carboxylic acid **44** (62 mg, 0.3 mmol, 1 equiv.) and benzylamine (33 μL, 0.3 mmol, 1 equiv.), EDCI (116 mg, 0.6 mmol, 2 equiv.) and DMAP (92 mg, 0.75 mmol, 2.5 equiv.) to give the title compound as a yellow solid. (0.056 g, 64% yield). **m.p.** 167–170°C (no lit m.p.). **IR** (film): ν$_{max}$ 3324, 1707, 1528, 1323, 1222, 1140 cm^{-1}. **¹H NMR** (400 MHz, DMSO-*d*$_6$) δ 11.42 (s, 2H), 9.06 (t, *J* = 6.0 Hz, 2H), 8.80 (s, 2H), 7.81 (d, *J* = 8.6 Hz, 2H), 7.78 – 7.64 (m, 2H), 7.34 (d, *J* = 4.4

Hz, 10H), 7.33 – 7.25 (m, 6H), 7.25 – 7.18 (m, 2H), 6.99 – 6.87 (m, 5H), 4.53 (d, J = 6.0 Hz, 4H). **^{13}C NMR** (126 MHz, DMSO) δ 161.00, 160.87, 148.19, 147.52, 139.06, 131.96, 131.26, 128.37, 127.34, 126.90, 114.35, 101.78, 42.60. **LC-MS** *m/z* (ESI+) 296.3 ([M+H]$^+$. Retention time: t_R = 3.62 min, >95%. **HRMS** (ESI): calculated for $C_{17}H_{13}NO_4$ [M+H]$^+$ 296.0923, found 296.0917.

7-Hydroxy-3-(piperidine-1-carbonyl)-2*H*-chromen-2-one (52)

Synthesised according to general method **C** from 7-hydroxy-chromene-3-carboxylic acid **44** (62 mg, 0.3 mmol, 1 equiv.) and piperidine (30 µL, 0.3 mmol, 1 equiv.), EDCI (116 mg, 0.6 mmol, 2 equiv.) and DMAP (92 mg, 0.75 mmol, 2.5 equiv.) to give the title compound as a white solid (0.060 g, 73% yield). **m.p.** 158–160°C (no lit m.p.). **IR** (film): v_{max} 2922, 1714, 1617, 1561, 1371, 1222, 1121, cm^{-1}.**^{1}H NMR** (500 MHz, DMSO-d_6) δ 8.04 (s, 1H), 7.58 (d, J = 8.5 Hz, 1H), 6.91 – 6.80 (m, 2H), 3.55 (t, J = 5.5 Hz, 2H), 3.34 – 3.22 (m, 2H), 1.74 – 1.36 (m, 6H). **^{13}C NMR** (126 MHz, DMSO) δ 163.05, 161.94, 157.98, 149.42, 142.33, 130.28, 120.36, 110.77, 102.03, 101.77, 47.47, 25.87, 25.19, 23.87. **LC-MS** *m/z* (ESI+) 274.2 ([M+H]$^+$. Retention time: t_R = 2.81 min, >95%. **HRMS** (ESI): calculated for $C_{15}H_{15}NO_4$ [M+H]$^+$ 274.1079, found 274.1090.

N,*N*-Diethyl-7-hydroxy-2-oxo-2*H*-chromene-3-carboxamide (53)
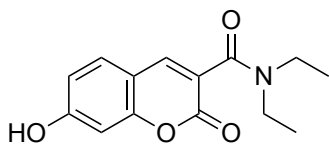
Synthesised according t to general method **C** from 7-hydroxy-chromene-3-carboxylic acid **44** (62 mg, 0.3 mmol, 1 equiv.) and diethyl amine (31 µL, 0.3 mmol, 1 equiv.), EDCI (116 mg, 0.6 mmol, 2 equiv.) and DMAP (92 mg, 0.75 mmol, 2.5 equiv.) to give the title compound as a white solid (0.058 g, 74%yield). **m.p.** 155–157°C (no lit m.p.). **IR** (film): v_{max} 2978, 1718, 1565, 1505, 1326, 1252, 1155, 1125, cm^{-1}.**^{1}H NMR** (500 MHz, DMSO-d_6) δ 10.88 (s, 1H), 8.74 (d, J = 3.9 Hz, 1H), 7.81 (t, J = 8.2 Hz, 1H), 6.91 (ddd, J = 9.2, 7.2, 2.3 Hz, 2H), 3.47 (t, J = 7.1 Hz, 2H), 3.29 (q, J = 7.0 Hz, 2H), 1.18 (t, J = 7.1 Hz,

2H), 1.12 (t, *J* = 7.0 Hz, 2H). **^{13}C NMR** (126 MHz, DMSO) δ 164.21, 161.90, 158.17, 155.43, 141.55, 130.28, 120.79, 113.66, 110.75, 102.11, 38.63, 14.05, 12.73. **LC-MS** *m/z* (ESI+) 262.3 ([M+H]$^+$. Retention time: t_R = 2.69 min, >95%. **HRMS** (ESI): calculated for $C_{15}H_{15}NO_4$ [M+H]$^+$ 262.1079, found 262.1083.

7-Methoxy-2-oxo-*N*-phenyl-2*H*-chromene-3-carboxamide (54)
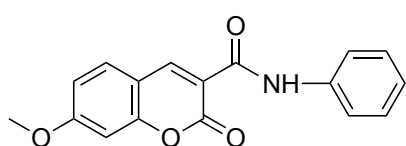
Synthesised according to general method **C** from 7-methoxy-chromene-3-carboxylic acid **47** (66 mg, 0.3 mmol, 1 equiv.) and aniline (22 µL, 0.3 mmol, 1 equiv.), EDCI (116 mg, 0.6 mmol, 2 equiv.) and DMAP (92 mg, 0.75 mmol, 2.5 equiv.) to give the title compound as a yellow solid. (0.065 g, 79%yield). **m.p.** 165–167°C (no lit m.p.). **^{1}H NMR** (400 MHz, DMSO-d_6) δ 10.66 (s, 1H), 8.92 (s, 1H), 7.96 (d, *J* = 8.7 Hz, 1H), 7.81 – 7.65 (m, 2H), 7.43 – 7.31 (m, 2H), 7.21 – 7.11 (m, 2H), 7.09 (dd, *J* = 8.7, 2.4 Hz, 1H), 3.93 (s, 3H). **^{13}C NMR** (126 MHz, DMSO) δ 164.64, 161.08, 160.07, 137.99, 131.67, 129.01, 119.81, 112.20, 100.37, 56.32, 39.31. **LC-MS** *m/z* (ESI+) 296.2 ([M+H]$^+$. Retention time: t_R = 4.11 min, >95%. Spectroscopic data matched those in the literature [174].

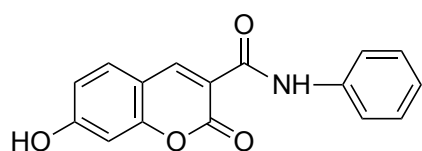### *N*-Benzyl-7-methoxy-2-oxo-2*H*-chromene-3-carboxamide (55)
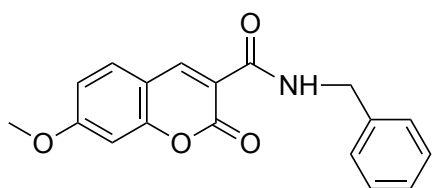
Synthesised according to general method **C** from 7-methoxy-chromene-3-carboxylic acid **47** (66 mg, 0.3 mmol, 1 equiv.) and benzylamine (33 µL, 0.3 mmol, 1 equiv.), EDCI (116 mg, 0.6 mmol, 2 equiv.) and DMAP (92 mg, 0.75 mmol, 2.5 equiv.) to give the title compound as a white solid (0.059 g, 63%yield). **m.p.** 182–185°C (no lit m.p.). **^{1}H NMR** (400 MHz, DMSO-d_6) δ 9.07 (t, *J* = 6.0 Hz, 1H), 8.86 (d, *J* = 0.7 Hz, 1H), 7.92 (d, *J* = 8.8 Hz, 1H), 7.40 – 7.31 (m, 4H), 7.31 – 7.20 (m, 2H), 7.06 (dd, *J* = 8.7, 2.4 Hz, 1H), 4.55 (d, *J* = 6.0 Hz, 2H), 3.91 (s, 3H). **^{13}C NMR** (126 MHz, DMSO) δ 161.44, 160.74, 149.14, 147.84, 138.92, 131.55, 131.46, 128.28, 127.26, 126.82, 112.05, 100.18, 56.15, 42.55. **LC-MS** *m/z* (ESI+) 310.3 ([M+H]$^+$.

Retention time: t_R = 3.89 min, >95%. Spectroscopic data matched those in the literature [175].

7-Methoxy-3-(piperidine-1-carbonyl)-2*H*-chromen-2-one (56)
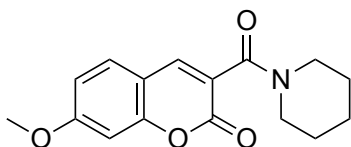
Synthesised according to general method **C** from 7-methoxy-chromene-3-carboxylic acid **47** (66 mg, 0.3 mmol, 1 equiv.) and piperidine (30 µL, 0.3 mmol, 1 equiv.), EDCI (116 mg, 0.6 mmol, 2 equiv.) and DMAP (92 mg, 0.75 mmol, 2.5 equiv.) to give the title compound as a white solid (0.054 g, 63%yield). **m.p.** 153–155°C (no lit m.p.). **¹H NMR** (400 MHz, DMSO-d_6) δ 8.10 (s, 1H), 7.70 (d, *J* = 8.6 Hz, 1H), 7.13 – 6.91 (m, 2H), 3.87 (s, 3H), 3.55 (t, *J* = 5.5 Hz, 2H), 3.29 (d, *J* = 11.0 Hz, 3H), 1.55 (ddt, *J* = 40.7, 11.2, 5.7 Hz, 6H). **¹³C NMR** (126 MHz, DMSO) δ 162.99, 162.88, 157.88, 155.37, 142.00, 129.99, 121.42, 112.87, 111.87, 100.58, 56.05, 47.2, 25.87, 25.19. **LC-MS** *m/z* (ESI+) 288.3 ([M+H]⁺. Retention time: t_R = 3.25 min, >95%. Spectroscopic data matched those in the literature [175].
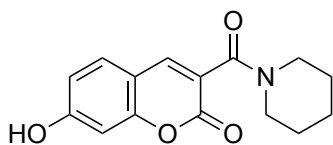
N,*N*-diethyl-7-methoxy-2-oxo-2*H*-chromene-3-carboxamide (57)
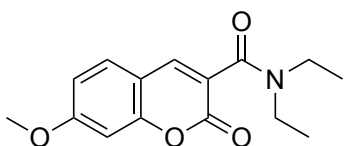
Synthesised according to general method **C** from 7-methoxy-chromene-3-carboxylic acid **47** (66 mg, 0.3 mmol, 1 equiv.) and diethyl amine (31 µL, 0.3 mmol, 1 equiv.), EDCI (116 mg, 0.6 mmol, 2 equiv.) and DMAP (92 mg, 0.75 mmol, 2.5 equiv.) to give the title compound as a yellow solid. (0.054 g, 66% yield). **m.p.** 122–124°C (no lit m.p.). **¹H NMR** (400 MHz, DMSO-d_6) δ 8.09 (d, *J* = 0.6 Hz, 1H), 7.69 (d, *J* = 8.6 Hz, 1H), 7.08 – 6.96 (m, 2H), 3.88 (s, 3H), 3.41 (d, *J* = 7.1 Hz, 3H), 3.24 (t, *J* = 7.1 Hz, 2H), 1.13 (t, *J* = 7.1 Hz, 3H), 1.06 (t, *J* = 7.1 Hz, 3H). **¹³C NMR** (126 MHz, DMSO) δ 163.74, 162.80, 149.17, 131.69, 128.21, 128.03, 113.86, 113.41, 111.58, 101.12, 60.94, 38.97, 14.10. **LC-MS** *m/z* (ESI+) 276.3 ([M+H]⁺. Retention time: t_R = 3.17 min, >95%. Spectroscopic data matched those in the literature [175].

Ethyl 7-(benzyloxy)-2-oxo-2*H*-chromene-3-carboxylate (48)
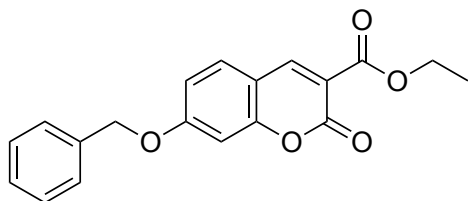
The 7-Hydroxy-chromene-3-carboxylic acid ethyl ester **41** (0.957 g, 4.16 mmol, 1 eq.) and potassium carbonate (6.9 g, 5.00 mmol, 1.2 eq.) were dissolved in DMF (8.5 mL) After stirring the mixture at room temperature for several minutes, benzyl bromide (0.7 ml, 5.85 mmol, 1.4 eq.) was added dropwise to the mixture. The reaction mixture was stirred at room temperature for 24 hours and monitored by TLC (70% EtOAc in hexanes) indicated that the reaction was completed. After completion of reaction, the residue taken up in CH_2Cl_2 (20 mL) and washed with H_2O (3 x 20 mL). The organic layer was dried over $MgSO_4$ and then added Brian (20 mL) on the organic layer then evaporate the solvent in vacuo, then added (20 mL) of hexane with stirring for 20 minutes, then take off the solution by pipet and filtrated. then we took the filtrated without further purification to give the title compound as white solid (1.20 g, 88% yield). **m.p.** 145–147°C (no lit m.p.). **¹H NMR** (400 MHz, DMSO-d_6) δ 8.73 (s, 1H), 7.87 (d, *J* = 8.7 Hz, 1H), 7.52 – 7.29 (m, 5H), 7.18 – 7.04 (m, 2H), 5.27 (s, 2H), 4.28 (q, *J* = 7.1 Hz, 2H), 1.31 (t, *J* = 7.1 Hz, 3H). **¹³C NMR** (126 MHz, DMSO) δ 163.74, 162.80, 156.85, 156.23, 149.17, 135.92, 131.69, 128.54, 128.21, 128.03, 113.86, 113.41, 111.58, 101.12, 70.17, 60.94, 14.10. **LC-MS** *m/z* (ESI+) 325.3 ([M+H]⁺. Retention time: t_R = 4.15 min, >95%. Spectroscopic data matched those in the literature [176].

7-(Benzyloxy)-2-oxo-2*H*-chromene-3-carboxylic acid (49)
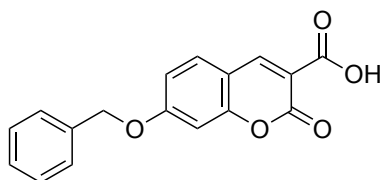
Synthesised according to general method **B** from ethyl 7-(benzyloxy)-2-oxo-2*H*-chromene-3-carboxylate **48** (0.8 g, 2.5 mmol, 1 equiv.) and NaOH (0.2 g, 5.0 mmol, 2 equiv.) to give the title compound as white solid (0.39 g, 54% yield). **m.p.** 192–195°C (no lit m.p.). **¹H NMR** (400 MHz, DMSO-d_6) δ 12.99 (s, 1H), 8.73 (s, 1H), 7.85 (d, *J* = 8.7 Hz, 1H), 7.59 – 7.23 (m, 5H), 7.21 – 6.97 (m, 2H), 5.27 (s, 2H). **¹³C NMR** (126 MHz, DMSO) δ 164.78, 164.05, 162.93, 162.81, 149.45, 149.22, 132.11, 131.64, 113.26, 112.04, 111.41, 110.40, 101.76,

100.25, 60.93. **LC-MS** *m/z* (ESI+) 297.3 ([M+H]⁺. Retention time: t$_R$ = 3.74 min, >95%. Spectroscopic data matched those in the literature [177].

### 6.5.5 General method D: Synthesis of diethyl 2-(2-nitrobenzylidene) malonates

The 2-nitrobenzaldehyde (2.75 mmol,1 equiv.) was dissolved in ethanol (5.5 mL), and diethyl malonate (3mmol, 1.1 equiv.), piperidine (0.55 mmol, 0.2 equiv.) and acetic acid (0.55 mmol, 0.2 equiv.) were added to the mixture. The mixture was stirred at 65°C for 36 hours and monitored by TLC (70% EtOAc in hexanes), which indicated that the reaction was completed. After completion of reaction, the reaction solution was allowed to cool to room temperature, and placed into ice bath, followed by extraction from 1N HCl (3 x10 mL) and ethyl acetate (25 mL). The organic layer was washed with 10%Na$_2$CO$_3$ (3 x 10mL) then washed by brine and dried over MgSO$_4$, filtered, and concentrated under reduced pressure *in vacuo* to give the crude product. The crude product was purified by open column chromatography (10–90%, EtOAc in hexanes) to give the tittle compound as a solid [178].

Diethyl 2-(4-methoxy-2- nitrobenzylidene) malonate (73)
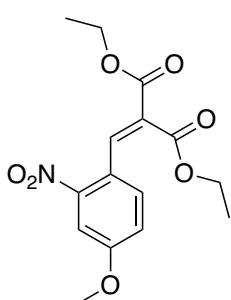
Synthesised according to general method **D** from 4-methoxy-2-nitrobenzaldehyde **70** (0.5 g, 2.75 mmol,1 equiv.), diethyl malonate (0.47 mL, 3mmol, 1.1 equiv.), piperidine (55 μL, 0.55 mmol, 0.2 equiv.) and acetic acid (26 μL, 0.55 mmol, 0.2 equiv.) Purified by open column chromatography (10–90%, EtOAc in hexanes) to give the title compound as a yellow solid (0.15 g, 17% yield).**¹H NMR** (500 MHz, DMSO-*d*$_6$) δ 8.02 (s, 1H), 7.73 (d, *J* = 2.5 Hz, 1H), 7.42 (d, *J* = 2.5 Hz, 1H), 7.40 (s, 1H), 4.27 (q, *J* = 7.1 Hz, 2H), 4.11 (q, *J* = 7.1 Hz, 2H), 3.91 (s, 3H), 1.27 (t, *J* = 7.1 Hz, 3H), 1.06 (t, *J* = 7.1 Hz, 3H). **LC-MS** *m/z* (ESI+) 324.3 ([M+H]⁺. Retention time: t$_R$ = 5.87 min, >95%.

Diethyl 2-(2-nitrobenzylidene) malonate (74)
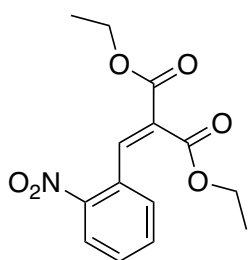
Synthesised according to general method **D** from 2-nitrobenzaldehyde **71** (1.66 g, 11 mmol, 1 equiv.), diethyl malonate (1.88 mL, 12 mmol, 1.1 equiv.), piperidine (0.22 mL, 2.2 mmol, 0.2 equiv.) and acetic acid (100 µL, 2.2 mmol, 0.2 equiv.). Purified by open column chromatography (10–90%, EtOAc in hexanes) to give the title compound as a yellow solid (0.8 g, 25% yield). **^{1}H NMR** ((500 MHz, DMSO-d_6) δ 8.24 (dd, J = 8.2, 1.2 Hz, 1H), 8.16 (s, 1H), 7.83 (td, J = 7.6, 1.3 Hz, 1H), 7.73 (qd, J = 7.6, 7.0, 1.4 Hz, 1H), 7.43 (dt, J = 7.7, 1.2 Hz, 1H), 4.28 (q, J = 7.1 Hz, 2H), 4.06 – 4.02 (q, J = 7.1 Hz, 2H), 1.27 (t, J = 7.1 Hz, 3H), 0.95 (t, J = 7.1 Hz, 3H). **LC-MS** m/z (ESI+) 294.3 ([M+H]$^+$. Retention time: t_R = 5.70 min, >95%.Spectroscopic data matched those in the literature [179].

**Diethyl 2-(4-bromo-2-nitrobenzylidene) malonate (75)**

Synthesised according to general method **D** from 4-bromo-2-nitrobenzaldehyde **72** (0.65 g, 2.75 mmol, 1 equiv.), diethyl malonate (0.47 mL, 3 mmol, 1.1 equiv.), piperidine (55 µL, 2.2 mmol, 0.2 equiv.) and acetic acid (26 µl, 0.2 equiv., 2.2 mmol). Purified by open column chromatography (10–90%, EtOAc in hexanes) to give the title compound as a yellow solid (0.475 g, 45% yield).**^{1}H NMR** (500 MHz, DMSO-d_6) δ 8.43 (d, J = 2.0 Hz, 1H), 8.10 – 8.01 (m, 2H), 7.38 (dd, J = 8.2, 0.9 Hz, 1H), 4.29 (q, J = 7.1 Hz, 2H), 4.10 (dq, J = 16.9, 7.1 Hz, 2H), 1.27 (t, J = 7.1 Hz, 3H), 1.01 (t, J = 7.1 Hz, 3H). **LC-MS** m/z (ESI+) 373.2 ([M+H]$^+$. Retention time: t_R = 7.91 min, >95%.

Diethyl 2-(4-fluoro-2-nitrobenzylidene) malonate (111)

Synthesised according to general method **D** from 4-floro-2-nitrobenzaldehyde **106** (0.47 g, 2.75 mmol,1 equiv.), diethyl malonate (0.47 mL, 3 mmol, 1.1 equiv.), piperidine (55 µL, 0.55 mmol, 0.2 equiv.) and acetic acid (26 µL, 0.55 mmol, 0.2 equiv.). Purified by open column chromatography (10–90%, EtOAc in hexanes) to give the title compound as a yellow solid (0.153 g, 18% yield).**^{1}H NMR** (500 MHz, DMSO-d_6) δ 8.18 (dd, *J* = 8.7, 2.7 Hz, 1H), 8.10 (s, 1H), 7.79 – 7.73 (m, 1H), 7.50 (dd, *J* = 8.7, 5.5 Hz, 1H),), 4.28 (q, *J* = 7.0 Hz, 2H), 4.08 (q, *J* = 14.1, 7.1 Hz, 2H),1.27 (t, *J* = 7.1 Hz, 3H), 1.00 (t, *J* = 7.1 Hz, 3H). **LC-MS** *m/z* (ESI+) 312.3 ([M+H]$^+$. Retention time: t$_R$ = 5.95 min, >95%.

Diethyl 2-(2,4-dinitrobenzylidene)malonate (112)

Synthesised according to general method **D** from 4-floro-2-nitrobenzaldehyde **107** (0.54 g, 2.75 mmol,1 equiv.), diethyl malonate (0.47 mL, 3 mmol, 1.1 equiv.), piperidine (55 µL, 0.55 mmol, 0.2 equiv.) and acetic acid (26 µL, 0.55 mmol, 0.2 equiv.). Purified by open column chromatography (10–90%, EtOAc in hexanes) to give the title compound as a yellow solid (0.184 g, 20% yield).**^{1}H NMR** (500 MHz, DMSO-d_6) δ 8.35 (d, *J* = 2.1 Hz, 1H), 8.18 (s, 1H), 8.05 (dd, *J* = 8.2, 2.2 Hz, 1H), 7.72 (dd, *J* = 7.1 Hz, 1H), 4.31 (q, *J* = 7.1 Hz, 2H), 4.05 (q, *J* = 7.1 Hz, 2H), 1.28 (t, *J* = 7.1 Hz, 3H), 1.01 (t, *J* = 7.1 Hz, 3H). **LC-MS** *m/z* (ESI+) 339.3 ([M+H]$^+$. Retention time: t$_R$ = 6.57 min, >95%.

2-(2-nitro-4-(trifluoromethyl)benzylidene) malonate (113)
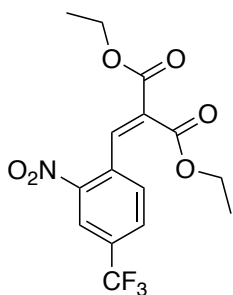
Synthesised according to general method **D** from 4-(trifluoromethyl)-2-nitrobenzaldehyde **108** (0.60 g, 2.75 mmol, 1 equiv.), diethyl malonate (0.47 mL, 3mmol, 1.1 equiv.), piperidine (55 µL, 0.55 mmol, 0.2 equiv.) and acetic acid (26 µL, 0.55 mmol, 0.2 equiv.). Purified by open column chromatography (10–90%, EtOAc in hexanes) to give the title compound as a yellow solid (0.25 g, 25% yield).**^{1}H NMR** (500 MHz, DMSO-d_6) δ 8.54 (d, J = 1.9 Hz, 1H), 8.24 (dd, J = 8.2, 1.9 Hz, 1H), 8.20 (s, 1H), 7.68 (d, J = 8.1 Hz, 1H), 4.30 (q, J = 7.0 Hz, 2H), 4.05 (q, J = 14.1, 7.1 Hz, 2H), 1.28 (t, J = 7.1 Hz, 3H), 0.96 (t, J = 7.1 Hz, 3H). **LC-MS** m/z (ESI+) 362.3 ([M+H]$^+$. Retention time: t_R = 6.25 min, >95%.

Diethyl 2-(4-(dimethylamino)-2-nitrobenzylidene) malonate (114)
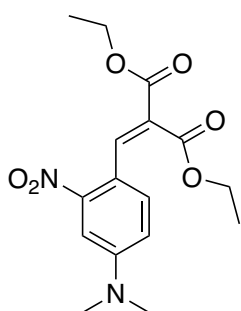
Synthesised according to general method **D** from 2-nitro-4-dimethylaminobenzaldehyde **109** (0.53 g, 2.75 mmol,1 equiv.), diethyl malonate (0.47 mL, 3 mmol, 1.1 equiv.), piperidine (55 µL, 0.55 mmol, 0.2 equiv.) and acetic acid (26 µL, 0.55 mmol, 0.2 equiv.). Purified by open column chromatography (10–90%, EtOAc in hexanes) to give the title compound as a yellow solid (0.219 g, 24% yield).**^{1}H NMR** (400 MHz, DMSO-d_6) δ 7.81 (s, 1H), 7.27 (s, 2H), 7.15 (d, J = 2.6 Hz, 1H), 4.26 (q, J = 14.1, 7.1 Hz, 2H), 4.16 (q, J = 7.0 Hz, 2H), 3.04 (s, 6H), 1.24 (t, J = 7.1 Hz, 3H), 1.15 (t, J = 7.1 Hz, 3H). **LR LC-MS MS** m/z (ESI+) 237.3 ([M+H]$^+$. Retention time: t_R = 6.13 min, >95%.
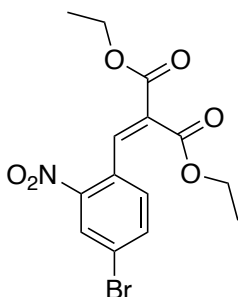
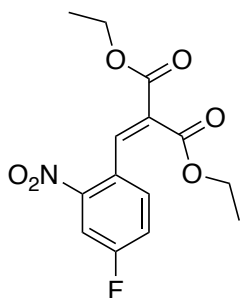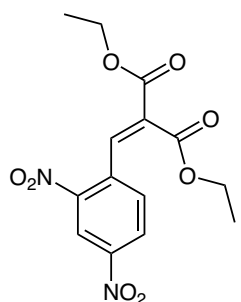**Diethyl 2-(4-chloro-2-nitrobenzylidene) malonate (115)**
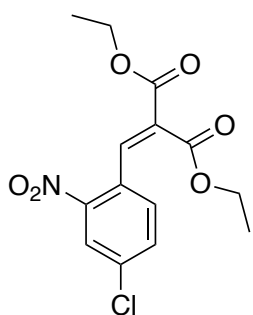
Synthesised according to general method **D** from 4-chloro-2-nitrobenzaldehyde **110** (0.51 g, 2.75 mmol, 1 equiv.), diethyl malonate (0.47 mL, 3 mmol, 1.1 equiv.), piperidine (55 µL, 0.55 mmol, 0.2 equiv.) and acetic acid (26 µL, 0.55 mmol, 0.2 equiv.). Purified by open column chromatography (10–90%, EtOAc in hexanes) to give the title compound as a yellow solid (0.24 g, 27% yield).[1]**H NMR** (500 MHz, DMSO-d_6) δ 8.33 (d, J = 2.1 Hz, 1H), 8.09 (s, 1H), 7.94 (dd, J = 8.3, 2.2 Hz, 1H), 7.46 (dd, J = 7.1 Hz, 1H), 4.28 (q, J = 7.1 Hz, 2H), 4.08 (q, J = 7.1 Hz, 2H), 1.27 (t, J = 7.1 Hz, 3H), 1.00 (t, J = 7.1 Hz, 3H). **LC-MS** m/z (ESI+) 328.6 ([M+H]+. Retention time: t_R = 6.16 min, >95%.

6.5.6 General method E: Synthesis of 2-quinolone-3-carboxylic acid ethyl esters

The crude product of 2-nitrobenzylidene malonate (0.434 mmol, 1 equiv.) was dissolved in acetic acid (5 mL). To the mixture, iron powder (1.735 mmol, 4 equiv.) was added. The mixture was stirred at 118°C for two hours and monitored by TLC (60% EtOAc in hexanes), which indicated that the reaction was completed. The reaction solution was allowed to cool to room temperature and placed into ice water, followed by extraction from H_2O (3 x 10 mL) and ethyl acetate (25 mL). The organic layer was washed with brine (3 x 10 mL) and dried over $MgSO_4$, filtered, and concentrated under reduced pressure *in vacuo* to yield a crude product containing the titled compound as a solid without purification.

Ethyl 7-methoxy-2-oxo-1,2-dihydroquinoline-3-carboxylate (76)
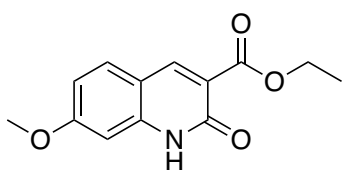
Synthesised according to general method **E** from diethyl 2-(4-methoxy-2-nitrobenzylidene) malonate **73** (0.135 g, 4.18 mmol,1 equiv.) and Fe (0.932 g, 16.70 mmol,4 equiv.) to give titled compound as an off-white solid (0.054 g, 52% yield). **^{1}H NMR** (500 MHz, DMSO-d_6) δ 11.89 (s,

1H), 8.47 (s, 1H), 7.76 (d, *J* = 8.8 Hz, 1H), 6.86 (dd, *J* = 8.8, 2.4 Hz, 1H), 6.80 (d, *J* = 2.4 Hz, 1H), 4.25 (q, *J* = 7.1 Hz, 2H), 1.30 (t, *J* = 7.1 Hz, 3H). **LC-MS** *m/z* (ESI+) 248.2 ([M+H]$^+$. Retention time: t_R = 4.44 min, >95%. Spectroscopic data matched those in the literature [180].

Ethyl 2-oxo-1,2-dihydroquinoline-3-carboxylate (77)
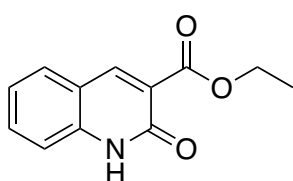
Synthesised according to general method **E** from diethyl 2-(2-nitrobenzylidene) malonate **74** (0.37 g, 1.27 mmol, 1 equiv.) and Fe (0.27 g, 4.80 mmol, 4 equiv.) to give titled compound as an off-white solid (0.25 g, 91% yield). **^{1}H NMR** (500 MHz, DMSO-d_6) δ 12.05 (s, 1H), 8.49 (s, 1H), 7.82 (dd, *J* = 7.9, 1.4 Hz, 1H), 7.61 (ddd, *J* = 8.5, 7.1, 1.4 Hz, 1H), 7.33 (d, *J* = 8.3 Hz, 1H), 7.26 – 7.20 (m, 1H), 4.27 (q, *J* = 7.1 Hz, 2H), 1.30 (t, *J* = 7.1 Hz, 3H). **LC-MS** *m/z* (ESI+) 218.1 ([M+H]$^+$. Retention time: t_R = 4.26 min, >95%.Spectroscopic data matched those in the literature [181].

Ethyl 7-bromo-2-oxo-1,2-dihydroquinoline-3-carboxylate (78)
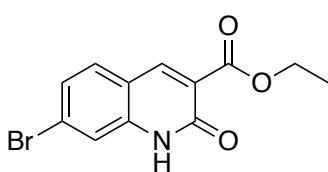
Synthesised according to general method **E** from diethyl 2-(4-bromo-2-nitrobenzylidene) malonate **75** (0.45 g, 1.20 mmol, 1 equiv.) and Fe (0.270 g, 4.8 mmol, 4 equiv.) to give titled compound as an off-white solid (0.20 g, 55% yield). **^{1}H NMR** (500 MHz, DMSO-d_6) δ 12.11 (s, 1H), 8.50 (s, 1H), 7.79 (d, *J* = 8.5 Hz, 1H), 7.50 (d, *J* = 1.8 Hz, 1H), 7.41 (dd, *J* = 8.4, 1.9 Hz, 1H), 4.28 (q, *J* = 7.1 Hz, 2H), 1.30 (t, *J* = 7.1 Hz, 3H). **LC-MS** *m/z* (ESI+) 297.1 ([M+H]$^+$. Retention time: t_R = 6.49 min, >95%.

Ethyl 7-fluoro-2-oxo-1,2-dihydroquinoline-3-carboxylate (116)

Synthesised according to general method **E** from diethyl 2-(4-fluoro-2-nitrobenzylidene) malonate **111** (0.135 g, 0.434 mmol, 1 equiv.) and Fe (0.097 g, 1.735 mmol, 4 equiv.) to give titled compound as an off-white solid (0.083 g, 81% yield). **¹H NMR** (400 MHz, DMSO-d_6) δ 12.12 (s, 1H), 8.53 (s, 1H), 7.93 (dd, J = 8.8, 6.1 Hz, 1H), 7.18 – 6.90 (m, 2H), 4.27 (q, J = 7.1 Hz, 2H), 1.30 (t, J = 7.1 Hz, 3H). **LC-MS** m/z (ESI+) 236.2 ([M+H]$^+$. Retention time: t_R = 4.50 min, >95%.

Ethyl 2-oxo-7-(trifluoromethyl)-1,2-dihydroquinoline-3-carboxylate (118)

Synthesised according to general method **E** from diethyl 2-(2-nitro-4-(trifluoromethyl)benzylidene)malonate **113** (0.200 g, 0.55 mmol, 1 equiv.) and Fe (0.124 g, 2.21 mmol, 4 equiv.) to give titled compound as an off-white solid (0.12 g, 76% yield). **¹H NMR** (500 MHz, DMSO-d_6) δ 12.33 (s, 1H), 8.58 (s, 1H), 8.07 (d, J = 8.2 Hz, 1H), 7.64 (m, 1H), 7.55 (dd, J = 8.2, 1.8 Hz, 1H), 4.29 (q, J = 7.1 Hz, 2H), 1.31 (t, J = 7.1 Hz, 3H). **LC-MS** m/z (ESI+) 286.2 ([M+H]$^+$. Retention time: t_R = 5.11 min, >95%.

Ethyl 7-(dimethylamino)-2-oxo-1,2-dihydroquinoline-3-carboxylate (119)

Synthesised according to general method **E** from 2-(4-(dimethylamino)-2-nitrobenzylidene) malonate **114** (0.185 g, 0.55 mmol, 1 equiv.) and Fe (0.123 g, 2.2 mmol, 4 equiv.) to give titled compound as an off-white solid (0.094 g, 66% yield). **¹H NMR** (500 MHz, DMSO-d_6) δ 14.82 (s, 1H), 12.63 (s, 1H), 8.80 (s, 1H), 7.79 (d, J = 9.1 Hz, 1H), 6.89 (dd, J = 9.1, 2.5 Hz, 1H), 6.46 (d, J = 2.4 Hz, 1H), 4.27 (q, J = 7.0 Hz, 2H), 3.09 (s, 6H), 1.24 (t, J

= 7.1 Hz, 3H). **LC-MS** *m/z* (ESI+) 261.3 ([M+H]$^+$. Retention time: t_R = 4.66 min, >95%.

Ethyl 7-chloro-2-oxo-1,2-dihydroquinoline-3-carboxylate (120)
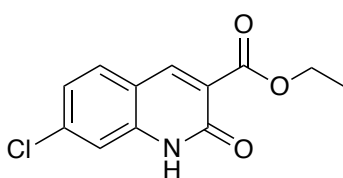
Synthesised according to general method **E** from diethyl 2-(4-chloro-2-nitrobenzylidene) malonate **115** (0.20 g, 0.61 mmol,1 equiv.) and Fe (0.136 g, 2.44 mmol, 4 equiv.) to give titled compound as an off-white solid (0.108 g, 70% yield). **^{1}H NMR** (500 MHz, DMSO-d_6) δ 12.14 (s, 1H), 8.52 (s, 1H), 7.87 (d, *J* = 7.1 Hz, 1H), 7.64 (d, *J* = 7.1 Hz, 2H), 4.28 (q, *J* = 7.1 Hz, 2H), 1.31 (d, *J* = 7.1 Hz, 3H). **LC-MS** *m/z* (ESI+) 252.6 ([M+H]$^+$. Retention time: t_R = 4.81 min, >95%. Spectroscopic data matched those in the literature [178].

6.5.7 General method F: Synthesis of 2-quinolone-3-carboxylic acids

The 2-quinolone-3-carboxylic acid ethyl esters (1 equiv.) and NaOH (2 equiv.) were dissolved in EtOH/H$_2$O (1:1 v/v) and added to the above reaction mixture. The reaction was stirred under reflux at 60° C. for 2 h, and the progress of the reaction was monitored by TLC (70% EtOAc in hexanes), which indicated that the reaction was completed. After the reaction was finished, the solution was cooled to room temperature, and hydrochloric acid was added dropwise to adjust the pH of the solution to 2-3. The solution was cooled over an ice bath for 2 hours, causing a large amount of precipitate to form. The precipitate was isolated via Buchner filtration, washed with H$_2$O, and dried *in vacuo* to yield a crude product containing the titled compound as a solid without purification [180].

7-Methoxy-2-oxo-1,2-dihydroquinoline-3-carboxylic acid (79)
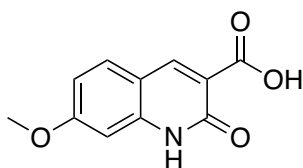
Synthesised according to general method **F** from ethyl 7-methoxy-2-oxo-1,2-dihydroquinoline-3-carboxylate **76** (0.05 g, 0.20 mmol, 1 equiv.) and NaOH (0.016 g ,0.40 mmol, 2 equiv.) to give titled compound as a white solid (0.023 g, 52%

yield). **m.p.** 258-260°C (no lit m.p.). **¹H NMR** (500 MHz, DMSO-d_6) δ 14.71 (s, 1H), 13.04 (s, 1H), 8.88 (s, 1H), 7.96 (d, J = 8.9 Hz, 1H), 7.04 (dd, J = 8.9, 2.5 Hz, 1H), 6.96 (d, J = 2.4 Hz, 1H), 3.89 (s, 3H). **¹³C NMR** (126 MHz, DMSO) δ 164.98, 164.40, 164.03, 146.14, 141.81, 132.16, 114.09, 113.87, 113.73, 98.04, 55.84. **LC-MS** *m/z* (ESI+) 221.0 ([M+H]⁺. Retention time: t_R = 4.41 min, >95%. Spectroscopic data matched those in the literature [180].

2-Oxo-1,2-dihydroquinoline-3-carboxylic acid (80)

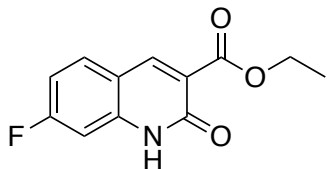Synthesised according to general method **F** from ethyl 2-oxo-1,2-dihydroquinoline-3-carboxylate **77** (0.200 g, 0.92 mmol, 1 equiv.) and NaOH (0.074 g ,1.8 mmol, 2 equiv.) to give titled compound as a white solid (0.098 g, 56% yield). **m.p.** 280–282°C (no lit m.p.). **¹H NMR** (500 MHz, DMSO-d_6) δ 15.06 (s, 1H), 13.24 (s, 1H), 8.95 (s, 1H), 8.04 (dd, J = 7.9, 1.4 Hz, 1H), 7.77 (ddd, J = 8.5, 7.1, 1.4 Hz, 1H), 7.53 (d, J = 8.3 Hz, 1H), 7.40 (ddd, J = 8.1, 7.0, 1.1 Hz, 1H). **¹³C NMR** (126 MHz, DMSO) δ 145.65, 133.66, 130.21, 123.68, 119.65, 117.60. **LC-MS** *m/z* (ESI+) 190.2 ([M+H]⁺. Retention time: t_R = 3.87 min, >95%. Spectroscopic data matched those in the literature [180].

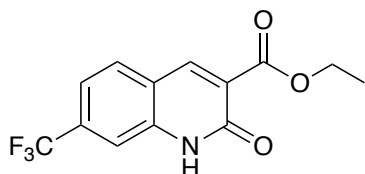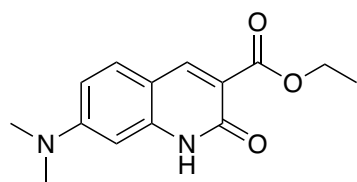### 7-Bromo-2-oxo-1,2-dihydroquinoline-3-carboxylic acid (81)

Synthesised according to general method **F** from ethyl 7-bromo-2-oxo-1,2-dihydroquinoline-3-carboxylate **78** (0.200 g, 0.200 mmol, 1 equiv.) and NaOH (0.065 g ,0.400 mmol, 2 equiv.) to give titled compound as a white solid (38 mg, 28% yield). **m.p.** 275–281°C (no lit m.p.). **IR (film)**: v_{max} 3138, 2973,1707,1658, ,1490, 879 cm⁻¹. **¹H NMR** (500 MHz, DMSO-d_6) δ 14.46 (s, 1H), 13.16 (s, 1H), 8.97 (s, 1H), 8.01 (d, J = 8.5 Hz, 1H), 7.68 (d, J = 1.8 Hz, 1H), 7.60 (dd, J = 8.4, 1.8 Hz, 1H). **¹³C NMR** (126 MHz, DMSO) δ 164.37, 163.69, 145.86, 140.23, 126.86, 132.14, 118.41, 118.37, 118.19. **LC-MS** *m/z* (ESI+) 269.9 ([M+H]⁺. Retention time: t_R = 5.37 min, >95%. **HRMS** (ESI+) measured 269.9587 [M+H]⁺. $C_{10}H_6BrNO_3^+$ calculated 267.9583.

7-Fluoro-2-oxo-1,2-dihydroquinoline-3-carboxylic acid (121)
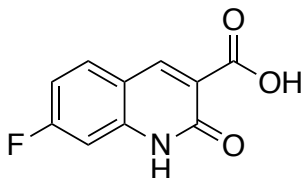
Synthesised according to general method **F** from ethyl 7-fluoro-2-oxo-1,2-dihydroquinoline-3-carboxylate **116** (0.075 g, 0.32 mmol, 1 equiv.) and NaOH (0.026 g, 0.64 mmol, 2 equiv.) to give titled compound as a white solid (0.038g, 58% yield). **m.p.** 128–130°C (no lit m.p.). **IR** (film): v_{max} 3153, 3071, 1714, 1662, 1625, 1509, 1464, 1084, 864 cm^{-1}. **^{1}H NMR** (500 MHz, DMSO-d_6) δ 14.63 (s, 1H), 13.25 (s, 1H), 8.98 (s, 1H), 8.15 (dd, J = 8.9, 6.1 Hz, 1H), 7.32 (td, J = 8.9, 2.5 Hz, 1H), 7.24 (dd, J = 10.0, 2.5 Hz, 1H). **^{13}C NMR** (126 MHz, DMSO) δ 164.12, 163.93, 145.80, 141.48, 116.92, 116.47, 112.85, 112.65, 102.34, 102.13. **LC-MS** m/z (ESI+) 208.1 ([M+H]$^+$. Retention time: t_R = 4.17 min, >95%. **HRMS** (ESI+) calculated for $C_{10}H_6FNO_3$ [M+Na]$^+$ 230.0229, found 230.0232.

2-Oxo-7-(trifluoromethyl)-1,2-dihydroquinoline-3-carboxylic acid (123)
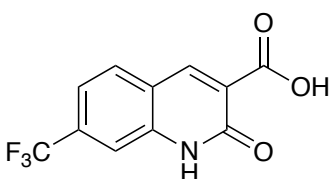
Synthesised according to general method **F** from ethyl 2-oxo-7-(trifluoromethyl)-1,2-dihydroquinoline-3-carboxylate **118** (0.1 g, 0.35 mmol, 1 equiv.) and NaOH (0.07 g, 1.75 mmol, 2 equiv.) to give titled compound as a white solid (0.053g, 59% yield). **m.p.** 148–150°C (no lit m.p.). **IR** (film): v_{max} 3164, 3078, 1718, 1647, 1472, 1323, 1207, 1133, 1069, 827 cm^{-1}. **^{1}H NMR** (500 MHz, DMSO-d_6) δ 16.33 (s, 1H), 13.40 (s, 1H), 9.02 (s, 1H), 8.28 (d, J = 8.3 Hz, 1H), 7.86 (s, 1H), 7.71 (d, J = 8.3 Hz, 1H). **^{13}C NMR** (126 MHz, DMSO) δ 164.26, 163.41, 145.20, 139.10, 132.63, 131.86, 124.53, 121.45, 120.86, 119.40, 113.07. **LC-MS** m/z (ESI+) 258.1 ([M+H]$^+$. Retention time: t_R = 4.89 min, >95%. **HRMS** (ESI+) calculated for $C_{11}H_6F_3NO_3$ [M+H]$^+$ 258.0378, found 258.0388.

7-(Dimethylamino)-2-oxo-1,2-dihydroquinoline-3-carboxylic acid (124)
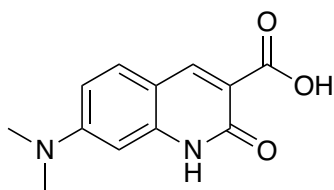
Synthesised according to general method **F** from ethyl 7-(dimethylamino)-2-oxo-1,2-dihydroquinoline-3-carboxylate **119** (0.08 g, 0.301 mmol, 1 equiv.) and NaOH (0.025 g, 0.615 mmol, 2 equiv.) to give titled compound as a white solid (0.041g, 57% yield). **m.p.** 190–192°C (no lit m.p.). **IR (film):** v_{max} 2922, 2881,1744,1625, 1509, 1394, 1192, 1155, 801 cm^{-1}. **^{1}H NMR** (500 MHz, DMSO-d_6) δ 14.75 (s, 1H), 12.58 (s, 1H), 8.68 (s, 1H), 7.77 (d, J = 9.1 Hz, 1H), 6.92 (dd, J = 9.1, 2.5 Hz, 1H), 6.51 (d, J = 2.4 Hz, 1H), 3.09 (s, 6H). **^{13}C NMR** (126 MHz, DMSO) δ 165.53, 164.87, 153.89, 145.49, 142.15, 131.51, 111.25, 110.56, 109.51, 94.21, 39.11. **LC-MS** m/z (ESI+) 233.2 ([M+H]$^+$. Retention time: t_R = 4.35 min, >95%. **HRMS** (ESI+) calculated for $C_{12}H_{12}N_2O_3$ [M+H]$^+$ 233.0926, found 233.0925.
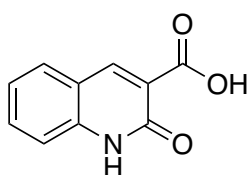
7-Chloro-2-oxo-1,2-dihydroquinoline-3-carboxylic acid (125)
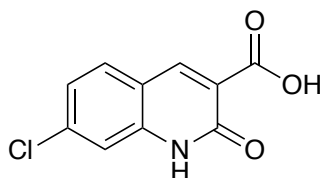
Synthesised according to general method **F** from ethyl 7-chloro-2-oxo-1,2-dihydroquinoline-3-carboxylate **120** (0.09 g, 0.36 mmol, 1 equiv.) and NaOH (0.029 g ,0.715 mm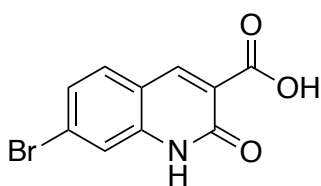ol, 2 equiv.) to give titled compound as a white solid (0.051g, 64% yield). **m.p.** 174–176°C (no lit m.p.). **^{1}H NMR** (500 MHz, DMSO-d_6) δ 15.68 (s, 1H), 13.29 (s, 1H), 8.98 (s, 1H), 8.09 (d, J = 8.4 Hz, 1H), 7.53 (dd, J = 60.1, 7.5 Hz, 2H).**^{13}C NMR** (126 MHz, DMSO) δ 164.41, 163.73, 145.75, 140.19, 138.37, 132.19, 124.17, 118.16, 117.95. **LC-MS** m/z (ESI+) 224.6 ([M+H]$^+$. Retention time: t_R = 4.53 min, >95%. Spectroscopic data matched those in the literature [180].

6.5.8 General method G: Synthesis of diethyl 2-amino methylene malonates

A solution of anilines (9.32 mmol, 1 equiv.) and diethyl ethoxy methylene malonate (9.32 mmol, 1 equiv.) in ethanol (20 mL) was prepared. The mixture was stirred at 90°C for 36 hours and monitored by TLC (70% EtOAc in hexanes),

which indicated that the reaction was completed. After cooling the reaction solution to room temperature and placing it in ice water, the solvent was removed under reduced pressure *in vacuo*, and the residue was extracted with H_2O (3 x 10 mL) and ethyl acetate (25 mL). The organic layer was washed with brine and dried over $MgSO_4$, filtered, and concentrated under reduced pressure *in vacuo* to yield the crude product. The crude product was purified by open column chromatography (20–80%, EtOAc in hexanes) to give the tittle compound as a solid. [182]

Diethyl 2-((*p*-tolylamino)methylene) malonate (88)
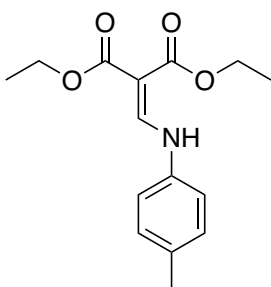
Synthesised according to general method **G** from *m*-toluidine **82** (1 mL, 9.32 mmol, 1 equiv.) and diethyl ethoxy methylene malonate (1.87 mL, 9.32 mmol, 1 equiv.). Purified by open column chromatography (20–80%, EtOAc in hexanes) to give the title compound as a yellow solid (0.406 g, 16% yield).[1]**H NMR** (500 MHz, DMSO-d_6) δ 10.65 (d, *J* = 13.9 Hz, 1H), 8.40 (d, *J* = 14.0 Hz, 1H), 7.27 (d, *J* = 7.8 Hz, 1H), 7.15 (t, *J* = 1.8 Hz, 1H), 6.99 (dd, *J* = 7.7, 1.3 Hz, 1H), 4.19 (q, *J* = 7.1 Hz, 2H), 4.11 (d, *J* = 7.1 Hz, 2H), 2.31 (s, 3H), 1.23 (dt, *J* = 9.3, 7.1 Hz, 6H). **LC-MS** *m/z* (ESI+) 278.3 ([M+H]$^+$. Retention time: t_R = 7.14 min, >95%. Spectroscopic data matched those in the literature [182]

Diethyl 2-(((4-ethylphenyl)amino)methylene) malonate (89)
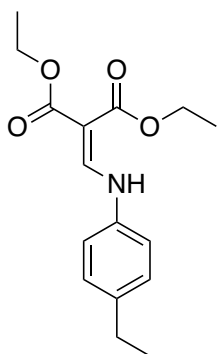
Synthesised according to general method **G** from 3-Ethylaniline **83** (1.16 mL, 9.32 mmol, 1 equiv.) and diethyl ethoxy methylene malonate (1.87 mL, 9.32 mmol, 1 equiv.). Purified by open column chromatography (20–80%, EtOAc in hexanes) to give the title compound as a yellow solid (0.433 g, 16% yield).[1]**H NMR** (500 MHz, DMSO-d_6) δ 10.67 (d, *J* = 13.9 Hz, 1H), 8.41 (d, *J* = 14.0 Hz, 1H), 7.30 (t, *J* = 7.8 Hz, 1H), 7.17 (t, *J* = 2.0 Hz, 1H), 7.14 (dd, *J* = 8.0, 2.4 Hz, 1H), 7.02 (d, *J* = 7.5 Hz, 1H), 4.19

(q, *J* = 7.1 Hz, 2H), 4.11 (q, *J* = 7.1 Hz, 2H), 2.60 (q, *J* = 7.6 Hz, 2H), 1.23 (dt, *J* = 9.8, 7.1 Hz, 6H), 1.19 – 1.15 (m, 3H). **LC-MS** *m/z* (ESI+) 292.3 ([M+H]⁺. Retention time: t$_R$ = 7.39 min, >95%.

Diethyl 2-(((4-isopropylphenyl)amino)methylene) malonate (90)
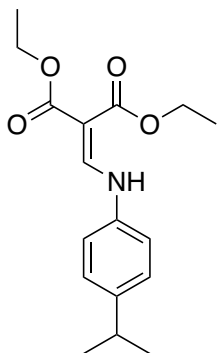
Synthesised according to general method **G** from 3-isopropylaniline **84** (1.26 mL, 9.32 mmol, 1 equiv.) and diethyl ethoxy methylene malonate (1.87 mL, 9.32 mmol, 1 equiv.). Purified by open column chromatography (20–80%, EtOAc in hexanes) to give the title compound as a yellow solid (0.607 g, 21% yield).**¹H NMR** (500 MHz, DMSO-*d₆*) δ 10.72 (d, *J* = 13.8 Hz, 1H), 8.43 (d, *J* = 13.9 Hz, 1H), 7.31 (t, *J* = 7.8 Hz, 1H), 7.25 (t, *J* = 2.0 Hz, 1H), 7.18 (ddd, *J* = 8.2, 2.4, 1.0 Hz, 1H), 7.05 (dt, *J* = 7.6, 1.3 Hz, 1H), 4.21 (q, *J* = 7.1 Hz, 2H), 4.16 – 4.10 (m, 2H), 2.91 (p, *J* = 6.9 Hz, 1H), 1.27 (dd, *J* = 10.4, 7.1 Hz, 6H), 1.19 (dd, *J* = 10.4, 7.1 Hz, 6H). **LC-MS** *m/z* (ESI+) 306.3 ([M+H]⁺. Retention time: t$_R$ = 7.59 min, >95%.

Diethyl 2-(((4-(trifluoromethyl)phenyl)amino)methylene) malonate (91)
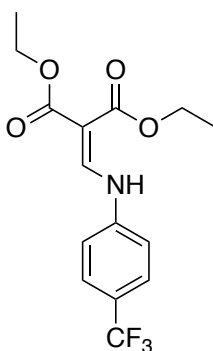
Synthesised according to general method **G** from 3-(trifluoromethyl)aniline **85** (1.15 mL, 9.32 mmol, 1 equiv.) and diethyl ethoxy methylene malonate (1.87 mL, 9.32 mmol, 1 equiv.). Purified by open column chromatography (20–80%, EtOAc in hexanes) to give the title compound as a yellow solid (0.846 g, 27% yield).**¹H NMR** (500 MHz, DMSO-*d₆*) δ 10.74 (s, 1H), 8.42 (s, 1H), 7.82 – 7.75 (m, 1H), 7.68 (dt, *J* = 7.8, 3.8 Hz, 1H), 7.63 – 7.56 (m, 1H), 7.46 (t, *J* = 7.5 Hz, 1H), 4.18 (dq, *J* = 38.7, 7.1 Hz, 4H), 1.26 (q, *J* = 7.6 Hz, 6H). **LC-MS** *m/z* (ESI+) 332.2 ([M+H]⁺. Retention time: t$_R$ = 7.31 min, >95%. Spectroscopic data matched those in the literature [182]

Diethyl 2-((benzo[*d*][1,3]dioxol-5-ylamino)methylene) malonate (92)
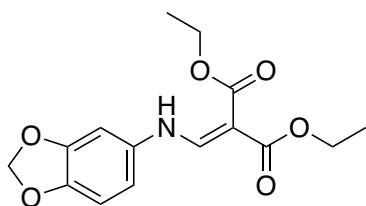
Synthesised according to general method **G** from 3,4-(methylenedioxy)aniline **86** (1.28 g, 9.32 mmol, 1 equiv.) and diethyl ethoxy methylene malonate (1.87 mL, 9.32 mmol, 1 equiv.). Purified by open column chromatography (20–80%, EtOAc in hexanes) to give the title compound as a yellow solid (0.988 g, 34% yield).**¹H NMR** (500 MHz, DMSO-*d₆*) δ 10.67 (d, *J* = 14.0 Hz, 1H), 8.29 (d, *J* = 13.9 Hz, 1H), 7.14 (d, *J* = 2.3 Hz, 1H), 6.92 (d, *J* = 8.3 Hz, 1H), 6.82 (dd, *J* = 8.4, 2.3 Hz, 1H), 6.05 (s, 2H), 4.20 (q, *J* = 7.1 Hz, 2H), 4.11 (q, *J* = 7.1 Hz, 2H), 1.25 (dt, *J* = 10.0, 7.1 Hz, 6H). **LC-MS** *m/z* (ESI+) 308.3 ([M+H]⁺. Retention time: t_R = 5.70 min, >95%. Spectroscopic data matched those in the literature [182]

Diethyl 2-(((4-chlorophenyl)amino)methylene) malonate (93)
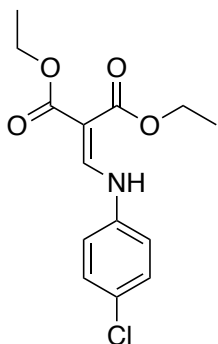
Synthesised according to general method **G** from 3-Chloroaniline **87** (1 mL, 9.32 mmol, 1equiv.) and diethyl ethoxy methylene malonate (1.87 mL, 9.32 mmol, 1 equiv.). Purified by open column chromatography (20–80%, EtOAc in hexanes) to give the title compound as a yellow solid (0.639 g, 23% yield).**¹H NMR** (400 MHz, DMSO-*d₆*) δ 10.63 (s, 1H), 8.37 (s, 1H), 7.56 (t, *J* = 2.0 Hz, 1H), 7.46 – 7.31 (m, 2H), 7.20 (dt, *J* = 7.6, 1.5 Hz, 1H), 4.11 (q, *J* = 7.0 Hz, 4H), 1.26 (t, *J* = 7.1 Hz, 6H). **LC-MS** *m/z* (ESI+) 298.1 ([M+H]⁺. Retention time: t_R = 6.20 min, >95%.

6.5.9 General method H: Synthesis of 4-quinolone-3-carboxylic acid ethyl esters

The crude product of diethyl 2-amino methylene malonates (1.5 mmol, 1 equiv.) in diphenyl ether (37.86 mmol, 25 equiv.) was heated at 250°C for 2 h and monitored by TLC (70% EtOAc in hexanes) indicated that the reaction was completed. After cooling to r.t it was diluted with an equal volume of n-hexane, precipitated solid was separated by filtration, washed with diethyl ether. The

residue was dried under reduced pressure *in vacuo* to give corresponding compound as a solid without further purification [182].

Ethyl 7-methyl-4-oxo-1,4-dihydroquinoline-3-carboxylate (94)
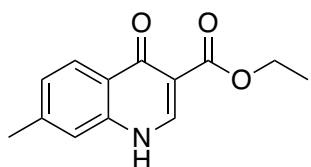
Synthesised according to general method **H** from diethyl 2-((*p*-tolylamino)methylene) malonate **88** (0.332 g, 1.2 mmol, 1 equiv.) and diphenyl ether (5 mL, 30 mmol, 25 equiv.) to give titled compound as a yellow solid (0.118 g, 43% yield). **^{1}H NMR** (400 MHz, DMSO-*d$_6$*) δ 12.18 (s, 1H), 8.49 (s, 1H), 8.04 (s, 1H), 7.38 (s, 1H), 7.24 (s, 1H), 4.36 – 4.01 (m, 2H), 2.44 (s, 3H), 1.28 (s, 3H). **LC-MS** *m/z* (ESI+) 232.1 ([M+H]$^+$. Retention time: t$_R$ = 5.45 min, >95%. Spectroscopic data matched those in the literature [182]

Ethyl 7-ethyl-4-oxo-1,4-dihydroquinoline-3-carboxylate (95)
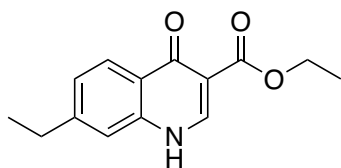
Synthesised according to general method **H** from diethyl 2-(((4-ethylphenyl)amino)methylene) malonate **89** (0.294 g, 1.0 mmol, 1 equiv.) and diphenyl ether (4 mL, 25 mmol, 25 equiv.) to give titled compound as a yellow solid (0.173 g, 70% yield). **^{1}H NMR** (500 MHz, DMSO-*d$_6$*) δ 12.23 (s, 1H), 8.51 (s, 1H), 8.07 (d, *J* = 8.2 Hz, 1H), 7.40 (d, *J* = 1.5 Hz, 1H), 7.29 (dd, *J* = 8.2, 1.6 Hz, 1H), 4.21 (q, *J* = 7.1 Hz, 2H), 2.75 (q, *J* = 7.6 Hz, 2H), 1.28 (t, *J* = 7.1 Hz, 3H), 1.24 (t, *J* = 7.6 Hz, 3H). **LC-MS** *m/z* (ESI+) 246.3 ([M+H]$^+$. Retention time: t$_R$ = 4.26 min, >95%. Spectroscopic data matched those in the literature [183].

Ethyl 7-isopropyl-4-oxo-1,4-dihydroquinoline-3-carboxylate (96)
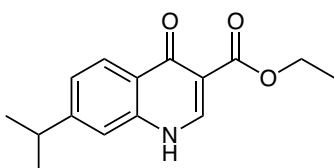
Synthesised according to general method **H** from diethyl 2-(((4-isopropylphenyl)amino)methylene) malonate **90** (0.366 g, 1.2 mmol, 1 equiv.) and diphenyl ether (5 mL, 30 mmol, 25 equiv.) to give titled compound as a yellow solid (0.213 g, 69% yield). **^{1}H NMR** (400 MHz, DMSO-*d$_6$*)

δ12.37 (s, 1H), 8.51 (s, 1H), 8.08 (d, *J* = 8.3 Hz, 1H), 7.42 (d, *J* = 1.6 Hz, 1H), 7.33 (d, *J* = 8.4 Hz, 1H), 4.26 – 4.13 (m, 2H), 2.98 (p, *J* = 29.4 Hz, 1H), 1.21 (dd, *J* = 33.4, 7.0 Hz, 6H), 1.14 (dd, *J* = 33.4, 7.0 Hz, 3H). **LC-MS** *m/z* (ESI+) 260.3 ([M+H]$^+$. Retention time: t$_R$ = 4.54 min, >95%. Spectroscopic data matched those in the literature [184].

Ethyl 4-oxo-7-(trifluoromethyl)-1,4-dihydroquinoline-3-carboxylate (97)
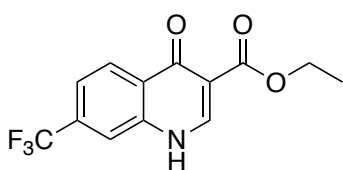
Synthesised according to general method **H** from diethyl 2-(((4-(trifluoromethyl)phenyl)amino)methylene) malonate **91** (0.398 g, 1.2 mmol, 1 equiv.) and diphenyl ether (5 mL, 30 mmol, 1 equiv.) to give titled compound as a yellow solid (0.211 g, 62% yield). **¹H NMR** (500 MHz, DMSO-*d₆*) δ 12.53 (s, 1H), 8.71 (s, 1H), 8.35 (d, *J* = 8.4 Hz, 1H), 7.98 (s, 1H), 7.68 (d, *J* = 8.5 Hz, 1H), 4.23 (q, *J* = 7.1 Hz, 2H), 1.29 (t, *J* = 7.1 Hz, 3H). **LC-MS** *m/z* (ESI+) 286.1 ([M+H]$^+$. Retention time: t$_R$ = 4.79 min, >95%. Spectroscopic data matched those in the literature [182]

Ethyl 8-oxo-5,8-dihydro-[1,3]dioxolo[4,5-*g*]quinoline-7-carboxylate (98)
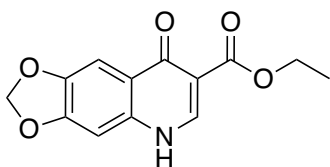
Synthesised according to general method **H** from diethyl 2-((benzo[*d*][1,3]dioxol-5-ylamino)methylene) malonate **92** (0.737 g, 2.4 mmol, 1 equiv.) and diphenyl ether (10 mL, 60 mmol, 25 equiv.) to give titled compound as a yellow solid (0.463 g, 73% yield). **¹H NMR** (400 MHz, DMSO-*d₆*) δ 12.17 (s, 1H), 8.43 (s, 1H), 7.45 (d, *J* = 6.8 Hz, 1H), 7.07 (s, 1H), 6.18 (s, 2H), 4.21 (qd, *J* = 7.2, 4.1 Hz, 2H), 1.28 (td, *J* = 7.1, 2.4 Hz, 3H). **LC-MS** *m/z* (ESI+) 262.3 ([M+H]$^+$. Retention time: t$_R$ = 3.76 min, >95%. Spectroscopic data matched those in the literature [182].

Ethyl 7-chloro-4-oxo-1,4-dihydroquinoline-3-carboxylate (99)
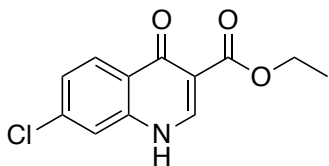
Synthesised according to general method **H** from diethyl 2-(((4-chlorophenyl)amino)methylene) malonate **93** (0.357 g, 1.2 mmol, 1 equiv.) and diphenyl ether (5 mL, 30 mmol, 25 equiv.) to give titled compound as a yellow solid (0.207 g, 69% yield). **¹H NMR** (400 MHz, DMSO-d_6) δ 12.35 (s, 1H), 8.60 (s, 1H), 8.14 (d, J = 8.6 Hz, 1H), 7.68 (d, J = 2.0 Hz, 1H), 7.45 (dd, J = 8.7, 2.0 Hz, 1H), 4.22 (q, J = 7.1 Hz, 2H), 1.28 (t, J = 7.1 Hz, 3H). **LC-MS** m/z (ESI+) 252.6 ([M+H]⁺. Retention time: t_R = 4.20 min, >95%. Spectroscopic data matched those in the literature [185].

6.5.10 General method I: Synthesis of 4-quinolone-3-carboxylic acids

The 4-quinolone-3-carboxylic acid ethyl esters (1 equiv.) and NaOH (2 equiv.) were dissolved in EtOH/H_2O (1:1 v/v) and added to the above reaction mixture. The reaction was stirred under reflux at 60° C. for 2 h, and the progress the reaction was detected by TLC (70% EtOAc in hexanes), which indicated that the reaction was completed. After the reaction was complete, the solution was cooled to room temperature, and hydrochloric acid was added dropwise to adjust the pH of the solution to 2-3. The solution was cooled over an ice bath for 2 hours, and a large amount of precipitate was generated. The precipitate was isolated via Buchner filtration, washed with H_2O, and dried *in vacuo* to yield a crude product containing the titled compound as a solid without purification. [182]

7-Methyl-4-oxo-1,4-dihydroquinoline-3-carboxylic acid (100)

Synthesised according to general method **I** from ethyl 7-methyl-4-oxo-1,4-dihydroquinoline-3-carboxylate **94** (0.080 g, 0.35 mmol, 1 equiv.) and NaOH (0.027 g ,0.69 mmol, 2 equiv.) to give titled compound as a white solid (0.041 g, 58% yield). **m.p.** 226 – 228 °C (no lit m.p.). **¹H NMR** (500 MHz, DMSO-d_6) δ 15.48 (s, 1H), 13.29 (s, 2H), 8.85 (s, 1H), 8.20 (d, J = 8.2 Hz, 1H), 7.59 (s, 1H), 7.45 (dd, J =

8.4, 1.6 Hz, 1H), 2.44 (s, 3H).**¹³C NMR** (126 MHz, DMSO) δ 177.74, 166.73, 145.18, 144.67, 127.97, 124.90, 122.23, 119.10, 117.05, 107.29, 21.41. **LC-MS** *m/z* (ESI+) 204.2 ([M+H]⁺. Retention time: t_R = 4.15 min, >95%. Spectroscopic data matched those in the literature [182]

7-Ethyl-4-oxo-1,4-dihydroquinoline-3-carboxylic acid (101)
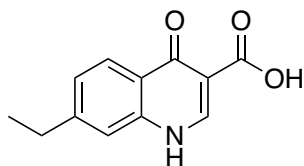
Synthesised according to general method **I** from ethyl 7-ethyl-4-oxo-1,4-dihydroquinoline-3-carboxylate **95** (0.15 g, 0.6 mmol, 1 equiv.) and NaOH (0.049 g ,1.2 mmol, 2 equiv.) to give titled compound as a white solid (0.068 g, 51% yield). **m.p.** 218 – 220 °C (no lit m.p.). **¹H NMR** (500 MHz, DMSO-d_6) δ 15.51 (s, 1H), 13.33 (s,12H), 8.86 (s, 1H), 8.22 (d, *J* = 8.4 Hz, 1H), 7.62 (d, *J* = 1.5 Hz, 1H), 7.50 (dd, *J* = 8.3, 1.6 Hz, 1H), 2.82 (q, *J* = 7.6 Hz, 2H), 1.27 (t, *J* = 7.6 Hz, 3H). **¹³C NMR** (126 MHz, DMSO) δ 178.01, 166.55, 150.50, 145.13, 139.98, 126.78, 125.04, 122.50, 117.80, 107.37, 28.27, 14.88. **LC-MS** *m/z* (ESI+) 218.2 ([M+H]⁺. Retention time: t_R = 3.50 min, >95%. Spectroscopic data matched those in the literature [183].

### 7-Isopropyl-4-oxo-1,4-dihydroquinoline-3-carboxylic acid (102)
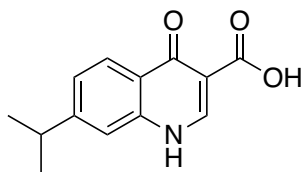
Synthesised according to general method **I** from ethyl 7-isopropyl-4-oxo-1,4-dihydroquinoline-3-carboxylate **96** (0.180 g, 0.7 mmol, 1 equiv.) and NaOH (0.056 g ,1.4 mmol, 2 equiv.) to give titled compound as a white solid (0.077g, 48% yield). **m.p.** 227–229°C (no lit m.p.). **IR** (film): v_{max} 2959, 2870, 1684, 1613, 1584,1472, 1364, 1274, 1215, 894, 797 cm⁻¹. **¹H NMR** (500 MHz, DMSO-d_6) δ 15.47 (s, 1H), 13.32 (s, 1H), 8.87 (s, 1H), 8.24 (d, *J* = 8.5 Hz, 1H), 7.65 (d, *J* = 1.6 Hz, 1H), 7.49 (d, *J* = 1.6 Hz 1H), 3.11 (p, *J* = 6.9 Hz, 1H), 1.24 (dd, *J* = 8.5 Hz, 6H). **¹³C NMR** (126 MHz, DMSO) δ 178.09, 166.47, 155.02, 145.01, 139.76, 125.14, 122.63, 116.26, 107.76, 107.15, 33.61, 23.30, 23.03. **LC-MS** *m/z* (ESI+) 232.2 ([M+H]⁺. Retention time: t_R = 4.03 min, >95%. **HRMS** (ESI+) measured 232.0976 [M+H]⁺. $C_{16}H_{17}{}^{35}ClFN_2O^+$ calculated 232.0974.

4-Oxo-7-(trifluoromethyl)-1,4-dihydroquinoline-3-carboxylic acid (103)
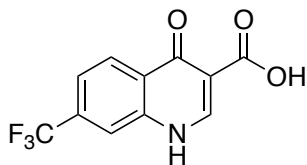
Synthesised according to general method **I** from ethyl 4-oxo-7-(trifluoromethyl)-1,4-dihydroquinoline-3-carboxylate **97** (0.180g, 0.63 mmol, 1 equiv.) and NaOH (0.050 g ,1.260 mmol, 2 equiv.) to give titled compound as a white solid (0.093g, 57% yield). **m.p.** 233–236°C (no lit m.p.). **^{1}H NMR** (400 MHz, DMSO-d_6) δ 14.92 (s, 1H), 13.61 (s, 1H), 9.08 (s, 1H), 8.51 (d, J = 8.2 Hz, 1H), 8.20 (s, 1H), 7.91 (d, J = 8.4 Hz, 1H). **^{13}C NMR** (126 MHz, DMSO) δ 180.28, 146.89, 139.80, 133.92, 127.55, 127.13, 121.65, 121.63, 117.61, 110.32, 61.48. **LC-MS** m/z (ESI+) 258.2 ([M+H]$^+$. Retention time: t_R = 3.72 min, >95%. Spectroscopic data matched those in the literature [182]

8-Oxo-5,8-dihydro-[1,3]dioxolo[4,5-*g*]quinoline-7-carboxylic acid (104)
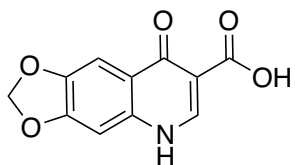
Synthesised according to general method **I** from ethyl 8-oxo-5,8-dihydro-[1,3]dioxolo[4,5-*g*]quinoline-7-carboxylate **98** (0.3 g, 1.15 mmol, 1 equiv.) and NaOH (0.09 g, 2.3 mmol, 2 equiv.) to give titled compound a white solid (0.174 g, 65% yield). **m.p.** 274–276°C (no lit m.p.). **^{1}H NMR** (400 MHz, DMSO-d_6) δ 15.19 (s, 1H), 13.44 (s, 1H), 8.74 (d, J = 4.1 Hz, 1H), 7.56 (s, 1H), 7.28 (s, 1H), 6.27 (s, 2H).**^{13}C NMR** (126 MHz, DMSO) δ 176.64, 166.61, 152.96, 147.34, 143.03, 137.14, 120.01, 106.91, 103.01, 101.25, 97.74. **LC-MS** m/z (ESI+) 234.2 ([M+H]$^+$. Retention time: t_R = 2.89 min, >95%. Spectroscopic data matched those in the literature [182]
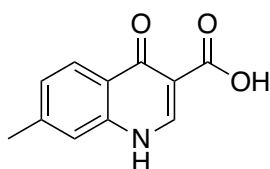
7-Chloro-4-oxo-1,4-dihydroquinoline-3-carboxylic acid (105)
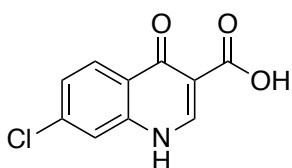
Synthesised according to general method **I** from ethyl 7-chloro-4-oxo-1,4-dihydroquinoline-3-carboxylate **99** (0.180 g, 0.7 mmol, 1 equiv.) and NaOH (0.057 g ,1.4 mmol, 2 equiv.) to give titled compound as a white solid (0.083g, 52% yield). **m.p.** 251–253°C (no lit m.p.). **^{1}H NMR** (400 MHz, DMSO-d_6)

δ 13.58 (s, 1H), 8.93 (d, *J* = 3.8 Hz, 1H), 8.29 (d, *J* = 8.7 Hz, 1H), 7.91 (d, *J* = 2.0 Hz, 1H), 7.64 (dd, *J* = 8.7, 2.0 Hz, 1H). **^{13}C NMR** (126 MHz, DMSO) δ 177.86, 166.01, 146.00, 140.24, 138.44, 127.33, 126.57, 123.17, 118.87, 108.08. **LC-MS** *m/z* (ESI+) 224.1 ([M+H]$^+$. Retention time: t_R = 3.49 min, >95%. Spectroscopic data matched those in the literature [186].

6.5.11 General method J: Synthesis of sulphonyl-1,2,3,4-tetrahydroquinolines

The 1,2,3,4-tetrahydroquinoline (4.2 mmol, 1.0 equiv.) was dissolved in dry pyridine (10 mL). sulphonyl chloride (5.9 mmol, 1.4 equiv.) was added dropwise, and the reaction mixture was stirred overnight at room temperature. Monitoring by TLC (70% EtOAc in hexanes) indicated that the reaction was completed. The solvent was evaporated under reduced pressure *in vacuo*. A solution of HCl 1N (50 mL) and EtOAc (50 mL) were added. The organic layer was separated, and the aqueous phase was extracted twice with EtOAc (2x50 mL). The combined organic phase was dried over MgSO$_4$ and the solvent was evaporated under reduced pressure *in vacuo* to yield the pure product containing the titled compound as a solid without further purification [187].

1-(Methylsulfonyl)-1,2,3,4-tetrahydroquinoline (135)
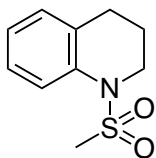
Synthesised according to general method **J** from 1,2,3,4-tetrahydroquinoline **136** (0.56 g, 4.2 mmol, 1.0 equiv.) and methane sulphonyl chloride **137** (0.67 g, 5.9 mmol, 1.4 equiv.) to give title compound as a pink solid (0.75 g, 84% yield). **m.p.** 78–81°C (no lit m.p.). **^{1}H NMR** (500 MHz, DMSO-*d$_6$*) δ 7.54 (dd, *J* = 8.1, 1.4 Hz, 1H), 7.20 – 7.13 (m, 2H), 7.07 (td, *J* = 7.4, 1.2 Hz, 1H), 3.72 – 3.67 (m, 2H), 3.02 (s, 3H), 2.80 (t, *J* = 6.6 Hz, 2H), 1.97 – 1.88 (m, 2H). **^{13}C NMR** (126 MHz, DMSO) δ 136.84, 129.59, 129.57, 126.27, 124.05, 122.37, 45.85, 38.35, 26.36, 21.72. **LC-MS** *m/z* (ESI+) 212.1 ([M+H]$^+$. Retention time: t_R = 5.19 min, >95%. Spectroscopic data matched those in the literature [187].

1-(Ethylsulphonyl)-1,2,3,4-tetrahydroquinoline (142)
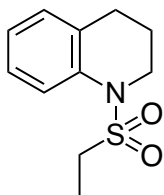
Synthesised according to general method **J** from 1,2,3,4-tetrahydroquinoline **136** (0.56 g, 4.2 mmol, 1.0 equiv.) and ethane sulphonyl chloride **138** (0.75 g, 5.9 mmol, 1.4 equiv.) to give title compound as a pink oil (0.54 g, 57% yield). **¹H NMR** (500 MHz, DMSO-d_6) δ 7.50 (dd, J = 8.3, 1.3 Hz, 1H), 7.19 – 7.11 (m, 2H), 7.04 (td, J = 7.4, 1.3 Hz, 1H), 3.72 – 3.66 (m, 2H), 3.24 (q, J = 7.3 Hz, 2H), 2.80 (t, J = 6.7 Hz, 2H), 1.97 – 1.88 (m, 2H), 1.20 (t, J = 7.3 Hz, 3H).**¹³C NMR** (126 MHz, DMSO) δ 136.98, 129.55, 129.11, 126.20, 123.73, 121.90, 45.94, 45.85, 26.34, 22.15, 7.76. **LC-MS** m/z (ESI+) 226.1 ([M+H]⁺, Retention time: t_R = 5.48 min, >95%. Spectroscopic data matched those in the literature [188].

1-(Cyclopropylsulphonyl)-1,2,3,4-tetrahydroquinoline (143)
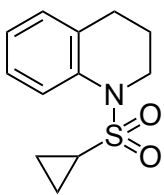
Synthesised according to general method **J** from 1,2,3,4-tetrahydroquinoline **136** (0.56 g, 4.2 mmol, 1.0 equiv.) and cyclopropanesulphonyl chloride **139** (0.65 g, 5.9 mmol, 1.4 equiv.) to give title compound as a pink solid (0.68 g, 68% yield). **m.p.** 28–30°C (no lit m.p.). **IR (film)**: v_{max} 1334, 1148, 1084,1039, 842, 756, 708 cm⁻¹. **¹H NMR** (500 MHz, DMSO-d_6) δ 7.53 (d, J = 8.2 Hz, 1H), 7.20 – 7.11 (m, 2H), 7.08 (t, J = 7.2 Hz, 1H), 3.69 (d, J = 3.9 Hz, 2H), 2.82 (t, J = 6.8 Hz, 2H), 2.71 (tt, J = 7.9, 4.9 Hz, 1H), 2.02 – 1.90 (m, 2H), 0.97 – 0.86 (m, 4H). **¹³C NMR** ¹³C NMR (126 MHz, DMSO) δ 136.96, 130.11, 129.47, 126.05, 124.40, 123.35, 46.10, 28.98, 26.14, 21.85, 4.92, 4.29. **LC-MS** m/z (ESI+) 238.1 ([M+H]⁺. Retention time: t_R = 5.59 min, >95%. **HRMS** (ESI+) measured 238.0895 [M+H]⁺, $C_{12}H_{15}N_2O_2S^+$ calculated 238.0896.

1-(Phenylsulphonyl)-1,2,3,4-tetrahydroquinoline (144)

Synthesised according to general method **J** from 1,2,3,4-tetrahydroquinoline **136** (0.56 g, 4.2 mmol, 1.0 equiv.) and benzene sulphonyl chloride **140** (1.04 g, 5.9 mmol, 1.4 equiv.) to give title compound as a pink solid (0.73 g, 64% yield). **m.p.** 64–66°C (no lit m.p.). **1H NMR** (500 MHz, DMSO-d_6) δ 7.70 – 7.51 (m, 6H), 7.23 – 7.16 (m, 1H), 7.13 – 7.04 (m, 2H), 3.80 – 3.75 (m, 2H), 2.41 (t, J = 6.6 Hz, 2H), 1.62 – 1.53 (m, 2H). **13C NMR** (126 MHz, DMSO) δ 138.87, 136.23, 133.31, 130.55, 129.42, 129.31, 126.65, 126.23, 124.86, 123.79, 46.17, 25.88, 21.01. **LC-MS** m/z (ESI+) 274.1 ([M+H]$^+$. Retention time: t_R = 6.08 min, >95%. Spectroscopic data matched those in the literature [189].

1-((4-Methoxyphenyl)sulphonyl)-1,2,3,4-tetrahydroquinoline (145)

Synthesised according to general method **J** from 1,2,3,4-tetrahydroquinoline **136** (0.56 g, 4.2 mmol, 1.0 equiv.) and 4-methoxybenzenesulphonyl chloride **141** (1.22 g, 5.9 mmol, 1.4 equiv.) to give title compound as a an off white solid (0.33 g, 26% yield). **m.p.** 72-75°C (no lit m.p.). **1H NMR** (500 MHz, DMSO-d_6) δ 7.62 (d, J = 8.2 Hz, 1H), 7.56 – 7.48 (m, 2H), 7.22 – 7.14 (m, 1H), 7.11 – 7.02 (m, 4H), 3.81 (s, 3H), 3.77 – 3.71 (m, 2H), 2.44 (t, J = 6.7 Hz, 2H), 1.62 – 1.53 (m, 2H). **13C NMR** (126 MHz, DMSO) δ 162.70, 140.76, 136.36, 130.49, 130.44, 129.30, 128.92, 127.00, 126.14, 123.83, 114.55, 112.73, 55.66, 55.09, 46.08, 25.97. **LC-MS** m/z (ESI+) 304.1 ([M+H]$^+$. Retention time: t_R = 6.10 min, >95%. Spectroscopic data matched those in the literature [190].

6.5.12 General method K: Synthesis of sulphonyl-1,2,3,4-tetrahydroisoquinolines
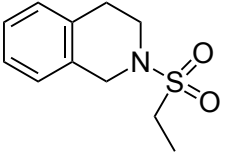
The 1,2,3,4-tetrahydroisoquinoline (4.2 mmol, 1.0 equiv.) was dissolved in dry pyridine (10 mL). sulphonyl chloride (5.9 mmol, 1.4 equiv.) was added dropwise, and the reaction mixture was stirred overnight at room temperature. Monitoring by TLC (70% EtOAc in hexanes) indicated that the reaction was completed. The

solvent was evaporated under reduced pressure *in vacuo*. A solution of HCl 1N (50 mL) and EtOAc (50 mL) were added. The organic layer was separated, and the aqueous phase was extracted twice with EtOAc (2x50 mL). The combined organic phase was dried over MgSO₄ and the solvent was evaporated under reduced pressure *in vacuo* to yield the pure product containing the titled compound   as a solid without further purification [187].

2-(Methylsulphonyl)-1,2,3,4-tetrahydroisoquinoline (147)

Synthesised according to general method **K** from 1,2,3,4-tetrahydroisoquinoline**146** (0.56 g, 4.2 mmol, 1.0 equiv.) and methane sulphonyl chloride **137** (0.67 g, 5.9 mmol, 1.4 equiv.) to give title compound as a yellow solid (0.79 g, 89% yield). **m.p.** 123–125°C (no lit m.p.). **¹H NMR** (500 MHz, DMSO-*d₆*) δ 7.20 (d, *J* = 1.5 Hz, 4H), 4.36 (s, 2H), 3.43 (t, *J* = 6.0 Hz, 2H), 2.95 (s, 3H), 2.92 (t, *J* = 6.0 Hz, 2H).**¹³C NMR** (126 MHz, DMSO) δ 133.23, 132.06, 128.77, 128.48, 126.59, 126.42, 126.12, 46.83, 43.03, 40.07, 28.17. **LC-MS** *m/z* (ESI+) 212.1 ([M+H]⁺. Retention time: t_R = 5.02 min, >95%. Spectroscopic data matched those in the literature [191].

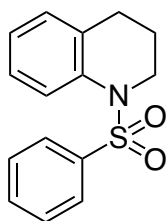**2-(Ethylsulphonyl)-1,2,3,4-tetrahydroisoquinoline (148)**

Synthesised according to general method **K** from 1,2,3,4-tetrahydroisoquinoline **146** (0.56 g, 4.2 mmol, 1.0 equiv.) and ethane sulphonyl chloride **138** (0.75 g, 5.9 mmol, 1.4 equiv.) to give title compound as an off-white solid (0.38 g, 40% yield). **m.p.** 56–59°C. **IR (film)**: ν_max 1319,1140,957, 920, 738 cm⁻¹. **¹H NMR** (500 MHz, DMSO-*d₆*) δ 7.23 – 7.14 (m, 4H), 4.42 (s, 2H), 3.50 (t, *J* = 6.0 Hz, 2H), 3.13 (q, *J* = 7.4 Hz, 2H), 2.89 (t, *J* = 6.0 Hz, 2H), 1.22 (t, *J* = 7.4 Hz, 3H). **¹³C NMR** (126 MHz, DMSO) δ 133.39, 132.43, 128.85, 126.54, 126.26, 126.08, 46.56, 43.20, 42.86, 28.39, 7.57. **LC-MS** *m/z* (ESI+) 226.2 ([M+H]⁺. Retention time: Rt= 5.25 (>95%). **HRMS** (ESI+) measured 226.1083 [M+H]⁺, C₁₄H₁₅NO₄⁺ calculated 226.1079.

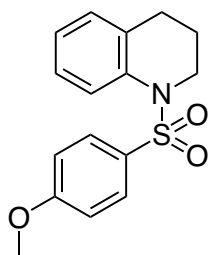**2-(Cyclopropylsulphonyl)-1,2,3,4-tetrahydroisoquinoline (149)**
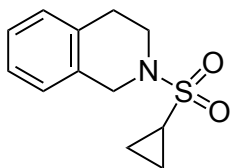
Synthesised according to general method **K** from 1,2,3,4-tetrahydroisoquinoline **146** (0.56 g, 4.2 mmol, 1.0 equiv.) and cyclopropanesulphonyl chloride **139** (0.65 g, 5.9 mmol, 1.4 equiv.) to give title compound as an off-white solid (0.61 g, 61% yield). **m.p.** 77–80 °C (no lit m.p.). **IR (film)**: v_{max} 1326, 1148, 1066, 1017, 954, 883, 741 cm^{-1}. **^{1}H NMR** (500 MHz, DMSO-d_6) δ 7.19 (d, J = 1.8 Hz, 4H), 4.43 (s, 2H), 3.50 (t, J = 6.0 Hz, 2H), 2.91 (t, J = 6.0 Hz, 2H), 2.63 (tt, J = 7.8, 5.1 Hz, 1H), 0.97 (tt, J = 8.0, 2.6 Hz, 4H). **^{13}C NMR** (126 MHz, DMSO) δ 133.22, 132.26, 127.92, 126.97, 126.59, 126.34, 47.16, 43.46, 37.21, 25.50, 4.27, 4.02. **LC-MS** m/z (ESI+) 238.2 ([M+H]$^+$. Retention time: t_R = 5.39 min, >95%. **HRMS** (ESI+) measured 260.0719 [M+Na]$^+$. $C_{12}H_{15}NO_2S^+$ calculated 260.0721.

2-(Phenylsulphonyl)-1,2,3,4-tetrahydroisoquinoline (150)
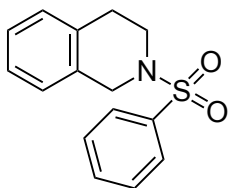
Synthesised according to general method **K** from 1,2,3,4-tetrahydroIsoquinoline **146** (0.56 g, 4.2 mmol, 1.0 equiv.) and benzene sulphonyl chloride **140** (1.04 g, 5.9 mmol, 1.4 equiv.) to give title compound as an off-white solid (0.85 g, 74% yield). **m.p.** 146–150°C (no lit m.p.). **^{1}H NMR** (500 MHz, DMSO-d_6) δ 7.87 – 7.81 (m, 2H), 7.75 – 7.68 (m, 1H), 7.65 (dd, J = 8.3, 6.9 Hz, 2H), 7.18 – 7.08 (m, 4H), 4.20 (s, 2H), 3.30 (t, J = 6.0 Hz, 3H), 2.85 (t, J = 6.0 Hz, 2H).**^{13}C NMR** (126 MHz, DMSO) δ 135.82, 133.21, 132.93, 131.52, 131.51, 129.42, 128.64, 127.38, 126.62, 126.40, 126.10, 125.44, 47.04, 43.28, 27.61. **LC-MS** m/z (ESI+) 274.2 ([M+H]$^+$. Retention time: t_R = 5.96 min, >95%. Spectroscopic data matched those in the literature [189].

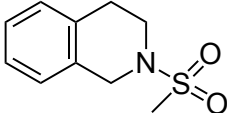## 2-((4-Methoxyphenyl)sulphonyl)-1,2,3,4-tetrahydroisoquinoline (151)
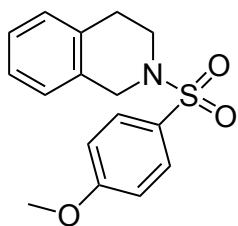
Synthesised according to general method **K** from 1,2,3,4-tetrahydroisoquinoline **146** (0.56 g, 4.2 mmol, 1.0 equiv.) and 4-methoxybenzenesulphonyl chloride **141** (1.22 g, 5.9 mmol, 1.4 equiv.) to give title compound as a yellow solid (0.53 g, 42% yield). **m.p.** 127–130°C (no lit m.p.). **IR (film)**: v_{max} 1336, 1151, 950, 920, 738 cm^{-1}. **^{1}H NMR** (500 MHz, DMSO-d_6) δ 7.80 – 7.74 (m, 2H), 7.15 (dq, J = 6.0, 3.1 Hz, 5H), 7.12 (dt, J = 7.1, 2.6 Hz, 1H), 4.15 (s, 2H), 3.85 (s, 3H), 3.25 (t, J = 6.0 Hz, 2H), 2.86 (t, J = 6.0 Hz, 2H). **^{13}C NMR** (126 MHz, DMSO) δ 162.72, 132.97, 131.61, 129.67, 128.63, 127.15, 126.59, 126.39, 126.06, 55.68, 47.25, 40.00, 39.83, 39.66, 39.49, 39.32, 39.16, 38.99, 27.99. **LC-MS** m/z (ESI+) 304.2 ([M+H]$^{+}$. Retention time: t_R = 6.02 min, >95%. **HRMS** (ESI+) measured 326.0828 [M+Na]$^{+}$. $C_{16}H_{17}NO_3S^{+}$ calculated 326.0827.

6.5.13 General method L: Synthesis of sulphonyl-1*H*-indole-carbonitriles

A mixture of indole-carbonitrile (2.11 mmol, 1.0 equiv.) and tetrabutylammonium hydrogen sulphate (TBAHS) (0.32 mmol, 0.15 equiv.) in toluene (6.25 mL) at 0 °C was added 50% aqueous sodium hydroxide (6.25 mL) and sulphonyl chloride (3.2 mmol, 1.5 equiv.). The resultant solution was stirred at room temperature for 16 h. After this time monitoring by TLC (70% EtOAc in hexanes) indicated that the reaction was completed. The organic layer was separated, washed with 1 N HCl (3 × 10 mL), saturated aqueous NaHCO₃ (3 × 10 mL), water (10 mL), brine (10 mL), dried over MgSO₄ and the solvent was evaporated under reduced pressure *in vacuo* to give a crude product. The crude product was purified by Biotage Selekt chromatography (5–40%, EtOAc in hexanes) to yield the corresponding compound as a solid [192] .

1-(Methylsulphonyl)-1*H*-indole-5-carbonitrile (152)
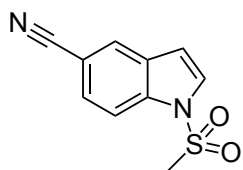
Synthesised according to general method **L** from indole-5-carbonitrile **127** (0.30g, 2.11 mmol, 1.0 equiv.), tetrabutylammonium hydrogen sulphate (TBAHS) (0.11g, 0.32 mmol, 0.15 equiv.) and methane sulphonyl chloride **137** (0.25 ml, 3.2 mmol, 1.5 equiv.). Purified by Biotage Selekt chromatography (5–40%, EtOAc in hexanes) to give the title compound as a white solid (0.11 g, 24% yield). **m.p.** 76–78°C. **IR (film)**: v_{max} 2221, 1372, 1133, 1088, 767, 730 cm^{-1}. **^{1}H NMR** ^{1}H NMR (400 MHz, DMSO-d_6) δ 8.27 (dd, *J* = 1.7, 0.7 Hz, 1H), 8.02 (dt, *J* = 8.7, 0.8 Hz, 1H), 7.83 – 7.74 (m, 2H), 6.96 (dd, *J* = 3.7, 0.9 Hz, 1H), 3.57 (s, 3H).**^{13}C NMR** (126 MHz, DMSO) δ 128.99, 127.31, 126.67, 125.72, 123.65, 114.11, 112.65, 107.67, 102.07, 41.49. **LC-MS** *m/z* (ESI+) 221.0 ([M+H]$^+$. Retention time: t_R = 5.08 min, >95%. **HRMS** (ESI+) measured 221. 0380 [M+H]$^+$. $C_{10}H_6N_2O_2S^+$ calculated 221.0379.

1-(Ethylsulphonyl)-1*H*-indole-5-carbonitrile (153)
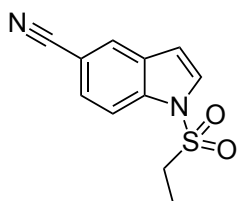
Synthesised according to general method **L** from indole-5-carbonitrile **127** (0.30g, 2.11 mmol, 1.0 equiv.), tetrabutylammonium hydrogen sulphate (TBAHS) (0.11g, 0.32 mmol, 0.15 equiv.) and ethane sulphonyl chloride **138** (0.30 ml, 3.2 mmol, 1.5 equiv.). Purified by Biotage Selekt chromatography (5–40%, EtOAc in hexanes) to give the title compound as a white solid (0.10 g, 20% yield). **m.p.** 66–70°C (no lit m.p.). **IR (film)**: v_{max} 2217, 1356, 1162,1136, 771, 723 cm^{-1}. **^{1}H** (500 MHz, DMSO-d_6) δ 8.28 (d, *J* = 1.7 Hz, 1H), 8.02 (d, *J* = 8.6 Hz, 1H), 7.82 (d, *J* = 3.7 Hz, 1H), 7.78 (dd, *J* = 8.7, 1.7 Hz, 1H), 6.97 (d, *J* = 3.6 Hz, 1H), 3.73 (q, *J* = 7.3 Hz, 2H), 1.08 (t, *J* = 7.3 Hz, 3H). **^{13}C NMR** (126 MHz, DMSO-d_6) δ 129.56, 127.36, 126.75, 125.71, 123.64, 114.12, 112.65, 107.57, 102.07, 48.65, 7.73. **LC-MS** *m/z* (ESI+) 235.0 ([M+H]$^+$. Retention time: t_R = 5.35 min, >95%. **HRMS** (ESI+) measured 235.0533 [M+H]$^+$. $C_{11}H_{10}N_2O_2S^+$ calculated 235.05336.

1-(Cyclopropylsulphonyl)-1H-indole-5-carbonitrile (154)
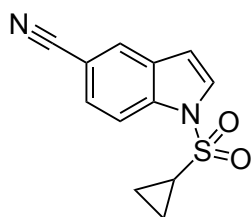
Synthesised according to general method **L** from indole-5-carbonitrile **127** (0.30g, 2.11 mmol, 1.0 equiv.), tetrabutylammonium hydrogen sulphate (TBAHS) (0.11g, 0.32 mmol, 0.15 equiv.) and cyclopropanesulphonyl chloride **139** (0.33 ml, 3.2 mmol, 1.5 equiv.). Purified by Biotage Selekt chromatography (5–40%, EtOAc in hexanes) to give the title compound as a white solid (0.12 g, 23% yield). **m.p.** 73–77°C (no lit m.p.). **IR (film)**: v_{max} 2220, 1363, 1136, 995, 775, 726 cm^{-1}. **^{1}H NMR** (500 MHz, DMSO-d_6) δ 8.28 (d, J = 1.9 Hz, 1H), 8.12 – 8.03 (m, 1H), 7.84 (d, J = 3.6 Hz, 1H), 7.78 (dd, J = 8.7, 1.7 Hz, 1H), 6.97 (d, J = 3.6 Hz, 1H), 3.22 (tt, J = 7.9, 4.7 Hz, 1H), 1.31 (qd, J = 5.7, 1.3 Hz, 2H), 1.15 – 1.10 (m, 2H). **^{13}C NMR** (126 MHz, DMSO-d_6) δ 129.40, 128.09, 127.36, 126.74, 125.72, 123.64, 114.26, 112.66, 107.85, 102.07, 39.96 – 38.61 (m), 31.24, 6.01. **LC-MS** m/z (ESI+) 247.0 ([M+H]$^+$. Retention time: t_R = 5.49 min, >95%. **HRMS** (ESI+) measured 247.0534 [M+H]$^+$. $C_{12}H_{10}N_2O_2S^+$ calculated 247.0536.

1-(Phenylsulphonyl)-1*H*-indole-5-carbonitrile (155)

Synthesised according to general method **L** from indole-5-carbonitrile **127** (0.30g, 2.11 mmol, 1.0 equiv.), tetrabutylammonium hydrogen sulphate (TBAHS) (0.11g, 0.32 mmol, 0.15 equiv.) and benzene sulphonyl chloride **140** (0.40 ml, 3.2 mmol, 1.5 equiv.). Purified by Biotage Selekt chromatography (5–40%, EtOAc in hexanes) to give the title compound as a white solid (0.14 g, 24% yield). **m.p.** 110–114°C (no lit m.p.). **^{1}H NMR** (500 MHz, DMSO-d_6) δ 8.19 (d, J = 1.6 Hz, 1H), 8.13 (d, J = 8.6 Hz, 1H), 8.09 – 8.00 (m, 3H), 7.78 – 7.72 (m, 2H), 7.67 – 7.60 (m, 2H), 6.97 (d, J = 3.7 Hz, 1H). **^{13}C NMR** (126 MHz, DMSO) δ 137.57, 130.43, 129.37, 129.16, 128.07, 127.85, 127.58, 127.38, 126.75, 119.18, 115.16, 112.68, 108.84, 105.85, 102.10, 55.91. **LC-MS** m/z (ESI+) 282.7 ([M+H]$^+$. Retention time: t_R = 5.89 min, >95%. Spectroscopic data matched those in the literature [193].

1-((4-Methoxyphenyl)sulphonyl)-1*H*-indole-5-carbonitrile (156)

Synthesised according to general method **L** from indole-5-carbonitrile **127** (0.30g, 2.11 mmol, 1.0 equiv.), tetrabutylammonium hydrogen sulphate (TBAHS) (0.11g, 0.32 mmol, 0.15 equiv.) and 4-methoxybenzenesulphonyl chloride **141** (0.66 g, 3.2 mmol, 1.5 equiv.). Purified by Biotage Selekt chromatography (5–40%, EtOAc in hexanes) to give the title compound as a white solid (0.27 g, 41% yield). **m.p.** 116–119°C (no lit m.p.). **IR (film)**: v_{max} 2219, 1263,1140, 1088, 832, 674 cm^{-1}. **^{1}H NMR** (500 MHz, DMSO-d_6) δ 8.19 (d, J = 1.6 Hz, 1H), 8.14 – 8.07 (m, 1H), 8.03 – 7.93 (m, 3H), 7.74 (dd, J = 8.7, 1.7 Hz, 1H), 7.17 – 7.07 (m, 2H), 6.94 (d, J = 3.7 Hz, 1H), 3.80 (s, 3H). **^{13}C NMR** (126 MHz, DMSO-d_6) δ 129.37, 129.17, 128.08, 127.59, 126.78, 125.72, 123.65, 115.20, 114.09, 112.66, 108.84, 102.09, 40.05 – 38.69 (m). **LC-MS** m/z (ESI+) 313.0 ([M+H]$^+$. Retention time: t_R = 5.99 min, >95%. **HRMS** (ESI+) measured 313.0652 [M+H]$^+$, $C_{16}H_{12}N_2O_3S^+$ calculated 313.0641.

1-(Methylsulphonyl)-1*H*-indole-6-carbonitrile (157)

Synthesised according to general method **L** from indole-6-carbonitrile **130** (0.30g, 2.11 mmol, 1.0 equiv.), tetrabutylammonium hydrogen sulphate (TBAHS) (0.11g, 0.32 mmol, 0.15 equiv.) and methane sulphonyl chloride **137** (0.25 ml, 3.2 mmol, 1.5 equiv.). Purified by Biotage Selekt chromatography (5–40%, EtOAc in hexanes) to give the title compound as a white solid (0.13 g, 28% yield). **m.p.** 131–135°C (no lit m.p.). **IR (film)**: v_{max} 2220, 1365, 1118,1006, 834, 761, 723 cm^{-1}. **^{1}H NMR** (500 MHz, DMSO-d_6) δ 8.31 – 8.24 (m, 1H), 7.94 – 7.86 (m, 2H), 7.71 (dd, J = 8.2, 1.4 Hz, 1H), 6.99 (dd, J = 3.6, 0.8 Hz, 1H), 3.61 (s, 3H). **^{13}C NMR** (126 MHz, DMSO) δ 133.62, 133.13, 130.45, 125.95, 122.75, 119.50, 117.46, 107.85, 106.04, 41.45. **LC-MS** m/z (ESI+) 221.0 ([M+H]$^+$. Retention time: t_R = 5.11 min, >95%. **HRMS** (ESI+) measured 221.0378 [M+H]$^+$. $C_{10}H_8N_2O_2S^+$ calculated 221.0379.

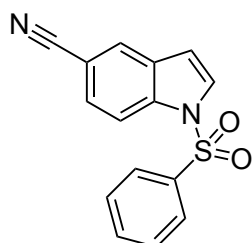## 1-(Ethylsulphonyl)-1*H*-indole-6-carbonitrile (158)
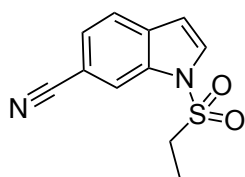
Synthesised according to general method **L** from indole-6-carbonitrile **130** (0.30g, 2.11 mmol, 1.0 equiv.), tetrabutylammonium hydrogen sulphate (TBAHS) (0.11g, 0.32 mmol, 0.15 equiv.) and ethane sulphonyl chloride **138** (0.30 ml, 3.2 mmol, 1.5 equiv.). Purified by Biotage Selekt chromatography (5–40%, EtOAc in hexanes) to give the title compound as a white solid (0.12 g, 24% yield). **m.p.** 127–130°C (no lit m.p.). **IR (film)**: v_{max} 2221, 1356, 1155, 1118, 1002, 816, 719 cm^{-1}. **^{1}H NMR** (500 MHz, DMSO-d_6) δ 8.26 (d, *J* = 1.3 Hz, 1H), 7.94 – 7.88 (m, 2H), 7.71 (dd, *J* = 8.2, 1.4 Hz, 1H), 7.00 (dd, *J* = 3.6, 0.8 Hz, 1H), 3.78 (q, *J* = 7.3 Hz, 2H), 1.09 (t, *J* = 7.3 Hz, 3H). **^{13}C NMR** (126 MHz, DMSO) δ 133.55, 133.45, 131.05, 126.02, 122.86, 119.45, 117.40, 107.75, 106.15, 48.49, 7.67. **LC-MS** *m/z* (ESI+) 235.0 ([M+H]$^+$. Retention time: t_R = 5.37 min, >95%. **HRMS** (ESI+) measured 235.0536 [M+H]$^+$. $C_{11}H_{10}N_2O_2S^+$ calculated 335.0545.
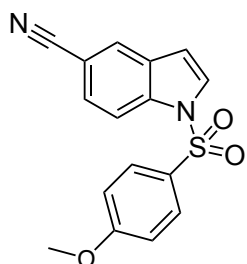
1-(Cyclopropylsulphonyl)-1*H*-indole-6-carbonitrile (159)
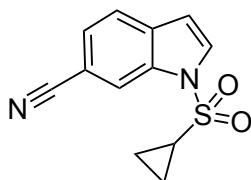
Synthesised according to general method **L** from indole-6-carbonitrile **130** (0.30g, 2.11 mmol, 1.0 equiv.), tetrabutylammonium hydrogen sulphate (TBAHS) (0.11g, 0.32 mmol, 0.15 equiv.) and cyclopropanesulphonyl chloride **139** (0.33 ml, 3.2 mmol, 1.5 equiv.). Purified by Biotage Selekt chromatography (5–40%, EtOAc in hexanes) to give the title compound as a white solid (0.10 g, 19% yield). **m.p.** 57–59°C (no lit m.p.). **^{1}H NMR** (500 MHz, DMSO-d_6) δ 8.31 (d, *J* = 3.3 Hz, 1H), 7.93 – 7.89 (m, 3H), 7.71 (dd, *J* = 8.1, 1.4 Hz, 1H), 7.00 (d, *J* = 3.6 Hz, 1H), 3.32 (tt, *J* = 7.8, 4.7 Hz, 1H), 1.32 (tt, *J* = 5.7, 3.0 Hz, 2H), 1.17 – 1.08 (m, 2H). **^{13}C NMR** (126 MHz, DMSO) δ 129.40, 127.36, 126.74, 125.72, 123.64, 114.26, 112.66, 107.85, 102.07, 39.62, 31.24, 6.01. **LC-MS** *m/z* (ESI+) 246.8 ([M+H]$^+$. Retention time: t_R = 5.49 min, >95%. Spectroscopic data matched those in the literature [194].

1-(Phenylsulphonyl)-1*H*-indole-6-carbonitrile (160)
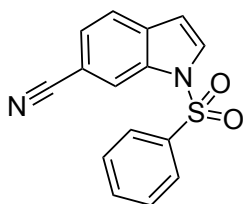
Synthesised according to general method **L** from indole-6-carbonitrile **130** (0.30g, 2.11 mmol, 1.0 equiv.), tetrabutylammonium hydrogen sulphate (TBAHS) (0.11g, 0.32 mmol, 0.15 equiv.) and benzene sulphonyl chloride **140** (0.40 ml, 3.2 mmol, 1.5 equiv.) Purified by Biotage Selekt chromatography (5–40%, EtOAc in hexanes) to give the title compound as a white solid (0.17 g, 29% yield). **m.p.** 97-101°C (no lit m.p.). **^{1}H NMR** (500 MHz, DMSO-d_6) δ 8.39 (s, 1H), 8.17 – 8.12 (m, 3H), 7.83 (d, *J* = 8.2 Hz, 1H), 7.73 (dd, *J* = 8.0, 2.8 Hz, 2H), 7.67 – 7.63 (m, 3H), 7.00 (d, *J* = 3.6 Hz, 1H). **^{13}C NMR** (126 MHz, DMSO) δ 135.11, 130.66, 130.04, 129.89, 126.99, 126.70, 123.01, 121.46, 121.14, 117.17, 116.33, 109.57, 102.01. **LC-MS** *m/z* (ESI+) 282.9 ([M+H]$^+$. Retention time: t_R = 5.89 min, >95%. Spectroscopic data matched those in the literature [194] .
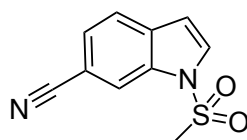
1-((4-Methoxyphenyl)sulphonyl)-1*H*-indole-6-carbonitrile (161)
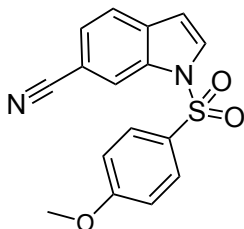
Synthesised according to general method **L** from indole-6-carbonitrile **130** (0.30g, 2.11 mmol, 1.0 equiv.), tetrabutylammonium hydrogen sulphate (TBAHS) (0.11g, 0.32 mmol, 0.15 equiv.) and 4-methoxybenzenesulphonyl chloride **141** (0.66 g, 3.2 mmol, 1.5 equiv.). Purified by Biotage Selekt chromatography (5–40%, EtOAc in hexanes) to give the title compound as a white solid (0.29 g, 44% yield). **m.p.** 100–104°C (no lit m.p.). **IR (film)**: v_{max} 2219, 1271, 1159,1086, 834, 674 cm^{-1}. **^{1}H NMR** (500 MHz, DMSO-d_6) δ 8.37 (dt, *J* = 1.4, 0.8 Hz, 1H), 8.10 (d, *J* = 3.6 Hz, 1H), 8.09 – 8.05 (m, 2H), 7.82 (dd, *J* = 8.2, 0.8 Hz, 1H), 7.68 – 7.64 (m, 1H), 7.14 – 7.09 (m, 2H), 6.97 (dd, *J* = 3.7, 0.9 Hz, 1H), 3.81 (s, 3H). **^{13}C NMR** (126 MHz, DMSO) δ 164.10, 133.91, 132.97, 130.66, 129.88, 129.52, 126.43, 122.94, 121.47, 121.15, 120.69, 117.12, 109.18, 106.48, 102.02, 55.89. **LC-MS** *m/z* (ESI+) 312.8 ([M+H]$^+$. Retention time: t_R = 5.99 min, >95%. **HRMS** (ESI+) measured 313.0636 [M+H]$^+$. $C_{16}H_{12}N_2O_2S^+$ calculated 313.0641.

6.5.14 General method M: Synthesis of 5-Arylisoxazol-3-amines

To a mixture of aryl acetonitrile (5 mmol, 1.0 equiv.) and H_2O (10 mL) was added NaOH (6.2 mmol, 1.25 equiv.). When the NaOH pellets had completely dissolved, hydroxylamine sulphate (5.45 mmol,1.1 equiv.) was added and the pH was measured (pH 7–8), after 5 minutes. The reaction was warmed to 45 °C and stirred for 72 h. HCl (0.65 mL, 7.9 mmol, 37%,1.6 equiv.) was added in one portion and the reaction was warmed to 50 °C for 2. 5 h. Monitoring by TLC (70% EtOAc in hexanes) indicated that the reaction was completed. The reaction mixture was removed from the oil bath and allowed to cool to room temperature. Then, a solution of NaOH (30% in H_2O) was added to adjust the pH of the solution to 11. EtOAc was then added, and the layers separated. The aqueous layer was extracted with EtOAc (3 x 10 mL) until no more product was found in the water layer as measured by LCMS. The combined organics were dried over $MgSO_4$ and the solvent was evaporated under reduced pressure *in vacuo* to yield the title compound [151].

5-(4-Chlorophenyl)isoxazol-3-amine (169)
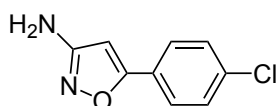
Synthesised according to general method **M** from 4-chlorobenzoylacetonitrile **162** (0.89 g, 5 mmol, 1.0 equiv.) and hydroxylamine sulphate (0.45 g, 5.45 mmol,1.1 equiv.) to give title compound as an off-white solid (0.55 g, 57% yield). **m.p.** 139–141°C (no lit m.p.). **^{1}H NMR** (500 MHz, DMSO-d_6) δ 7.82 – 7.76 (m, 2H), 7.59 – 7.53 (m, 2H), 6.37 (s, 1H), 5.73 (s, 2H), 3.38 (s, 4H). **^{13}C NMR** (126 MHz, DMSO) δ 134.37, 129.11, 128.11, 127.01,126.33, 93.31. **LC-MS** *m/z* (ESI+) 195.2 ([M+H]$^+$ Retention time: t_R = 5.05 min, >95%. Spectroscopic data matched those in the literature [195].

5-(*p*-Tolyl)isoxazol-3-amine (170)
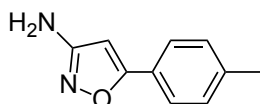
Synthesised according to general method **M** from 4-methylbenzoylacetonitrile **163** (0.79 g, 5 mmol, 1.0 equiv.) and hydroxylamine sulphate (0.45 g, 5.45 mmol,1.1 equiv.)

to give title compound as an off-white solid (0.62 g, 72% yield). **m.p.** 149–151°C (no lit m.p.). **^{1}H NMR** (500 MHz, DMSO-d_6) δ 7.66 – 7.59 (m, 2H), 7.30 (d, J = 8.0 Hz, 2H), 6.25 (s, 1H), 5.64 (s, 2H), 2.34 (s, 3H). **^{13}C NMR** (126 MHz, DMSO) δ 167.21, 164.50, 139.62, 129.56, 129.31, 125.08, 92.08, 20.96. **LC-MS** m/z (ESI+) 175.2 ([M+H]$^+$. Retention time: t_R = 4.91 min, >95%. Spectroscopic data matched those in the literature [196].

5-(Furan-2-yl)isoxazol-3-amine (171)

Synthesised according to general method **M** from 3-(furan-3-yl)-3-oxopropanenitrile **164** (0.67 g, 5 mmol, 1.0 equiv.) and hydroxylamine sulphate (0.45 g, 5.45 mmol,1.1 equiv.) to give title compound as a white solid (0.49 g, 66% yield). **m.p.** 134–137°C (no lit m.p.). **^{1}H NMR** (400 MHz, DMSO-d_6) δ 7.66 (d, J = 1.8 Hz, 1H), 6.93 (s, 1H), 6.90 (s, 2H), 6.55 (dd, J = 3.4, 1.8 Hz, 1H), 6.41 (d, J = 3.4 Hz, 1H). **^{13}C NMR** (126 MHz, DMSO) δ 142.07, 122.45, 117.72, 112.10, 111.54, 110.59, 104.01. **LC-MS** m/z (ESI+) 151.2 ([M+H]$^+$. Retention time: t_R = 3.04 min, >95%. Spectroscopic data matched those in the literature [197].

5-(3-Chlorophenyl)isoxazol-3-amine (173)

Synthesised according to general method **M** from 3-chlorobenzoylacetonitrile **166** (0.89 g, 5 mmol, 1.0 equiv.)and hydroxylamine sulphate (0.45 g, 5.45 mmol,1.1 equiv.) to give title compound as a white solid (0.48 g, 50% yield). **m.p.** 92–95°C (no lit m.p.). **^{1}H NMR** (500 MHz, DMSO-d_6) δ 7.77 (t, J = 1.8 Hz, 1H), 7.71 (dt, J = 7.0, 1.7 Hz, 1H), 7.55 – 7.46 (m, 2H), 6.88 (s, 2H), 5.49 (s, 1H). **^{13}C NMR** (126 MHz, DMSO) δ 133.36, 130.45, 126.14, 124.14, 123.28, 85.11. **LC-MS** m/z (ESI+) 195.2 ([M+H]$^+$. Retention time: t_R = 5.06 min, >95%. Spectroscopic data matched those in the literature [198].

5-(4-Methoxyphenyl)isoxazol-3-amine (174)

Synthesised according to general method **M** from 4-methoxybenzoyl acetonitrile **167** (0.87g, 5 mmol, 1.0 equiv.) and hydroxylamine sulphate (0.45 g, 5.45 mmol,1.1 equiv.) to give title compound as a white solid (0.51 g, 54% yield). **m.p.** 128–131°C (no lit m.p.). **^{1}H NMR** (500 MHz, DMSO-d_6) δ 7.69 – 7.62 (m, 2H), 7.03 – 6.96 (m, 2H), 6.72 (s, 2H), 5.34 (s, 1H), 3.80 (s, 3H). **^{13}C NMR** (126 MHz, DMSO) δ 170.69, 162.05, 160.13, 127.56, 122.32, 114.12, 74.77, 55.15. **LC-MS** *m/z* (ESI+) 191.2 ([M+H]$^+$. Retention time: t_R = 4.55 min, >95%. Spectroscopic data matched those in the literature [199].

5-Phenylisoxazol-3-amine (175)

Synthesised according to general method **M** from 4-methoxybenzoyl acetonitrile **168** (0.87 g, 5 mmol, 1.0 equiv.) and hydroxylamine sulphate (0.45 g, 5.45 mmol,1.1 equiv.) to give title compound as an off-white solid (0.58 g, 73% yield). **m.p.** 129–132°C (no lit m.p.). **^{1}H NMR** (500 MHz, DMSO-d_6) δ 7.79 – 7.73 (m, 2H), 7.53 – 7.49 (m, 1H), 7.49 – 7.42 (m, 2H), 6.32 (s, 1H), 5.69 (s, 2H).**^{13}C NMR** (126 MHz, DMSO) δ 164.54, 129.82, 129.01, 127.51, 125.13, 92.73. **LC-MS** *m/z* (ESI+) 161.2 ([M+H]$^+$. Retention time: t_R = 4.39 min, >95%. Spectroscopic data matched those in the literature [200] .

**6.5.15 General method N: Synthesis of 5-Arylpyrazol-3-amines**

To a mixture of aryl acetonitrile (5 mmol, 1.0 equiv.) and H_2O (10 mL) was added NaOH (6.2 mmol, 2.5 equiv.). When the NaOH pellets had completely dissolved, hydrazine sulphate (2.7 mmol,1.1 equiv.) was added and, after 5 min, the pH was measured (pH 7–8). The reaction is warmed to 45 °C and stirred for 72 h. HCl (0.65 mL, 7.9 mmol, 37%, 1.6 equiv.) was added in one portion and the reaction was warmed to 50 °C for 2.5 h. After this time monitoring by TLC (70% EtOAc in hexanes) indicated that the reaction was completed. The reaction was removed from the oil bath and allowed to cool to room temperature, then a solution of NaOH (30% in H_2O) was added to adjust the solution to pH 11. EtOAc was then

added, and the layers separated. The aqueous layer was extracted with EtOAc (3 x 10 mL) until no more product was found in the water layer as measured by LCMS. The combined organics were dried over MgSO₄ and the solvent was evaporated under reduced pressure *in vacuo* to give the pure product and with yield [151].

5-(4-chlorophenyl)-1*H*-pyrazol-3-amine (177)

Synthesised according to general method **N** from 4-chlorobenzoylacetonitrile **162** (0.44 g, 2.5 mmol, 1.0 equiv.) and hydrazine sulphate (0.35 g, 2.7 mmol, 1.1 equiv.) to give title compound as a white solid (0.23 g, 49% yield). **m.p.** 162–166°C (no lit m.p.). **¹H NMR** (500 MHz, DMSO-d_6) δ 11.71 (d, *J* = 71.5 Hz, 1H), 7.74 – 7.62 (m, 2H), 7.42 (d, *J* = 8.4 Hz, 2H), 5.76 (d, *J* = 4.4 Hz, 1H), 4.90 (s, 2H). **¹³C NMR** (126 MHz, DMSO) δ 165.89, 164.57, 134.36, 129.13, 129.11, 127.02, 127.00, 126.34, 93.31. **LC-MS** *m/z* (ESI+) 194.0 ([M+H]⁺. Retention time: t_R = 4.22 min, >95%. Spectroscopic data matched those in the literature [201].

5-(*p*-Tolyl)-1*H*-pyrazol-3-amine (178)
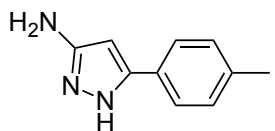
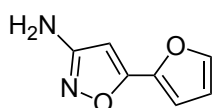Synthesised according to general method **N** from 4-methylbenzoylacetonitrile **163** (0.40 g, 2.5 mmol, 1.0 equiv.) and hydrazine sulphate (0.35 g, 2.7 mmol, 1.1 equiv.) to give title compound as an off- white solid (0.32 g, 74% yield). **m.p.** 118–120°C (no lit m.p.). **¹H NMR** (500 MHz, DMSO-d_6) δ 11.76 (s, 0H), 7.53 (d, *J* = 7.9 Hz, 2H), 7.18 (d, *J* = 7.8 Hz, 3H), 5.74 (d, *J* = 18.9 Hz, 1H), 4.79 (d, *J* = 89.6 Hz, 2H), 2.30 (s, 4H). **¹³C NMR** (126 MHz, DMSO) δ 154.37, 153.52, 129.13, 128.81, 126.90, 124.59, 91.37, 20.75. **LC-MS** *m/z* (ESI+) 174.1 ([M+H]⁺. Retention time: t_R = 3.96 min, >95%. Spectroscopic data matched those in the literature [201].

225

5-(Furan-2-yl)-1*H*-pyrazol-3-amine (179)
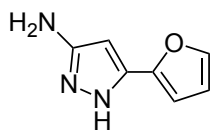
Synthesised according to general method **N** from 3-(furan-3-yl)-3-oxopropanenitrile **164** (0.67 g, 5 mmol, 1.0 equiv.) and hydrazine sulphate (0.70 g, 6.2 mmol, 1.1 equiv.) to give title compound as an off- white solid (0.50 g, 67% yield). **m.p.** 97–100°C (no lit m.p.). **¹H NMR** (500 MHz, DMSO-d_6) δ 11.77 (s, 0H), 7.64 (s, 1H), 6.68 – 6.39 (m, 2H), 5.76 – 5.41 (m, 1H), 4.87 (s, 2H).**¹³C NMR** (126 MHz, DMSO) δ 1144.88, 141.79, 112.80, 111.54, 111.38, 104.96, 89.81. **LC-MS** *m/z* (ESI+) 150.1 ([M+H]⁺. Retention time: t_R = 2.99 min, >95%. Spectroscopic data matched those in the literature. [202].

5-(3-Chlorophenyl)-1*H*-pyrazol-3-amine (181)
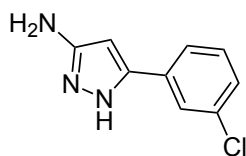
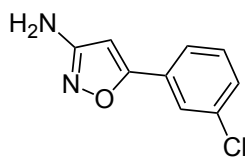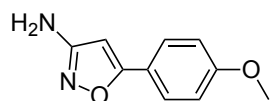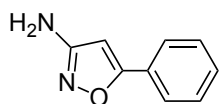Synthesised according to general method **N** from 3-chlorobenzoylacetonitrile **166** (0.44 g, 2.5 mmol, 1.0 equiv.) and hydrazine sulphate (0.35 g, 2.7 mmol, 1.1 equiv.) to give title compound as an off- white solid (0.29 g, 62% yield). **m.p.** 95–99°C (no lit m.p.). **¹H NMR** (500 MHz, DMSO-d_6) δ 11.74 (s, 1H), 7.71 (t, *J* = 1.9 Hz, 1H), 7.62 (dt, *J* = 7.8, 1.4 Hz, 1H), 7.40 (t, *J* = 7.9 Hz, 1H), 7.31 (dd, *J* = 7.9, 2.2 Hz, 1H), 5.80 (s, 1H), 4.94 (s, 2H).**¹³C NMR** (126 MHz, DMSO) δ 130.45, 126.14, 124.14, 123.28, 101.49, 39.39, 39.23, 39.07. **LC-MS** *m/z* (ESI+) 194.0 ([M+H]⁺. Retention time: t_R = 4.26 min, >95%. Spectroscopic data matched those in the literature. [201].

5-(4-methoxyphenyl)-1*H*-pyrazol-3-amine (182)
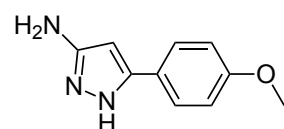
Synthesised according to general method **N** from 4-methoxybenzoyl acetonitrile **167** (0.44 g, 2.5 mmol, 1.0 equiv.) and hydrazine sulphate (0.35 g, 2.7 mmol, 1.1 equiv.) to give title compound as a white solid (0.36 g, 75% yield). **m.p.** 113–115°C (no lit m.p.). **¹H NMR** (500 MHz, DMSO-d_6) δ 11.74 (s, 1H), 8.00 – 7.84 (m, 2H), 7.20 – 7.01 (m, 2H), 4.69 (s, 2H), 3.86 (s, 3H). **¹³C NMR** (126 MHz,

DMSO) δ 163.93, 130.86, 129.18, 127.97, 127.43, 116.07, 114.13, 55.68. **LC-MS** *m/z* (ESI+) 190.1 ([M+H]⁺. Retention time: t_R = 3.72 min, >95%. Spectroscopic data matched those in the literature [201].
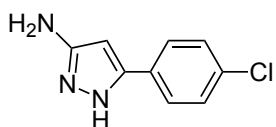
5-Phenyl-1*H*-pyrazol-3-amine (183)
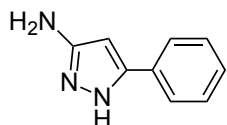
Synthesised according to general method **N** from benzoyl acetonitrile **168** (0.36 g, 2.5 mmol, 1.0 equiv.) and hydrazine sulphate (0.35 g, 2.7 mmol, 1.1 equiv.) to give title compound as a white solid (0.27 g, 68% yield). **m.p.** 114–117°C (no lit m.p.). **¹H NMR** (500 MHz, DMSO-*d₆*) δ 11.74 (d, *J* = 142.8 Hz, 1H), 7.77 – 7.53 (m, 2H), 7.32 (dt, *J* = 55.1, 7.5 Hz, 3H), 5.77 (s, 1H), 4.77 (s, 2H). **¹³C NMR** (126 MHz, DMSO) δ 150.69, 128.58, 127.86, 126.46, 124.84, 124.64, 73.41. **LC-MS** *m/z* (ESI+) 160.1 ([M+H]⁺. Retention time: t_R = 3.60 min, >95%. Spectroscopic data matched those in the literature [202].

6.5.16 General method S: Synthesis of 2-nitro-benzamides

The 2-nitrobenzoic acid (2.0 mmol, 1 eq.) and amine (2.0 mmol, 1 eq.) were dissolved in anhydrous CH_2Cl_2 (7 mL). After stirring the mixture at room temperature for several minutes, EDCI (4.0 mmol, 2 eq.) and DMAP (5.0 mmol, 2.5 eq.). were added to the mixture. The mixture was stirred at room temperature for 24 hours and monitored by TLC (60% EtOAc in hexanes) indicated that the reaction was completed. The solvent was removed under reduce pressure *in vacuo,* and the residue was diluted with EtOAc (25 mL) and washed with 1 M HCl solution (3 x 10 mL) and brine (10 mL) then saturated $NaHCO_3$ solution (3 x10 mL) only with methoxy substituted compounds and brine (10 mL). The organic fraction was dried over $MgSO_4$ and the solvent was evaporated under reduced pressure *in vacuo* to give a crude product which was purified by Biotage Selekt chromatography (5–40%, EtOAc in hexanes) to yield the pure product of the 2-nitro-benzamide as a solid [173].

5-Chloro-2-nitro-*N*-phenylbenzamide (190)
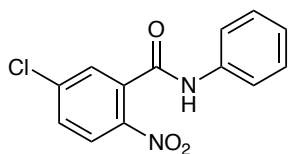
Synthesised according to general method **S** from 5-chloro-2-nitrobenzoic acid **185** (0.40 g, 2.0 mmol, 1.0 equiv.), aniline (0.181 mL, 2.0 mmol, 1.0 equiv.), EDCI (0.77 g, 4.0 mmol, 2.0 equiv.) and DMAP (0. 60 g, 5.0 mmol, 2.5 equiv.). Purified by Biotage Selekt chromatography (5–40%, EtOAc in hexanes) to give the title compound as a white solid (0.38 g, 69% yield).**¹H NMR** (500 MHz, DMSO-d_6) δ 10.73 (s, 1H), 8.19 (d, *J* = 8.8 Hz, 1H), 7.96 (d, *J* = 2.3 Hz, 1H), 7.85 (dd, *J* = 8.8, 2.3 Hz, 1H), 7.69 – 7.58 (m, 2H), 7.43 – 7.29 (m, 2H), 7.14 (tt, *J* = 7.4, 1.2 Hz, 1H). **LC-MS** *m/z* (ESI+) 277.7 ([M+H]⁺. Retention time: t_R = 5.54 min, >95%. Spectroscopic data matched those in the literature [203].

N-benzyl-5-chloro-2-nitrobenzamide (191)
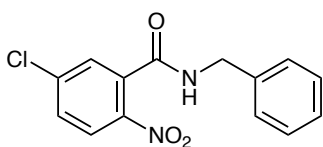
Synthesised according to general method **S** from 5-chloro-2-nitrobenzoic acid **186** (0.40 g, 2.0 mmol, 1.0 equiv.), benzylamine (0.22 ml, 2.0 mmol, 1.0 equiv.), EDCI (0.77 g, 4.0 mmol, 2.0 equiv.) and DMAP (0. 60 g, 5.0 mmol, 2.5 equiv.). Purified by Biotage Selekt chromatography (5–40%, EtOAc in hexanes) to give the title compound as a white solid (0.34 g, 59% yield). **¹H NMR** (500 MHz, DMSO-d_6) δ 9.27 (t, *J* = 5.9 Hz, 1H), 8.09 (d, *J* = 8.6 Hz, 1H), 7.85 – 7.75 (m, 2H), 7.38 – 7.34 (m, 4H), 7.28 (ddt, *J* = 8.6, 5.5, 2.7 Hz, 1H), 4.45 (d, *J* = 5.9 Hz, 2H). **LC-MS** *m/z* (ESI+) 291.7 ([M+H] ⁺. Retention time: t_R = 5.42 min, >95%.

5-Chloro-*N,N*-diethyl-2-nitrobenzamide (192)
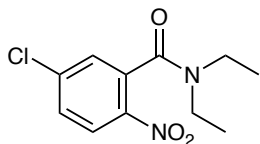
Synthesised according to general method **S** from 5-chloro-2-nitrobenzoic acid **187** (0.40 g, 2.0 mmol, 1.0 equiv.), diethylamine (0.21ml, 2.0 mmol, 1.0 equiv.) EDCI (0.77 g, 4.0 mmol, 2.0 equiv.) and DMAP (0. 60 g, 5.0 mmol, 2.5 equiv.). Purified by Biotage Selekt chromatography (5–40%, EtOAc in hexanes) to give the title compound as a white solid (0.19 g, 37% yield). **¹H NMR** (500 MHz, DMSO-d_6) δ 8.23 (d, *J* =

8.8 Hz, 1H), 7.89 – 7.66 (m, 2H), 3.44 (s, 3H), 3.12 (q, *J* = 7.2 Hz, 2H), 1.17 (t, *J* = 7.1 Hz, 3H), 1.02 (t, *J* = 7.1 Hz, 3H). **LC-MS** *m/z* (ESI+) 257.7 ([M+H]+. Retention time: t_R = 5.26 min, >95%.

5-Chloro-*N*-ethyl-2-nitrobenzamide (193)
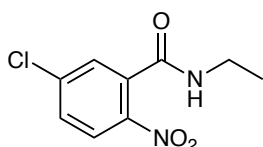
Synthesised according to general method **S** from 5-chloro-2-nitrobenzoic acid **188** (0.40 g, 2.0 mmol, 1.0 equiv.), ethylamine hydrochloride (0.162 g, 2.0 mmol, 1.0 equiv.), EDCI (0.77 g, 4.0 mmol, 2.0 equiv.), DMAP (0. 60 g, 5.0 mmol, 2.5 equiv.) and triethylamine (0.28 mL, 2.0 mmol, 1.0 equiv.). Purified by Biotage Selekt chromatography (5–40%, EtOAc in hexanes) to give the title compound as a white solid (0.20 g, 44% yield). **¹H NMR** (500 MHz, DMSO-*d₆*) δ 8.73 (t, *J* = 5.6 Hz, 1H), 8.08 (d, *J* = 8.6 Hz, 1H), 7.77 (dd, *J* = 8.7, 2.3 Hz, 1H), 7.71 (d, *J* = 2.3 Hz, 1H), 3.24 (qd, *J* = 7.2, 5.5 Hz, 2H), 1.11 (t, *J* = 7.2 Hz, 3H). **LC-MS** *m/z* (ESI+) 229.6 ([M+H]+. Retention time: t_R = 4.49 min, >95%.

5-Chloro-*N*-methyl-2-nitrobenzamide (194)
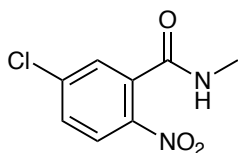
Synthesised according to general method **S** from 5-chloro-2-nitrobenzoic acid **189** (0.40 g, 2.0 mmol, 1.0 equiv.), methylamine hydrochloride (0.134 g, 2.0 mmol, 1.0 equiv.), EDCI (0.77 g, 4.0 mmol, 2.0 equiv.), DMAP (0. 60 g, 5.0 mmol, 2.5 equiv.) and triethylamine (0.28 mL, 2.0 mmol, 1.0 equiv.). Purified by Biotage Selekt chromatography (5–40%, EtOAc in hexanes) to give the title compound as a white solid (0.15 g, 35% yield). **¹H NMR** (500 MHz, DMSO-*d₆*) δ 8.68 (d, *J* = 5.3 Hz, 1H), 8.07 (d, *J* = 8.7 Hz, 1H), 7.83 – 7.71 (m, 2H), 2.75 (d, *J* = 4.6 Hz, 3H). **LC-MS** *m/z* (ESI+) 215.6 ([M+H]+. Retention time: t_R = 4.04 min, >95%. Spectroscopic data matched those in the literature [204].

5-Methoxy-2-nitro-*N*-phenylbenzamide (195)
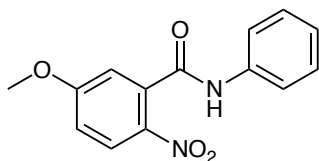
Synthesised according to general method **S** from 5-methoxy-2-nitrobenzoic acid **185** (0.4 g, 2.0 mmol, 1.0 equiv.), aniline (0.18 mL, 2.0 mmol, 1.0 equiv.), EDCI (0.77 g, 4.0 mmol, 2.0 equiv.) and DMAP (0. 60 g, 5.0 mmol, 2.5 equiv.). Purified by Biotage Selekt chromatography (5–40%, EtOAc in hexanes) to give the title compound as a white solid (0.26 g, 48% yield). **^{1}H NMR** (500 MHz, DMSO-d_6) δ 10.58 (s, 1H), 8.19 (d, *J* = 8.9 Hz, 1H), 7.66 (d, *J* = 8.0 Hz, 2H), 7.36 (t, *J* = 7.8 Hz, 2H), 7.30 – 7.19 (m, 2H), 7.12 (t, *J* = 7.4 Hz, 1H), 3.94 (s, 3H). **LC-MS** *m/z* (ESI+) 273.3 ([M+H]$^+$. Retention time: t_R = 5.26 min, >95%. Spectroscopic data matched those in the literature [205].

**N-Benzyl-5-methoxy-2-nitrobenzamide (196)**
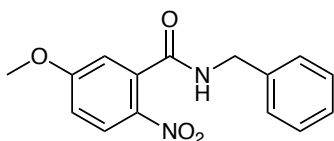
Synthesised according to general method **S** from 5-methoxy-2-nitrobenzoic acid **186** (0.4 g, 2.0 mmol, 1.0 equiv.), benzylamine (0.22 mL, 2.0 mmol, 1.0 equiv.) EDCI (0.77 g, 4.0 mmol, 2.0 equiv.) and DMAP (0. 60 g, 5.0 mmol, 2.5 equiv.). Purified by Biotage Selekt chromatography (5–40%, EtOAc in hexanes) to give the title compound as a white solid (0.14 g, 25% yield). **^{1}H NMR** (500 MHz, DMSO-d_6) δ 9.08 (d, *J* = 6.2 Hz, 1H), 8.10 (d, *J* = 9.1 Hz, 1H), 7.36 (d, *J* = 8.4 Hz, 4H), 7.28 (d, *J* = 6.9 Hz, 1H), 7.18 (d, *J* = 9.0 Hz, 1H), 7.08 (s, 1H), 4.46 (d, *J* = 5.9 Hz, 2H), 3.91 (s, 3H). **LC-MS** *m/z* (ESI+) 287.3 ([M+H]$^+$. Retention time: t_R = 5.13 min, >95%. Spectroscopic data matched those in the literature [206].

N,N-diethyl-5-methoxy-2-nitrobenzamide (197)

Synthesised according to general method **S** from 5-methoxy-2-nitrobenzoic acid **187** (0.4 g, 2.0 mmol, 1.0 equiv.), diethylamine (0.21 mL, 2.0 mmol, 1.0 equiv.) EDCI (0.77 g, 4.0 mmol, 2.0 equiv.) and DMAP (0. 60 g, 5.0 mmol, 2.5 equiv.). Purified by Biotage Selekt chromatography (5–40%, EtOAc in hexanes) to give the title

compound as an off-white solid (0.14 g, 28% yield). **¹H NMR** (500 MHz, DMSO-d_6) δ 8.21 (d, J = 9.2 Hz, 1H), 7.18 (dd, J = 9.1, 2.8 Hz, 1H), 6.99 (d, J = 2.8 Hz, 1H), 3.91 (s, 3H), 3.37 (d, J = 11.8 Hz, 2H), 3.08 (s, 3H), 1.17 (t, J = 7.1 Hz, 3H), 1.01 (t, J = 7.1 Hz, 3H). **LC-MS** m/z (ESI+) 253.3 ([M+H]⁺. Retention time: t_R = 4.96 min, >95%.

N-ethyl-5-methoxy-2-nitrobenzamide (198)

Synthesised according to general method **S** from 5-methoxy-2-nitrobenzoic acid **188** (0.4 g, 2.0 mmol, 1.0 equiv.) ethylamine hydrochloride (0.135 g, 2.0 mmol, 1.0 equiv.) EDCI (0.77 g, 4.0 mmol, 2.0 equiv.), DMAP (0. 60 g, 5.0 mmol, 2.5 equiv.) and triethylamine (0.28 mL, 2.0 mmol, 1.0 equiv.). Purified by Biotage Selekt chromatography (5–40%, EtOAc in hexanes) to give the title compound as an off-white solid (0.13 g, 29% yield). **¹H NMR** ¹H NMR (500 MHz, DMSO-d_6) δ 8.52 (t, J = 5.5 Hz, 1H), 8.08 (d, J = 9.1 Hz, 1H), 7.16 (dd, J = 9.1, 2.8 Hz, 1H), 7.02 (d, J = 2.7 Hz, 1H), 3.90 (s, 3H), 3.23 (qd, J = 7.2, 5.5 Hz, 2H), 1.11 (t, J = 7.2 Hz, 3H). **LC-MS** m/z (ESI+) 225.2 ([M+H]⁺ . Retention time: t_R = 4.11 min, >95%. Spectroscopic data matched those in the literature [207].

5-Methoxy-*N*-methyl-2-nitrobenzamide (199)

Synthesised according to general method **S** from 5-methoxy-2-nitrobenzoic acid **189** (0.4 g, 2.0 mmol, 1.0 equiv.) methylamine hydrochloride (0.163 g, 2.0 mmol, 1.0 equiv.), EDCI (0.77 g, 4.0 mmol, 2.0 equiv.) and DMAP (0. 60 g, 5.0 mmol, 2.5 equiv.) and triethylamine (0.28 mL, 2.0 mmol, 1.0 equiv.). Purified by Biotage Selekt chromatography (5–40%, EtOAc in hexanes) to give the title compound as a white solid (0.18 g, 43% yield). **¹H NMR** (500 MHz, DMSO-d_6) δ 8.48 (d, J = 4.8 Hz, 1H), 8.08 (d, J = 9.1 Hz, 1H), 7.16 (dd, J = 9.1, 2.8 Hz, 1H), 7.05 (d, J = 2.8 Hz, 1H), 3.90 (s, 3H), 2.75 (d, J = 4.7 Hz, 3H). **LC-MS** m/z (ESI+) 211.2 ([M+H]⁺. Retention time: t_R = 3.69 min, >95%.

5-Hydroxy-2-nitro-*N*-phenylbenzamide (200)
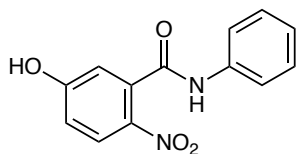
Synthesised according to general method **S** from 5-hydroxy-2-nitrobenzoic acid **185** (0.55 g, 3.0 mmol, 1.0 equiv.), aniline (0.27 mL, 3.0 mmol, 1.0 equiv.), EDCI (1.16 g, 6.0 mmol, 2.0 equiv.) and DMAP (0. 90 g, 5.0 mmol, 7.5 equiv.). Purified by Biotage Selekt chromatography (5–40%, EtOAc in hexanes) to give the title compound as an off-white solid (0.42 g, 54% yield).**¹H NMR** (400 MHz, DMSO-d_6) δ 11.23 (s, 1H),10.51 (s, 1H), 8.14 – 8.07 (m, 1H), 7.96 (dd, *J* = 8.8, 1.7 Hz, 1H), 7.65 (d, *J* = 8.1 Hz, 2H), 7.35 (t, *J* = 8.1 Hz, 2H), 7.11 (t, *J* = 7.4 Hz, 1H), 6.94 (d, *J* = 2.6 Hz, 1H). **LC-MS** *m/z* (ESI+) 259.3 ([M+H]⁺. Retention time: t_R = 4.82 min, >95%.

N-Benzyl-5-hydroxy-2-nitrobenzamide (201)
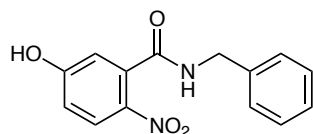
Synthesised according to general method **S** from 4-hydroxy-2-nitrobenzoic acid **186** (0.55 g, 3.0 mmol, 1.0 equiv.), benzylamine (0.33 mL, 3.0 mmol, 1.0 equiv.) EDCI (1.16 g, 6.0 mmol, 2.0 equiv.) and DMAP (0. 90 g, 5.0 mmol, 7.5 equiv.). Purified by Biotage Selekt chromatography (5–40%, EtOAc in hexanes) to give the title compound as an off-white solid (0.19 g, 23% yield). **¹H NMR** (400 MHz, DMSO-d_6) δ 11.19 (s, 1H),9.02 (t, *J* = 6.1 Hz, 1H), 8.01 (dd, *J* = 9.1, 1.6 Hz, 1H), 7.43 – 7.20 (m, 5H), 6.94 (dt, *J* = 9.0, 2.2 Hz, 1H), 6.83 (d, *J* = 2.4 Hz, 1H), 4.44 (d, *J* = 6.0 Hz, 2H). **LC-MS** *m/z* (ESI+) 273.3 ([M+H]⁺. Retention time: t_R = 4.73 min, >95%. Spectroscopic data matched those in the literature [206].

### *N,N*-Diethyl-5-hydroxy-2-nitrobenzamide (202)
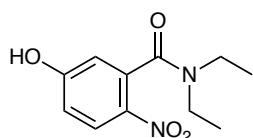
Synthesised according to general method **S** from 5-hydroxy-2-nitrobenzoic acid **187** (0.55 g, 3.0 mmol, 1.0 equiv.), diethylamine (0.32 mL, 3.0 mmol, 1.0 equiv.), EDCI (1.16 g, 6.0 mmol, 2.0 equiv.) and DMAP (0. 90 g, 5.0 mmol, 7.5 equiv.). Purified by Biotage Selekt chromatography (5–40%, EtOAc in hexanes) to give the title

compound as an off-white solid (0.09 g, 12% yield). **¹H NMR** (400 MHz, DMSO-d_6) δ 11.27 (s, 1H), 8.12 (dd, J = 9.1, 1.5 Hz, 1H), 6.94 (dt, J = 9.1, 2.1 Hz, 1H), 6.68 (t, J = 2.0 Hz, 1H), 1.15 (t, J = 7.1 Hz, 3H), 0.99 (t, J = 7.1 Hz, 3H). **LC-MS** *m/z* (ESI+) 239.2 ([M+H]⁺. Retention time: t_R = 4.47 min, >95%.

N-ethyl-5-hydroxy-2-nitrobenzamide (203)
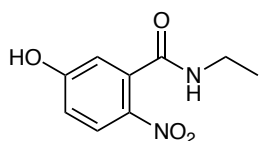
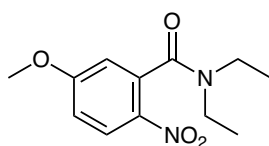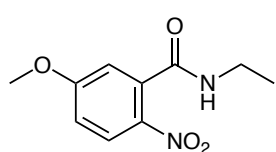

Synthesised according to general method **S** from 5-hydroxy-2-nitrobenzoic acid **188** (0.55 g, 3.0 mmol, 1.0 equiv.), ethylamine hydrochloride (0.245 g, 3.0 mmol, 1.0 equiv.), EDCI (1.16 g, 6.0 mmol, 2.0 equiv.), DMAP (0. 90 g, 5.0 mmol, 7.5 equiv.) and triethylamine (0.42 mL, 6.0 mmol, 1.0 equiv.). Purified by Biotage Selekt chromatography (5–40%, EtOAc in hexanes) to give the title compound as an off-white solid (0.06 g, 9% yield). **¹H NMR** (400 MHz, DMSO-d_6) δ 11.14 (s, 1H), 8.43 (t, J = 5.7 Hz, 1H), 8.09 – 7.90 (m, 1H), 6.92 (dd, J = 9.1, 2.6 Hz, 1H), 6.76 (d, J = 2.4 Hz, 1H), 3.22 (dd, J = 7.6, 5.8 Hz, 2H), 1.09 (dd, J = 7.9, 6.4 Hz, 3H). **LC-MS** *m/z* (ESI+) 211.0 ([M+H]⁺. Retention time: t_R = 3.58 min, >95%.

5-Hydroxy-*N*-methyl-2-nitrobenzamide (204)
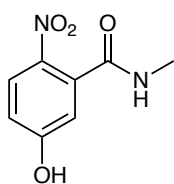
Synthesised according to general method **S** from 5-hydroxy-2-nitrobenzoic acid **189** (0.55 g, 3.0 mmol, 1.0 equiv.), methylamine hydrochloride (0.202 g, 3.0 mmol, 1.0 equiv.) EDCI (1.16g, 6.0 mmol, 2.0 equiv.), DMAP (0. 90g, 5.0 mmol, 7.5 equiv.) and triethylamine (0.42 mL, 6.0 mmol, 1.0 equiv.). Purified by Biotage Selekt chromatography (5–40%, EtOAc in hexanes) to give the title compound as an off-white solid (0.36 g, 61% yield). **¹H NMR** (400 MHz, DMSO-d_6) δ 11.15 (s, 1H), 8.38 (q, J = 4.7 Hz, 1H), 7.99 (dd, J = 9.0, 1.6 Hz, 1H), 6.93 (dt, J = 9.1, 2.2 Hz, 1H), 6.77 (t, J = 2.2 Hz, 1H), 2.82 – 2.64 (m, 3H). **LC-MS** *m/z* (ESI+) 197.2 ([M+H]⁺. Retention time: t_R = 2.73 min, >95%.

5-Bromo-2-nitro-*N*-phenylbenzamide (205)
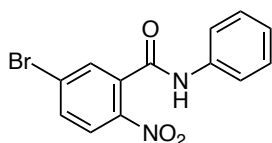
Synthesised according to general method **S** from 2-amino-5-bromo-*N*-phenylbenzamide **185** (0.5 g, 2.0 mmol, 1.0 equiv.), aniline (0.181 mL, 2.0 mmol, 1.0 equiv.), EDCI (0.77 g, 4.0 mmol, 2.0 equiv.) and DMAP (0.60 g, 5.0 mmol, 2.5 equiv.). Purified by Biotage Selekt chromatography (5–40%, EtOAc in hexanes) to give the title compound as a white solid (0.38 g, 59% yield). **^{1}H NMR** (400 MHz, DMSO-d_6) δ 10.69 (s, 1H), 8.14 – 8.02 (m, 2H), 7.98 (dt, *J* = 8.9, 2.2 Hz, 1H), 7.66 – 7.62 (m, 2H), 7.37 (t, *J* = 7.4 Hz, 2H), 7.13 (t, *J* = 7.5 Hz, 1H). **LC-MS** *m/z* (ESI+) 322.6 ([M+H]$^+$. Retention time: t_R = 5.61 min, >95%. Spectroscopic data matched those in the literature [208].

N-Benzyl-5-bromo-2-nitrobenzamide (206)
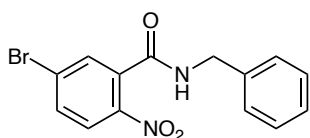
Synthesised according to general method **S** from 2-amino-5-bromo-*N*-phenylbenzamide **186** (0.5 g, 2.0 mmol, 1.0 equiv.), benzylamine (0.22 mL, 2.0 mmol, 1.0 equiv.), EDCI (0.77g, 4.0 mmol, 2.0 equiv.) and DMAP (0.60 g, 5.0 mmol, 2.5 equiv.). Purified by Biotage Selekt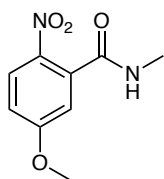 chromatography (5–40%, EtOAc in hexanes) to give the title compound as a white solid (0.35 g, 52% yield). **^{1}H NMR** (400 MHz, DMSO-d_6) δ 9.25 (d, *J* = 6.1 Hz, 1H), 8.00 (dd, *J* = 8.5, 1.5 Hz, 1H), 7.92 (dt, *J* = 8.7, 1.9 Hz, 1H), 7.88 (d, *J* = 1.9 Hz, 1H), 7.41 – 7.31 (m, 5H), 4.45 (d, *J* = 6.0 Hz, 2H). **LC-MS** *m/z* (ESI+) 336.2 ([M+H]$^+$. Retention time: t_R = 5.66 min, >95%.

5-Bromo-*N,N*-diethyl-2-nitrobenzamide (207)
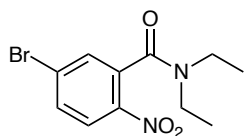
Synthesised according to general method **S** from 2-amino-5-bromo-*N*-phenylbenzamide **187** (0.5 g, 2.0 mmol, 1.0 equiv.), diethylamine (0.21 mL, 2.0 mmol, 1.0 equiv.), EDCI (0.77g, 4.0 mmol, 2.0 equiv.) and DMAP (0.60 g, 5.0 mmol, 2.5 equiv.). Purified by Biotage Selekt chromatography (5–40%, EtOAc in hexanes) to give the title compound as a white solid (0.38 g, 62% yield). **^{1}H NMR** (400 MHz, DMSO-d_6) δ

8.13 (dd, *J* = 8.9, 1.5 Hz, 1H), 7.91 (dd, *J* = 8.8, 2.1 Hz, 1H), 7.83 (d, *J* = 2.1 Hz, 1H), 1.21 – 1.13 (m, 3H), 1.06 – 0.96 (m, 3H). **LC-MS** *m/z* (ESI+) 302.7 ([M+H]$^+$. Retention time: t_R = 5.49 min, >95%.

5-Bromo-*N*-ethyl-2-nitrobenzamide (208)
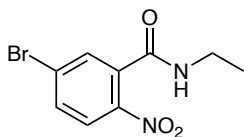
Synthesised according to general method **S** from 2-amino-5-bromo-*N*-phenylbenzamide **188** (0.5 g, 2.0 mmol, 1.0 equiv.), ethylamine hydrochloride (0.166 g, 2.0 mmol, 1.0 equiv.), EDCI (0.77 g, 4.0 mmol, 2.0 equiv.), DMAP (0. 60g, 5.0 mmol, 2.5 equiv.) and triethylamine (0.28 mL, 2.0 mmol, 1.0 equiv.). Purified by Biotage Selekt chromatography (5–40%, EtOAc in hexanes) to give the title compound as a white solid (0.36 g, 65% yield). **^{1}H NMR** (400 MHz, DMSO-d_6) δ 8.69 (s, 1H), 8.02 – 7.95 (m, 1H), 7.90 (dd, *J* = 8.7, 2.3 Hz, 1H), 7.82 (d, *J* = 2.2 Hz, 1H), 3.26 – 3.21 (m, 2H), 1.11 (t, *J* = 7.3 Hz, 3H). **LC-MS** *m/z* (ESI+) 274.0 ([M+H]$^+$. Retention time: t_R = 4.62 min, >95%.

5-Bromo-*N*-methyl-2-nitrobenzamide (209)
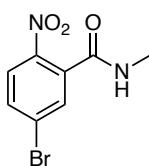
Synthesised according to general method **S** from 2-amino-5-bromo-*N*-phenylbenzamide **189** (0.5 g, 2.0 mmol, 1.0 equiv.), methylamine hydrochloride (0.137 g, 2.0 mmol, 1.0 equiv.), EDCI (0.77 g, 4.0 mmol, 2.0 equiv.), DMAP (0.60 g, 5.0 mmol, 2.5 equiv.) and triethylamine (0.28 mL, 2.0 mmol, 1.0 equiv.). Purified by Biotage Selekt chromatography (5–40%, EtOAc in hexanes) to give the title compound as a white solid (0.45 g, 86% yield). **^{1}H NMR** (400 MHz, DMSO-d_6) δ 8.66 (s, 1H), 7.97 (dd, *J* = 8.6, 1.6 Hz, 1H), 7.91 (dd, *J* = 8.7, 2.1 Hz, 1H), 7.85 (d, *J* = 2.0 Hz, 1H), 2.75 (dd, *J* = 4.7, 1.5 Hz, 3H). **LC-MS** *m/z* (ESI+) 260.0 ([M+H]$^+$. Retention time: t_R = 4.22 min, >95%.

6.5.17 General method Q: Synthesis of 2-amino-benzamides

A mixture of the 2-nitro-benzamide (1 equiv.) and (NH$_4$Cl) ammonium Chloride (5.2 equiv.) in acetone/H$_2$O (10mL, 4:1 v/v) was refluxed. (Fe) iron powder (5

equiv.) was then added portion-wise and stirring was continued for 2 h and monitored by TLC. Upon completion, the reaction was left to cool to room temperature, diluted with H_2O (20 mL) and basified to pH 8 – 9 with saturated $NaHCO_3$. The reaction mixture was filtered through celite, and the filtrate was extracted with EtOAc (3 x 20 mL). The combined organic layers were washed with H_2O (3 x 20 mL), brine (3 x 20 mL), dried over $MgSO_4$ and evaporated under reduced pressure *in vacuo*. The crude product was purified through by Biotage Selekt chromatography (0-100% EtOAc in hexanes) to yield the pure product of the 2-amino-benzamide as a solid [209].

2-Amino-5-chloro-*N*-phenylbenzamide (210)
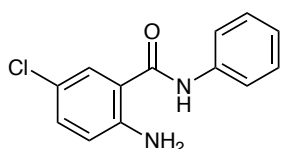
Synthesised according to general method **Q** from 5-chloro-2-nitro-*N*-phenylbenzamide **190** (0.50 g, 1.80 mmol, 1equiv.), NH_4Cl (0.50 g, 9.40 mmol, 5.2 equiv.) and Fe (0.50g, 9.04 mmol, 5.0 equiv.). Purified by Biotage Selekt chromatography (5–100%, EtOAc in hexanes) to give the title compound as a white solid (0.11 g, 25% yield). **m.p.** 124–126°C (no lit m.p.). **¹H NMR** (400 MHz, DMSO-d_6) δ 10.08 (s, 1H), 7.70 – 7.65 (m, 3H), 7.34 (dd, *J* = 8.4, 7.3 Hz, 2H), 7.23 (dd, *J* = 8.8, 2.5 Hz, 1H), 7.09 (t, *J* = 7.4 Hz, 1H), 6.78 (d, *J* = 8.8 Hz, 1H), 6.44 (s, 2H). **¹³C NMR** (126 MHz, DMSO) δ 166.43, 148.49, 138.83, 131.72, 128.75, 128.41, 127.75, 123.51, 120.51, 119.49, 117.90, 117.90, 117.67, 115.90. **LC-MS** *m/z* (ESI+) 247.0 ([M+H]⁺. Retention time: t_R = 5.71 min, >95%. Spectroscopic data matched those in the literature [210].

2-Amino-*N*-benzyl-5-chlorobenzamide (211)
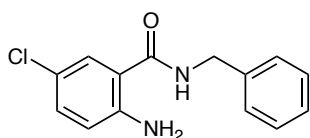
Synthesised according to general method **Q** from *N*-benzyl-5-chloro-2-nitrobenzamide **191** (0.28 g, 0.96 mmol, 1equiv.), NH_4Cl (0.27 g, 5.01 mmol, 5.2 equiv.) and Fe (0.27 g, 4.82 mmol, 5.0 equiv.). Purified by Biotage Selekt chromatography (5–100%, EtOAc in hexanes) to give the title compound as a white solid (0.19 g, 74% yield). **m.p.** 116–119°C (no lit m.p.). **¹H NMR** (400 MHz,

DMSO-d_6) δ 8.89 (t, *J* = 6.1 Hz, 1H), 7.61 (d, *J* = 2.3 Hz, 1H), 7.33 – 7.30 (m, 4H), 7.27 – 7.21 (m, 1H), 7.18 – 7.13 (m, 1H), 6.72 (dd, *J* = 8.9, 1.5 Hz, 1H), 6.57 (s, 2H), 4.41 (d, *J* = 5.9 Hz, 2H). **^{13}C NMR** (126 MHz, DMSO) δ 167.54, 148.64, 139.61, 131.51, 128.82, 128.65, 128.25, 127.28, 127.19, 126.69, 118.06, 117.71, 115.03, 39.83. **LC-MS** *m/z* (ESI+) 261.0 ([M+H]$^+$. Retention time: t_R = 5.58 min, >95%. Spectroscopic data matched those in the literature [211].

2-Amino-5-chloro-*N,N*-diethylbenzamide (212)
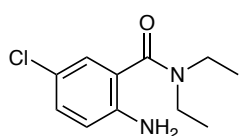
Synthesised according to general method **Q** from 5-chloro-*N,N*-diethyl-2-nitrobenzamide **192** (0.170 g, 0.662 mmol, 1equiv.), NH$_4$Cl (0.184 g, 3.44 mmol, 5.2 equiv.) and Fe (0.185 g, 3.31 mmol, 5.0 equiv.). Purified by Biotage Selekt chromatography (5–100%, EtOAc in hexanes) to give the title compound as a white solid (0.11 g, 73% yield). **m.p.** 73–75°C (no lit m.p.). **^{1}H NMR** (400 MHz, DMSO-d_6) δ 7.10 (dt, *J* = 8.8, 1.9 Hz, 1H), 6.95 (t, *J* = 1.9 Hz, 1H), 6.72 (dd, *J* = 8.7, 1.3 Hz, 1H), 5.09 (s, 2H), 1.07 (d, *J* = 7.3 Hz, 6H).**^{13}C NMR** (126 MHz, DMSO) δ 167.98, 143.58, 129.27, 125.83, 122.51, 119.17, 117.04, 48.56, 42.58, 13.62, 12.90. **LC-MS** *m/z* (ESI+) 227.0 ([M+H]$^+$. Retention time: t_R = 5.47 min, >95%. Spectroscopic data matched those in the literature [212].

2-Amino-5-chloro-*N*-ethylbenzamide (213)
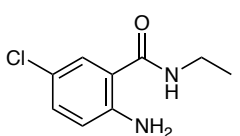
Synthesised according to general method **Q** from 5-chloro-*N*-ethyl-2-nitrobenzamide **193** (0.150 g, 0.656 mmol, 1equiv.), NH$_4$Cl (0.182 g, 3.41 mmol, 5.2 equiv.) and Fe (0.183 g, 3.28 mmol, 5.0 equiv.). Purified by Biotage Selekt chromatography (5–100%, EtOAc in hexanes) to give the title compound as a white solid (0.08 g, 64% yield). **m.p.** 118–120°C (no lit m.p.). **^{1}H NMR** (400 MHz, DMSO-d_6) δ 8.31 (t, *J* = 5.5 Hz, 1H), 7.51 (t, *J* = 2.0 Hz, 1H), 7.14 (dt, *J* = 8.9, 2.0 Hz, 1H), 6.70 (dd, *J* = 8.7, 1.5 Hz, 1H), 6.51 (s, 2H), 3.25 – 3.12 (m, 2H), 1.09 (td, *J* = 7.2, 1.5 Hz, 3H).**^{13}C NMR** (126 MHz, DMSO) δ 167.36, 148.44, 131.22, 127.23, 117.91, 117.65, 115.61,

33.69, 14.62. **LC-MS** *m/z* (ESI+) 199.0 ([M+H]$^+$. Retention time: t_R = 4.71 min, >95%. Spectroscopic data matched those in the literature [213].

2-Amino-5-chloro-*N*-methylbenzamide (214)
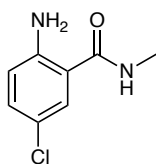
Synthesised according to general method **Q** from 5-chloro-*N*-methyl-2-nitrobenzamide **194** (0.10 g, 0.47 mmol, 1equiv.), NH$_4$Cl (0.13 g, 2.42 mmol, 5.2 equiv.) and Fe (0.13 g, 2.33 mmol, 5.0 equiv.) Purified by Biotage Selekt chromatography (5–100%, EtOAc in hexanes) to give the title compound as an off-white solid (0.07 g, 81% yield). **m.p.** 124–126°C (no lit m.p.). **^{1}H NMR** (400 MHz, DMSO-d_6) δ 8.28 (s, 1H), 7.49 (t, *J* = 2.0 Hz, 1H), 7.15 (dd, *J* = 8.9, 2.2 Hz, 1H), 6.70 (dd, *J* = 8.9, 1.4 Hz, 1H), 6.52 (s, 2H), 2.71 (dd, *J* = 4.6, 1.4 Hz, 3H). **^{13}C NMR** (126 MHz, DMSO) δ 168.05, 148.36, 131.26, 127.18, 117.96, 117.68, 115.50, 25.96. **LC-MS** *m/z* (ESI+) 185.0 ([M+H]$^+$. Retention time: t_R = 4.26 min, >95%. Spectroscopic data matched those in the literature [214].

2-Amino-5-methoxy-*N*-phenylbenzamide (215)

Synthesised according to general method **Q** from 5-methoxy-2-nitro-*N*-phenylbenzamide **195** (0.20 g, 0.734 mmol, 1equiv.), NH$_4$Cl (0.20 g, 3.82 mmol, 5.2 equiv.) and Fe (0.20 g, 3.67 mmol, 5.0 equiv.). Purified by Biotage Selekt chromatography (5–100%, EtOAc in hexanes) to give the title compound as a white solid (0.05 g, 27% yield). **m.p.** 139–141°C (no lit m.p.). **^{1}H NMR** (400 MHz, DMSO-d_6) δ 10.00 (s, 1H), 7.73 – 7.66 (m, 2H), 7.34 (t, *J* = 7.8 Hz, 2H), 7.18 (d, *J* = 3.0 Hz, 1H), 7.09 (t, *J* = 7.4 Hz, 1H), 6.91 (d, *J* = 9.7 Hz, 1H), 6.73 (d, *J* = 9.0 Hz, 1H), 5.85 (s, 2H). **^{13}C NMR** (126 MHz, DMSO) δ 129.87, 129.05, 128.48, 123.46, 120.62, 120.38, 119.72, 118.23, 117.70, 112.66, 110.72, 55.57. **LC-MS** *m/z* (ESI+) 243.0 ([M+H]$^+$. Retention time: t_R = 5.46 min, >95%. Spectroscopic data matched those in the literature [215].

2-Amino-*N*-benzyl-5-methoxybenzamide (216)

Synthesised according to general method **Q** from *N*-benzyl-5-methoxy-2-nitrobenzamide **196** (0.18 g, 0.629 mmol, 1equiv.), NH$_4$Cl (0.175 g, 3.27 mmol, 5.2 equiv.) and Fe (0.175 g, 3.14 mmol, 5.0 equiv.). Purified by Biotage Selekt chromatography (5–100%, EtOAc in hexanes) to give the title compound as a white solid (0.03 g, 19% yield). **m.p.** 98–99°C (no lit m.p.). **IR (film)**: v_{max} 3272, 1520, 1494, 1233, 1036, 831,738, 697 cm^{-1}. **^{1}H NMR** (400 MHz, DMSO-d_6) δ 8.85 (t, *J* = 6.1 Hz, 1H), 7.43 – 7.33 (m, 4H), 7.29 (ddt, *J* = 6.9, 5.1, 2.6 Hz, 1H), 7.19 (d, *J* = 2.6 Hz, 1H), 6.91 (dt, *J* = 9.0, 2.4 Hz, 1H), 6.72 (dd, *J* = 9.0, 1.6 Hz, 1H), 6.06 (s, 2H), 4.49 (d, *J* = 6.6 Hz, 2H), 3.74 (d, *J* = 1.7 Hz, 3H).**^{13}C NMR** (126 MHz, DMSO) δ 168.51, 149.26, 144.03, 139.89, 128.23, 127.11, 126.61, 119.67, 117.75, 111.80, 55.53, 42.17. **LC-MS** *m/z* (ESI+) 257.0 ([M+H]$^+$. Retention time: t_R = 5.34 min, >95%. **HRMS** (ESI+) measured 257.1301. [M+H]$^+$, C$_{15}$H$_{16}$N$_2$O$_2^+$ calculated 257.1290.

2-Amino-*N*,*N*-diethyl-5-methoxybenzamide (217)
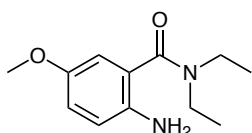
Synthesised according to general method **Q** from *N*,*N*-diethyl-5-methoxy-2-nitrobenzamide **197** (0.135 g, 0.535 mmol, 1equiv.), NH$_4$Cl (0.15 g, 2.78 mmol, 5.2 equiv.) and Fe (0.15 g, 2.68 mmol, 5.0 equiv.). Purified by Biotage Selekt chromatography (5–100%, EtOAc in hexanes) to give the title compound as a white solid (0.09 g, 73% yield). **^{1}H NMR** (400 MHz, DMSO-d_6) δ 6.73 (dd, *J* = 8.8, 2.6 Hz, 1H), 6.67 (dd, *J* = 8.7, 1.5 Hz, 1H), 6.54 (d, *J* = 2.6 Hz, 1H), 4.48 (s, 2H), 3.64 (d, *J* = 1.5 Hz, 3H), 3.17 (s, 1H), 1.12 – 1.04 (m, 6H). **^{13}C NMR** ((126 MHz, DMSO) δ 168.95, 150.25, 138.58, 122.13, 116.84, 115.85, 111.32, 55.32, 42.39, 13.39. **LC-MS** *m/z* (ESI+) 223.0 ([M+H]$^+$. Retention time: t_R = 5.18 min, >95%. Spectroscopic data matched those in the literature [216].

2-Amino-*N*-ethyl-5-methoxybenzamide (218)
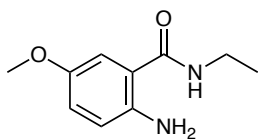
Synthesised according to general method **Q** from *N*-ethyl-5-methoxy-2-nitrobenzamide **198** (0.10 g, 0.45 mmol, 1equiv.), NH$_4$Cl (0.125 g, 2.32 mmol, 5.2 equiv.) and Fe (0.125 g, 2.23 mmol, 5.0 equiv.). Purified by Biotage Selekt chromatography (5–100%, EtOAc in hexanes) to give the title compound as a white solid (0.05 g, 60% yield). **m.p.** 52–55°C (no lit m.p.). **¹H NMR** (400 MHz, DMSO-d_6) δ 8.21 (s, 1H), 7.03 (d, *J* = 2.9 Hz, 1H), 6.83 (dd, *J* = 8.8, 2.8 Hz, 1H), 6.64 (d, *J* = 9.2 Hz, 1H), 5.93 (s, 2H), 3.68 (d, *J* = 1.3 Hz, 3H), 3.24 (dd, *J* = 7.4, 5.7 Hz, 2H), 1.15 – 1.04 (m, 3H). **¹³C NMR** (126 MHz, DMSO) δ 168.33, 149.26,143.67, 119.19, 117.59,115.21, 111.97, 55.53, 33.61, 14.81. **LC-MS** *m/z* (ESI+) 195.0 ([M+H]⁺. Retention time: t$_R$ = 4.35 min, >95%. Spectroscopic data matched those in the literature [216].

2-Amino-5-methoxy-*N*-methylbenzamide (219)
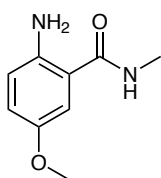
Synthesised according to general method **Q** from 5-methoxy-*N*-methyl-2-nitrobenzamide **199** (0.20 g, 0.952 mmol, 1equiv.), NH$_4$Cl (0.26 g, 4.95 mmol, 5.2 equiv.) and Fe (0.27 g, 4.76 mmol, 5.0 equiv.). Purified by Biotage Selekt chromatography (5–100%, EtOAc in hexanes) to give the title compound as a white solid (0.13 g, 73% yield). **m.p.** 79–82°C (no lit m.p.). **¹H NMR** (400 MHz, DMSO-d_6) δ 8.17 (d, *J* = 6.2 Hz, 1H), 7.03 (d, *J* = 2.9 Hz, 1H), 6.82 (dd, *J* = 8.9, 2.8 Hz, 1H), 6.64 (dd, *J* = 8.8, 2.7 Hz, 1H), 5.95 (s, 2H), 3.68 (d, *J* = 1.3 Hz, 3H), 2.73 (dd, *J* = 4.5, 1.2 Hz, 3H). **¹³C** (126 MHz, DMSO) δ 121.06, 119.29, 117.65, 115.82, 111.76, 110.19, 55.47, 25.50. **LC-MS** *m/z* (ESI+) 181.0 ([M+H]⁺ Retention time: t$_R$ = 3.91 min, >95%. Spectroscopic data matched those in the literature [214].

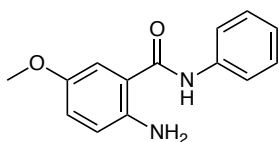**2-Amino-5-hydroxy-*N*-phenylbenzamide (220)**

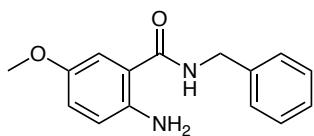Synthesised according to general method **Q** from 5-hydroxy-2-nitro-*N*-phenylbenzamide **200** (0.2 g, 0.77 mmol, 1equiv.), NH$_4$Cl (0.215 g, 4.00 mmol, 5.2 equiv.) and Fe (0.215 g, 3.85 mmol, 5.0 equiv.). Purified by Biotage Selekt chromatography (5–100%, EtOAc in hexanes) to give the title compound as a white solid (0.02 g, 12% yield). **m.p.** 126–128°C (no lit m.p.). **IR (film)**: v_{max} 3302, 3056, 1640, 1584, 1524, 1438, 745, 689 cm^{-1}. **¹H NMR** (400 MHz, DMSO-d_6) δ 10.01 (s, 1H), 8.68 (d, *J* = 1.7 Hz, 1H), 7.71 (d, *J* = 8.0 Hz, 2H), 7.32 (t, *J* = 7.7 Hz, 2H), 7.10 – 7.03 (m, 1H), 7.01 (d, *J* = 2.7 Hz, 1H), 6.76 – 6.70 (m, 1H), 6.63 (d, *J* = 8.8 Hz, 1H), 5.58 (s, 2H). **¹³C NMR** (126 MHz, DMSO) δ 167.67, 139.30, 128.19, 127.11, 126.74, 126.58, 126.44, 121.48, 120.01, 117.54, 113.68. **LC-MS** *m/z* (ESI+) 229.0 ([M+H]$^+$. Retention time: t$_R$ = 5.03 min, >95%. **HRMS** (ESI+) measured 229.0985 [M+H]$^+$, C$_{13}$H$_{12}$N$_2$O$_2$$^+$ calculated 229.0977.

2-Amino-*N*-benzyl-5-hydroxybenzamide (221)

Synthesised according to general method **Q** from *N*-benzyl-5-hydroxy-2-nitrobenzamide **201** (0.15 g, 0.55 mmol, 1equiv.), NH$_4$Cl (0.153 g, 2.86 mmol, 5.2 equiv.) and Fe (0.154 g, 2.75 mmol, 5.0 equiv.). Purified by Biotage Selekt chromatography (5–100%, EtOAc in hexanes) to give the title compound as a white solid (0.03 g, 19% yield). **m.p.** 132–135°C (no lit m.p.). **IR (film)**: v_{max} 3287, 2978, 1606, 1576, 1509, 1289, 1215, 816 ,756, 697cm^{-1}. **¹H NMR** (400 MHz, DMSO-d_6) δ 8.70 (t, *J* = 6.1 Hz, 1H), 8.54 (d, *J* = 1.4 Hz, 1H), 7.36 – 7.20 (m, 5H), 6.95 (d, *J* = 2.7 Hz, 1H), 6.68 (dd, *J* = 8.6, 2.6 Hz, 1H), 6.56 (dd, *J* = 8.6, 4.0 Hz, 1H), 5.67 (s, 2H), 4.39 (d, *J* = 6.0 Hz, 2H). **¹³C NMR** (126 MHz, DMSO) δ 168.62, 146.83, 142.11, 139.86, 128.09, 127.01, 126.49, 119.92, 117.44, 113.59, 39.75. **LC-MS** *m/z* (ESI+) 243.1 ([M+H]$^+$. Retention time: t$_R$ = 4.97 min, >95%. **HRMS** (ESI+) measured 243.1138 [M+H]$^+$, C$_{14}$H$_{14}$N$_2$O$_2$$^+$ calculated 243.1134.

2-Amino-*N*,*N*-diethyl-5-hydroxybenzamide (222)
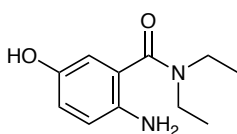
Synthesised according to general method **Q** from *N,N*-diethyl-5-hydroxy-2-nitrobenzamide **202** (0.15 g, 0.63 mmol, 1equiv.), NH$_4$Cl (0.175 g, 3.27 mmol, 5.2 equiv.) and Fe (0.176 g, 3.15 mmol, 5.0 equiv.). Purified by Biotage Selekt chromatography (5–100%, EtOAc in hexanes) to give the title compound as a white solid (0.03 g, 20% yield). **m.p.** 98–101°C (no lit m.p.). **IR (film)**: v_{max}3175, 2967, 1587, 1565, 1494, 1297, 693 cm^{-1}. **^{1}H NMR** (400 MHz, DMSO-d_6) δ 8.62 (s, 1H), 6.56 (t, *J* = 1.9 Hz, 2H), 6.38 (d, *J* = 2.4 Hz, 1H), 4.30 (s, 2H), 1.07 (t, *J* = 7.2 Hz, 6H). **^{13}C NMR** (126 MHz, DMSO) δ 169.20, 147.93, 137.07, 122.41, 117.00, 116.99, 112.64, 39.71, 39.66, 39.51. **LC-MS** *m/z* (ESI+) 209.1 ([M+H]$^+$. Retention time: t_R = 4.66 min, >95%. **HRMS** (ESI+) measured 209.1294 [M+H]$^+$, C$_{11}$H$_{16}$N$_2$O$_2^+$ calculated 209.1290**.**

2-Amino-*N*-ethyl-5-hydroxybenzamide (223)
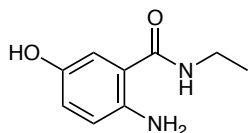
Synthesised according to general method **Q** rom *N*-ethyl-5-hydroxy-2-nitrobenzamide **203** (0.2 g, 0.95 mmol, 1equiv.), NH$_4$Cl (0.27 g, 4.95 mmol, 5.2 equiv.) and Fe (0.27 g, 4.76 mmol, 5.0 equiv.). Purified by Biotage Selekt chromatography (5–100%, EtOAc in hexanes) to give the title compound as a brown oil (0.02 g, 11% yield). **IR (film)**: v_{max} 3179, 2929, 1572, 1513, 1394, 1230, 1025, 820,760 cm^{-1}. **^{1}H NMR** (400 MHz, DMSO-d_6) δ 8.51 (d, *J* = 1.2 Hz, 1H), 8.11 (s, 1H), 6.85 (d, *J* = 2.7 Hz, 1H), 6.66 (dd, *J* = 8.6, 2.7 Hz, 1H), 6.53 (d, *J* = 8.5 Hz, 1H), 5.62 (s, 2H), 3.23 – 3.08 (m, 2H), 1.08 (t, *J* = 7.1 Hz, 3H). **^{13}C NMR** (126 MHz, DMSO) δ 168.45, 146.81, 141.82, 119.52, 117.32, 116.43, 113.64, 33.47, 14.68. **LC-MS** *m/z* (ESI+) 181.2 ([M+H]$^+$. Retention time: t_R = 3.82 min, >95%. **HRMS** (ESI+) measured 181.0973 [M+H]$^+$, C$_9$H$_{12}$N$_2$O$_2^+$ calculated 181.0977.

2-Amino-5-bromo-*N*-phenylbenzamide (225)
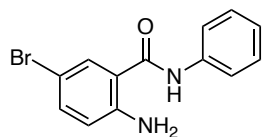
Synthesised according to general method **Q** from 2-amino-5-bromo-*N*-phenylbenzamide **205** (0.3 g, 0.93 mmol, 1equiv.), NH$_4$Cl (0.26 g, 4.86 mmol, 5.2 equiv.) and Fe (0.26 g, 4.65 mmol, 5.0 equiv.). Purified by Biotage Selekt chromatography (5–100%, EtOAc in hexanes) to give the title compound as a white solid (0.09 g, 33% yield). **m.p.** 157–159°C (no lit m.p.). **^{1}H NMR** (400 MHz, DMSO-d_6) δ 10.09 (s, 1H), 7.78 (d, *J* = 2.4 Hz, 1H), 7.69 (d, *J* = 8.1 Hz, 2H), 7.38 – 7.29 (m, 3H), 7.12 – 7.02 (m, 1H), 6.73 (dd, *J* = 8.8, 1.4 Hz, 1H), 6.46 (s, 2H). **^{13}C NMR** (126 MHz, DMSO) δ 166.44, 148.90, 138.91, 134.50, 130.62, 128.49, 123.65, 120.62, 118.40, 116.61. **LC-MS** *m/z* (ESI+) 292.9 ([M+H]$^+$. Retention time: t$_R$ = 5.78 min, >95%. Spectroscopic data matched those in the literature [217].

2-Amino-*N*-benzyl-5-bromobenzamide (226)
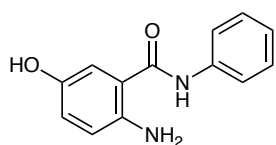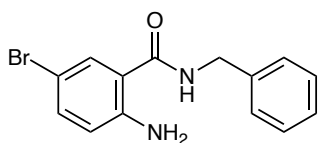
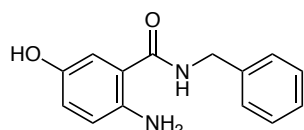Synthesised according to general method **Q** from *N*-benzyl-5-bromo-2-nitrobenzamide **206** (0.3 g, 1.00 mmol, 1equiv.), NH$_4$Cl (0.28 g, 5.2 mmol, 5.2 equiv.) and Fe (0.28 g, 5.0 mmol, 5.0 equiv.). Purified by Biotage Selekt chromatography (5–100%, EtOAc in hexanes) to give the title compound as a white solid (0.08 g, 33% yield). **m.p.** 116–119°C (no lit m.p.). **^{1}H NMR** (400 MHz, DMSO-d_6) δ 8.90 (t, *J* = 6.0 Hz, 1H), 7.72 (d, *J* = 2.3 Hz, 1H), 7.35 – 7.29 (m, 4H), 7.27 – 7.19 (m, 2H), 6.68 (dd, *J* = 8.6, 1.4 Hz, 1H), 6.59 (s, 2H), 4.41 (d, *J* = 5.9 Hz, 2H). **^{13}C NMR** (126 MHz, DMSO) δ 167.38, 148.93, 139.53, 134.12, 130.00, 128.16, 127.12, 126.60, 118.38, 115.51, 39.25. **LC-MS** *m/z* (ESI+) 306.9 ([M+H]$^+$. Retention time: t$_R$ = 5.96 min, >95%. Spectroscopic data matched those in the literature [218].

2-Amino-5-bromo-*N*,*N*-diethylbenzamide (227)
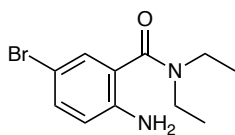
Synthesised according t to general method **Q** from 5-bromo-*N*,*N*-diethyl-2-nitrobenzamide **207** (0.3 g, 1 mmol, 1equiv.), NH$_4$Cl (0.28 g, 5.2 mmol, 5.2 equiv.) and Fe (0.28 g, 5 mmol,

5.0 equiv.). Purified by Biotage Selekt chromatography (5–100%, EtOAc in hexanes) to give the title compound as a white solid (0.21 g, 87% yield). **m.p.** 98–101°C (no lit m.p.). **IR (film)**: v_{max} 3339, 1610, 1483, 1431,1282, 827, 760, 689 cm^{-1}. **^{1}H NMR** (400 MHz, DMSO-d_6) δ 7.21 (dd, J = 8.6, 2.3 Hz, 1H), 7.06 (d, J = 2.4 Hz, 1H), 6.68 (d, J = 8.7 Hz, 1H), 5.12 (s, 2H), 3.14 (dd, J = 5.6 Hz, 4H), 1.08 (d, J = 7.3 Hz, 6H). **^{13}C NMR** (126 MHz, DMSO) δ 167.62, 141.89, 131.92, 128.68, 122.78, 117.35, 106.01, 39.58, 39.25, 13.58, 12.80. **LC-MS** m/z (ESI+) 272.9 ([M+H]$^+$. Retention time: t_R = 5.78 min, >95%. **HRMS** (ESI+) measured 271.0458 [M+H]$^+$, $C_{11}H_{15}BrN_2O^+$ calculated 271.0446.

2-Amino-5-bromo-N-ethylbenzamide (228)
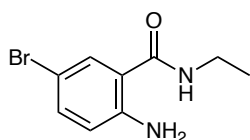
Synthesised according to general method **Q** from 5-bromo-N-ethyl-2-nitrobenzamide **208** (0.3 g, 1.1 mmol, 1equiv.), NH$_4$Cl (0.31 g, 5.7 mmol, 5.2 equiv.) and Fe (0.31 g, 5.5 mmol, 5.0 equiv.). Purified by Biotage Selekt chromatography (5–100%, EtOAc in hexanes) to give the title compound as a white solid (0.22 g, 82% yield). **m.p.** 87–89°C (no lit m.p.). **^{1}H NMR** (500 MHz, DMSO-d_6) δ 8.34 (t, J = 5.5 Hz, 1H), 7.62 (d, J = 2.3 Hz, 1H), 7.25 (dd, J = 8.8, 2.3 Hz, 1H), 6.66 (d, J = 8.7 Hz, 1H), 6.59 – 6.47 (m, 2H), 3.22 (qd, J = 7.2, 5.4 Hz, 2H), 1.07 (td, J = 7.2, 1.5 Hz t, 3H). **^{13}C NMR** (126 MHz, DMSO) δ 162.31, 148.77, 133.96, 127.68, 118.34, 117.20, 109.61, 33.83, 33.69, 14.62. **LC-MS** m/z (ESI+) 244.9 ([M+H]$^+$. Retention time: t_R = 4.91 min, >95%. Spectroscopic data matched those in the literature [219].

2-Amino-5-bromo-N-methylbenzamide (229)
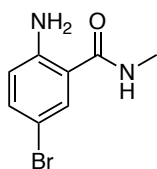
Synthesised according to general method **Q** from 5-bromo-N-methyl-2-nitrobenzamide **209** (0.3 g, 1.16 mmol, 1equiv.), NH$_4$Cl (0.32 g, 6 mmol, 5.2 equiv.) and Fe (0.32 g, 5.8 mmol, 5.0 equiv.). Purified by Biotage Selekt chromatography (5–100%, EtOAc in hexanes) to give the title compound as a white solid (0.10 g, 38% yield). **m.p.** 92–95°C (no lit m.p.). **^{1}H NMR** (400 MHz, DMSO-d_6) δ 8.28 (s, 1H), 7.60 (t, J = 1.8 Hz, 1H), 7.25 (dt, J = 8.9, 1.9 Hz, 1H), 6.66 (dd, J = 8.9, 1.4 Hz, 1H), 6.55 (s, 2H),

2.71 (dd, *J* = 4.5, 1.3 Hz, 3H). **¹³C NMR** (126 MHz, DMSO) δ 169.23, 149.03, 140.04, 129.75, 128.74, 128.66, 126.43,126.03, 125,98, 125,56, 116.85, 114.83, 25.94. **LC-MS** *m/z* (ESI+) 231.1 ([M+H]⁺. Retention time: t_R = 4.51 min, >95%. Spectroscopic data matched those in the literature [220].

N-methyl-4-nitro-[1,1'-biphenyl]-3-carboxamide (230)
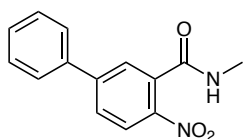
The 2-amino-4-bromo-*N*-phenylbenzamide **209** (0.200 g, 0.772 mmol, 1. 0 equiv.), the phenylboronic acid (0.113 g, 0.93 mmol., 1.2 equiv.), K_2CO_3 (0.320 g, 2.32 mmol, 3.0 equiv.) and Pd(PPh₃)₄ (0.18 g, 0.154 mmol, 0.02 equiv.) were added to a round bottomed flask containing a magnetic stirrer under a nitrogen atmosphere in a microwave vial. Solvent mixture (ethanol: toluene: water (9:3:1), 5 mL for every 125 mg of substrate) was added under a nitrogen atmosphere. The suspension was heated at 100 °C for 15 minutes under microwave radiation depending on the substrate. For heterocyclic bromides, water was added to the reaction, and it was extracted with EtOAc (3 x 40 mL). The extracts were combined and dried over MgSO₄, and then concentrated under reduced pressure *in vacuo*. The resulting crude product which was purified by Biotage Selekt chromatography (5–100%, EtOAc in hexanes) to give the title compound as an off-white solid (0.11 g, 53%). **¹H NMR** (400 MHz, DMSO) δ 8.66 (s, 1H), 8.09 (d, J = 8.6 Hz, 1H), 7.97 (dd, J = 8.5, 2.2 Hz, 1H), 7.87 (d, J = 2.1 Hz, 1H), 7.81 (d, J = 7.7 Hz, 2H), 7.52 (dt, J = 15.3, 7.1 Hz, 3H), 2.79 (d, J = 4.4 Hz, 3H). **LC-MS** *m/z* (ESI+) 257.2 ([M+H]⁺. Retention time: t_R = 3.59 min, >95%.

4-Amino-*N*-methyl-[1,1'-biphenyl]-3-carboxamide (231)
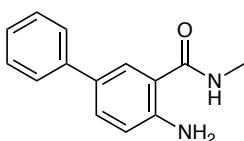
Synthesised according to general method **Q** from *N*-methyl-4-nitro-[1,1'-biphenyl]-3-carboxamide **230** (0.080 g, 0.31 mmol, 1equiv.), NH₄Cl (0.087 g, 1.62 mmol, 5.2 equiv.) and Fe (0.087 g, 1.56 mmol, 5.0 equiv.). Purified by Biotage Selekt chromatography (5–100%, EtOAc in hexanes) to give the title compound as a white solid (0.04 g, 52% yield). **m.p.** 109–111°C (no lit m.p.). **IR (film)**: v_{max}

3287,1632, 1543, 1483, 1263, 760, 693 cm^{-1}. **^{1}H NMR** (400 MHz, DMSO-d_6) δ 8.28 (s, 1H), 7.60 (t, J = 1.8 Hz, 1H), 7.25 (dt, J = 8.9, 1.9 Hz, 1H), 6.66 (dd, J = 8.9, 1.4 Hz, 1H), 6.55 (s, 2H), 2.71 (dd, J = 4.5, 1.3 Hz, 3H). **^{13}C NMR** (126 MHz, DMSO) δ 169.23, 149.03, 140.04, 129.75, 128.74, 128.66, 126.43,126.03, 125,98, 125,56, 116.85, 114.83, 25.94. **LC-MS** *m/z* (ESI+) 227.20 ([M+H]$^+$. Retention time: t_R = 3.68 min, >95%. **HRMS** (ESI+) measured 227.1190 [M+H]$^+$, C$_{14}$H$_{14}$N$_2$O$^+$ calculated 227.1184.

7 References

1.   Rath, O. and F. Kozielski, *Kinesins and cancer.* Nature Reviews Cancer, 2012. **12**(8): p. 527-539.

2.   Wang, W., et al., *Kinesin, 30 years later: Recent insights from structural studies.* Protein Science, 2015. **24**(7): p. 1047-1056.

3.   Crosby, M.E., *Cell cycle: principles of control.* The Yale journal of biology and medicine, 2007. **80**(3): p. 141.

4.   Schafer, K., *The cell cycle: a review.* Veterinary pathology, 1998. **35**(6): p. 461-478.

5.   Tuck, C., et al., *Robust mitotic entry is ensured by a latching switch.* Biology open, 2013. **2**(9): p. 924-931.

6.   Marieb, E.N. and K. Hoehn, *Human anatomy & physiology*. 2007: Pearson education.

7.   Raven, P., et al., *Proteins: Molecules with diverse structures and functions*. 2014, McGraw-Hill, New York. p. 44-53.

8.   Kavallaris, M., *Microtubules and resistance to tubulin-binding agents.* Nature Reviews Cancer, 2010. **10**(3): p. 194-204.

9.   Jordan, M.A. and L. Wilson, *Microtubules as a target for anticancer drugs.* Nature Reviews Cancer, 2004. **4**(4): p. 253-265.

10.   Tripathi, S., G. Srivastava, and A. Sharma, *Molecular dynamics simulation and free energy landscape methods in probing L215H, L217R and L225M βI-tubulin mutations causing paclitaxel resistance in cancer cells.* Biochemical and Biophysical Research Communications, 2016. **476**(4): p. 273-279.

11.   Walczak, C.E. and R. Heald, *Mechanisms of Mitotic Spindle Assembly and Function*, in *International Review of Cytology*. 2008, Elsevier. p. 111-158.

12.   Campbell, N.A. and J.B. Reece, *Biology*. 2005: Pearson Education India.

13.   Musacchio, A. and E.D. Salmon, *The spindle-assembly checkpoint in space and time.* Nature Reviews Molecular Cell Biology, 2007. **8**(5): p. 379-393.

14.   Salehi, B., et al., *Phytotherapeutics in cancer invasion and metastasis.* Phytotherapy Research, 2018. **32**(8): p. 1425-1449.

15.   Dai, X., et al., *Cancer Hallmarks, Biomarkers and Breast Cancer Molecular Subtypes.* Journal of Cancer, 2016. **7**(10): p. 1281-1294.

16.   Hanahan, D. and Robert A. Weinberg, *Hallmarks of Cancer: The Next Generation.* Cell, 2011. **144**(5): p. 646-674.

17.   Hanahan, D. and R.A. Weinberg, *The Hallmarks of Cancer.* Cell, 2000. **100**(1): p. 57-70.

18.   McClatchey, A.I. and A.S. Yap, *Contact inhibition (of proliferation) redux.* Current Opinion in Cell Biology, 2012. **24**(5): p. 685-694.

19.   Evan, G.I. and K.H. Vousden, *Proliferation, cell cycle and apoptosis in cancer.* Nature, 2001. **411**(6835): p. 342-348.

20.   Greenberg, R., *Telomeres, Crisis and Cancer.* Current Molecular Medicine, 2005. **5**(2): p. 213-218.

21.   Bergers, G. and L.E. Benjamin, *Tumorigenesis and the angiogenic switch.* Nature Reviews Cancer, 2003. **3**(6): p. 401-410.

22.   van Zijl, F., G. Krupitza, and W. Mikulits, *Initial steps of metastasis: cell invasion and endothelial transmigration.* Mutation research, 2011. **728**(1-2): p. 23-34.

23.   Jones, R.G. and C.B. Thompson, *Tumor suppressors and cell metabolism: a recipe for cancer growth.* Genes & development, 2009. **23**(5): p. 537-548.

24.   Hsu, P.P. and D.M. Sabatini, *Cancer cell metabolism: Warburg and beyond.* Cell, 2008. **134**(5): p. 703-707.

25.   DeBerardinis, R.J., et al., *The biology of cancer: metabolic reprogramming fuels cell growth and proliferation.* Cell metabolism, 2008. **7**(1): p. 11-20.

26.   Vajdic, C.M. and M.T. Van Leeuwen, *Cancer incidence and risk factors after solid organ transplantation.* International journal of cancer, 2009. **125**(8): p. 1747-1754.

27.   Negrini, S., V.G. Gorgoulis, and T.D. Halazonetis, *Genomic instability--an evolving hallmark of cancer.* Nat Rev Mol Cell Biol, 2010. **11**(3): p. 220-8.

28. Jackson, S.P. and J. Bartek, *The DNA-damage response in human biology and disease.* Nature, 2009. **461**(7267): p. 1071-1078.

29. Grivennikov, S.I., F.R. Greten, and M. Karin, *Immunity, inflammation, and cancer.* Cell, 2010. **140**(6): p. 883-899.

30. Wong, R.S.Y., *Role of Nonsteroidal Anti-Inflammatory Drugs (NSAIDs) in Cancer Prevention and Cancer Promotion.* Adv Pharmacol Sci, 2019. **2019**: p. 3418975.

31. Gutschner, T. and S. Diederichs, *The hallmarks of cancer: a long non-coding RNA point of view.* RNA Biol, 2012. **9**(6): p. 703-19.

32. Segovia-Mendoza, M., et al., *Combinations of Calcitriol with Anticancer Treatments for Breast Cancer: An Update.* International Journal of Molecular Sciences, 2021. **22**(23): p. 12741.

33. Patrick, G.L., *An introduction to medicinal chemistry.* 2013: Oxford university press.

34. Hirokawa, N. and Y. Tanaka, *Kinesin superfamily proteins (KIFs): Various functions and their relevance for important phenomena in life and diseases.* Experimental Cell Research, 2015. **334**(1): p. 16-25.

35. Vale, R.D., T.S. Reese, and M.P. Sheetz, *Identification of a novel force-generating protein, kinesin, involved in microtubule-based motility.* Cell, 1985. **42**(1): p. 39-50.

36. Bloom, G.S., et al., *Native structure and physical properties of bovine brain kinesin and identification of the ATP-binding subunit polypeptide.* Biochemistry, 1988. **27**(9): p. 3409-3416.

37. Kolomeisky, A.B., *Motor proteins and molecular motors: how to operate machines at the nanoscale.* Journal of physics. Condensed matter : an Institute of Physics journal, 2013. **25**(46): p. 463101-463101.

38. Kalantari, S. and I. Filges, *'Kinesinopathies': emerging role of the kinesin family member genes in birth defects.* Journal of medical genetics, 2020. **57**(12): p. 797-807.

39. Hirokawa, N., et al., *Kinesin superfamily motor proteins and intracellular transport.* Nature Reviews Molecular Cell Biology, 2009. **10**(10): p. 682-696.

40.   Steinmetz, M.O. and A. Akhmanova, *Capturing protein tails by CAP-Gly domains.* Trends in biochemical sciences, 2008. **33**(11): p. 535-545.

41.   Hummel, J.J.A. and C.C. Hoogenraad, *Specific KIF1A-adaptor interactions control selective cargo recognition.* The Journal of cell biology, 2021. **220**(10): p. e202105011.

42.   Nangaku, M., et al., *KIF1B, a novel microtubule plus end-directed monomeric motor protein for transport of mitochondria.* Cell, 1994. **79**(7): p. 1209-1220.

43.   Hirose, K., et al., *Large conformational changes in a kinesin motor catalyzed by interaction with microtubules.* Molecular cell, 2006. **23**(6): p. 913-923.

44.   Kull, F.J., et al., *Crystal structure of the kinesin motor domain reveals a structural similarity to myosin.* Nature, 1996. **380**(6574): p. 550-555.

45.   Woehlke, G., et al., *Microtubule Interaction Site of the Kinesin Motor.* Cell, 1997. **90**(2): p. 207-216.

46.   *38*, in *Each and Her*. 2022, University of Arizona Press. p. 38-38.

47.   Turner, J., et al., *Crystal Structure of the Mitotic Spindle Kinesin Eg5 Reveals a Novel Conformation of the Neck-linker.* Journal of Biological Chemistry, 2001. **276**(27): p. 25496-25502.

48.   de Cuevas, M., T. Tao, and L.S. Goldstein, *Evidence that the stalk of Drosophila kinesin heavy chain is an alpha-helical coiled coil.* The Journal of cell biology, 1992. **116**(4): p. 957-965.

49.   Grummt, M., et al., *Importance of a flexible hinge near the motor domain in kinesin-driven motility.* The EMBO journal, 1998. **17**(19): p. 5536-5542.

50.   Verhey, K.J. and J.W. Hammond, *Traffic control: regulation of kinesin motors.* Nature Reviews Molecular Cell Biology, 2009. **10**(11): p. 765-777.

51.   Verhey, K.J., et al., *Cargo of kinesin identified as JIP scaffolding proteins and associated signaling molecules.* The Journal of cell biology, 2001. **152**(5): p. 959-970.

52.   Hackney, D.D. and M.F. Stock, *Kinesin's IAK tail domain inhibits initial microtubule-stimulated ADP release.* Nature Cell Biology, 2000. **2**(5): p. 257-260.

53. Talapatra, S.K., B. Harker, and J.P.I. Welburn, *Author response: The C-terminal region of the motor protein MCAK controls its structure and activity through a conformational switch*. 2015, eLife Sciences Publications, Ltd.

54. Wendt, T., et al., *A Structural Analysis of the Interaction between ncd Tail and Tubulin Protofilaments.* Journal of Molecular Biology, 2003. **333**(3): p. 541-552.

55. Ulaganathan, V., et al., *Structural Insights into a Unique Inhibitor Binding Pocket in Kinesin Spindle Protein.* Journal of the American Chemical Society, 2013. **135**(6): p. 2263-2272.

56. Wood, K.W., et al., *Antitumor activity of an allosteric inhibitor of centromere-associated protein-E.* Proceedings of the National Academy of Sciences of the United States of America, 2010. **107**(13): p. 5839-5844.

57. Myers, S.M. and I.J.F.m.c. Collins, *Recent findings and future directions for interpolar mitotic kinesin inhibitors in cancer therapy.* 2016. **8**(4): p. 463-489.

58. Park, H.-W., et al., *Structural basis of small molecule ATPase inhibition of a human mitotic kinesin motor protein.* Scientific reports, 2017. **7**(1): p. 15121-15121.

59. Kapitein, L.C., et al., *Microtubule cross-linking triggers the directional motility of kinesin-5.* The Journal of cell biology, 2008. **182**(3): p. 421-428.

60. Blangy, A., et al., *Phosphorylation by p34cdc2 regulates spindle association of human Eg5, a kinesin-related motor essential for bipolar spindle formation in vivo.* Cell, 1995. **83**(7): p. 1159-1169.

61. Castoldi, M. and I. Vernos, *Chromokinesin Xklp1 contributes to the regulation of microtubule density and organization during spindle assembly.* Molecular biology of the cell, 2006. **17**(3): p. 1451-1460.

62. Garcia-Saez, I. and D.A. Skoufias, *Eg5 targeting agents: From new anti-mitotic based inhibitor discovery to cancer therapy and resistance.* Biochemical Pharmacology, 2021. **184**: p. 114364.

63. Milic, B., et al., *KIF15 nanomechanics and kinesin inhibitors, with implications for cancer chemotherapeutics.* Proceedings of the National Academy of Sciences of the United States of America, 2018. **115**(20): p. E4613-E4622.

64. Endow, S.A., F.J. Kull, and H. Liu, *Kinesins at a glance.* Journal of cell science, 2010. **123**(Pt 20): p. 3420-3424.

65. Hirokawa, N., *Organelle transport along microtubules — the role of KIFs.* Trends in Cell Biology, 1996. **6**(4): p. 135-141.

66. Cole, D.G., *Intraflagellar Transport: Keeping the Motors Coordinated.* Current Biology, 2005. **15**(19): p. R798-R801.

67. Hao, L., et al., *Analysis of Intraflagellar Transport in C. elegans Sensory Cilia*, in *Methods in Cell Biology*. 2009, Elsevier. p. 235-266.

68. Liu, X., H. Gong, and K. Huang, *Oncogenic role of kinesin proteins and targeting kinesin therapy.* Cancer science, 2013. **104**(6): p. 651-656.

69. Henderson, M.C., et al., *UA62784, a novel inhibitor of centromere protein E kinesin-like protein.* Molecular cancer therapeutics, 2009. **8**(1): p. 36-44.

70. Bergnes, G., K. Brejc, and L. Belmont, *Mitotic Kinesins: Prospects for Antimitotic Drug Discovery.* Current Topics in Medicinal Chemistry, 2005. **5**(2): p. 127-145.

71. Liu, M., et al., *Ectopic expression of the microtubule-dependent motor protein Eg5 promotes pancreatic tumourigenesis.* The Journal of Pathology, 2010. **221**(2): p. 221-228.

72. Lad, L., et al., *Mechanism of Inhibition of Human KSP by <i>Ispinesib</i>.* Biochemistry, 2008. **47**(11): p. 3576-3585.

73. Woessner, R., et al., *Combination of the KSP Inhibitor ARRY-520 with Bortezomib or Revlimid Causes Sustained Tumor Regressions and Significantly Increased Time to Regrowth in Models of Multiple Myeloma.* Blood, 2009. **114**(22): p. 2858-2858.

74. Tcherniuk, S., et al., *Relocation of Aurora B and Survivin from Centromeres to the Central Spindle Impaired by a Kinesin-Specific MKLP-2 Inhibitor.* Angewandte Chemie International Edition, 2010. **49**(44): p. 8228-8231.

75. Peters, N.T. and D.L. Kropf, *Kinesin-5 motors are required for organization of spindle microtubules in Silvetia compressa zygotes.* BMC plant biology, 2006. **6**: p. 19-19.

76.   Catarinella, M., et al., *BTB-1: A Small Molecule Inhibitor of the Mitotic Motor Protein Kif18A.* Angewandte Chemie International Edition, 2009. **48**(48): p. 9072-9076.

77.   Aoki, S., et al., *Mammalian mitotic centromere-associated kinesin (MCAK).* FEBS Journal, 2005. **272**(9): p. 2132-2140.

78.   Wu, J., et al., *Discovery and Mechanistic Study of a Small Molecule Inhibitor for Motor Protein KIFC1.* ACS Chemical Biology, 2013. **8**(10): p. 2201-2208.

79.   Janisch, K.M., et al., *Kinesin-6 KIF20B is required for efficient cytokinetic furrowing and timely abscission in human cells.* Molecular biology of the cell, 2018. **29**(2): p. 166-179.

80.   Abaza, A., et al., *M phase phosphoprotein 1 is a human plus-end-directed kinesin-related protein required for cytokinesis.* The Journal of biological chemistry, 2003. **278**(30): p. 27844-27852.

81.   Hardin, J., et al., *Zygotic loss of ZEN-4/MKLP1 results in disruption of epidermal morphogenesis in the C. elegans embryo.* Developmental Dynamics, 2008. **237**(3): p. 830-836.

82.   Kamimoto, T., et al., *Identification of a Novel Kinesin-related Protein, KRMP1, as a Target for Mitotic Peptidyl-prolyl Isomerase Pin1.* Journal of Biological Chemistry, 2001. **276**(40): p. 37520-37528.

83.   Talapatra, S.K., A.W. Schüttelkopf, and F. Kozielski, *The structure of the ternary Eg5-ADP-ispinesib complex.* Acta crystallographica. Section D, Biological crystallography, 2012. **68**(Pt 10): p. 1311-1319.

84.   Atherton, J., et al., *The divergent mitotic kinesin MKLP2 exhibits atypical structure and mechanochemistry.* Elife, 2017. **6**: p. e27793.

85.   Talapatra, S.K., et al., *Depsidones from Lichens as Natural Product Inhibitors of M-Phase Phosphoprotein 1, a Human Kinesin Required for Cytokinesis.* Journal of Natural Products, 2016. **79**(6): p. 1576-1585.

86.   Cole, C., J.D. Barber, and G.J. Barton, *The Jpred 3 secondary structure prediction server.* Nucleic acids research, 2008. **36**(Web Server issue): p. W197-W201.

87.   Arnold, K., et al., *The SWISS-MODEL workspace: a web-based environment for protein structure homology modelling.* Bioinformatics, 2006. **22**(2): p. 195-201.

88. Kanehira, M., et al., *Oncogenic Role of MPHOSPH1, a Cancer-Testis Antigen Specific to Human Bladder Cancer.* Cancer Research, 2007. **67**(7): p. 3276-3285.

89. Chandra, R., et al., *Structural and functional domains of the Drosophila ncd microtubule motor protein.* Journal of Biological Chemistry, 1993. **268**(12): p. 9005-9013.

90. Pannu, V., P.C.G. Rida, and R. Aneja, *The Human Kinesin-14 Motor KifC1/HSET Is an Attractive Anti-cancer Drug Target*, in *Kinesins and Cancer*. 2015, Springer Netherlands. p. 101-116.

91. Sharma, N., et al., *Computational benchmarking of putative KIFC1 inhibitors.* Medicinal Research Reviews, 2023. **43**(2): p. 293-318.

92. Zhi, E., et al., *Decreased Expression of KIFC1 in Human Testes with Globozoospermic Defects.* Genes, 2016. **7**(10): p. 75.

93. Krämer, A., K. Neben, and A.D. Ho, *Centrosome aberrations in hematological malignancies.* Cell Biology International, 2005. **29**(5): p. 375-383.

94. Nigg, E.A., *Centrosome aberrations: cause or consequence of cancer progression?* Nature Reviews Cancer, 2002. **2**(11): p. 815-825.

95. Osmanova, N., W. Schultze, and N. Ayoub, *Azaphilones: a Class of Fungal Metabolites with Diverse Biological Activities*. Vol. 9. 2010. 315-342.

96. Dong, P., et al., *Innovative nano-carriers in anticancer drug delivery-a comprehensive review.* Bioorganic chemistry, 2019. **85**: p. 325-336.

97. Zhang, X., et al., *Podophyllotoxin derivatives as an excellent anticancer aspirant for future chemotherapy: a key current imminent needs.* Bioorganic & Medicinal Chemistry, 2018. **26**(2): p. 340-355.

98. Fang, W.-Y., et al., *Synthetic approaches and pharmaceutical applications of chloro-containing molecules for drug discovery: A critical review.* European journal of medicinal chemistry, 2019. **173**: p. 117-153.

99. Liu, H., et al., *Structure-activity relationships (SAR) of triazine derivatives: Promising antimicrobial agents.* European journal of medicinal chemistry, 2020. **185**: p. 111804.

100. Xu, M., et al., *Triazole derivatives as inhibitors of Alzheimer's disease: current developments and structure-activity relationships.* European journal of medicinal chemistry, 2019. **180**: p. 656-672.

101. Zhao, C., et al., *Arylnaphthalene lactone analogues: synthesis and development as excellent biological candidates for future drug discovery.* RSC advances, 2018. **8**(17): p. 9487-9502.

102. Zhao, C., et al., *Pharmaceutical and medicinal significance of sulfur (SVI)-Containing motifs for drug discovery: A critical review.* European journal of medicinal chemistry, 2019. **162**: p. 679-734.

103. McNaught, A.D. and A. Wilkinson, *Compendium of chemical terminology. IUPAC recommendations.* 1997.

104. Gomtsyan, A., *Heterocycles in drugs and drug discovery.* Chemistry of Heterocyclic Compounds, 2012. **48**(1): p. 7-10.

105. Dua, R., et al., *Pharmacological significance of synthetic heterocycles scaffold: a review.* Advances in Biological Research, 2011. **5**(3): p. 120-144.

106. Broughton, H.B. and I.A. Watson, *Selection of heterocycles for drug design.* Journal of Molecular Graphics and Modelling, 2004. **23**(1): p. 51-58.

107. Cao, X., et al., *Design, Synthesis, and Structure–Activity Relationship Studies of Novel Fused Heterocycles-Linked Triazoles with Good Activity and Water Solubility.* Journal of Medicinal Chemistry, 2014. **57**(9): p. 3687-3706.

108. El-Sawy, E.R., et al., *Synthesis, anti-inflammatory, analgesic and anticonvulsant activities of some new 4,6-dimethoxy-5-(heterocycles)benzofuran starting from naturally occurring visnagin.* Arabian Journal of Chemistry, 2014. **7**(6): p. 914-923.

109. Abd El-Salam, N.M., et al., *Synthesis and Antimicrobial Activities of Some New Heterocyclic Compounds Based on 6-Chloropyridazine-3(2<i>H</i>)-thione.* Journal of Chemistry, 2013. **2013**: p. 1-8.

110. Salem, M.S., et al., *Synthesis, Antibacterial, and Antiviral Evaluation of New Heterocycles Containing the Pyridine Moiety.* Archiv der Pharmazie, 2013. **346**(10): p. 766-773.

111. Chen, Y., et al., *Synthesis, characterization and anti-proliferative activity of heterocyclic hypervalent organoantimony compounds.* European Journal of Medicinal Chemistry, 2014. **79**: p. 391-398.

112. El-Sawy, E.R., et al., *Synthesis, antimicrobial and anticancer activities of some new N-methylsulphonyl and N-benzenesulphonyl-3-indolyl heterocycles.* Arabian Journal of Chemistry, 2013. **6**(1): p. 67-78.

113. Mabkhot, Y.N., et al., *Synthesis, reactions and biological activity of some new bis-heterocyclic ring compounds containing sulphur atom.* Chemistry Central journal, 2013. **7**(1): p. 112-112.

114. Sanders, M.P.A., et al., *Snooker: A Structure-Based Pharmacophore Generation Tool Applied to Class A GPCRs.* Journal of Chemical Information and Modeling, 2011. **51**(9): p. 2277-2292.

115. Goto, J., R. Kataoka, and N. Hirayama, *Ph4Dock: Pharmacophore-Based Protein−Ligand Docking.* Journal of Medicinal Chemistry, 2004. **47**(27): p. 6804-6811.

116. Ferreira, L.G., et al., *Molecular docking and structure-based drug design strategies.* Molecules (Basel, Switzerland), 2015. **20**(7): p. 13384-13421.

117. Anderson, A.C., *The Process of Structure-Based Drug Design.* Chemistry & Biology, 2003. **10**(9): p. 787-797.

118. Imam, S.S. and S.J. Gilani, *Computer aided drug design: A novel loom to drug discovery.* Organic & Medicinal Chemistry International Journal, 2017. **1**(3): p. 113-118.

119. Rost, B., *Twilight zone of protein sequence alignments.* Protein Engineering, Design and Selection, 1999. **12**(2): p. 85-94.

120. Cavasotto, C.N. and S.S. Phatak, *Homology modeling in drug discovery: current trends and applications.* Drug Discovery Today, 2009. **14**(13-14): p. 676-683.

121. Shoichet, B.K., et al., *Lead discovery using molecular docking.* Current Opinion in Chemical Biology, 2002. **6**(4): p. 439-446.

122. Gohlke, H. and G. Klebe, *Approaches to the Description and Prediction of the Binding Affinity of Small-Molecule Ligands to Macromolecular Receptors.* Angewandte Chemie International Edition, 2002. **41**(15): p. 2644-2676.

123. Bottegoni, G., *Protein-ligand docking.* Frontiers in Bioscience, 2011. **16**(1): p. 2289.

124. Trott, O. and A.J. Olson, *AutoDock Vina: improving the speed and accuracy of docking with a new scoring function, efficient optimization, and multithreading.* Journal of computational chemistry, 2010. **31**(2): p. 455-461.

125. McInnes, C., *Virtual screening strategies in drug discovery.* Current Opinion in Chemical Biology, 2007. **11**(5): p. 494-502.

126. Geppert, H., M. Vogt, and J. Bajorath, *Current Trends in Ligand-Based Virtual Screening: Molecular Representations, Data Mining Methods, New Application Areas, and Performance Evaluation.* Journal of Chemical Information and Modeling, 2010. **50**(2): p. 205-216.

127. Wermuth, C.-G., et al., *Glossary of Terms Used in Medicinal Chemistry (IUPAC Recommendations 1997)*, in *Annual Reports in Medicinal Chemistry*. 1998, Elsevier. p. 385-395.

128. *Pharmacophores and Pharmacophore Searches*, in *Methods and Principles in Medicinal Chemistry*. 2006, Wiley.

129. Yang, S.-Y., *Pharmacophore modeling and applications in drug discovery: challenges and recent advances.* Drug Discovery Today, 2010. **15**(11-12): p. 444-450.

130. Oprea, T.I. and H. Matter, *Integrating virtual screening in lead discovery.* Current Opinion in Chemical Biology, 2004. **8**(4): p. 349-358.

131. Dey, F. and A. Caflisch, *Fragment-Based de Novo Ligand Design by Multiobjective Evolutionary Optimization.* Journal of Chemical Information and Modeling, 2008. **48**(3): p. 679-690.

132. Hubbard, R.E., W. Jahnke, and D. Erlanson, *Fragment-based Drug Discovery: Lessons and Outlook.* Weinheim, Germany: wiley-vch verlag gmbh & co. kgaa. doi, 2016. **10**(1002): p. 9783527683604.

133. Rath, O. and F. Kozielski, *Kinesins and cancer.* Nat Rev Cancer, 2012. **12**(8): p. 527-39.

134. Shrestha, G., St. Clair, L.L. Lichens: a promising source of antibiotic and anticancer drugs. Phytochem Rev 12, 229–244 (2013). https://doi.org/10.1007/s11101-013-9283-7.

135. Talapatra, S.K., et al., *Depsidones from Lichens as Natural Product Inhibitors of M-Phase Phosphoprotein 1, a Human Kinesin Required for Cytokinesis.* J Nat Prod, 2016. **79**(6): p. 1576-85.

136. Singh, R., et al., *Ascochyta rabiei: A threat to global chickpea production.* Mol Plant Pathol, 2022. **23**(9): p. 1241-1261.

137. Wei, W.-G. and Z.-J. Yao, *Synthesis Studies toward Chloroazaphilone and Vinylogous γ-Pyridones: Two Common Natural Product Core Structures.* The Journal of Organic Chemistry, 2005. **70**(12): p. 4585-4590.

138. Gao, J.-M., S.-X. Yang, and J.-C. Qin, *Azaphilones: Chemistry and Biology.* Chemical Reviews, 2013. **113**(7): p. 4755-4811.

139. Osmanova, N., W. Schultze, and N. Ayoub, *Azaphilones: a class of fungal metabolites with diverse biological activities.* Phytochemistry Reviews, 2010. **9**(2): p. 315-342.

140. Liu, N. and Z. Xu. *Using LeDock as a docking tool for computational drug design*. in *IOP Conference Series: Earth and Environmental Science*. 2019. IOP Publishing.

141. Wei, G.-W., *Protein structure prediction beyond AlphaFold.* Nature Machine Intelligence, 2019. **1**(8): p. 336-337.

142. Terwilliger, T.C., et al., *AlphaFold predictions are valuable hypotheses and accelerate but do not replace experimental structure determination.* Nature Methods, 2023: p. 1-7.

143. Sulaiman Al-Ayed, A., *4-Hydroxy-3-carboxycoumarin as an efficient building block for new ruthenium (II) complexes: synthesis, characterization, antibacterial, antioxidant and anti-inflammatory activities.* Applied Organometallic Chemistry, 2017. **31**(5): p. e3605.

144. Woods, L. and D. Johnson, *Coumarins from 2-Hydroxyaryl Acids and Malonic Acid.* The Journal of Organic Chemistry, 1965. **30**(12): p. 4343-4344.

145. Godinho, S.A., M. Kwon, and D. Pellman, *Centrosomes and cancer: how cancer cells divide with too many centrosomes.* Cancer and Metastasis Reviews, 2009. **28**(1-2): p. 85-98.

146. Wu, J., et al., *Discovery and mechanistic study of a small molecule inhibitor for motor protein KIFC1.* ACS chemical biology, 2013. **8**(10): p. 2201-2208.

147.   Watts, C.A., et al., *Design, synthesis, and biological evaluation of an allosteric inhibitor of HSET that targets cancer cells with supernumerary centrosomes.* Chemistry & biology, 2013. **20**(11): p. 1399-1410.

148.   Kumar, B.K., et al., *Medicinal chemistry perspectives of 1, 2, 3, 4-tetrahydroisoquinoline analogs–biological activities and SAR studies.* RSC advances, 2021. **11**(20): p. 12254-12287.

149.   Brown, N., *Bioisosterism in medicinal chemistry.* Bioisosteres in medicinal chemistry, 2012: p. 1-14.

150.   Khan, M.F., et al., *The therapeutic voyage of pyrazole and its analogs: a review.* European journal of medicinal chemistry, 2016. **120**: p. 170-201.

151.   Johnson, L., et al., *A reliable synthesis of 3-amino-5-alkyl and 5-amino-3-alkyl isoxazoles.* Synthesis, 2013. **45**(02): p. 171-173.

152.   Adhikari, N., et al., *HDAC3 is a potential validated target for cancer: An overview on the benzamide-based selective HDAC3 inhibitors through comparative SAR/QSAR/QAAR approaches.* European journal of medicinal chemistry, 2018. **157**: p. 1127-1142.

153.   Zhang, W., et al., *Discovery of a novel inhibitor of kinesin-like protein KIFC1.* Biochemical Journal, 2016. **473**(8): p. 1027-1035.

154.   Cosconati, S., et al., *Virtual Screening with AutoDock: Theory and Practice.* Expert Opin Drug Discov, 2010. **5**(6): p. 597-607.

155.   Puranen, J.S., M.J. Vainio, and M.S. Johnson, *Accurate conformation-dependent molecular electrostatic potentials for high-throughput in silico drug discovery.* Journal of Computational Chemistry, 2010. **31**(8): p. 1722-1732.

156.   O'Boyle, N.M., et al., *Open Babel: An open chemical toolbox.* Journal of Cheminformatics, 2011. **3**(1): p. 33.

157.   Stewart, J., *MOPAC2012. Stewart Computational Chemistry, Colorado Springs.* CO, USA, 2012.

158.   Case, D., et al., *AMBER 2018; 2018.* University of California, San Francisco, 2018.

159.   Pettersen, E.F., et al., *UCSF Chimera--a visualization system for exploratory research and analysis.* J Comput Chem, 2004. **25**(13): p. 1605-12.

160. Biovia, D., *Discovery Studio Modeling Environment, Dassault Syst. Release, San Diego, 2015.*

161. Gelfand, V.I., et al., *A dominant negative approach for functional studies of the kinesin II complex.* Kinesin Protocols, 2001: p. 191-204.

162. Tang, J., *Structural and functional studies of the human mitotic kinesins MPP1 and KifC1, kinase DYRK2, and antibody A33 Fab and their potential as targets for development of cancer chemotherapy drugs.* 2022, UCL (University College London).

163. Sukhen, S. and K.K. Doddi, *SYNTHESIS OF NOVEL BENZOPYRONE SUBSTITUTED BENZIMIDAZOLE ANALOGUES AS ANTIBACTERIAL AGENTS.* International research journal of pharmacy, 2015. **6**: p. 138-142.

164. Vieira, L.C., M.W. Paixão, and A.G. Corrêa, *Green synthesis of novel chalcone and coumarin derivatives via Suzuki coupling reaction.* Tetrahedron Letters, 2012. **53**(22): p. 2715-2718.

165. da Silveira Pinto, L.S. and M.V. de Souza, *Sonochemistry as a general procedure for the synthesis of coumarins, including multigram synthesis.* Synthesis, 2017. **49**(12): p. 2677-2682.

166. Sugino, T. and K. Tanaka, *Solvent-free coumarin synthesis.* Chemistry Letters, 2001. **30**(2): p. 110-111.

167. Zhang, Y., et al., *Comparative study of two near-infrared coumarin–BODIPY dyes for bioimaging and photothermal therapy of cancer.* Journal of Materials Chemistry B, 2019. **7**(30): p. 4717-4724.

168. Prashanth, T., et al., *Synthesis of coumarin analogs appended with quinoline and thiazole moiety and their apoptogenic role against murine ascitic carcinoma.* Biomedicine & Pharmacotherapy, 2019. **112**: p. 108707.

169. Luo, X., et al., *FRET-based Fluorescent and Colorimetric Probe for Selective Detection of Hg (II) and Cu (II) with Dual-mode.* Journal of Heterocyclic Chemistry, 2017. **54**(5): p. 2650-2655.

170. Wells, G., et al., *Fluorescent 7-diethylaminocoumarin pyrrolobenzodiazepine conjugates: Synthesis, DNA interaction, cytotoxicity and differential cellular localization.* Bioorganic & medicinal chemistry letters, 2008. **18**(6): p. 2147-2151.

171. Tsao, K.K., et al., *Site-specific fluorogenic protein labelling agent for bioconjugation.* Biomolecules, 2020. **10**(3): p. 369.

172. Ma, Y., et al., *Design, synthesis, physicochemical properties, and evaluation of novel iron chelators with fluorescent sensors.* Journal of medicinal chemistry, 2004. **47**(25): p. 6349-6362.

173. Thacker, P.S., et al., *Design, synthesis and biological evaluation of coumarin-3-carboxamides as selective carbonic anhydrase IX and XII inhibitors.* Bioorganic Chemistry, 2019. **86**: p. 386-392.

174. Robert, S., et al., *Novel 3-carboxamide-coumarins as potent and selective FXIIa inhibitors.* Journal of medicinal chemistry, 2008. **51**(11): p. 3077-3080.

175. TAKADATE, A., et al., *3-(7-methoxycoumarin-3-carbonyl)-and 3-(7-dimethylaminocoumarin-3-carbonyl)-2-oxazolones as new fluorescent labeling reagents for high-performance liquid chromatography.* Chemical and pharmaceutical bulletin, 1989. **37**(2): p. 373-376.

176. Ji, H., et al., *Synthesis and anticancer activity of new coumarin-3-carboxylic acid derivatives as potential lactate transport inhibitors.* Bioorganic & Medicinal Chemistry, 2021. **29**: p. 115870.

177. Ghanei-Nasab, S., et al., *Synthesis and anticholinesterase activity of coumarin-3-carboxamides bearing tryptamine moiety.* European Journal of Medicinal Chemistry, 2016. **121**: p. 40-46.

178. Yoshikawa, K., et al., *Design, synthesis, and SAR of cis-1,2-diaminocyclohexane derivatives as potent factor Xa inhibitors. Part II: Exploration of 6–6 fused rings as alternative S1 moieties.* Bioorganic & Medicinal Chemistry, 2009. **17**(24): p. 8221-8233.

179. Beignet, J., et al., *Science of Synthesis: Houben-Weyl Methods of Molecular Transformations Vol. 20b: Three Carbon-Heteroatom Bonds: Esters, and Lactones; Peroxy Acids and R (CO) OX Compounds; R (CO) X, X= S, Se, Te.* 2014.

180. Elias, R., et al., *Antifungal activity, mode of action variability, and subcellular distribution of coumarin-based antifungal azoles.* European Journal of Medicinal Chemistry, 2019. **179**: p. 779-790.

181. Shi, J., et al., *Structure–activity relationships studies of the anti-angiogenic activities of linomide.* Bioorganic & Medicinal Chemistry Letters, 2003. **13**(6): p. 1187-1189.

182. Mori, S., et al., *Structural development of a type-1 ryanodine receptor (RyR1) Ca2+-release channel inhibitor guided by endoplasmic reticulum Ca2+ assay.* European Journal of Medicinal Chemistry, 2019. **179**: p. 837-848.

183. Büyükbingöl, E., N. Daş, and G. Klopman, *Synthesis of 1,4-dihydro-4-oxo-quinoline-3-carboxylic acid derivatives as inhibitors of rat lens aldose reductase.* Arch Pharm (Weinheim), 1994. **327**(3): p. 129-31.

184. Lucero, B.d.A., et al., *Synthesis and anti-HSV-1 activity of quinolonic acyclovir analogues.* Bioorganic & Medicinal Chemistry Letters, 2006. **16**(4): p. 1010-1013.

185. Forezi, L.D.S.M., et al., *Synthesis, Cytotoxicity and Mechanistic Evaluation of 4-Oxoquinoline-3-carboxamide Derivatives: Finding New Potential Anticancer Drugs.* Molecules, 2014. **19**(5): p. 6651-6670.

186. Su, T., et al., *Design, synthesis and biological evaluation of new quinoline derivatives as potential antitumor agents.* European Journal of Medicinal Chemistry, 2019. **178**: p. 154-167.

187. Yacovan, A., et al., *1-(sulfonyl)-5-(arylsulfonyl)indoline as activators of the tumor cell specific M2 isoform of pyruvate kinase.* Bioorganic & Medicinal Chemistry Letters, 2012. **22**(20): p. 6460-6468.

188. Knauber, T. and J. Tucker, *Palladium Catalyzed Monoselective α-Arylation of Sulfones and Sulfonamides with 2, 2, 6, 6-Tetramethylpiperidine· ZnCl· LiCl Base and Aryl Bromides.* The Journal of Organic Chemistry, 2016. **81**(13): p. 5636-5648.

189. Uchiyama, M., et al., *Development of a catalytic electron transfer system mediated by transition metal ate complexes: applicability and tunability of electron-releasing potential for organic transformations.* Journal of the American Chemical Society, 2004. **126**(28): p. 8755-8759.

190. Pagliero, R.J., et al., *Design, synthesis and 3-D characterization of 1-benzenesulfonyl-1, 2, 3, 4-tetrahydroquinolines as lead scaffold for antiparasitic drug.* Letters in Drug Design & Discovery, 2010. **7**(6): p. 461-470.

191. Gerber, P., D. Swinnen, and A. Bombrun, *Sulfonamide derivatives and use thereof for the modulation of metalloproteinases.* 2011, Google Patents.

192. Berry, J.M., et al., *Quinols as novel therapeutic agents. 2.(1) 4-(1-Arylsulfonylindol-2-yl)-4-hydroxycyclohexa-2,5-dien-1-ones and related*

agents as potent and selective antitumor agents. J Med Chem, 2005. **48**(2): p. 639-44.

193.   Bhurruth-Alcor, Y., et al., *Synthesis of novel PPARα/γ dual agonists as potential drugs for the treatment of the metabolic syndrome and diabetes type II designed using a new de novo design program protobuild.* Organic & Biomolecular Chemistry, 2011. **9**(4): p. 1169-1188.

194.   Mueller, C.E., et al., *(aza) indole-, benzothiophene-, and benzofuran-3-sulfonamides.* 2018, Google Patents.

195.   Makisumi, Y., A. Murabayashi, and T. Sasatani, *Verfahren zur herstellung von 3-amino-isoxazolen.* 1983, Google Patents.

196.   Nenajdenko, V., et al., *The study of reactions of α-chlorocinnamonitriles with hydroxylamine.* Russian chemical bulletin, 2005. **54**: p. 1728-1732.

197.   Jöhnisch, K., H. Seeboth, and N. Catasus, *β-Fur-2-yl-α-halogen-acrylonitrile; Darstellung von 3-Amino-5-für-2-yl-isoxazolen.* Zeitschrift für Chemie, 1984. **24**(3): p. 93-94.

198.   Stockley, M.L., M.I. Kemp, and A. Madin, *Cyano-substituted Heterocycles with Activity as Inhibitors of USP30.* 2018, Google Patents.

199.   Kumar, R., et al., *Novel benzenesulfonamide-bearing pyrazoles and 1,2,4-thiadiazoles as selective carbonic anhydrase inhibitors.* Archiv der Pharmazie, 2022. **355**(1): p. 2100241.

200.   Francisco, K.R., et al., *Structure property relationships of N-acylsulfonamides and related bioisosteres.* European journal of medicinal chemistry, 2021. **218**: p. 113399.

201.   Kallman, N.J., et al., *Synthesis of aminopyrazoles from isoxazoles: Comparison of preparative methods by in situ NMR analysis.* Synthesis, 2016. **48**(20): p. 3537-3543.

202.   Tomala, M.D., et al., *Identification of small-molecule inhibitors of USP2a.* European Journal of Medicinal Chemistry, 2018. **150**: p. 261-267.

203.   Meijer, F.A., et al., *Covalent occlusion of the RORγt ligand binding pocket allows unambiguous targeting of an allosteric site.* ACS Medicinal Chemistry Letters, 2021. **12**(4): p. 631-639.

204.   Geng, A., et al., *Discovery of novel phenoxybenzamide analogues as Raf/HDAC dual inhibitors.* Bioorganic & Medicinal Chemistry Letters, 2019. **29**(13): p. 1605-1608.

205.   Wang, H., et al., *Iron-catalyzed one-pot 2, 3-diarylquinazolinone formation from 2-Nitrobenzamides and alcohols.* Organic letters, 2013. **15**(18): p. 4900-4903.

206.   Scheuerman, R.A. and D. Tumelty, *The reduction of aromatic nitro groups on solid supports using sodium hydrosulfite (Na2S2O4).* Tetrahedron Letters, 2000. **41**(34): p. 6531-6535.

207.   Wu, X. and Z. Yu, *Metal and phosgene-free synthesis of 1H-quinazoline-2,4-diones by selenium-catalyzed carbonylation of o-nitrobenzamides.* Tetrahedron Letters, 2010. **51**(11): p. 1500-1503.

208.   Liu, S., L. Xu, and Y. Wei, *One-pot, multistep reactions for the modular synthesis of N, N'-diarylindazol-3-ones.* The Journal of Organic Chemistry, 2018. **84**(3): p. 1596-1604.

209.   Ramadas, K. and N. Srinivasan, *Iron-Ammonium Chloride - A Convenient and Inexpensive Reductant.* Synthetic Communications, 1992. **22**: p. 3189-3195.

210.   Liu, S., L. Xu, and Y. Wei, *One-Pot, Multistep Reactions for the Modular Synthesis of N,N'-Diarylindazol-3-ones.* The Journal of Organic Chemistry, 2019. **84**(3): p. 1596-1604.

211.   Patel, S.M., et al., *Copper-Catalyzed Intramolecular α-C–H Amination via Ring-Opening Cyclization Strategy to Quinazolin-4-ones: Development and Application in Rutaecarpine Synthesis.* Synthesis, 2019. **51**(16): p. 3160-3170.

212.   Zhang, Y., et al., *Synthesis of novel N-pyridylpyrazole derivatives containing 1,2,4-oxadiazole moiety via 1,3-dipolar cycloaddition and their structures and biological activities.* Chinese Chemical Letters, 2020. **31**(5): p. 1276-1280.

213.   Shepherd, S.A., et al., *Extending the biocatalytic scope of regiocomplementary flavin-dependent halogenase enzymes.* Chemical science, 2015. **6**(6): p. 3454-3460.

214.   Morgentin, R., et al., *Two-Directional Approach for the Rapid Synthesis of 2, 4-Bis-Aminoaryl Pyridine Derivatives.* Synthetic Communications, 2012. **42**(1): p. 8-24.

215. Oh, B.K., et al., *Synthesis of N-heteropolycyclic compounds including quinazolinone skeleton using Friedel–Crafts alkylation.* Synthetic Communications, 2015. **45**(6): p. 758-766.

216. Reed, J.N. and V. Snieckus, *Ortho-amination of lithiated tertiary benzamides. Short route to polysubstituted anthranilamides.* Tetrahedron Letters, 1983. **24**(36): p. 3795-3798.

217. Govindan, K., et al., *Metal-Free N–H/C–H Carbonylation by Phenyl Isocyanate: Divergent Synthesis of Six-Membered N-Heterocycles.* The Journal of Organic Chemistry, 2022. **87**(13): p. 8719-8729.

218. Malinowski, Z., et al., *Synthesis and biological evaluation of some amino- and sulfanyl-3 H-quinazolin-4-one derivatives as potential anticancer agents.* Monatshefte für Chemie-Chemical Monthly, 2015. **146**: p. 1723-1731.

219. Fernández, A., et al., *Piperazinyl Bicyclic Derivatives as Selective Ligands of the α2δ-1 Subunit of Voltage-Gated Calcium Channels.* ACS Medicinal Chemistry Letters, 2021. **12**(11): p. 1802-1809.

220. Jang, Y., et al., *Synthesis of 2-aryl quinazolinones via iron-catalyzed cross-dehydrogenative coupling (CDC) between N–H and C–H bonds.* Organic & Biomolecular Chemistry, 2020. **18**(28): p. 5435-5441.

Chapter 7 References